# Time Reversed Acoustics and Applications to Earthquake Location and Salt Dome Flank Imaging

by

Rongrong Lu

M.S., Nanjing University, China, 2002
B.S., Nanjing University, China, 1999

Submitted to the Department of Earth, Atmospheric and Planetary Sciences
in partial fulfillment of the requirements for the degree of

Doctor of Philosophy

at the

MASSACHUSETTS INSTITUTE OF TECHNOLOGY

February 2008



Author . . . . . . . . . . . . . . . . . . . . . . . . . . . . . . . . . . . . . . . . . . . . . . . . . . . . .

Department of Earth, Atmospheric and Planetary Sciences
December 18, 2007

Certified by . . . . . . . . . . . . . . . . . . . . . . . . . . . . . . . . . . . . . . . . . . . . . . . . . . .

M. Nafi Toksöz
Robert R. Shrock Professor of Geophysics
Thesis Supervisor

Accepted by. . . . . . . . . . . . . . . . . . . . . . . . . . . . . . . . . . . . . . . . . . . . . . . . . . .

Maria Zuber
E.A. Griswold Professor of Geophysics
Head, Department of Earth, Atmospheric and Planetary Sciences

# Time Reversed Acoustics and Applications to Earthquake Location and Salt Dome Flank Imaging

by

Rongrong Lu

Submitted to the Department of Earth, Atmospheric and Planetary Sciences
on December 18, 2007, in partial fulfillment of the
requirements for the degree of
Doctor of Philosophy

## Abstract

The objective of this thesis is to investigate the applications of Time Reversed Acoustics (TRA) to locate seismic sources and image subsurface structures. The back-propagation process of the TRA experiment can be divided into the acausal and causal time domain. Studying the acausal process of TRA enables us to locate the source, such as an earthquake, inside a medium. The causal domain allows us to create a new datum through the TRA-based redatuming operators and then image the subsurface structures.

The source location application directly uses the retro-focusing feature of the TRA technique. An earthquake is traditionally located using the arrival times of individual phases, such as P and S. As a supplementary tool, TRA provides an opportunity to locate earthquakes using whole waveforms. In this TRA technique, we first record the full seismograms due to an earthquake at an array of stations. The traces are then time-reversed and numerically sent back into the medium at those station locations using an *a priori* model of the medium. The wavefield of the back-propagation is tracked and in the end energy will concentrate at a focal spot which gives the original earthquake location. Both synthetic and field experiments show the capability of the TRA technique to locate the source. TRA, combined with the idea of empirical Green's function, also provides an alternative approach to quickly estimating the focal depth for shallow events. In several field studies, solutions from other independent methodologies confirm the validity of the results.

The subsurface imaging application extends the TRA principle into a redatuming method, which allows us to image the target more effectively by bypassing the overburden – which could potentially be very complicated in certain situations – between the sources and receivers. An accurate subsurface model required by conventional imaging techniques, which can be difficult and time-consuming to obtain, is no longer the prerequisite with this data-driven, TRA-based redatuming technique. Meanwhile, by imaging from a new datum that is closer to the target, the uncertainty of the imaging operator is dramatically reduced. The applicability of imaging the salt flank with the presence of a salt canopy is investigated in both acoustic and elastic scenarios with synthetic examples. Resulting images show very good delineation of the salt edge and dipping sediments abutting the salt dome. Then with the theoretical knowledge of the technique, we apply it to a 3D field experiment. In this complex field problem, with its challenge of the 3D geometry of the salt and acquisition, together with the limitation of the single well imaging, we propose a new directional imaging approach to implementing

the TRA-based redatuming algorithm. The result is consistent with previous studies in this field, given the uncertainties on positioning of steep events from surface seismic data.

Thesis Supervisor: M. Nafi Toksöz
Title: Robert R. Shrock Professor of Geophysics

# Biography

## EDUCATION

- B.S., Department of Electronic Science and Engineering, Nanjing University, Nanjing, China. *June 1999.*
- M.S., Department of Electronic Science and Engineering, Nanjing University, Nanjing China. *June 2002.*

## WORK EXPERIENCE

- Shell International Exploration and Production Inc., Houston, TX. Intern in the Reservoir Surveillance Division. *June ~ August 2006*.
- State Street Global Advisors, Boston, MA. Intern in the Advanced Research Center. *January 2006*.
- Chevron Energy Technology Company, San Ramon, CA. Intern in the Seismic Analysis and Property Estimation Division. *June ~ August 2005*.
- ExxonMobil Upstream Research Company, Houston, TX. Intern in the Reservoir Characterization and Subsurface Imaging Division. *June ~ August 2004*.

## RESEARCH & TEACHING EXPERIENCE

- Research Assistant, Department of Earth, Atmospheric and Planetary Science, MIT. *August 2003 ~ present.*
- Teaching Assistant, Department of Earth, Atmospheric and Planetary Science, MIT. *September 2007 ~ present.*
- Research Assistant, State Key Lab of Acoustics, Nanjing University, China. *September 1998 ~ June 2002.*
- Teaching Assistant, Department of Electronic Science and Engineering, Nanjing University, China. *September 1998 ~ June 2002.*

## CERTIFICATES & AWARDS

- Certificate of completion: Two-day intensive course in "Seismic Anisotropy – Basic Theory and Applications in Exploration and Reservoir Characterization", provided by SEG Continuing Education Program. *September 2007.*
- Certificate of completion: Financial Technology Option program, provided by Sloan School of Management, MIT. *May 2007.*
- Awarded one of the Top Papers Presented at 2006 SEG Annual Meeting, New Orleans. *September*, *2006.*
- Presidential Fellowship, MIT. *2002*.

## REFEREED PUBLICATIONS

- **Lu, R.**, Willis, M. E., Campman, X., Ajo-Franklin, J., and Toksöz, M. N., 2007, Redatuming through a Salt Canopy and Target Oriented Salt Flank Imaging: accepted for ***Geophysics***.
- **Lu, R.**, Willis, M. E., Campman, X., and Toksöz, M. N., 2007, Evaluation of Elastodynamic Interferometric Redatuming: a Synthetic Study on Salt Dome Flank Imaging: in review for ***Geophysical Journal International***.
- Willis, M. E., D. R. Burns, **R. Lu**, M. N. Toksöz, and N. J. House, 2007, Fracture quality from integrating time-lapse VSP and microseismic data: ***The Leading Edge***, **26**, 1198-1202.
- Willis, M. E., **R. Lu**, X. Campman, M. N. Toksöz, Y. Zhang, and M. de Hoop, 2006, A Novel Application of Time-Reverse Acoustics: Salt Dome Flank Imaging Using Walkaway VSP Surveys: ***Geophysics***, **71**, A7-A11.

## CONFERENCE ABSTRACTS & PRESENTATIONS

- **Lu, R.**, M. E. Willis, X. Campman, J. Ajo-Franklin, and M. N. Toksöz, 2007, Redatuming through a salt canopy - Another salt-flank imaging strategy: *77$^{th}$ SEG Annual Meeting*, San Antonio, TX, *SEG Technical Program* ***Expanded Abstracts***, **26**, 3054-3058.
- **Lu, R.**, M. Willis, and N. Toksöz, 2007, Acoustic and Elastodynamic Redatuming for VSP Salt Dome Flank Imaging: *American Geophysical Union Annual Meeting*, San Francisco, CA.
- **Lu, R.**, N. Toksöz, and S. Sarkar, 2007, Earthquake Location Using Time Reversed Acoustics: *Seismological Society of America Annual Meeting*, Big Island, HI.
- **Lu, R.**, M. Willis, X. Campman, J. Ajo-Franklin, and M. N. Toksöz, 2006, Imaging dipping sediments at a salt dome flank - VSP seismic interferometry and reverse-time migration: *76$^{th}$ SEG Annual Meeting*, New Orleans, LA, *SEG Technical Program* ***Expanded Abstracts***, **25**, 2191-2195.
- **Lu, R.**, J. Rickett, and J. Stefani, 2006, Angle-dependent attenuation estimates from a walk-away VSP: *76$^{th}$ SEG Annual Meeting*, New Orleans, LA, *SEG Technical Program* ***Expanded Abstracts***, **25**, 2136-2140.
- **Lu, R.**, S. Byrne, and M. T. Zuber, 2006, Seasonal Albedo Changes on Mars from MOLA Radiometry and TES: Seeking an Explanation for Apparent "Summer Snow": *37th Annual Lunar and Planetary Science Conference*, Houston, TX, ***Expanded Abstracts***.
- **Lu, R.**, X. Campman, M. Willis, M. Toksöz, and M. de Hoop, 2006, An application of TRA to the pre-and post- stack imaging of a salt-dome flank: *68th EAEG Annual Meeting*, Vienna, ***Expanded Abstracts***.
- Toksöz, N., S. Chi, and **R. Lu**, 2006, SH-Wave Generation by an Explosion in a Complex Scattering Medium: *Seismological Society of America Annual Meeting*, San Francisco, CA.
- Willis, M. E., **R. Lu**, X. Campman, N. Toksöz, Y. Zhang, and M. V. de Hoop, 2005, An application of time-reversed acoustics to the imaging of a salt-dome flank: *American Geophysical Union Annual Meeting*, San Francisco, CA.
- **Lu, R.**, M. Willis, X. Campman, N. Toksöz, Y. Zhang, and M. V. d. Hoop, 2005, A Novel Application of Time-Reversed Acoustics: Salt Dome Flank Imaging Using Walk Away VSP Surveys: *SEG Workshop: Seismic Interferometry, Daylight Imaging and Time-reversal*, Houston, TX.
- Toksöz, N., X. Li, **R. Lu**, and M. Willis, 2005, Focal Depth Determination from P and S Coda Waves at Regional Distances: A Time-reversed Acoustics Approach: *Seismological Society of America Annual Meeting*, Memphis, TN.
- **Lu, R.**, and M. Toksöz, 2005, Application of Time Reversed Acoustics for Seismic Source Characterization: *AGU-SEG Joint Assembly Spring Meeting*, New Orleans, LA.

**Dedicated to my wife, Zhenming Song. I could not have accomplished this without her love and support.**

# Acknowledgements

I would like to first thank my advisor, Nafi Toksöz, for his encouragement, advice and guidance throughout my whole study at MIT. His scientific insight and commitment led to this immensely rewarding thesis research, despite its clear departure from my background on acoustic biomedical imaging. I need to thank for him not only for his help in completing this work, but also for help in selecting what has proved to be a fascinating and timely topic. Every conversation and discussion with Nafi during the past five years was an enjoyable one. His enthusiasm for new research topics continues to amaze me.

Another person from whom I have greatly benefited is Mark Willis, who was of great assistance in my learning about seismic migration. His extensive knowledge and experiences on seismic imaging was a huge and ready resource for consultation. Discussions with him on the insight of correlogram space were particularly inspiring.

I would also like to thank my thesis committee, Professor Nafi Toksöz, Professor Stéphane Rondenay, Professor Robert van der Hilst, Professor Thomas Herring, Dr. Mark Willis, and Dr. Richard Coates. I appreciate your time, effort and interest in my study.

Many people, currently or formerly at ERL, have contributed to my education at MIT. Professor Dale Morgan is a great teacher that can unleash students' creativity. The course taken with him was very enjoyable and has broadened my perception of inversion. I thank Dan Burns and Rama Rao for the technical discussions on some of the topics in

the thesis. Sadi Kuleli taught me how to create the beautiful maps with GMT. Bill Rodi was of great help in ray tracing algorithms and travel time calculations. Zhenya Zhu taught me experiment skills step by step. Arthur Cheng has always been a source of help on finding the right person to discuss problems in industry. Xiaojun Huang provided a lot feedback on my project. Michel Bouchon kindly shared his discrete wave number code that makes a lot of numerical tests possible. Michael Fehler is a very knowledgeable person to talk with and his presentation several years ago was the first jumpstart on my interest of Time Reversed Acoustics. Mary Krasovec was very helpful on the elastic finite difference code which makes a critical part of this thesis. Jonathan Ajo-Franklin, being very knowledgeable and having broad expertise, is also a great programmer given his background in computer science. His well-written acoustic Finite Difference code provided me a foundation framework on which I was able to advance to meet my own thesis research requirements. Xander Campman has been very helpful over the course of many fruitful discussions and consultations on mathematics and interferometry theories. Sue Turbak and Liz Henderson have been very helpful in logistical matters.

Fellow students who made my life at MIT a pleasant journey are another group of people that I want to thank. Burke Minsley not only showed me capability of inversions but also showed me how a Red Sox fan should be. Sudipta Sarkar, providing me a lot of help on the data collection for source location, is a great office mate to exchange ideas. Youshun Sun is not only a great researcher, but also a big information resource for MIT stories and Boston food. Yang Zhang, being very helpful on coding and mathematics, is also a great cooker indeed. Being another fantastic cooker, Ping Wang also has a very solid math and physics background that one can consult with. Chang Li, having a broad

expertise in seismology, also gave many hours of good competitions on the tennis court. I would also like to thank Samantha Grandi, Darrell Coles, Lili Xu, Xin Zhan, Huajian Yao, Fuxian Song, Fred Pearce, and many others for their help and encouragement.

Outside MIT, I would like to acknowledge Shell International Exploration and Production Inc. for funding the salt flank imaging project. Their data and support made this research possible. I want to especially thank Albena Mateeva, Jorge Lopez, and Andrey Bakulin for guidance and many very helpful suggestions and discussions. I also thank Javier Ferrandis for providing ancillary study data and Carol Gentry and Patsy Jorgensen for providing help copying and transmitting the data to us. I would also like to extend my thanks to Wenjie Dong, Chris Finn, Rebecca Saltzer, and Michael Payne at ExxonMobil, Bob Langan, James Rickett, Joe Stefani, and John Toldi at Chevron, who provided me great opportunities to work as an intern in their group. Those experiences not only helped me gain technological expertise, but also inspired my interests and broadened my horizon.

Most of all, I am deeply grateful to my parents, for their unconditional love and support throughout this endeavor. Thank you, Mom and Dad!

# Contents

# List of Figures

# Chapter 1

# Introduction

## 1.1 Objectives

Time Reversed Acoustics (TRA) and its applications have been an active research area for the last decade. In a typical TRA experiment, the acoustic waves due to a source inside a medium are first recorded by an array of receivers located at the boundary of the domain, then reversed in time and re-emitted into the medium at the receiver locations. The energy then propagates back to and focuses on the original source point [Fink, 1999]. The objective of this thesis is to investigate the applications of TRA to geophysical problems. I will approach this subject with a focus on two areas – one locating seismic sources and the other imaging subsurface structures. The two applications of TRA are related to the acausal and causal parts of the back-propagation process.

The first contribution of this thesis is that it demonstrates the applicability of the TRA technique, using a full waveform to locate an earthquake in a reservoir monitoring system. Over the last twenty years, reservoir monitoring has attracted a lot of attention. One of the challenges in reservoir monitoring is locating the microseismic events in the field. Traditionally, an earthquake is located by using the arrival times of P and S phases.

The retro-focusing feature of TRA can be directly applied to the source location problems and provides an opportunity to locate the earthquake using the whole waveforms. In the TRA approach, we first record the full seismograms due to an earthquake at an array of stations. The traces are then time-reversed and numerically sent back to the medium at those station locations using an *a priori* model of the medium. The wavefield of the back-propagation is tracked and in the end energy will concentrate at a focal spot that gives the original earthquake location. The TRA technique is particularly amenable at reservoir scale, in that a detailed subsurface velocity structure is usually available. This thesis also attempts to find a monitoring network with a minimum number of array elements to identify events with reasonable confidence.

The second contribution of this thesis is that it investigates an alternative approach based on TRA combined with the *empirical Green's function* for estimating the focal depth of shallow events. Source depth is an important parameter for determining whether a seismic event is an earthquake or an explosion. For deep events (>30 km) focal depth can be determined from the time differences between the primary phases (P, S) and surface reflected phases (pP, sP, sS, pS), frequently called depth phases. In the case of shallow events, the surface reflected phases are often buried in the codas of P and S waves. The scattered coda waves become particularly problematic for seismic events at regional distances; thus, the tradeoff between the focal depth and origin time becomes a typical problem in these cases. The TRA approach does not require picking phases that are buried in the coda, and provides a short cut to estimate depths of shallow events and can be automated with minimum human interaction.

The third contribution of this thesis is that it studies the applicability of using a TRA-based redatuming technique to image a salt dome flank in an environment like the Gulf of Mexico (GOM) using a Vertical Seismic Profile (VSP) dataset. Salt flank and subsalt imaging is a significant challenge in exploration seismology. It is becoming extremely difficult and computationally expensive when a complex overburden exists in the same area. After the focus is formed in a TRA experiment, wave propagation mimics a forward wavefield excited by a pseudo source located at the focal spot. This feature extends the TRA principle into a redatuming method, which is especially effective in bypassing the complicated overburden between the sources and receivers, and in imaging the targets from a closer observation position. An accurate subsurface model, required by conventional imaging techniques, can be very time-consuming to build in some situations and is no longer a prerequisite with this data-driven, TRA-based redatuming technique. Meanwhile, by imaging from a new datum that is closer to the target, the uncertainty of the imaging operator is dramatically reduced. The thesis also explores the possibility of implementing a full elastodynamic redatuming scheme and contrasts it with the prevailing simplified acoustic redatuming method.

The fourth contribution of this thesis is that it applies the TRA-based redatuming technique to a 3D field experiment. The specific acquisition geometry in the field and the complex structure of the salt pose several challenges, including the limited imaging volume due to the receiver array aperture, the spatial ambiguity of imaging a 3D volume from a single well, etc. The conventional prestack depth migration of the raw VSP records does not produce any identifiable salt flank images. A new directional imaging method, in which the redatuming operation can be considered a beam steering operation that could be used to preferentially illuminate different subsurface directions, is proposed in the thesis to address those challenges. The redatuming technique is particularly suitable for such a complex problem because it does not require knowledge of the velocity structure between the surface shots and the downhole receivers. The possible mispositioning of the salt flank due to errors in the velocity model is also dramatically reduced. This is because the imaging volume is confined in a much smaller area compared to conventional VSP migration, where the errors in the velocity model can accumulate and become serious when waves travel through a much larger volume.

## 1.2 Outline of the Thesis

Beyond the introduction (Chapter 1), I will pursue the objectives mentioned above in four chapters.

Chapter 2 describes the basic theory of TRA with an acoustic numerical experiment. The fundamental concept involved in TRA is that the wave equation is symmetric with respect to time. Based on this time-symmetry concept, I will organize the output from the numerical TRA experiment along a time axis. If taking the time when the focus is formed as time-zero, the negative time axis then denotes the period during which the waves, reinjected into the medium backwards in time, are back-propagating and forming the focus. At time-zero, the energy that focused on the source does not suddenly disappear because there is no energy sink at that spot. The concentrated energy will act as a pseudo source at the focus position. This pseudo source will excite a wavefield and propagate in a positive time axis. If one tracks only the positive time axis, it mimics a forward propagation problem due to a physical source at the focal point. This forms the basis of the TRA-based redatuming technique, which in practice is the key to bypassing the complex overburden without knowledge of its properties. This also differentiates the TRA-based redatuming methodology from the well-known Reverse Time Migration (RTM) method, although both are built on the notion of the time-symmetry property of the wave equation.

In Chapter 3, I will focus on the negative time axis (acausal domain) and time-zero, during which the wavefield back-propagates and focuses on the original source. This feature allows us to locate earthquakes with full waveforms. The advancements of modern reservoir networks can provide a wide receiver coverage that can potentially make TRA practical. I will demonstrate the feasibility of applying TRA to locate microseismic events with both numerical simulations and a field data experiment. In the numerical study, I will investigate questions involved in implementing the TRA location technique in reservoir surveillance projects, such as what kind of monitoring network is suitable for the achievement of a good focusing, how sparse the stations in a network can be, what the focal resolution is in different setups, etc. In the field experiment, I test the methodology using data collected by a microseismic monitoring network in an oil field. The location of the source using TRA requires a large computational effort. In some situations where the lateral location of the earthquake is well constrained while the depth is poorly determined (shallow events), one can estimate the focal depth with little effort by using TRA combined with the *empirical Green's function*. This application will be discussed in the last section of Chapter 3.

In Chapter 4, I will move on to the positive time axis (causal domain) to study the wavefield excited by the pseudo source, and use it to help image the subsurface structure with a Vertical Seismic Profile (VSP) dataset. Although the acquisition geometry is now changed – the sources are at the boundary of the domain and the receivers are inside the medium – the methodology is not affected thanks to the source-receiver reciprocity. The question to be answered here is this: with the TRA-based redatuming technique, can we effectively and efficiently bypass the complicated overburden by creating pseudo sources that are closer to the target so that large dipping reflectors, such as salt dome flanks, can be imaged with minimum effort? I will first describe the redatuming strategy using an acoustic synthetic 2D GOM model, and demonstrate its capability of imaging a salt flank through a salt canopy. In this target-oriented strategy, the computationally fast redatuming process eliminates the need for the traditional complex process of velocity estimation, model building, and iterative depth migration to remove the effects of the salt canopy and surrounding overburden. This may allow the strategy to be used in the field, in near real time. After this, I extend the strategy to an elastic redatuming scheme for walk-away VSPs, using P- and S-wave potentials which are derived from the spatial derivatives of the measured wavefields. The elastic redatuming scheme is tested on data simulated with an elastic finite difference algorithm. The elastic, multicomponent Green's functions between receiver locations in a vertical borehole are extracted from data recorded using P- and S-wave sources at the surface. The wavefields are redatumed into four parts: two related to the P-wave potential, and another two related to the S-wave potential. These parts are migrated separately and form four independent images of the reservoir providing a more complete elastic description of the rocks.

In Chapter 5, I demonstrate the above redatuming and imaging strategy with a 3D offshore field experiment. The 3D subsurface structure and acquisition geometry pose several new challenges to our methodology. To address those issues, I propose a directional imaging strategy that allows us to beam-form the pseudo sources to illuminate different azimuths in a 3D coordinate system. The redatuming methodology is particularly appropriate for such a complex problem because it does not require knowledge of the velocity structure between the surface shots and the downhole receivers, and the salt flank reflections are easily seen on the resulting virtual shot gathers. In contrast, applying prestack depth migration to the raw VSP records does not produce any identifiable salt flank image. The final result from our strategy is consistent with the previous study in the same field, given the uncertainties on positioning of steep events from surface seismic data.

Finally, the main results of this study are summarized in Chapter 6.

# Chapter 2

# Theory of TRA and Extensions

## 2.1 Background

Over the last decade, techniques based on the time reversal of wave fields have been investigated for applications to ultrasonic therapy (tumor or kidney stone destruction) [Hinkelman *et al.*, 1994; Thomas *et al.*, 1996], to material characterization and nondestructive evaluation [Fink *et al.*, 2000], and to acoustic communication enhancement in the ocean [Feuillade and Clay, 1992; Fink, 1999, 2006; Hodgkiss *et al.*, 1999; Kuperman *et al.*, 1998; Song *et al.*, 1999]. In Time Reversed Acoustics (TRA), the sound waves are first recorded, then reversed in time, and re-emitted simultaneously into the media at the location where they are recorded. The energy propagates back to and focuses on the original source point [Fink, 1999].

The basic concept involved in TRA is that the wave equation is symmetric with respect to time. This means that the wave equation can be run forward or backward in time with equally valid results. Suppose a source is excited at time-zero, $t_0$, at a spatial location, $\mathbf{x}_s$, and the resulting wavefield is captured and recorded on a closed surface, $\Omega$, surrounding the source. If the recorded wavefield is reversed in time and re-injected back into the medium from the surface, $\Omega$, then the wave equation guarantees that the energy will propagate back to and focus on the original source point, $\mathbf{x}_s$. This has been shown in the literature many times for both numerical [Borcea *et al.*, 2002; Delsanto *et al.*, 2002] and field experiments [Fink, 1999, 2006; Draeger *et al.*, 1997; Derode *et al.*, 2000; Sutin *et al.*, 2003].

The physical foundation of the TRA technique is rooted in the time reversal invariance of the wave equation:

$$\nabla^2\Phi + k^2 \frac{\partial^2\Phi}{\partial t^2} = 0 \tag{2-1}$$

In the equation, both the temporal and the spatial parts are second-order derivatives, which are self-adjoint in time and space, and satisfy the temporal and spatial reciprocity [Claerbout, 1976]. A typical TRA experiment is illustrated by Figure 2-1a for the forward propagation period, and by Figure 2-1b for the back-propagation period. In the forward propagation period, we record the full waveform of signals at an array of stations due to a source inside the medium. The traces are then time-reversed and put back at those station locations such that the receivers now become the sources. The wavefield back-propagates through the medium and, in the end, energy will concentrate at a focal spot which is the original source location [Fink, 1999].

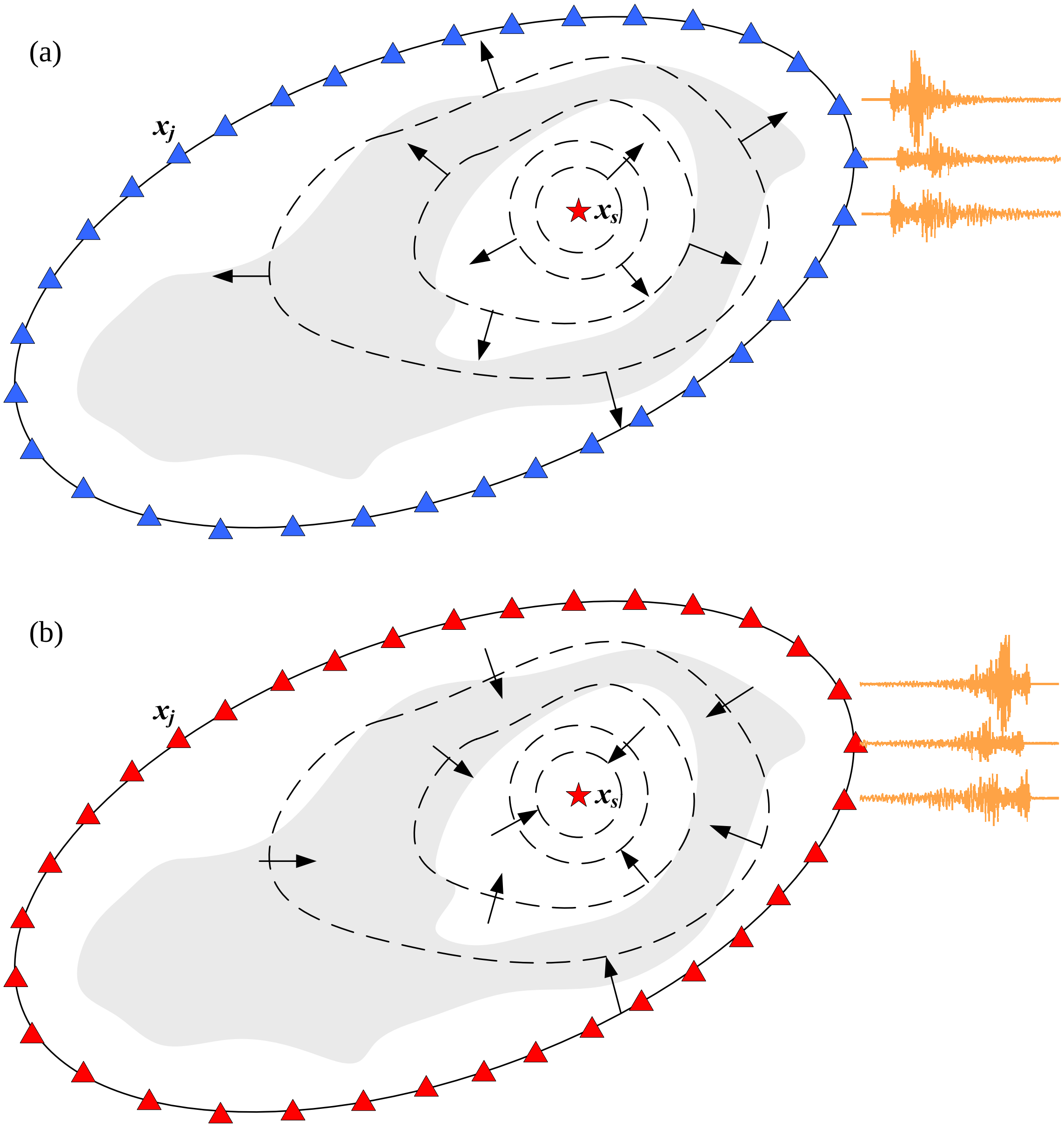


Figure 2-1: Illustration of a Time Reversed Acoustics experiment. (a) Forward propagation period: waves excited by the source travel through the complex medium and are recorded at stations marked as triangles. (b) Back-propagation period: the recorded signal are reversed in time and pumped back into the medium at the corresponding stations. The waves then propagate through the medium and converge on the original source position.

The underlying key of TRA is measuring the Green's function, $G(\mathbf{x}_j, \mathbf{x}_s, t)$, of a medium between source $\mathbf{x}_s$ and receiver $\mathbf{x}_j$. In this thesis, I will follow a similar notational convention for Green's functions as used by Wapenaar [2006]. The first term inside the parentheses denotes the spatial coordinates of the receiver, the second term denotes the spatial coordinates of the source, and the third term denotes time dependence.

First let's consider the simplest case in which we excite at the source location $\mathbf{x}_s$ a delta function signal, $\delta(t)$. The impulse response, $H(\mathbf{x}_j, \mathbf{x}_s, t)$, recorded at a receiver $\mathbf{x}_j$ on a closed surface, is then a direct measurement of the Green's function of the medium, $G(\mathbf{x}_j, \mathbf{x}_s, t)$, between the source and the receiver:

$$H(\mathbf{x}_j, \mathbf{x}_s, t) = \delta(t) \otimes G(\mathbf{x}_j, \mathbf{x}_s, t) = G(\mathbf{x}_j, \mathbf{x}_s, t). \quad (2\text{-}2)$$

where "$\otimes$" denotes a convolution operator. In practice, the source is typically band-limited, $s(t)$. So instead of measuring the direct Green's function, we obtain as our recorded signal, $r(\mathbf{x}_j, \mathbf{x}_s, t)$,

$$r(\mathbf{x}_j, \mathbf{x}_s, t) = s(t) \otimes G(\mathbf{x}_j, \mathbf{x}_s, t). \quad (2\text{-}3)$$

To back propagate the wavefield, we first time-reverse this recorded signal, $r(\mathbf{x}_j, \mathbf{x}_s, -t)$, and then inject it at the position of the corresponding receiver. Applying the source-receiver reciprocity [Claerbout, 1976], Green's function used in back-propagation is the same as Green's function used in forward propagation:

$$G(\mathbf{x}_s, \mathbf{x}_j, t) = G(\mathbf{x}_j, \mathbf{x}_s, t). \quad (2\text{-}4)$$

The recovered signal, $\tilde{s}_j(t)$, recorded at the original source location, $\mathbf{x}_s$, due to the contribution of receiver $\mathbf{x}_j$ on the closed surface, is then given by

$$\tilde{s}_j(t) = r(\mathbf{x}_j, \mathbf{x}_s, -t) \otimes G(\mathbf{x}_s, \mathbf{x}_j, t) = s(-t) \otimes [G(\mathbf{x}_j, \mathbf{x}_s, -t) \otimes G(\mathbf{x}_j, \mathbf{x}_s, t)]. \quad (2\text{-}5)$$

The convolution term, $[G(\mathbf{x}_j, \mathbf{x}_s, -t) \otimes G(\mathbf{x}_j, \mathbf{x}_s, t)]$, acts as a role of a typical matched filter. Given a signal as input, a matched filter is a linear filter whose output is optimal in some sense [Fink, 2006]. Whatever the impulse response $G(\mathbf{x}_j, \mathbf{x}_s, t)$, the convolution term $[G(\mathbf{x}_j, \mathbf{x}_s, -t) \otimes G(\mathbf{x}_j, \mathbf{x}_s, t)]$ is at a maximum at time $t = 0$ with amplitude equaling $\int G^2(\mathbf{x}_j, \mathbf{x}_s, t)\,\mathrm{d}t$, i.e., the energy of the signal $G(\mathbf{x}_j, \mathbf{x}_s, t)$. If we perform the same convolution process for all recorded signals at all stations surrounding the source, and sum them up, we can then obtain a recovered signal that would have been recorded at the source location:

$$\tilde{s}(t) = \sum_j \tilde{s}_j(t) = s(-t) \otimes \sum_j G(\mathbf{x}_j, \mathbf{x}_s, -t) * G(\mathbf{x}_j, \mathbf{x}_s, t). \quad (2\text{-}6)$$

Each representation of the $G(\mathbf{x}_j, \mathbf{x}_s, t)$ might have a different behavior, but every term in this stacking operation reaches its maximum value at time $t = 0$, which means all contributions add constructively around $t = 0$, whereas before or after time zero, uncorrelated contributions will stack out. In fact, the re-creation of a sharp peak after time reversal on an $N$-elements array can be viewed as an interference process between the $N$ outputs of $N$ matched filters [Fink, 2006]. If we only look at the time around $t = 0$, equation (2-6) indicates that the reconstructed signal at the focal spot is the time reversed version of the original source wavelet modulated by the matched filter.

## 2.2 A Simple Numerical TRA Experiment

To help illustrate this TRA process, I design an acoustic numerical experiment. I start with a velocity model that is purely acoustic and inspired by the logo of my lab, the Earth Resources Laboratory, as shown in Figure 2-2. The model consists of 8 layers including a low velocity zone. A point source with an asymmetric wavelet, as shown in Figure 2-3a, is placed at the location indicated by the yellow star in Figure 2-2. A series of receivers that form a circular array are deployed surrounding the source as indicated by the triangles in Figure 2-2.

Figure 2-4 shows the signals recorded by the receiver array, which clearly

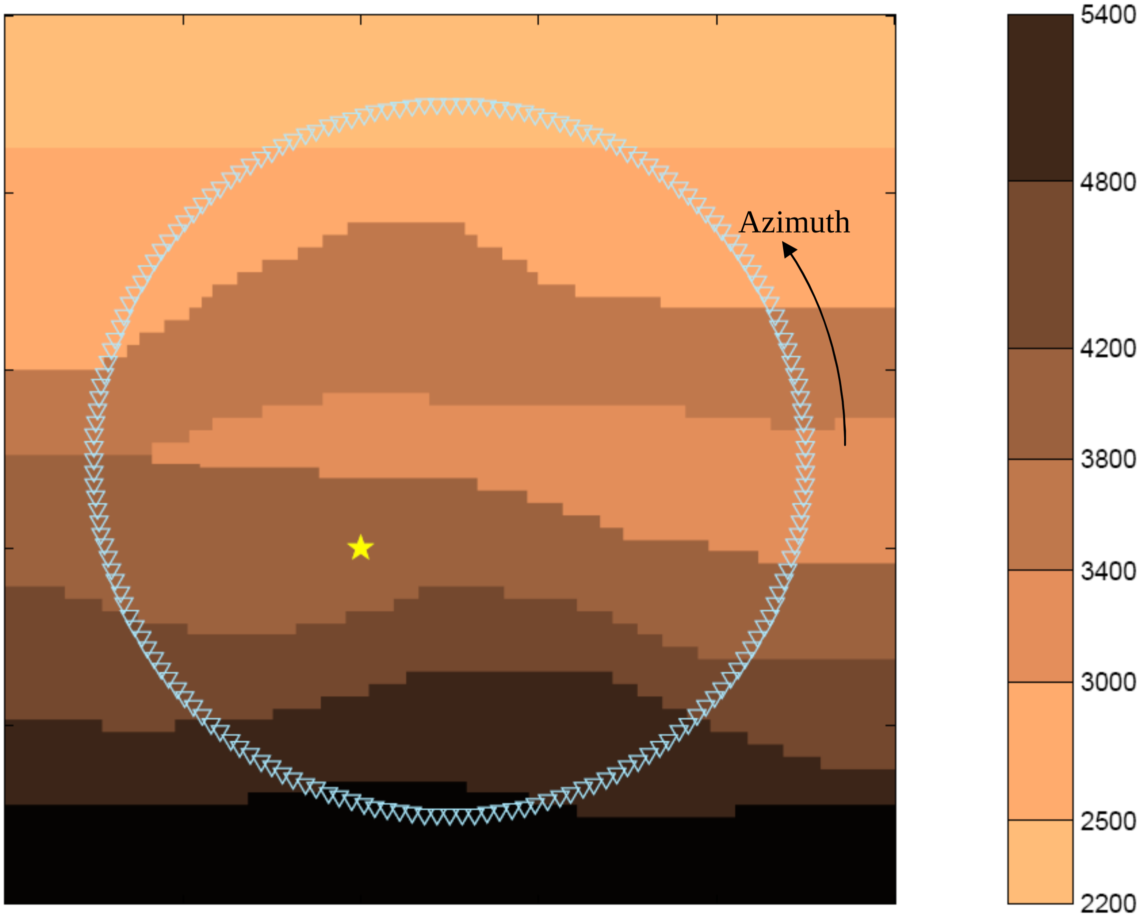


Figure 2-2: Acoustic velocity model used in the numerical TRA experiment. The model was inspired by the logo of the Earth Resources Laboratory. The yellow star denotes the position of the source and a circular array of receivers are deployed, as indicated by the triangles.

demonstrates the complexity of the acoustic wave propagation within the medium. The azimuth on the horizontal axis indicates the angle between a receiver in the array and the east-most receiver, counterclockwise. These traces will serve as the data for the back-propagation. During the forward propagation period, a series of snapshots of the wavefield captured at different time are also saved, as shown in Figure 2-5.

I then time-reverse the recorded signals, re-inject them at the corresponding receivers, and watch the back-propagating wavefield develop. The entire back-propagation can be divided into three periods separated by “time-zero” – the time when the focus forms.

(1) **Before “time-zero”**: signals are injected into the medium from the position where they are recorded, with the time axis reversed. A wavefield starts to develop from the individual receivers, which can be understood in terms of Huygens’ Principle. Figure 2-6 shows a series of snapshot taken during this period until the focus is formed, which is shown in the last panel. If only looking at the wavefield inside the receiver array and comparing it to Figure 2-5, we can see that snapshots during the back-propagation are very similar to the ones in the forward propagation except that we need to watch them backwards in time. Also notice that during the back-propagation, the energy excited from the receiver array not only propagates inwards to the focus but also creates an outgoing wavefield that propagates away from the receivers and dissipates into the surrounding medium. An absorbing boundary is used in this numerical experiment to guarantee those outgoing waves do not bounce back into the receiver enclosed domain.

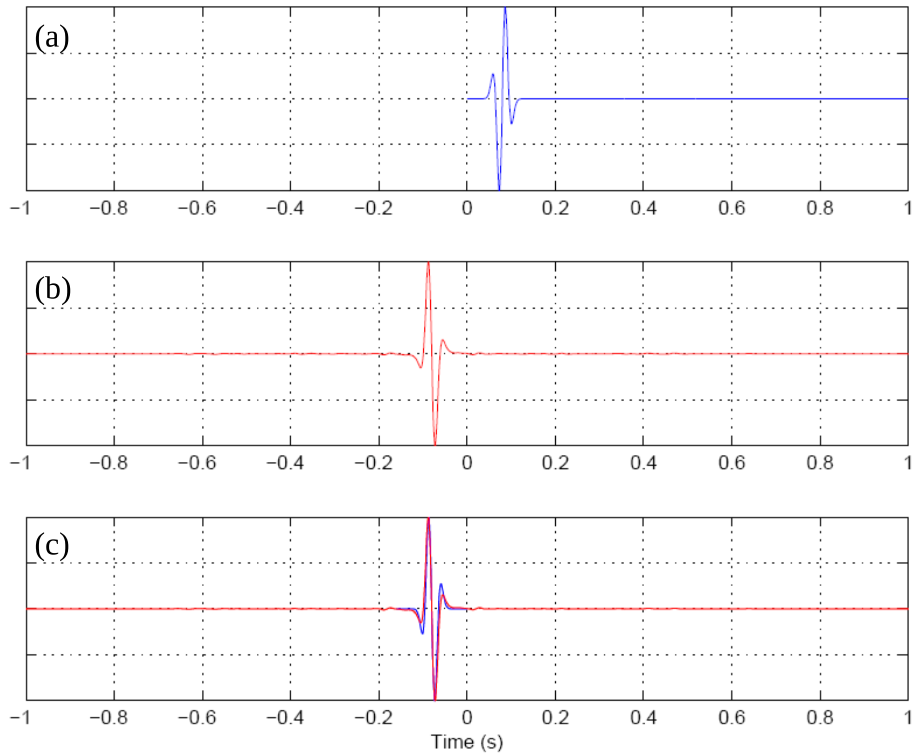


Figure 2-3: (a) Source wavelet. (b) Signal recovered at the source position during the back-propagation. (c) A time reversed version of (a) plotted on top of (b).

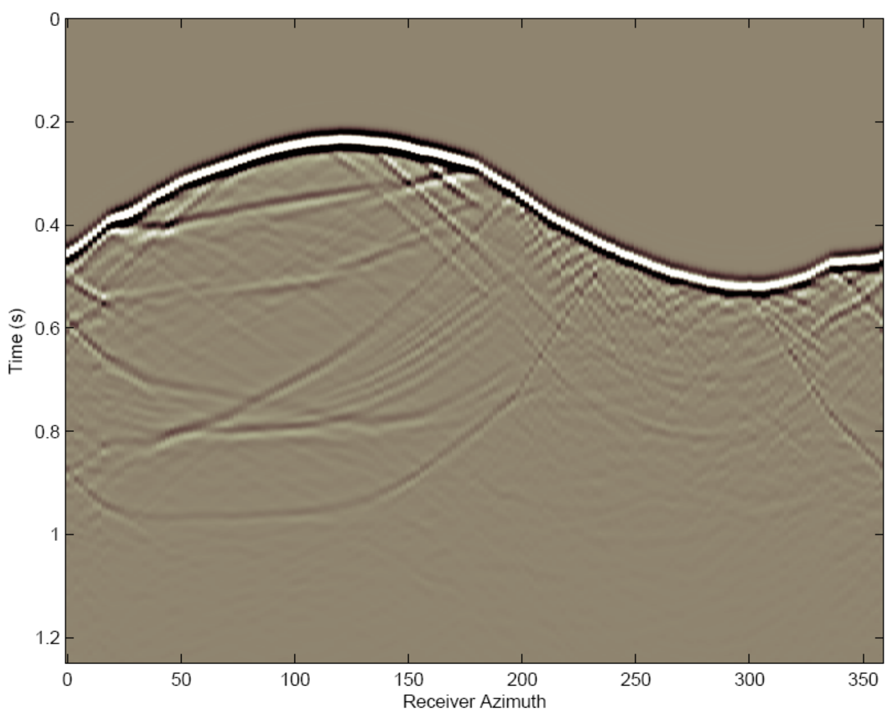


Figure 2-4: Seismograms recorded by the receivers during the forward propagation period. The azimuth indicates the angle between the East-most receiver and individual receiver in the circular array counterclockwise as shown in Figure 2-2.

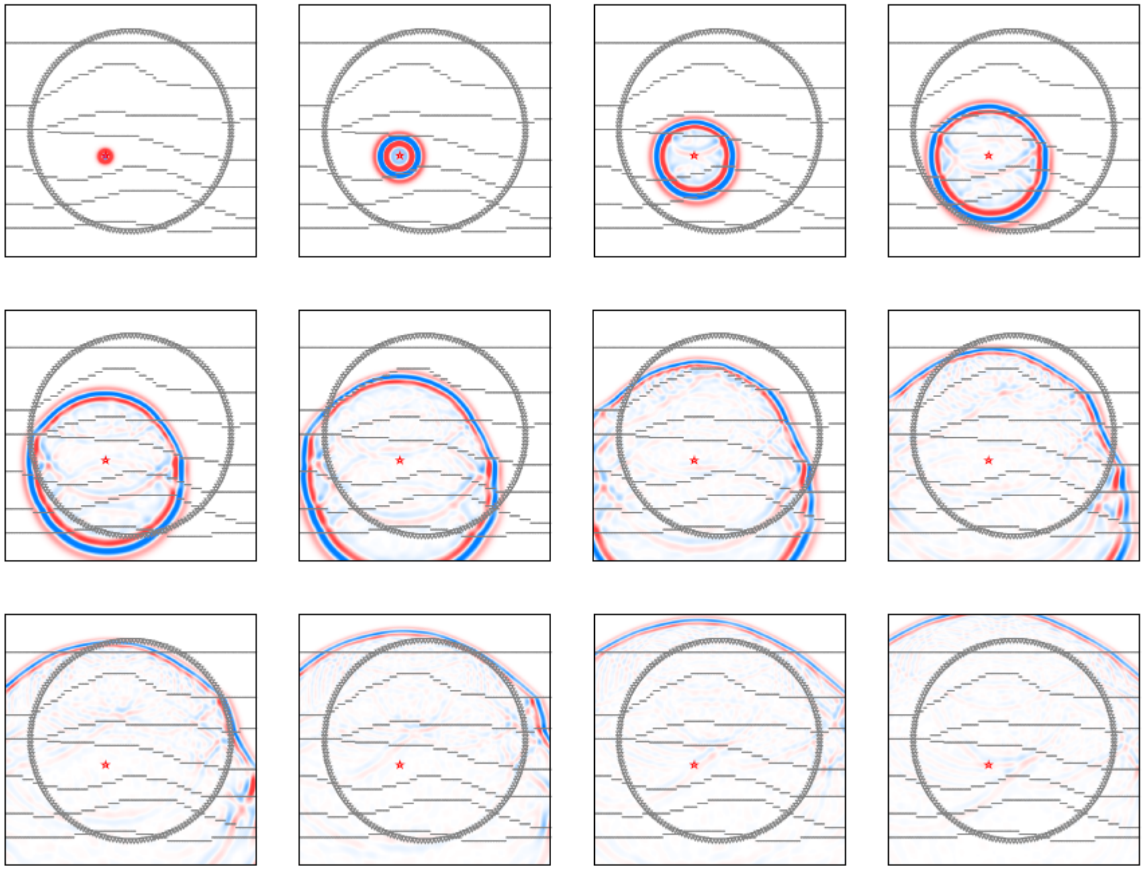

Figure 2-5: Snap shots of the wavefield captured during the forward propagation period at different time steps.

(2) **At "time-zero"**: the energy from the receiver array is concentrated at the position where the original source is located, as shown in the last panel of Figure 2-6. As indicated in equation (2-6), the recovered signal at the source is the time-reversed version of the original source wavelet. To demonstrate this, we can extract the time series recorded at the source position, assuming we put a receiver there, during the back-propagation period, as shown in Figure 2-3b. It is clear that the recovered signal at the focus point is simply the flipped version of the source wavelet, as shown in Figure 2-3a. This can be better observed in Figure 2-3c, where we plot the time-reversed version of

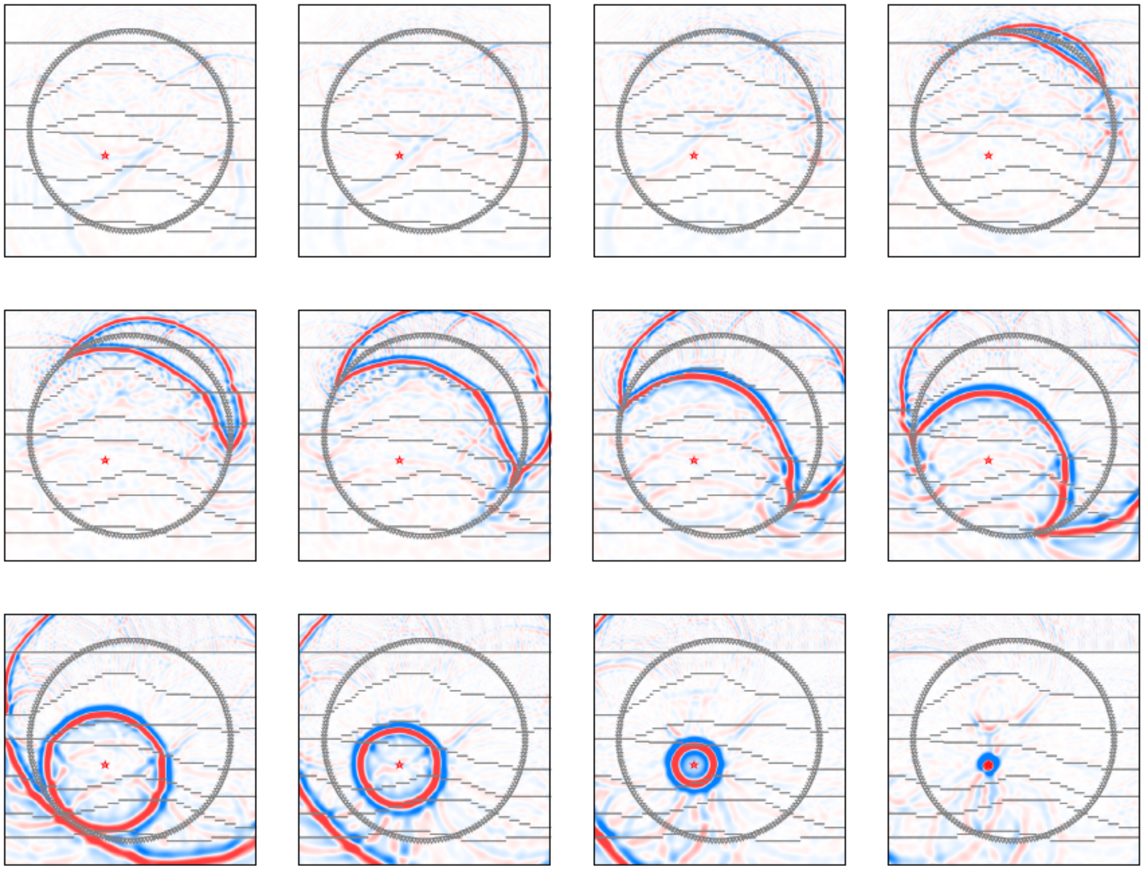

Figure 2-6: Snap shots of the wavefield captured during the back-propagation period at different time steps until the “time-zero” when the focus is formed (the last panel).

the source wavelet in blue on top of the recovered signal at focus in red. The two signals match each other very well. We can observe some small mismatches at tips on both ends of the wavelets, which could be due to (a) the limited maximum frequency that the numerical solution can resolve, or (b) the envelope of the matched filter caused by the limited number of elements in the array.

(3) **After “time-zero”**: time does not stop when the focus forms, and the energy that concentrates at the source position cannot just disappear from the medium. Because there is no energy sink in the medium, the focused energy has to continue propagating. But this time, it is propagating outwards from the focal point. Continuing from Figure 2-6, Figure 2-7 shows snapshots of the wavefield that continues propagating after time-zero,

which is shown in the first panel in Figure 2-7 and is the same shown in the last panel in Figure 2-6. Comparing Figure 2-7 to the snapshots captured during the forward propagation in Figure 2-5, we find that they are almost identical. By focusing the wavefield from several locations at the boundary of a medium onto a specific point inside the medium, one effectively creates a pseudo source at that specific point. Berkhout [1997] refers to this as *focusing in emission*. This pseudo source illuminates the surrounding area from the advantage point of the new datum (in this case the focal point) just as if an actual source excited at the focus. This is extremely useful in that as long as one can measure the focusing operators directly it is very easy to redatum the signal measured at a boundary to somewhere inside the medium. I will discuss in the next section how to use the measured signals themselves as the focusing operators in order to effectively create such a pseudo source at the focal point.

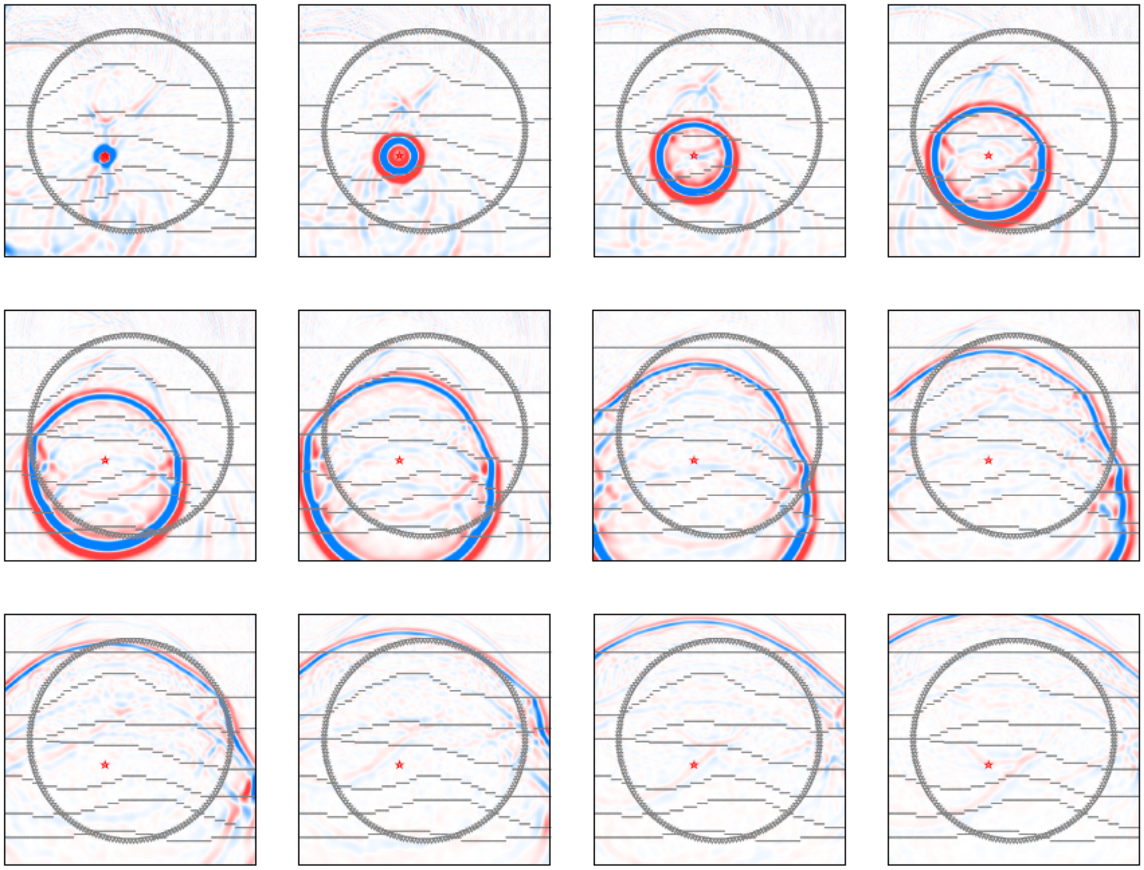

Figure 2-7: Snap shots of the wavefield captured during the back-propagation period at different time steps after the "time-zero" when the focus is formed (first panel).

## 2.3 Extensions of TRA – Redatuming

### 2.3.1 Limited Aperture and VSP Geometry

In physical TRA experiments, the wavefield from a source inside a medium is measured on a boundary surrounding that medium. The recorded wavefield is time reversed and sent back into the medium from the locations of the original recordings. The result of such an experiment is that the wavefield collapses (retro-focuses) back at the location of the source [Fink, 1999]. If the measurements are made on only part of the boundary, then the geometry corresponds to what is called a Time Reversed Mirror (TRM) in the literature.

In earth applications, such as earthquake monitoring and active exploration surveys, we generally deal with TRM, in which the time reversal operator is only applied on a limited aperture, thus apparently limiting focus quality [Fink, 2006].

The earthquake monitoring system is a typical TRM setup, in which the source is inside the earth and the monitoring stations usually cluster and occupy only a very limited area on the earth's surface. Larmat *et al.* [2006] has demonstrated that with a global station distribution and the power of supercomputers, the TRA experiment can be tested at a much larger scale. They applied the TRA to the Sumatra-Andaman earthquake (26 Dec. 2004) and showed that seismic wave energy was focused on the correct location of the earthquake. In situations where only sparse networks are available, such as reservoir monitoring systems, it is necessary to study how the limited aperture could affect focus quality. In Chapter 3, I will discuss this issue in more detail using a field example.

In the area of active exploration surveys, TRM is also very common. In Vertical Seismic Profile (VSP) acquisition geometry, as shown in Figure 2-8a, the sources are typically on the surface and the receivers are deployed inside a borehole that penetrates into the earth. In this case, the sources on the surface form the TRM; however, it is impractical to form a contour of sources that completely enclose the borehole. To mimic a TRA experiment, as shown in Figure 2-1, we can invoke reciprocity to exchange the sources and receivers. After this exchange, the geometry mimics a Reverse VSP (RVSP) acquisition (Figure 2-8b) with a collection of shot gathers acquired from many receivers on a part of an enclosing contour at surface due to downhole sources. With this data set it is straightforward to apply the retro-focusing concepts of TRA/TRM.

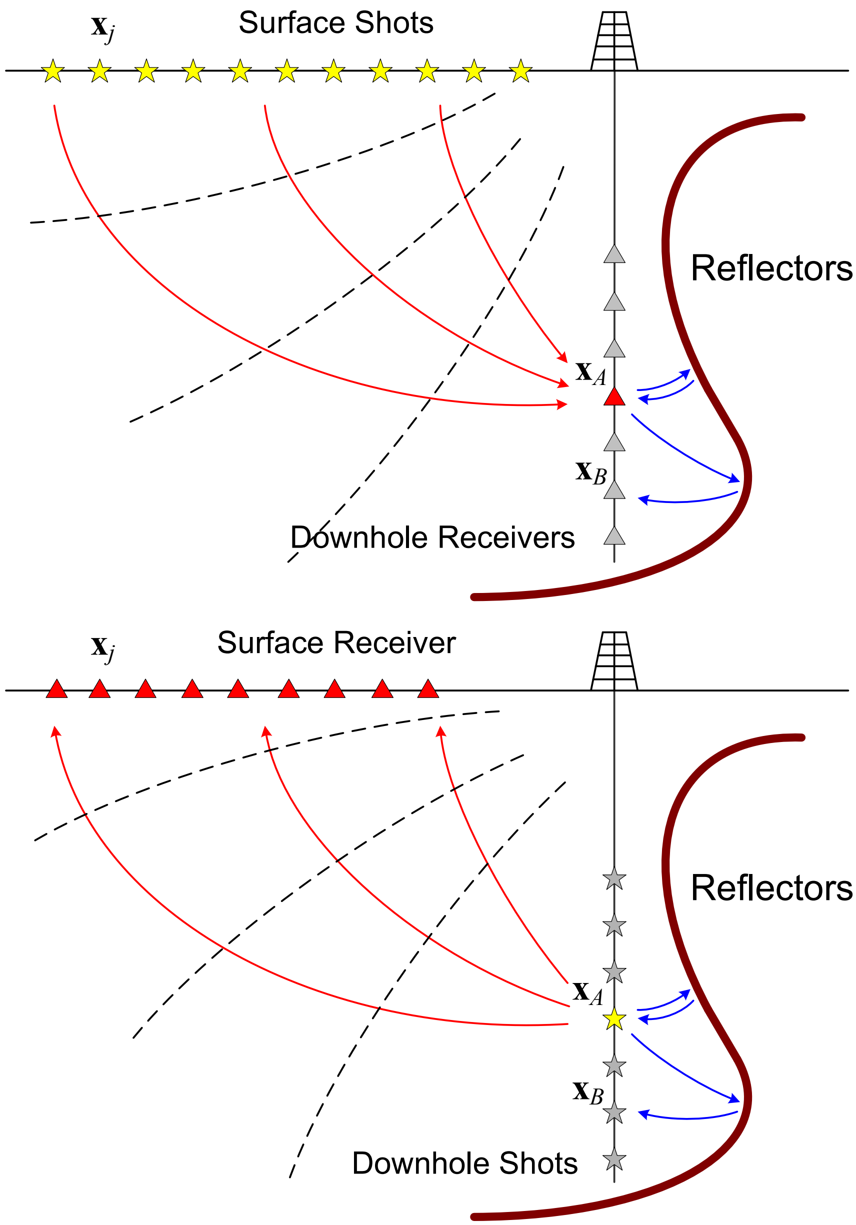


Figure 2-8: Illustration of (a) VSP and (b) RVSP acquisition geometry. In the VSP geometry, the sources are fired on the surface (yellow stars) and the receivers are located along a borehole inside the medium (red triangles). In the RVSP geometry, the sources and receivers are swapped.

### 2.3.2 Constructing Green's Function

As described in previous numerical TRA demonstration, in order to create a pseudo source at the focal spot, it is crucial to correctly estimate the focusing operator, or the extrapolation operator, which is the Green's function between the source and receiver $G(\mathbf{x}_j, \mathbf{x}_s, t)$ (Figure 2-1). Once we calculate the focusing operator, we are able to redatum the signal measured at a boundary to the focal spot inside the medium, such that it appears to have a pseudo source sitting at the original focal point. Typically, however, the calculation of this Green's function involves lots of complexity. Therefore, instead of using the exact Green's function, we could use the recorded signal itself as an *empirical Green's function* [Li and Toksöz, 1993]. In that sense, similar to equation (2-5), we use the recorded signal $r(\mathbf{x}_j, \mathbf{x}_s, t)$ – which is equivalent to $r(\mathbf{x}_s, \mathbf{x}_j, t)$ due to source-receiver reciprocity – as the back-propagation operator instead of the actual Green's function $G(\mathbf{x}_s, \mathbf{x}_j, t)$. We may then express the wavefield that would have been measured at the original source location as a convolution of the recorded waveform, $r(\mathbf{x}_j, \mathbf{x}_s, t)$ and its time reversed version, $r(\mathbf{x}_j, \mathbf{x}_s, -t)$:

$$
\begin{aligned}
\tilde{s}_j(t) &= r(\mathbf{x}_j, \mathbf{x}_s, -t) \otimes G(\mathbf{x}_s, \mathbf{x}_j, t) \\
&\approx r(\mathbf{x}_j, \mathbf{x}_s, -t) \otimes r(\mathbf{x}_s, \mathbf{x}_j, t) \\
&= [s(-t) \otimes G(\mathbf{x}_j, \mathbf{x}_s, -t)] \otimes [s(t) \otimes G(\mathbf{x}_j, \mathbf{x}_s, t)] \\
&= [s(-t) \otimes s(t)] \otimes [G(\mathbf{x}_j, \mathbf{x}_s, -t) \otimes G(\mathbf{x}_j, \mathbf{x}_s, t)]
\end{aligned}
\quad (2\text{-}7)
$$

By replacing the actual focusing operator $G(\mathbf{x}_s, \mathbf{x}_j, t)$ with the recorded waveform, we can accomplish the back-propagation of the energy from this receiver to the source location with only one complication (compare the right hand side of equation (2-5) and

(2-7)): we end up with the autocorrelation of the original source function convolved with the autocorrelation of the Green's function. Thus, by only performing its autocorrelation, it is easy to redatum any trace from its recorded location to the original source location.

Equation (2-7) illustrates how to back-propagate a single recorded trace from its receiver location to the source location using the empirical Green's function. We must now perform this same task for all recorded traces on the contour that encloses the source. This is a simple matter of summing up the autocorrelations for all individual receivers of a common source:

$$\begin{aligned}\tilde{s}(t) &= \sum_j \tilde{s}_j(t) \\ &= [s(-t)\otimes s(t)]\otimes \sum_j [G(\mathbf{x}_j,\mathbf{x}_s,-t)\otimes G(\mathbf{x}_j,\mathbf{x}_s,t)]\end{aligned}. \tag{2-8}$$

Comparing the right hand side of equation (2-6) and (2-8), the *empirical Green's function* allows us to recover the autocorrelation of the original source wavelet around time-zero instead of the exact original source time function. By using the *empirical Green's function*, we dramatically reduce the computational effort of the back-propagation into simple autocorrelation operations. However, the price we pay for this reduction is that we lose all the phase information in the recovered signal, which is now a zero-phased signal. Although obtaining the correct source wavelet still requires the phase information, the autocorrelation of the original source function itself, $s(-t)\otimes s(t)$, has already provided us with valuable information in kinematic imaging problems.

In addition, as discussed in the previous section, after the focus is formed, the causal part of the recovered signal is equivalent to the signal recorded by a receiver that is located at the focal spot. From this perspective, the causal part of the recovered signal can be seen as the zero-offset Green's function between the original source and itself; that is

$$G(\mathbf{x}_s, \mathbf{x}_s, t) + G(\mathbf{x}_s, \mathbf{x}_s, -t) \approx \frac{2}{\rho c} \sum_j G(\mathbf{x}_j, \mathbf{x}_s, t) \otimes G(\mathbf{x}_j, \mathbf{x}_s, -t) . \tag{2-9}$$

This result is equivalent to the one derived by other researchers [Derode *et al.*, 2003; Wapenaar *et al.*, 2005] from a seismic interferometry approach.

The zero-offset methodology can be extended to the non-zero-offset case by noting that the wavefield between any two points, $\mathbf{x}_A$ and $\mathbf{x}_B$, in the medium can be obtained with an expression similar to equation (2-9) [Derode, *et al.*, 2003]:

$$G(\mathbf{x}_A, \mathbf{x}_B, t) + G(\mathbf{x}_A, \mathbf{x}_B, -t) \approx \frac{2}{\rho c} \sum_j G(\mathbf{x}_j, \mathbf{x}_A, t) \otimes G(\mathbf{x}_j, \mathbf{x}_B, -t) . \tag{2-10}$$

Similar to the acoustic Green function representations in Wapenaar and Fokkema [2005], expression (2-10) forms the basis of seismic redatuming. Derode *et al.* [2003] give an excellent derivation of this expression based on physical arguments.

### 2.3.3 Redatuming with VSP Dataset

Seismic redatuming is the process of extrapolating the wave field measured at one datum to a new datum, usually at a greater depth. Traditional redatuming methods [Berryhill, 1979, 1984] use a wave equation modeling algorithm and a velocity model to numerically extrapolate the recorded data to a new datum. These methods typically attempt to regularize a field dataset recorded on a rugged surface with a variable near surface velocity to a datum that is at a depth below the surface and with a much simpler velocity field.

Recently, various novel redatuming methods have been proposed based on the principles of Time Reversed Acoustics (TRA) and source-receiver reciprocity [Wapenaar and Fokkema, 2005]. The key departure from traditional methods is that the recorded traces themselves are used as extrapolation operators, such that pseudo sources can be created inside the medium. The earth's response from the source to receiver is completely eliminated, making it useful for acquisition geometries where the source and receivers are at different datums, as in VSP or RVSP geometry.

The Green's function reconstruction principles can be directly applied to the VSP problem, forming the basis of VSP redatuming methodology. Consider a walk-away VSP (WVSP) geometry with sources $\mathbf{x}_j$ at the surface and a receiver $\mathbf{x}_A$ in the borehole, as shown in Figure 2-8a. As mentioned above, we can invoke reciprocity to exchange the sources and receivers, which creates an effective RVSP from our WVSP dataset. Keeping our original notation, we now want to retro-focus the wavefield to the downhole receiver (which is the shot location in terms of RVSP). Source-receiver reciprocity states that $G(\mathbf{x}_A,\mathbf{x}_j,t) = G(\mathbf{x}_j,\mathbf{x}_A,t)$. This means that the zero-offset Green's function at the downhole receiver is given as equation (2-9)

$$G(\mathbf{x}_A,\mathbf{x}_A,t) + G(\mathbf{x}_A,\mathbf{x}_A,-t) \approx \sum_j G(\mathbf{x}_A,\mathbf{x}_j,t) \otimes G(\mathbf{x}_A,\mathbf{x}_j,-t)\,, \tag{2-11}$$

which is the sum of the autocorrelations of the observed traces.

If instead of a delta function source, we have a conventional band-limited source, denoted as $s(t)$, the zero-offset signal, $H(\mathbf{x}_A,\mathbf{x}_A,t)$ – created by redatuming the original sources at the surface back to the borehole receiver location – is then given as the autocorrelated source wavelet convolved with the actual zero-offset Green's function:

$$\begin{aligned} H(\mathbf{x}_A,\mathbf{x}_A,t) &= [s(t)\otimes s(-t)] \otimes \sum_j G(\mathbf{x}_A,\mathbf{x}_j,t) \otimes G(\mathbf{x}_A,\mathbf{x}_j,-t) \\ &= [s(t)\otimes s(-t)] \otimes G(\mathbf{x}_A,\mathbf{x}_A,t) \end{aligned}\,. \tag{2-12}$$

The representation for $H(\mathbf{x}_A,\mathbf{x}_A,t)$ gives only kinematically correct results [Wapenaar and Fokkema, 2005], which are quite acceptable for imaging applications since we are interested in creating an image of the high impedance contrast reflectors. (To obtain a true-amplitude representation of equation (2-12) is still an ongoing research area [Mehta *et al.*, 2007].) A zero-offset section is created by gathering all the autocorrelated and summed common receiver gathers.

Essentially, the correlation-and-summation operation redatums each of the surface sources to the location of each receiver in the borehole, without having to perform velocity analysis or moveout corrections. This process retro-focuses the sources to each receiver location, creating a trace from an effective coincident source and receiver pair in the borehole. The same principle can be extended to create downhole, non-zero offset (prestack) traces. Just as in surface seismic imaging methods, the migration results using non-zero offset (prestack) data will show a significant improvement over those using zero offset (poststack) data only. This is because the non-zero offset data contain reflections from many different directions, allowing a more complete image to be reconstructed.

For a non-zero-offset case, the redatumed non-zero-offset signal between two receivers $\mathbf{x}_A$ and $\mathbf{x}_B$, $H(\mathbf{x}_A,\mathbf{x}_B,t)$, contains the autocorrelated source wavelet convolved with the actual non-zero-offset Green's function:

$$\begin{aligned} H(\mathbf{x}_A,\mathbf{x}_B,t) &= [s(t)\otimes s(-t)]\otimes \sum_j G(\mathbf{x}_A,\mathbf{x}_j,t)\otimes G(\mathbf{x}_B,\mathbf{x}_j,-t) \\ &= [s(t)\otimes s(-t)]\otimes G(\mathbf{x}_A,\mathbf{x}_B,t) \end{aligned}. \tag{2-13}$$

Repeating equation (2-13) for each combination of down-hole receivers creates the redatumed, downhole common shot gather. The zero-offset case can then be viewed as a special case of the non-zero offset where the two points, $\mathbf{x}_A$ and $\mathbf{x}_B$, in the medium are coincident.

Equation (2-13) forms the foundation of the redatuming operation, which is implemented by summing cross-correlations of the response from sources on one datum (usually at the surface) recorded by receivers on another datum (usually in the subsurface). The result is the extraction of a new dataset as if each receiver had also been a source. The result for each receiver pair can be interpreted as the Green's function between the two receiver locations. In this way, the new redatuming methods are based on the same principles as seismic interferometry [Wapenaar and Fokkema, 2006]. In contrast to traditional redatuming methods, TRA-based redatuming has the potential to overcome the complexities of the overburden without having to know its properties, as pointed out by Bakulin and Calvert [2004]. Another important application is the imaging of salt-dome flanks (Willis et al, 2005, 2006, Lu et al 2007), which will be discussed in detail in Chapter 4 and Chapter 5.

### 2.3.4 Difference with Reverse Time Migration

Reverse Time Migration (RTM) is an imaging method that has been well developed in the literature during the past 20 years [Whitmore, 1983; Baysal *et al.*, 1983; Levin, 1984; Hellman *et al.*, 1986]. However, it is important to understand that reverse time migration is distinctly different from TRA-based redatuming, although both are built upon the notion of time symmetric properties of the wave equation. TRA-based redatuming is a much more recent development coming from the medical and laboratory environments in the past few years, and only now starting to be applied to seismic data. It is a way of collapsing acoustic energy back to the source location. It does not perform any imaging.

It is actually a way of redatuming, or retro-focusing, a recorded wavefield back to the original source location.

RTM uses a numerical modeling scheme, such as finite differences or Kirchhoff extrapolation, to implement running the wave equation backward in time, and then invokes an imaging condition to create the migrated section. The entire process consists of two operations: (1) a wave equation propagation of a recorded wavefield, and (2) an application of an imaging condition. For prestack Reverse Time Depth Migration, there are actually two propagated wavefields. One is the recorded shot record, which is propagated backward in time, and the other is a synthetic shot record, which is propagated forward in time. An imaging condition is applied to corresponding snapshots of these wavefields, which amounts to a multiplication (or division) of the back-propagated shot record and the forward modeled shot record. The propagation steps are accomplished by finite difference or other numerical modeling techniques. For this method to work at all, the velocity field of the medium must be known very well.

In contrast, TRA redatuming does not require this knowledge. The velocity of the medium and sometimes even the locations of the receivers are not required. In physical experiments, the measured wavefield is re-injected back into the rock/medium and the energy retro-focuses to the source location. In computational analysis, the back-propagation is accomplished by invoking reciprocity and performing the appropriate auto- and cross-correlations. No velocity information is required, no modeling software is used, and no imaging step is performed in the redatuming.

Redatuming only creates new pseudo shot gathers with which one can further apply any imaging algorithms to obtain a final image of the structure. In fact, for the salt flank imaging application discussed in chapters 4 and 5, we frequently apply RTM imaging algorithms after redatuming to achieve an image of the target.

# Chapter 3

# Applications to Earthquake Location

## 3.1 Earthquake Location

In this study we investigate the applicability of the Time Reversed Acoustics (TRA) technique, and thus the whole waveform of the recorded signal, to earthquake locations. The basic concept involved in TRA is the fundamental symmetry of time reversal invariance -- injecting the recorded signal, with time running backwards, can focus the wavefield to the source. TRA has emerged as an important technique in acoustics with applications to medicine, underwater sound, and many other disciplines.

In the previous chapter, I show with a 2D acoustic model that by putting receivers completely surrounding the source, we are able to achieve a very good focusing at the original source location. But can we still achieve good focusing in an elastic world using complete receiver coverage? With advances in modern reservoir surveillance techniques, massive monitoring array deployment is becoming possible, which provides a good environment to implement TRA source location method in practice. However, even in the most aggressive reservoir monitoring network, it is impossible to have stations completely cover all the boundaries of a field. Thus two questions emerge: what happens when we only have partial receiver coverage, and what is the minimum requirement for TRA to be working effectively?

In this section, I experiment with different receiver coverage on a 3D model to further investigate TRA's retro-focusing properties using a full elastic model that is based on an actual reservoir monitoring network in a Middle Eastern oil field. Various issues involved in the TRA earthquake location technique will be discussed using the synthetic model data. At the end of the section, I will test the technique using real data acquired in that field.

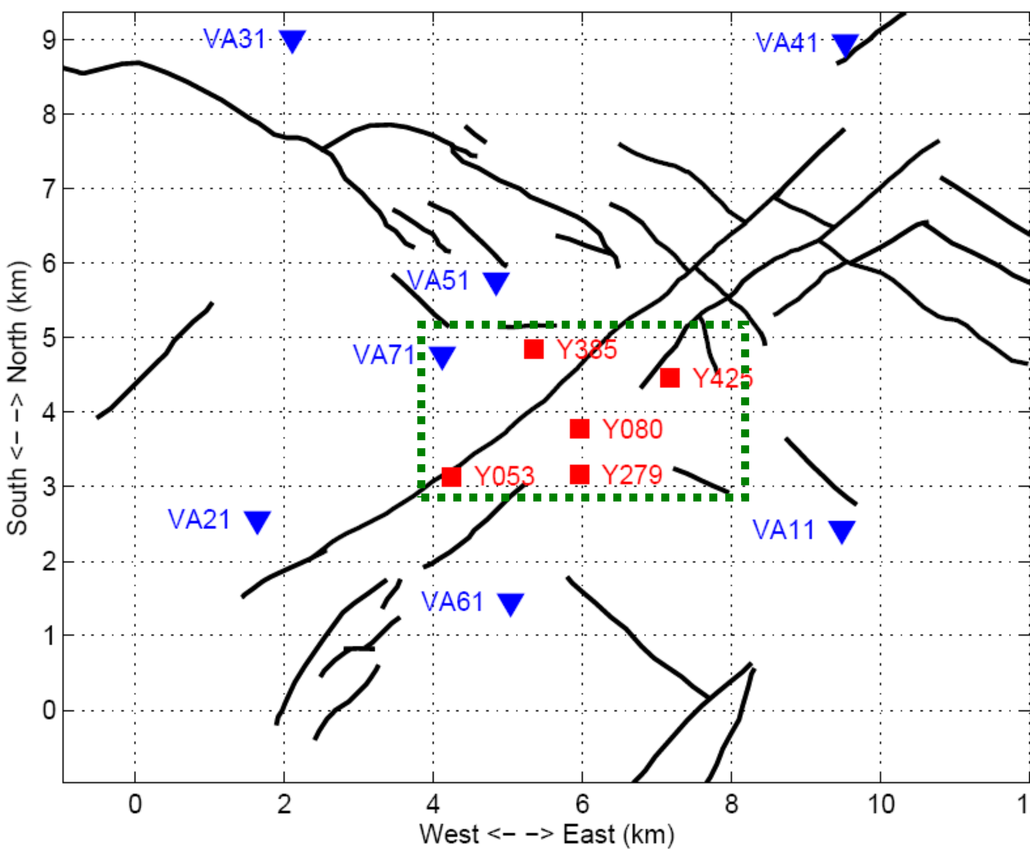


Figure 3-1: Map view of the field with faults (black line) and stations marked, blue triangles denote the surface stations in one network and red squares denote the wellhead in another network, in which five boreholes are used to deploy downhole receivers. Area enclosed by the green dashed line is shown in a 3D perspective in Figure 3-2.

### 3.1.1 Field Description

A map view of the field in a local coordinate system is shown in Figure 3-1. There are two sets of networks in this field – one is deployed on the surface with 7 stations marked as blue squares, while the other is a downhole network consisting of 5 boreholes and 8 stations in each, at a depth range of 650 m to 1200 m. Most recorded microseismic events are located at a depth range of 700 m to 1300 m. I will focus primarily on the area where the downhole network is present, as marked by the green dashed line in Figure 3-1.

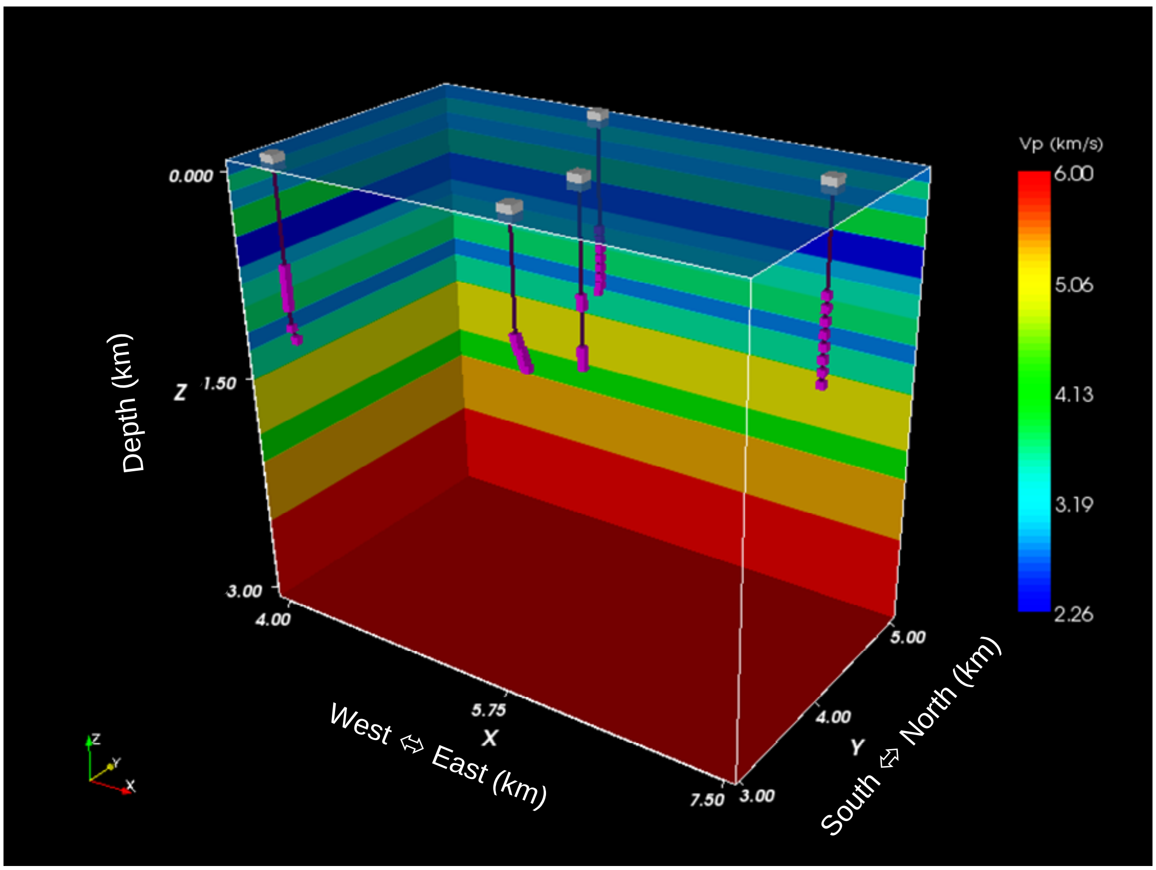


Figure 3-2: A 3D view of the field model showing the five boreholes in the second monitoring network. The cubes on the surface denote the wellhead location as shown in the red squares in Figure 3-1. Black lines draw the path of the five observation wells and purple dots indicate the position of downhole receivers. A P-wave velocity model is shown in the background which consists of 14 layers.

A 3D view of the area enclosed by the dashed line is shown in Figure 3-2 in the same coordinate system, in which the path of the five monitoring wells (black line) and location of downhole stations (purple dots) are also marked.

The velocity model (indicated by the color layers in Figure 3-2) used in this study is provided by the company operating the field. A 14-layer elastic model was built based on their best knowledge of the field. The model dimensions are 3.5 km in West-East direction (X) by 2.0 km in South-North direction (Y) by 3.0 km in depth (Z), as shown in Figure 3-2. The corresponding P- and S-wave velocity profiles are shown in Figure 3-3. (The S-wave velocity is obtained by scaling the P-wave velocity using a constant Vp/Vs

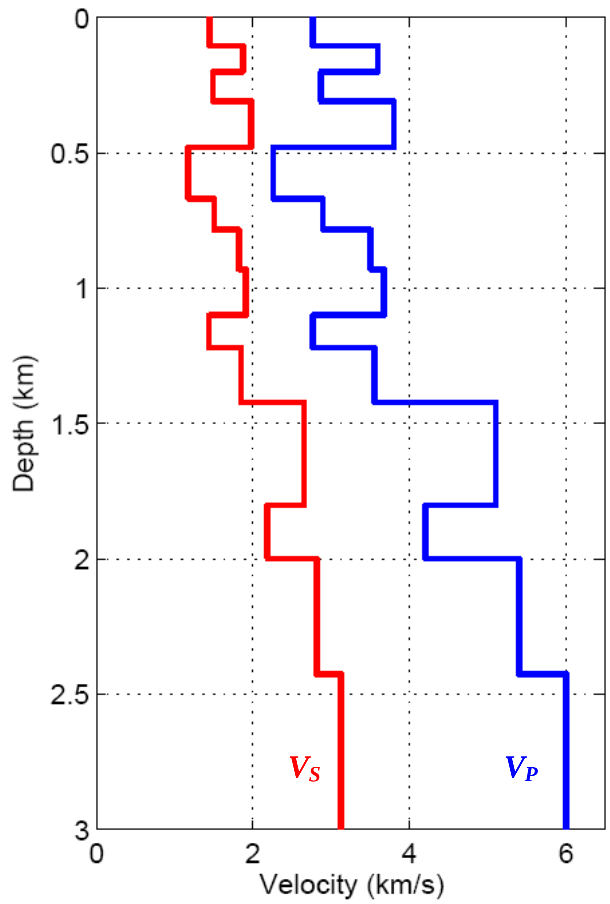


Figure 3-3: Velocity profile used in the synthetic and field experiments. P-wave velocity is plotted in blue and S-wave velocity in red.

ratio.)

### 3.1.2 Retro-Focusing Properties

It is critical to discover whether TRA also works in an elastic world. Figure 3-4a shows a “perfect” source-receiver setup for a TRA experiment using the model depicted in Figure 3-3, in which six panels of receiver array are deployed to completely surround the volume of the monitored area: one top panel on the surface (top blue dots), 4 side panels with downhole stations along the well (blue lines), and one bottom panel buried at a given depth (bottom blue dots). Given this ideal setup, if a source is excited inside the volume (red dot), can TRA back-propagate the recorded multi-component seismograms at all stations and retro-focus to the original source location? If TRA works with elastic waves, the next question is how to configure the monitoring system to implement this technique with the minimum required elements. The two typical ways of deploying reservoir surveillance are surface monitoring stations (Figure 3-4b) and downhole monitoring stations (Figure 3-4c). Which system is more effective for implementing the TRA technique? What is the focal resolution? How far can the monitoring stations be separated and remain effective? All these questions will be addressed by the following experiments.

I start with the ideal scenario as shown in Figure 3-4a in which a single source is centered in the XY plane at a depth of 1 km. A 15Hz Ricker wavelet is used as the source time function. The receivers are distributed around the volume forming an enclosed monitoring surface, which consists of one array of 30-by-15 stations, on the surface at 100 m spacing, another such array buried at a depth of 3km at 100 m spacing, and 90 vertical boreholes separated by 100 m between neighboring wells with a stream of 27 levels in each well (100 m spacing between the two levels). The receiver/well spacing is chosen to be less than half the predominant wavelength. Although this complete and dense receiver coverage is not feasible for a realistic reservoir surveillance setup, I will start with it to show what could be achieved with such a dense array distribution. The results from this experiment will also serve as the benchmark for later tests, in which the density of stations and wells will be reduced in order to examine how receiver density impacts the retro-focusing quality.

In this experiment, a point source is excited at the location indicated by the red dot in Figure 3-4a. All the receivers record the 3C seismograms for a period of time such that both P and S waves can be captured. (The S energy in this case is mostly due to the P-to-S conversions occurring at layer interfaces. In a later section, I will also demonstrate the retro-focusing capability using a slipping fault in which a large amount of shear energy is directly generated by the faulting mechanism.) Figure 3-5 shows a section of recorded traces for this forward propagation and Figure 3-6 shows the 3C seismogram

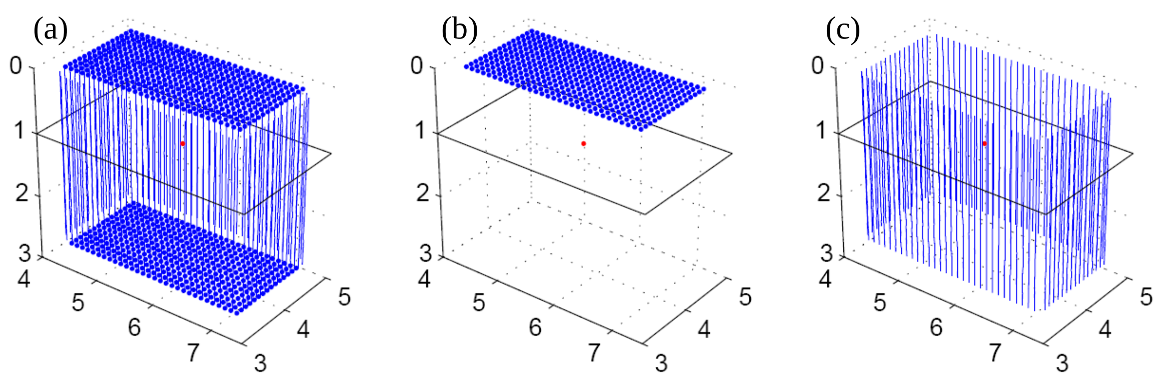


Figure 3-4: Source and receiver setup for TRA retro-focusing experiments in which a single source (red dot) is located at the center of the XY plane at depth of 1km: (a) complete receiver coverage with both surface stations (top plane), downhole stations (side planes), and buried stations (bottom plane); (b) only surface receivers are used, which is a 30 by 15 stations array; (c) only the downhole receivers are used, which contains 90 wells with 27 levels in each well.

recorded by the left-most receiver in the middle panel of Figure 3-5. Then, all of the seismograms (without gating for different phases) are time-reversed and injected back at the receiver locations as sources. At the end of the input signal (ie. at the original time-zero), snapshots of the wavefield at three orthogonal planes are captured, as shown in Figure 3-7. A clean and clear focal spot is observed at the original source location. A close look at the focal shape in different planes shows that the focus is well resolved as a symmetric sphere and its position is nicely constrained in all three directions.

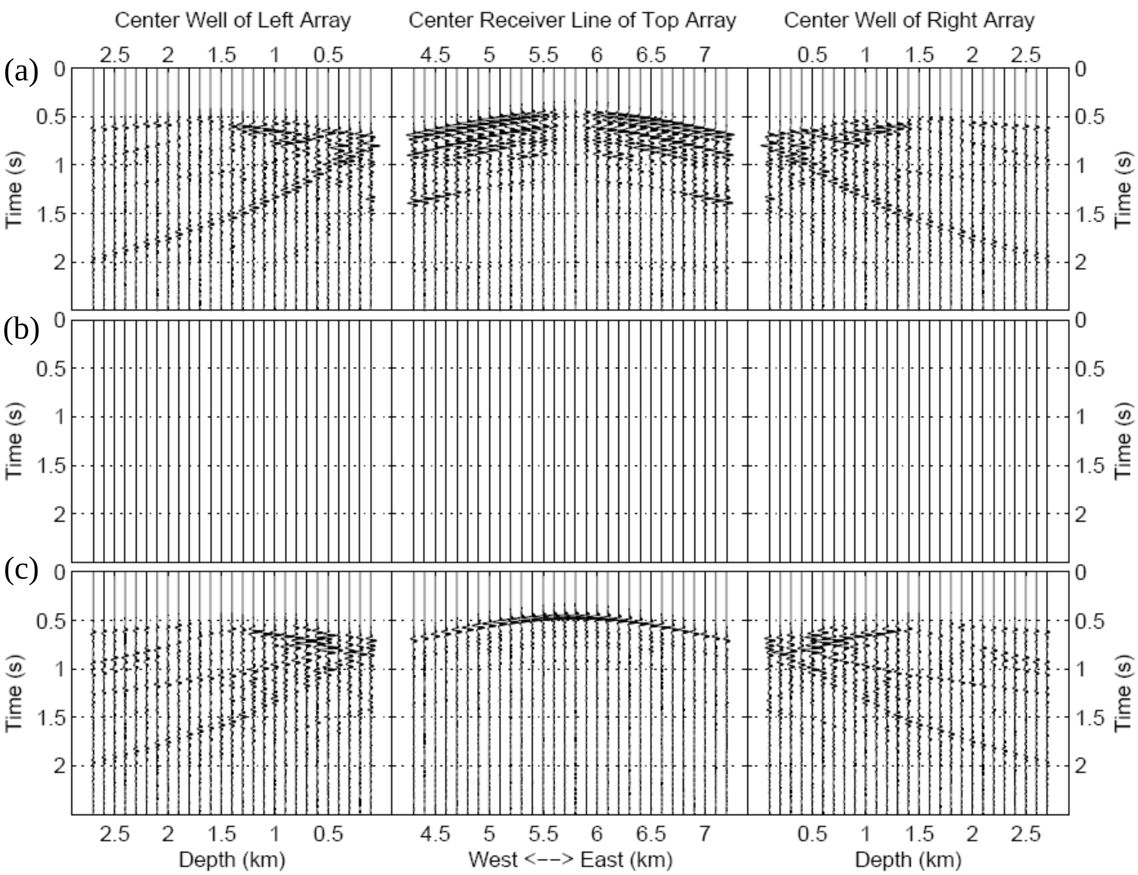


Figure 3-5: Recorded 3C seismograms during the forward propagation period. (a) X component (West-East); (b) Y component (South-North); (c) Z component. In each row, the left panel shows traces recorded by stations in the center well of the left array plane (X=4, Y=4), the middle panel shows traces recorded by stations along the center receiver line on the top array plane (Y=4, Z=0), the right panel shows traces recorded by stations in the center well of the right array plane (X=7.5, Y=4).

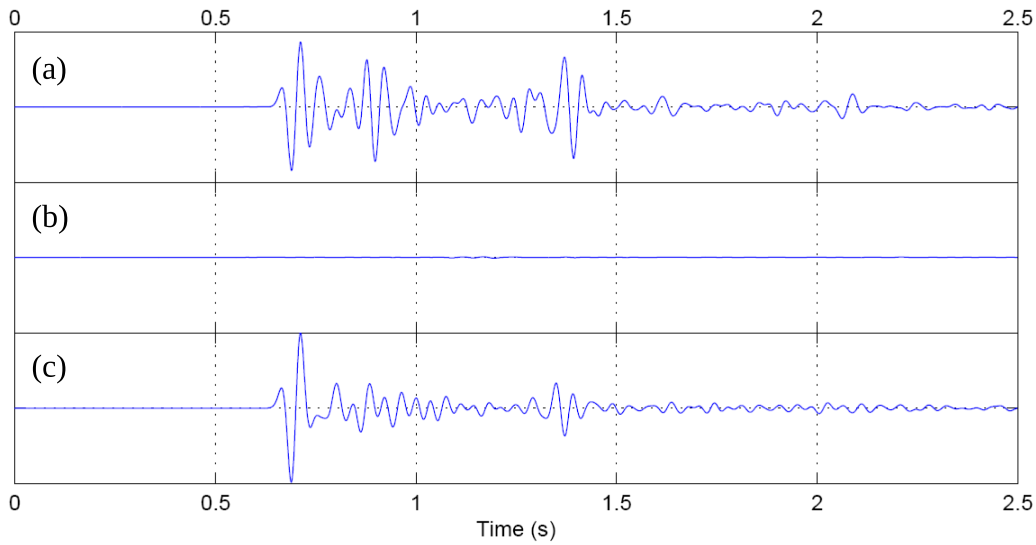


Figure 3-6: The 3C seismograms recorded by the left-most receiver in the middle panel of Figure 3-5: (a) X component, (b) Y component, and (c) Z component.

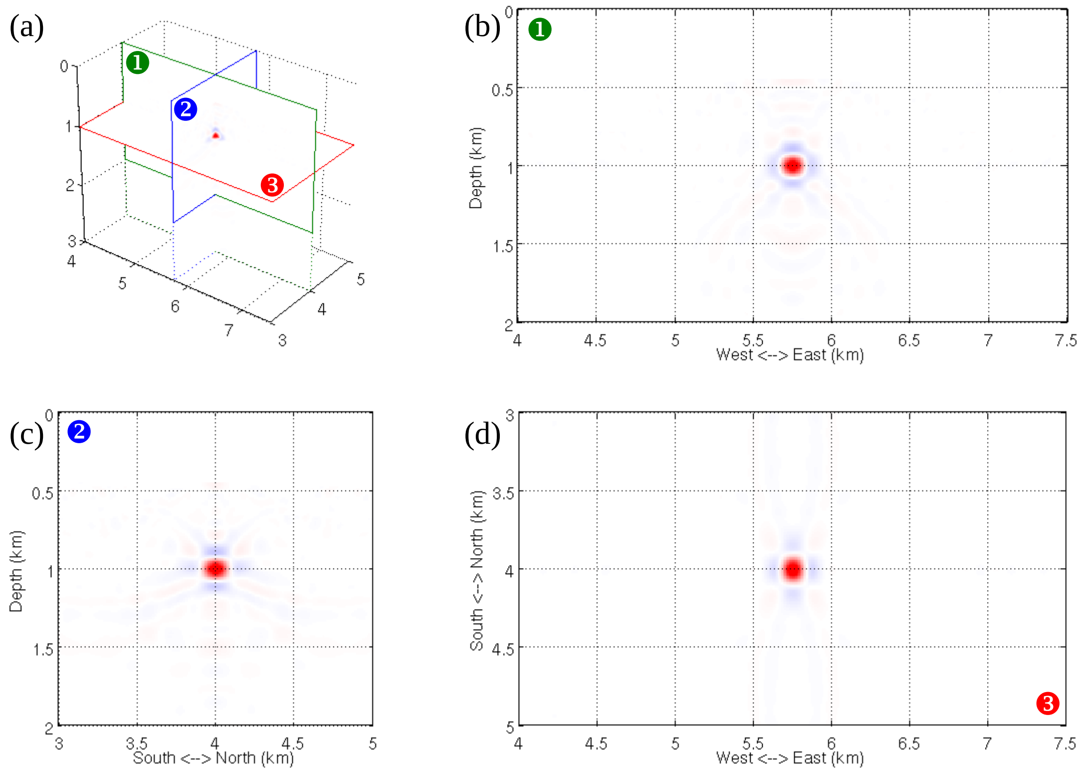


Figure 3-7: TRA results for the single source experiment with complete receiver coverage (Figure 3-4a). (a) 3D view of the three snapshot planes indicated by different colors and numbers; (b) snapshot in XZ plane; (c) snapshot in YZ plane; (d) snapshot in XY plane.

**Measurement of Retro-focusing Quality**

Two quantitative measurements, borrowed from the image processing community, are designed to check the quality of TRA's retro-focusing property.

The first index measures the correlation coefficient with respect to a benchmark output, which is achieved using the complete array coverage as shown in Figure 3-7. It verifies the accuracy of the focusing operator, and is defined as:

$$C = \frac{\int_{\forall \mathbf{x} \in D} [F(\mathbf{x}) - \bar{F}] \cdot [F_{ref}(\mathbf{x}) - \bar{F}_{ref}] \,\mathrm{d}\,\mathbf{x}}{\sqrt{\int_{\forall \mathbf{x} \in D} [F(\mathbf{x}) - \bar{F}]^2 \,\mathrm{d}\,\mathbf{x} \cdot \int_{\forall \mathbf{x} \in D} [F_{ref}(\mathbf{x}) - \bar{F}_{ref}]^2 \,\mathrm{d}\,\mathbf{x}}}, \tag{3-1}$$

where $F_{ref}(\mathbf{x})$ is the output of the benchmark experiment (Figure 3-7), $F(\mathbf{x})$ is the output of a new experiment, and $D$ denotes the output domain. $C$ reaches maximum (+1) when $F(\mathbf{x})$ is identical to the reference $F_{ref}(\mathbf{x})$; and $C$ reaches minimum (1) when $F(\mathbf{x})$ is opposite to the reference $F_{ref}(\mathbf{x})$.

The second index measures the Peak Signal to Noise Ratio (PSNR) of the output of an experiment. It provides a score which indicates how easy and confident one can locate the focal spot, and is defined as:

$$MPSNR = 20 \log_{10} \left[ \frac{\max[F(\mathbf{x})]}{\sqrt{\frac{1}{N} \int_{\forall \mathbf{x} \in D_n} n^2(\mathbf{x}) \,\mathrm{d}\,\mathbf{x}}} \right], \tag{3-2}$$

where the numerator denotes peak amplitude of an output, and the denominator denotes the overall noise level in the same output. $D_n$ is a sub-domain of the total output domain $D$, which is composed of pixels whose amplitude is less then a specific threshold. $n(\mathbf{x}) = F(\mathbf{x}|_{\mathbf{x} \in D_n})$ and $N$ is the total number of samples in domain $D_n$. The threshold is chosen in this study as the half the peak amplitude (3dB) of the output. A noise level at

5% of the peak amplitude gives *MPSNR* = 26dB; a noise level at 10% of the peak amplitude gives *MPSNR* = 20dB. In an extreme situation where the whole image is filled with random noise, the *MPSNR* score is about 10dB. Performing this measurement on the benchmark output (Figure 3-7) gives a score of 36.5dB, 38.7 dB, and 35.9dB for XY, XZ, and YZ planes.

**Surface Stations vs. Downhole Stations:**

Two commonly used monitoring setups are surface stations and downhole stations. The surface monitoring setup is shown in Figure 3-4b, in which stations are only deployed at the surface of the reservoir. I repeat the previous experiment for this scenario and the results are shown in Figure 3-8. We observe that although the focal spot is still well resolved in the XY plane, side lobes and other artifacts are present along the depth axis as shown in both XZ and YZ plane. This is expected because no downhole receivers are used in this scenario such that there is less constraint on the vertical direction compared to the idealized complete coverage. The 2D correlation coefficients are very high in this scenario – 0.93, 0.92, and 0.89 for the XY, XZ, and YZ planes – indicating a high fidelity of the location. The coefficients are less than 1.0 due to the loss of aperture. It is also interesting to see in the XY plot that the focal zone is elongated along the Y direction. This elongation is caused by the more sparse receiver coverage along the Y direction compared to the one along the X direction, hence a better constraint is received along the X direction. The MPSNR scores are also very high – 34.9dB, 36.2dB, and 32.6dB for the XY, XZ, and YZ planes – demonstrating an easily identifiable focal spot.

The downhole monitoring setup is shown in Figure 3-4c, in which only downhole receivers are deployed along a line inside the borehole. The same experiment is performed and the results are shown in Figure 3-9. It is encouraging to observe a focusing effect that is almost identical to the results from the benchmark scenario as shown in Figure 3-7. The correlation coefficients are 0.97, 0.98, and 0.97 for the XY, XZ, and YZ planes, showing an almost identical result compared to the benchmark scenario. The MPSNR scores are also higher than the surface station scenario at 35.7dB, 38.5dB, and 35.6dB for the XY, XZ, and YZ planes, which means a quieter background of the reconstructed wavefield exists thanks to the more numerous receivers deployed downhole.

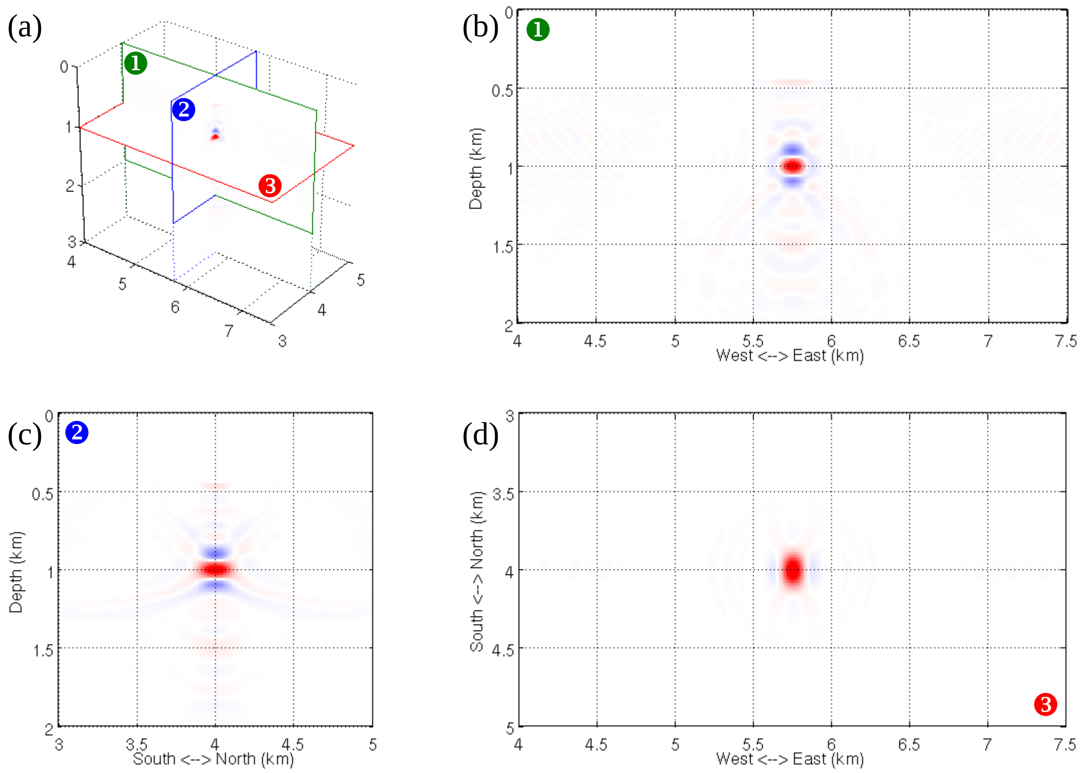


Figure 3-8: TRA results for the single source experiment with surface receivers only (Figure 3-4b). Snapshots in (a) 3D view; (b) XZ plane; (c) YZ plane; (d) XY plane.

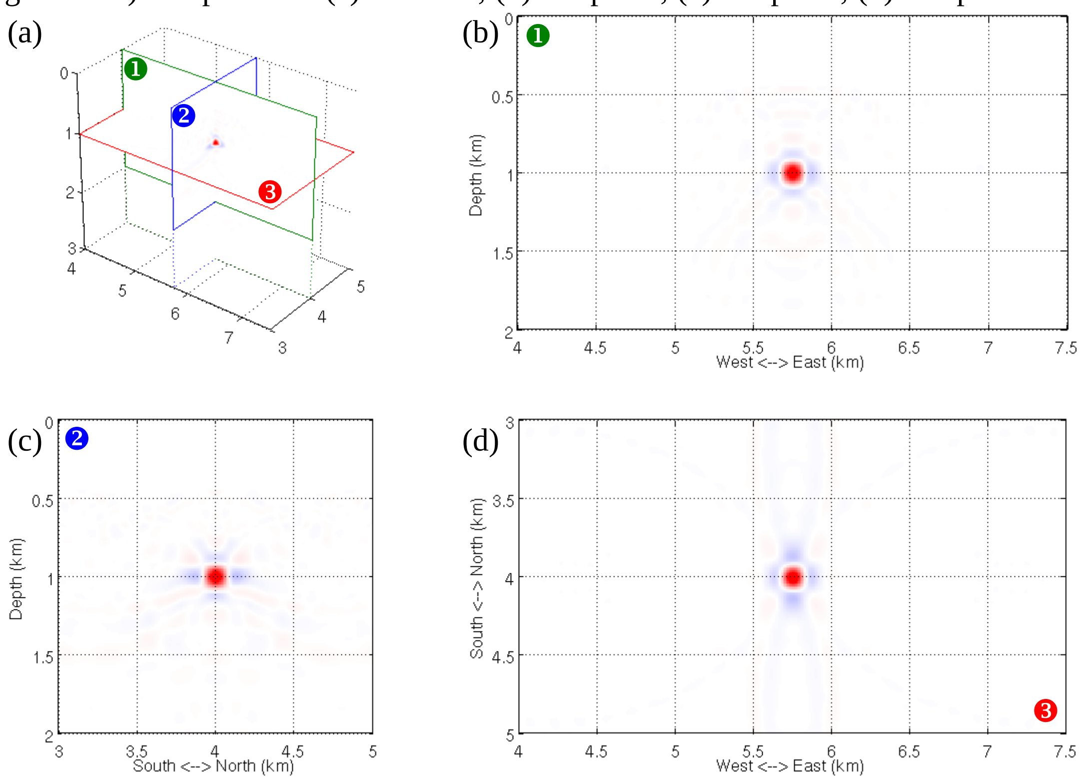


Figure 3-9: TRA results for the single source experiment with downhole receivers only (Figure 3-4c). Snapshots in (a) 3D view; (b) XZ plane; (c) YZ plane; (d) XY plane.

**Effect of Surface Station and Borehole Density**

The number of receivers used in the above experiments is far beyond any practical reservoir monitoring system. A natural question is whether the good retro-focusing quality can be preserved when decrease the station coverage. The following two experiments with sparse networks are designed to answer this question.

The first experiment uses only surface stations in an array identical to the previous experiment, as shown in Figure 3-10a: 30-by-15 stations with a spacing of 100 m (less than half wavelength). The surface array size is first reduced to 10-by-6 (Figure 3-10b) with a spacing of 300 m (about one wavelength) and then further reduced to a very sparse network of a 4-by-3 array (Figure 3-10c) with a spacing of 900 m in the X direction and the 700 m in Y direction (larger than 2 wavelengths). The corresponding results are shown in Figure 3-11 and Figure 3-12, respectively, and the correlation coefficients are calculated. Comparing these results with the one shown in Figure 3-8, it is obvious that although a sharp focus is still observable in the XY plane, the artifacts (upward arcs on both side of the focus due to wave front residues) in both the XZ and YZ planes increases dramatically. These artifacts could interfere with other sources if multiple sources are present.

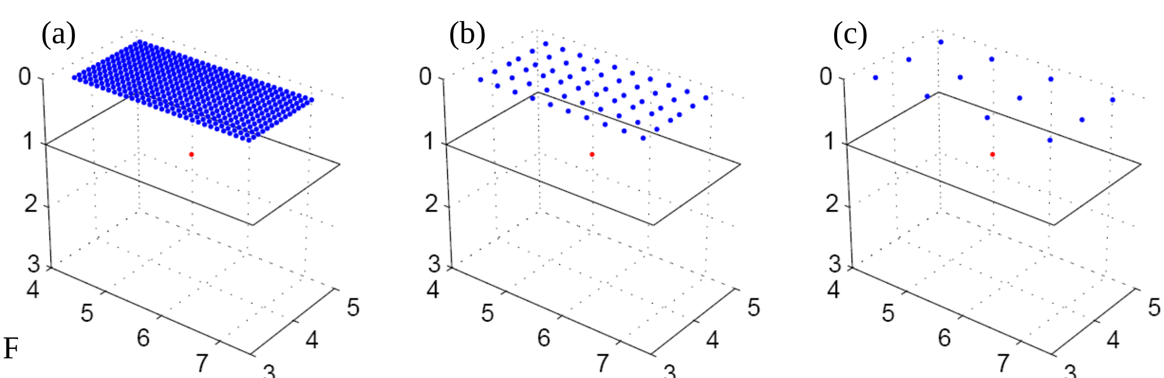


F
source TRA experiments. (a) 30-by-15 array, same as in Figure 3-4b; (b) 10-by-6 array,
(c) 4-by-3 array.

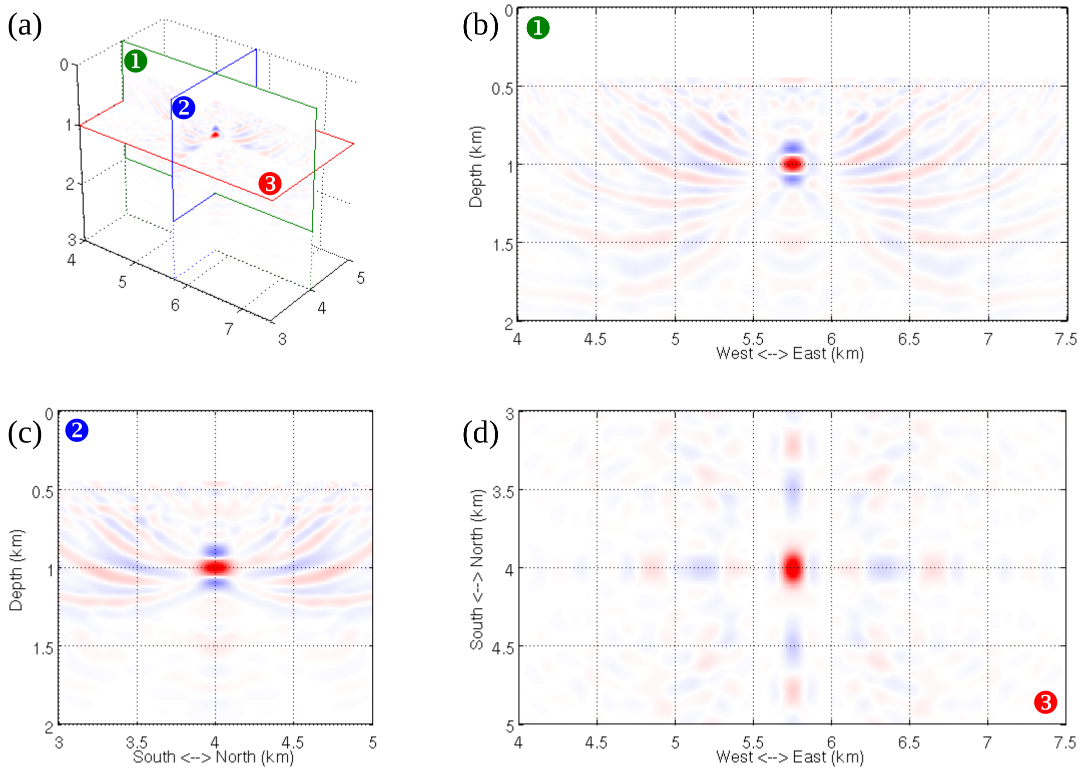


Figure 3-11: TRA results for the single source experiment with a 10-by-6 surface receiver array (Figure 3-10b). Snapshots in (a) 3D view; (b) XZ plane; (c) YZ plane; (d) XY plane.

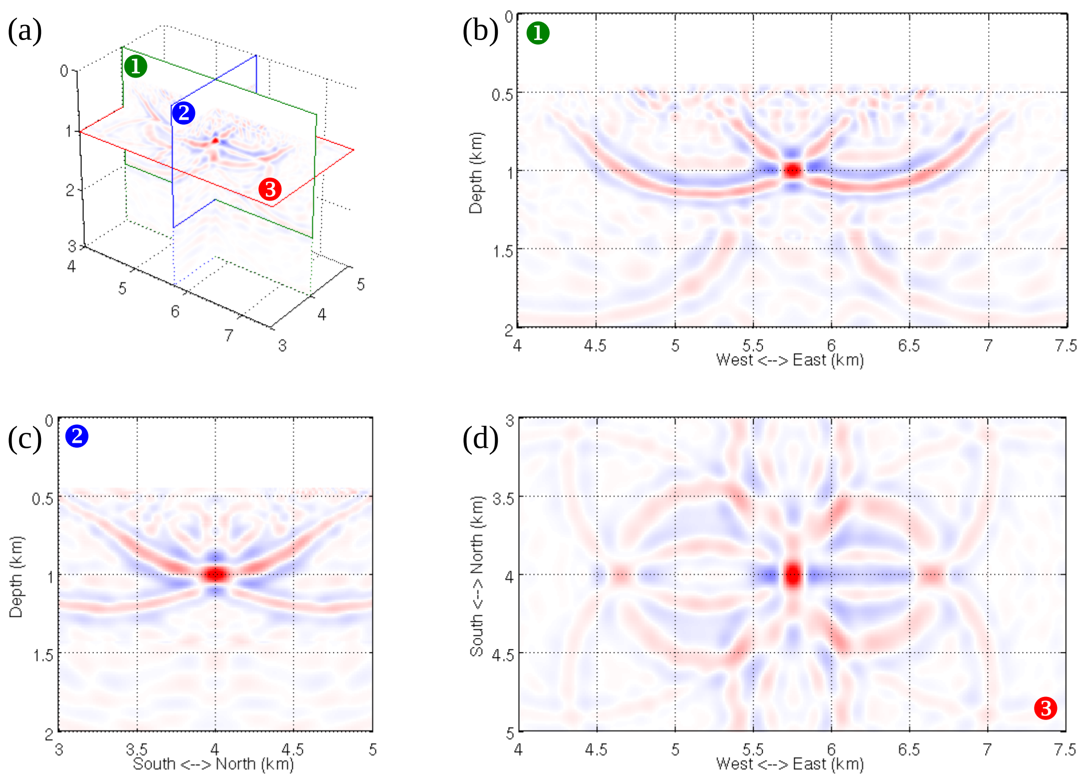


Figure 3-12: TRA results for the single source experiment with a 4-by-3 surface receiver array (Figure 3-10c). Snapshots in (a) 3D view; (b) XZ plane; (c) YZ plane; (d) XY plane.

The second experiment uses downhole stations only. The 90-well network shown in Figure 3-13a with 100 m well-to-well distance (less then half wavelength) is first reduced to a 32-well (Figure 3-13b) system with a spacing of 300 m (about one wavelength) and the results are shown in Figure 3-14. With this number of wells, very good focusing of the original source remains despite slight artifacts on the XY plane and little evidence of a space aliasing effect on the XZ and YZ plane. Then the number of wells is further reduced to a 10-well (Figure 3-13c) system with a spacing of 1000 m (larger than 2 wavelengths) and the results are shown in Figure 3-15. We can see significant artifacts in the XY plane (similar to Figure 3-12d), although TRA is still capable of creating an energy spike at the original source location. On the other side, the focusing quality in the two vertical planes is better preserved, in contrast to Figure 3-12b and c.

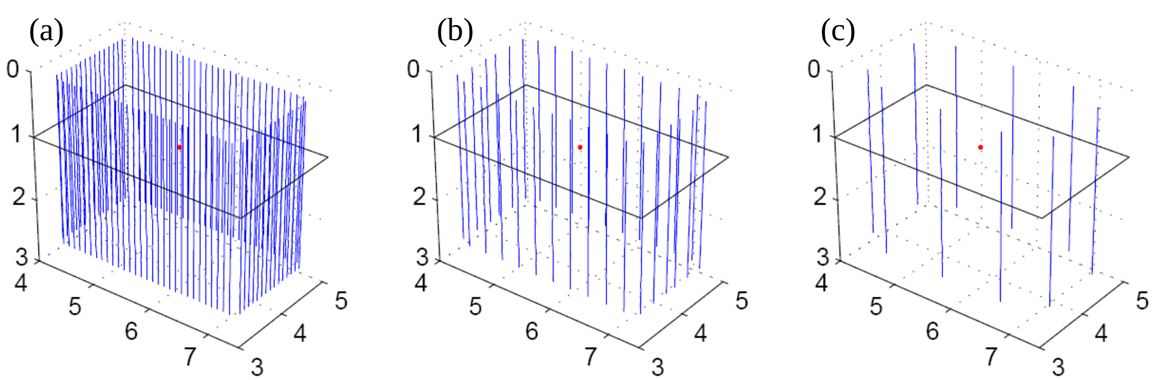


Figure 3-13: Source and receivers setups with different number of surrounding boreholes in the single source TRA experiments: (a) 90 wells, same as in Figure 3-4c; (b) 32 wells; (c) 10 wells.

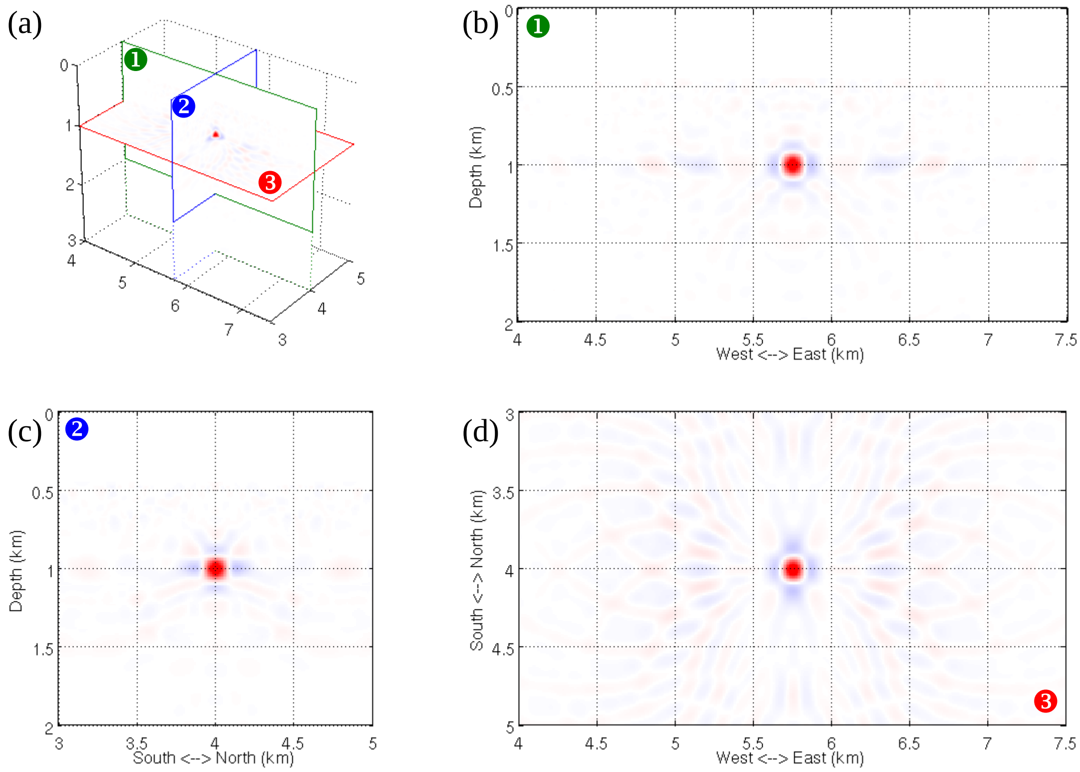


Figure 3-14: TRA results for the single source experiment with 32 boreholes (Figure 3-13b). Snapshots in (a) 3D view; (b) XZ plane; (c) YZ plane; (d) XY plane.

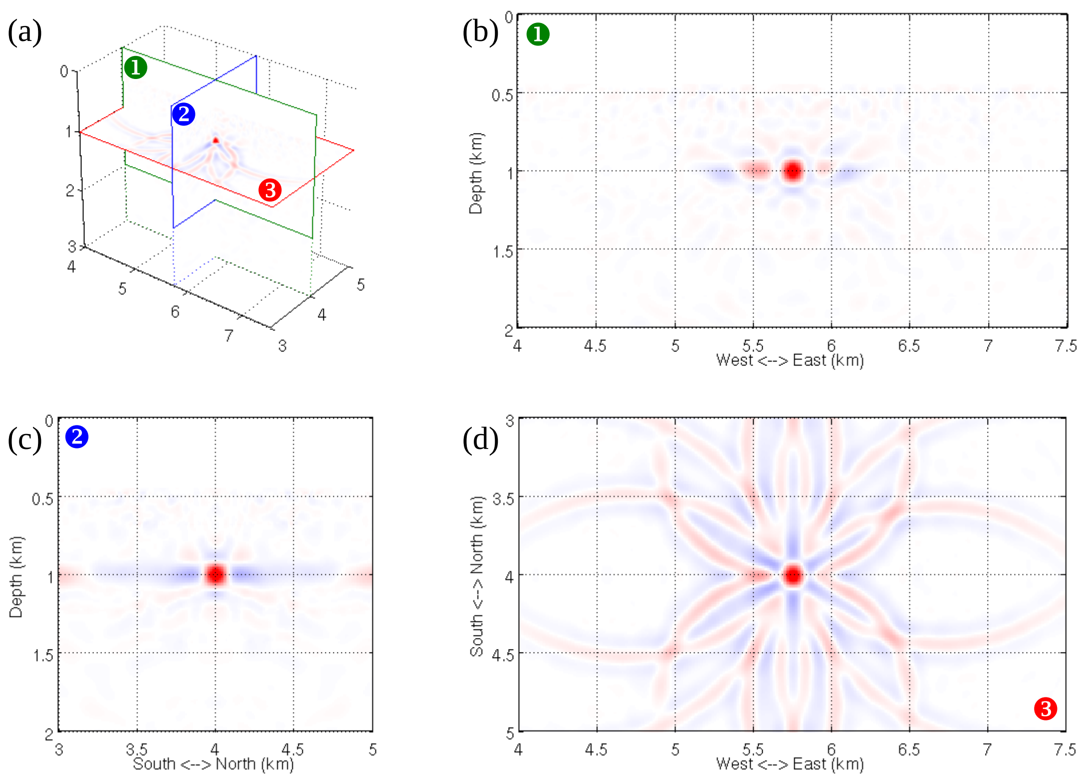


Figure 3-15: TRA results for the single source experiment with 10 boreholes (Figure 3-13c). Snapshots in (a) 3D view; (b) XZ plane; (c) YZ plane; (d) XY plane.

The correlation coefficients and MPSNR scores for these two experiments are summarized in Figure 3-16.

Both indexes decrease when receiver coverage shrinks, although the focal spot can still be easily identified in all the single source experiments. In the surface-station-only experiments, the quality change in all three planes is synchronous. In the downhole-station-only experiments, the focusing quality in the two vertical planes (blue and black

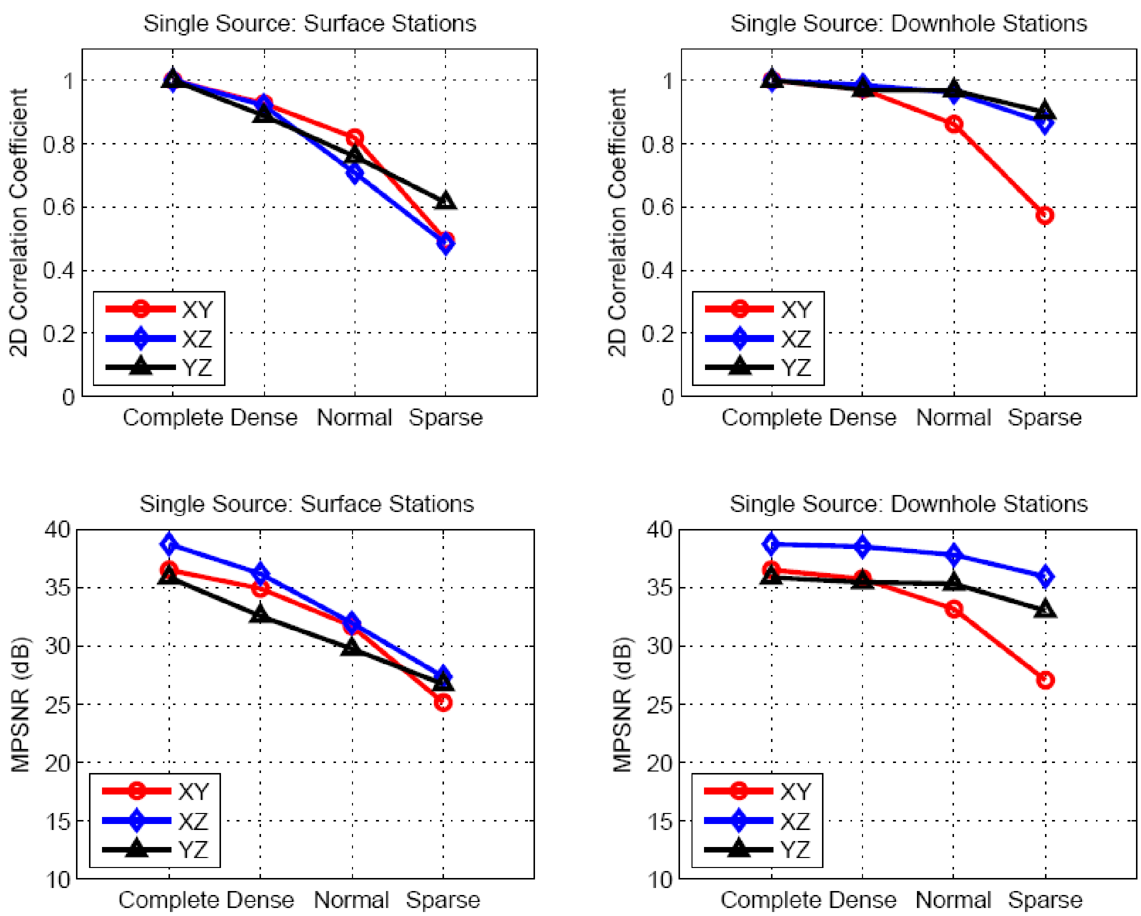


Figure 3-16: TRA retro-focusing quality for different receiver setups in the single source experiments: (a) 2D correlation coefficients for surface-station-only experiments, (b) 2D correlation coefficients for downhole-station-only experiments; (c) MPSNR score for surface-station-only experiments, (d) MPSNR score for downhole-station-only experiments. The horizontal axis in all plots indicates different receiver setups, where "Complete" corresponds to Figure 3-4a, "Dense" corresponds to Figure 3-4b and Figure 3-4c, "Normal" corresponds to Figure 3-10b and Figure 3-13b, and "Sparse" corresponds to Figure 3-10c and Figure 3-13c.

line in Figure 3-16b) are well preserved across all the scenarios, but the quality in the XY plane behaves similarly to surface-station-only experiments. The MPSNR scores in the downhole-station-only experiments for all three planes are higher than the scores in the surface-station-only experiments, indicating that the downhole-station network is better than the surface-station network, especially in situations where only a sparse network is available.

**TRA Resolution:**

To test the capability of TRA to resolve multiple sources close to each other, I design the following experiments in which an array of 11-by-5 point sources are scattered at the same plane at a depth of 1 km, as shown in Figure 3-17a. The sources are separated one wavelength apart to ensure the separation of focal spots. I repeat the previous experiments with different receiver coverages: complete coverage (Figure 3-17a, also as the benchmark case), surface stations only (Figure 3-17b), and downhole receivers only (Figure 3-17c). The correlation coefficients and the MPSNR score for three planes are also calculated in each case.

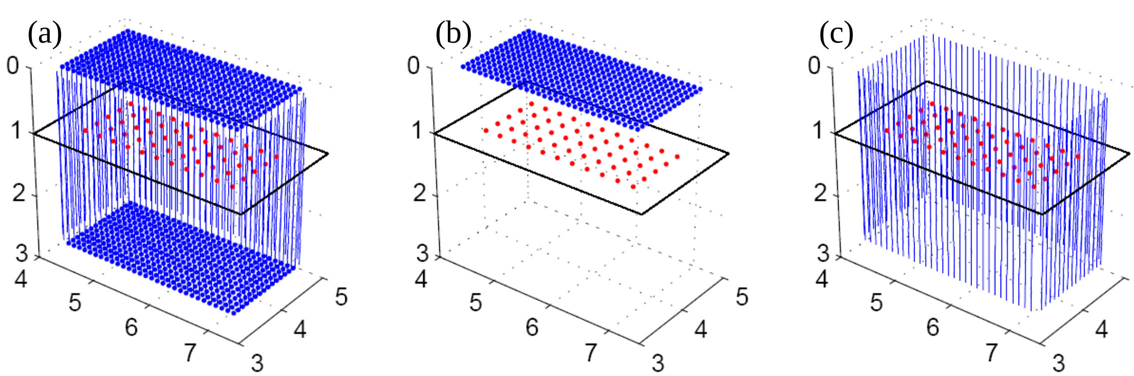


Figure 3-17: Source and receiver setups for TRA retro-focusing experiments in which multiple sources (red dot) are spread in XY plane at depth of 1km: (a) complete receiver coverage with both surface stations, downhole stations, and buried stations; (b) only surface receivers are used, which is a 30–by-15 station array; (c) only the downhole receivers are used, which contains 90 wells with 27 levels in each well.

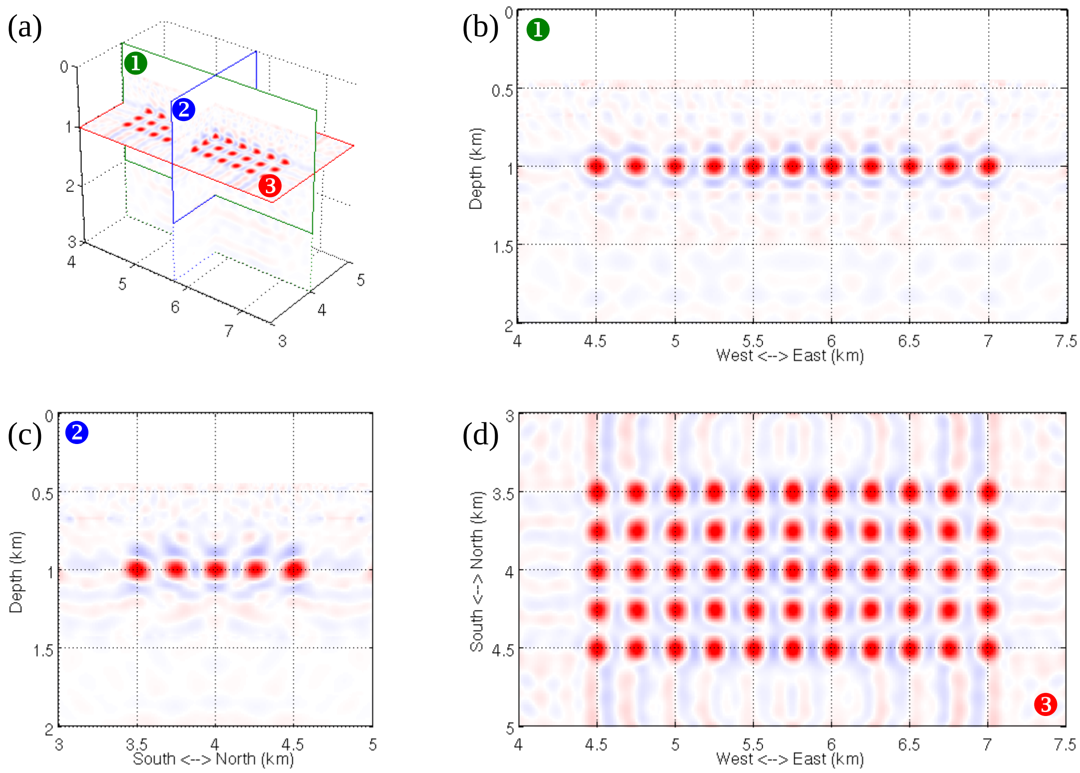


Figure 3-18: TRA results for the multiple sources experiment with complete receiver array (Figure 3-17a). Snapshots in (a) 3D view; (b) XZ plane; (c) YZ plane; (d) XY plane.

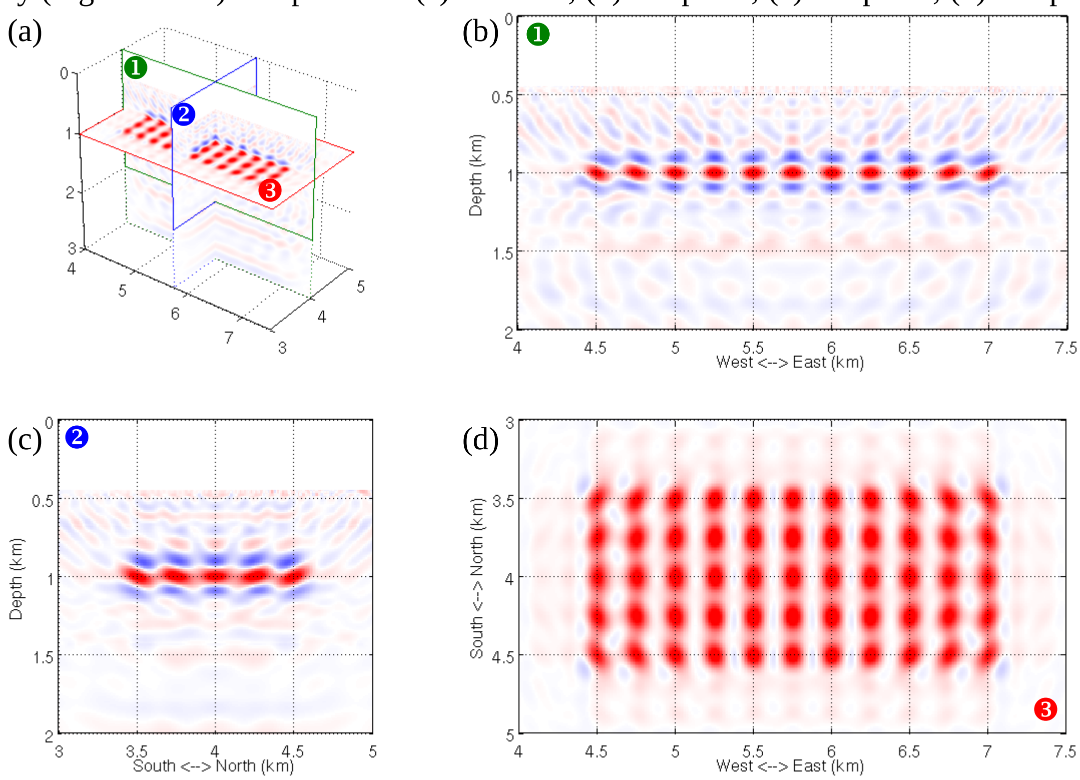


Figure 3-19: TRA results for the multiple sources experiment with surface receivers only (Figure 3-17b). Snapshots in (a) 3D view; (b) XZ plane; (c) YZ plane; (d) XY plane.

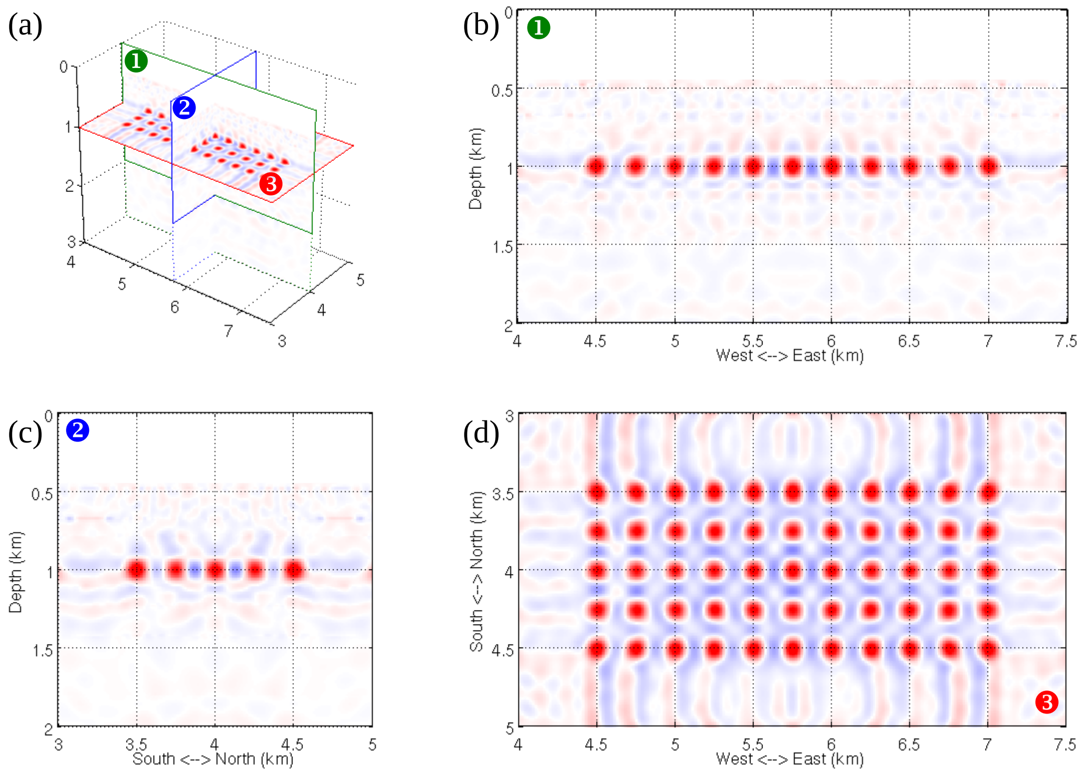


Figure 3-20: TRA results for the multiple sources experiment with downhole receivers only (Figure 3-17c). Snapshots in (a) 3D view; (b) XZ plane; (c) YZ plane; (d) XY plane.

With complete receiver coverage (Figure 3-17a), the results (Figure 3-18) show excellent separation of focal spots in all three planes with a small amount of artifacts. If only using the surface array, the focal spots in all three planes become smeared, although they are still distinguishable (Figure 3-19). As in the single source case, if only using downhole receivers, the focusing results (Figure 3-20) are very close to the ones shown by complete receiver coverage (Figure 3-18).

Things become more interesting when the receiver density is decreased. In the first experiment, only a surface array is used, but the number of receivers is reduced from 30-by-15 (Figure 3-21a) to 10-by-6 (Figure 3-21b, results shown in Figure 3-23), and further to 4-by-3 (Figure 3-21c, results shown in Figure 3-24). The correlation coefficients with respect to the benchmark (Figure 3-18) and MPSNR scores in three planes are summarized in Figure 3-27a and c. The results show that the fewer surface stations, the poorer the quality of the focal spot. In the case where the station spacing is close to one wavelength, which is also the separation of two nearby sources, the focal spots are still distinguishable in spite of the higher level of artifacts. In the case where only a 4-by-3 receiver array is used, the artifacts on the XY plane are significantly greater due to the spatial aliasing; thus the focal spots are indistinguishable. In the XZ and YZ plots, the depth of the source plane is impossible to determine due to the fact that little constraints are imposed along the depth axis. Especially in the XZ plane, the wavefront artifacts would result in incorrect focal depth if interpreted with the maximum energy.

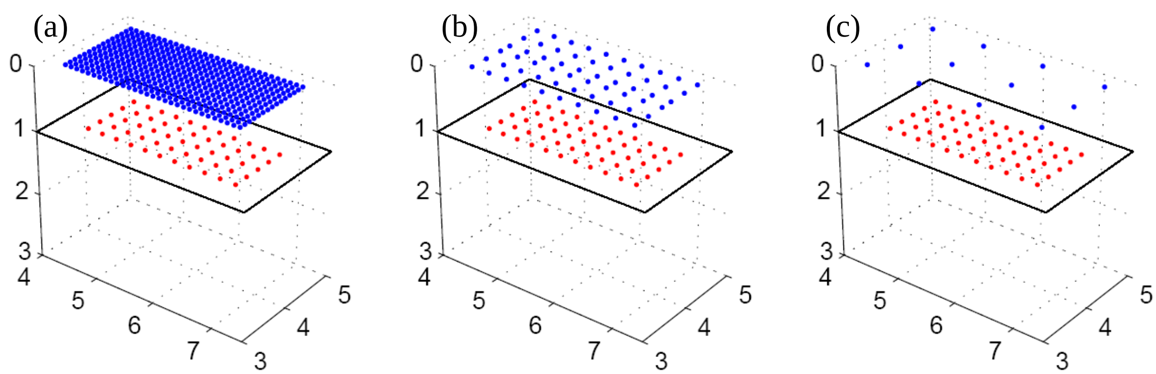


Figure 3-21: Sources and receivers setups with different surface arrays (a) 30-by-15 array, same as in Figure 3-17b; (b) 10-by-6 array; (c) 4-by-3 array.

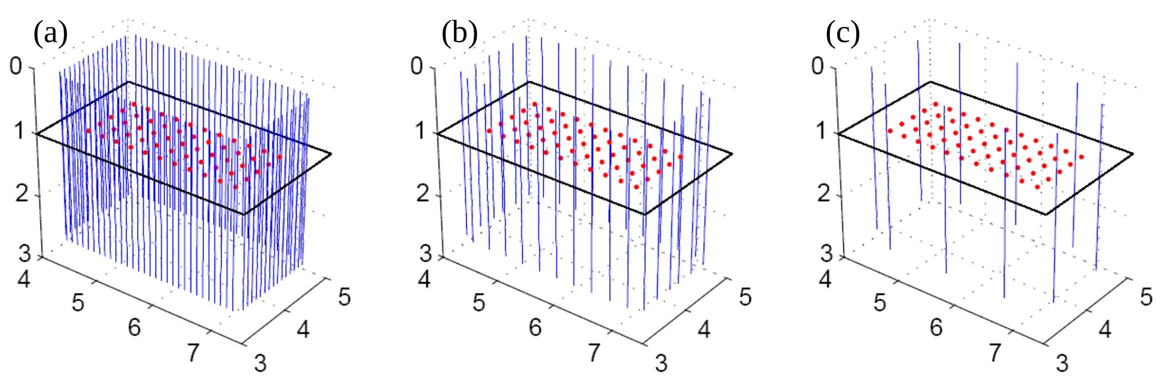


Figure 3-22: Sources and receivers setups with different number of boreholes: (a) 90 wells, same as in Figure 3-17c; (b) 32 wells; (c) 10 wells.

In the second experiment, only the downhole receiver array is used, but the number of wells is reduced from 90 (Figure 3-22a) to 32 (Figure 3-22b, results shown in Figure 3-25), and further to 10 (Figure 3-22c, results shown in Figure 3-26). The correlation coefficients and MPSNR scores in three planes are summarized in Figure 3-27b and d. In this set of results, we also observe a significant drop in the focusing quality when the number of well decreases. The artifacts are much fewer in the vertical planes than in the horizontal planes, giving less uncertainty in depth determination. However, the resolution in the horizontal plane also becomes very poor in the case where only 10 wells are used, and it is almost impossible to discriminate different sources.

In summary, the surface station array has the advantage of achieving better lateral resolution of the TRA focus, although the uncertainty of the depth determination increases with sparse station distributions. The downhole station array provides better constraints on the depth determination and also has fairly good lateral resolution when the wells are close together. The station separation for a cost-effective network is related to the closest distance between two neighboring events. On the other hand, both networks have the capability of resolving a single event with limited artifacts. In the following section, I will show this capability in a field data example where only 5 boreholes with 8 levels of receivers in each well are used.

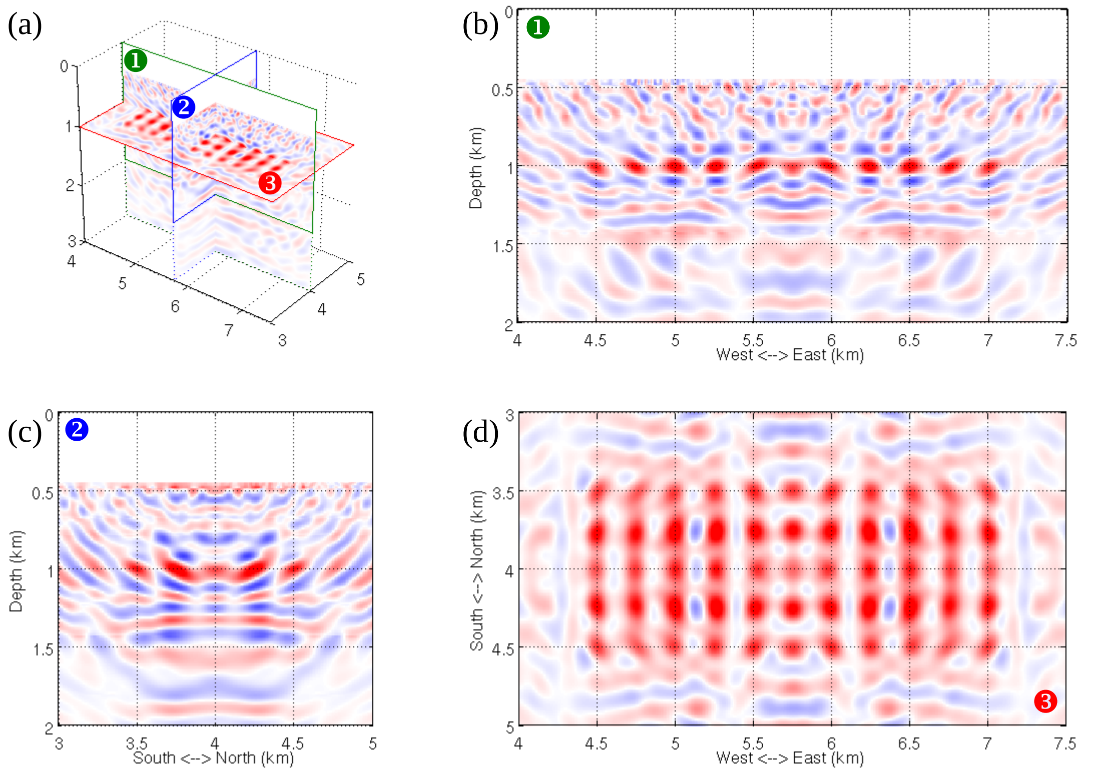


Figure 3-23: TRA results for the multiple sources experiment with a 10-by-6 surface array (Figure 3-21b). Snapshots in (a) 3D view; (b) XZ plane; (c) YZ plane; (d) XY plane.

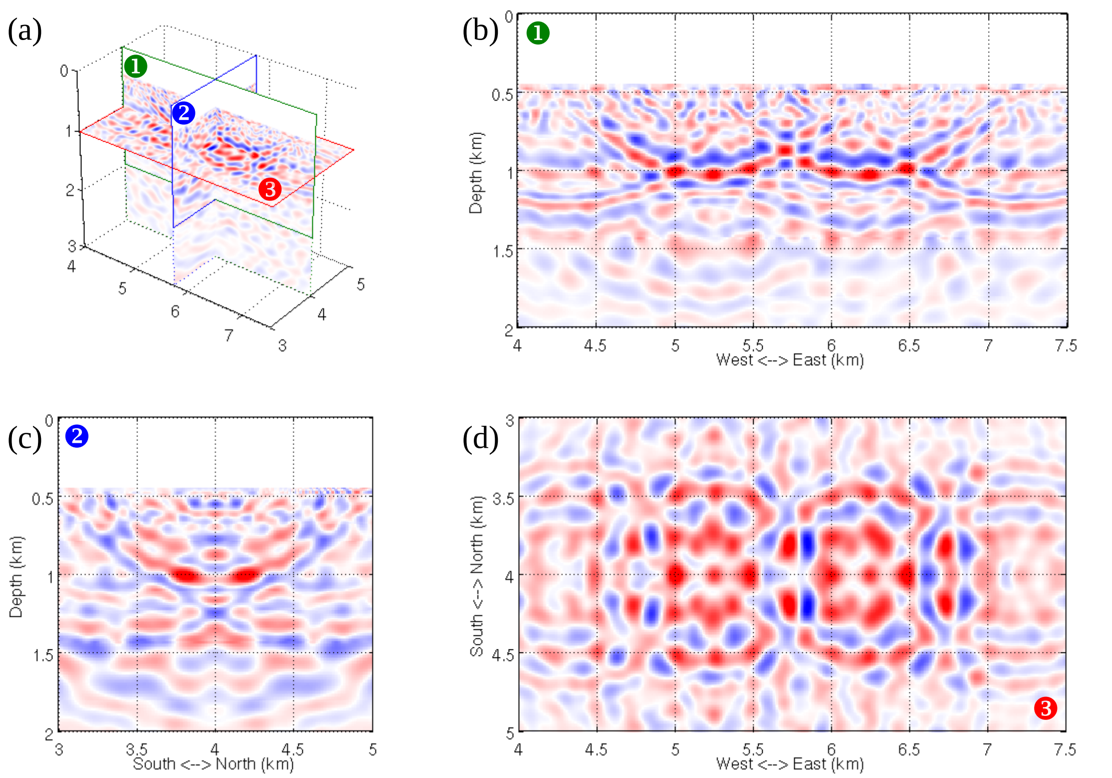


Figure 3-24: TRA results for the multiple sources experiment with a 4-by-3 surface array (Figure 3-21c). Snapshots in (a) 3D view; (b) XZ plane; (c) YZ plane; (d) XY plane.

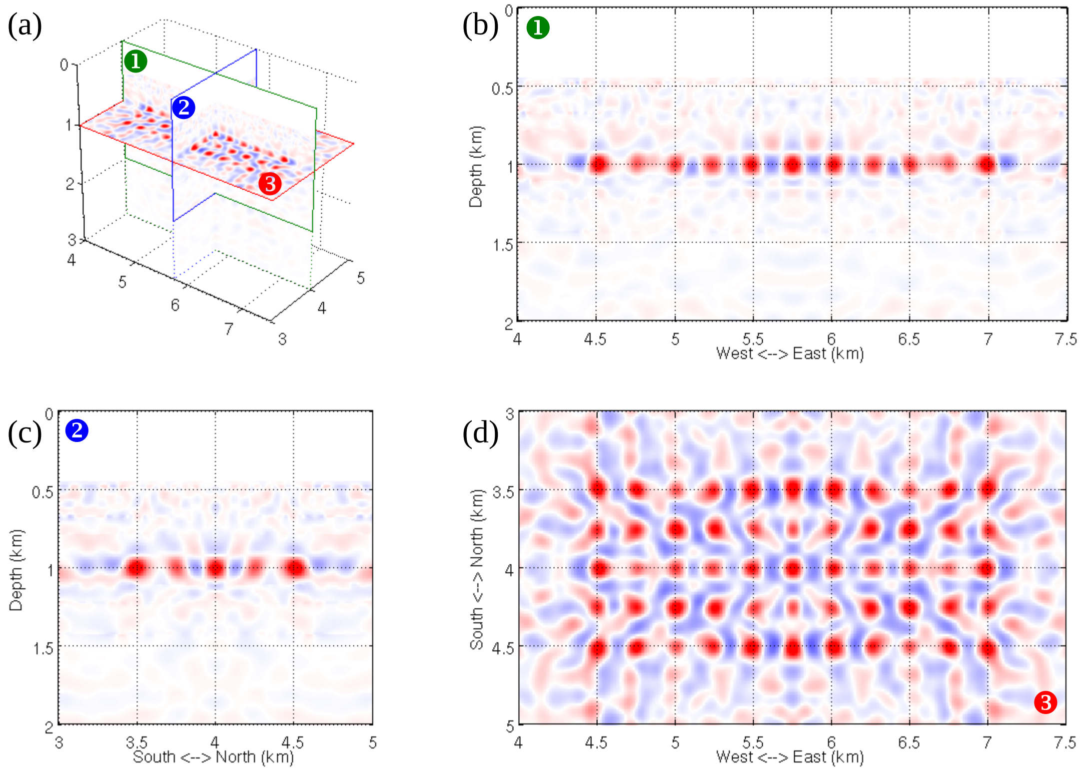


Figure 3-25: TRA results for the multiple sources experiment with 32 boreholes (Figure 3-22b). Snapshots in (a) 3D view; (b) XZ plane; (c) YZ plane; (d) XY plane.

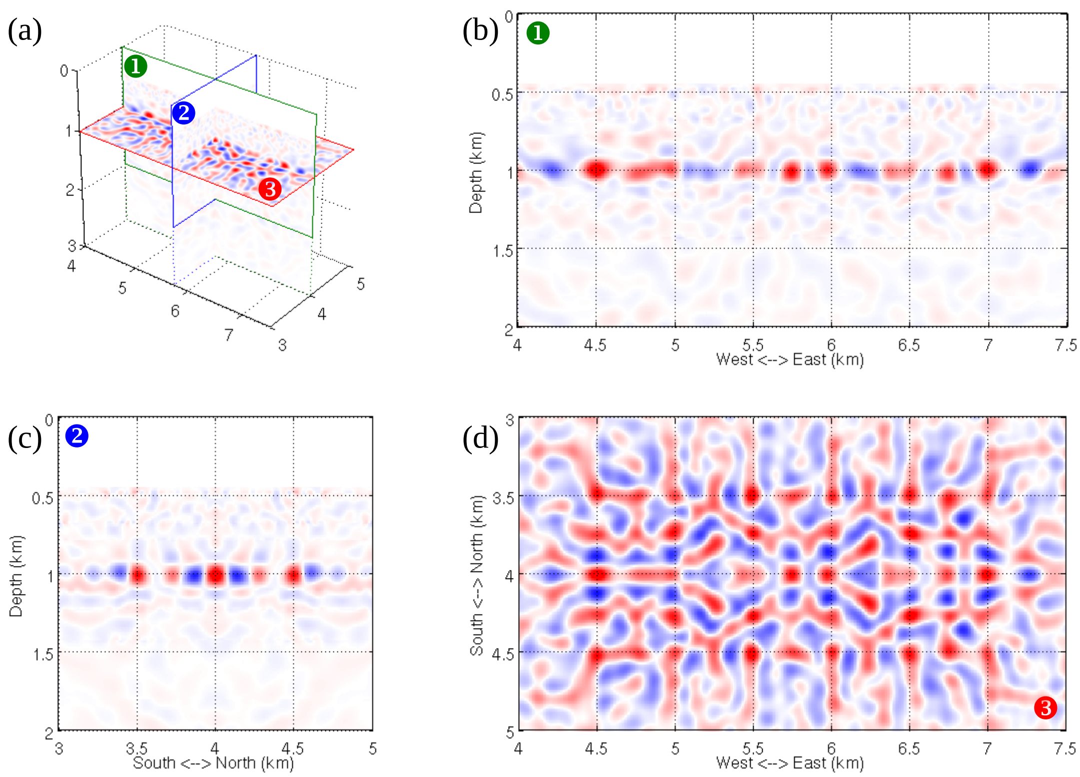


Figure 3-26: TRA results for the multiple sources experiment with 10 boreholes (Figure 3-22c). Snapshots in (a) 3D view; (b) XZ plane; (c) YZ plane; (d) XY plane.

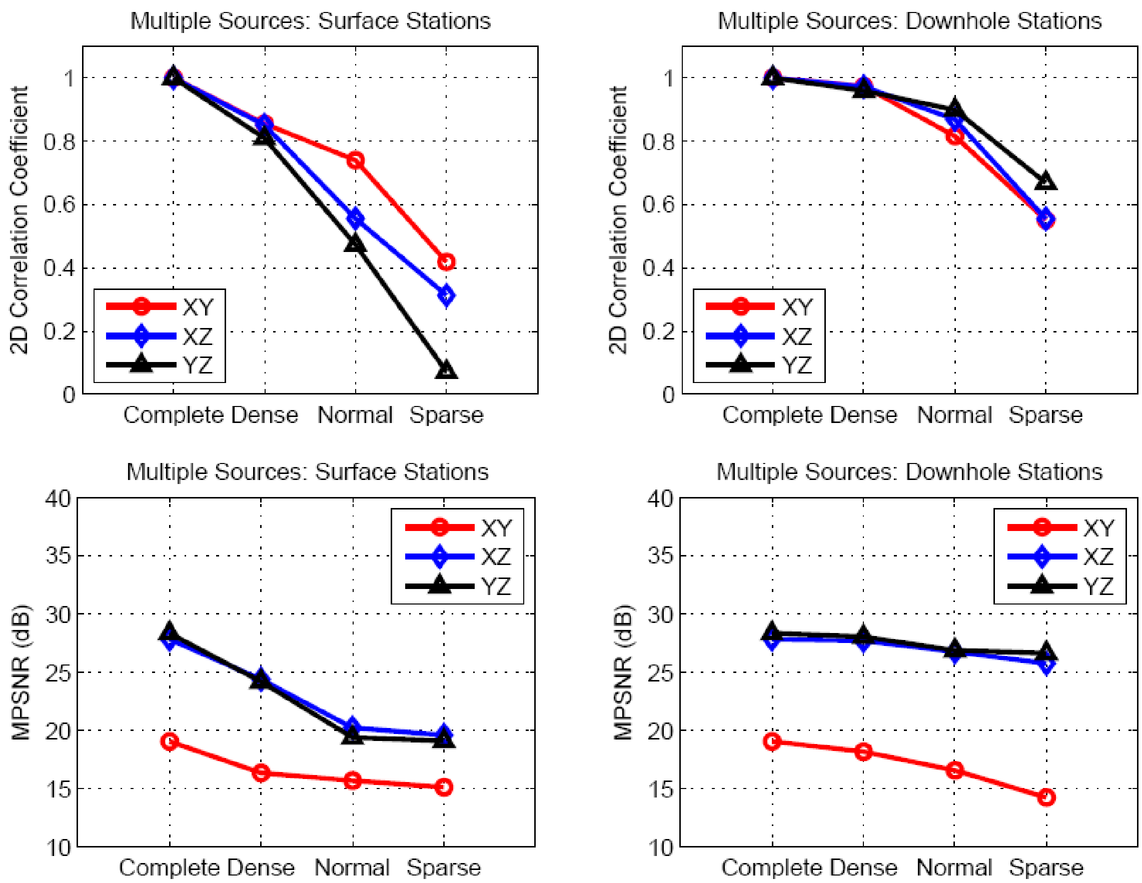


Figure 3-27: Retro-focusing quality for different planes in the single source TRA experiments: (a) 2D correlation coefficients for surface stations only experiments, (b) 2D correlation coefficients for downhole stations only experiments; (c) MPSNR score for surface stations only experiments, (d) MPSNR score for downhole stations only experiments. The X axis in both plots indicates the receiver coverage, where “Complete” corresponds to Figure 3-17a setup, “Dense” corresponds to Figure 3-17b and Figure 3-17c setups, “Normal” corresponds to Figure 3-21b and Figure 3-22b setups, and “Sparse” corresponds to Figure 3-21c and Figure 3-22c setups.

**Focus on Faults**

Previous examples show a very good focus using an isotropic point source, which generates P energy mostly. An interesting topic is whether the same TRA retro-focusing feature is also applicable in sources generating a lot of shear energy, such as a fault. We use a moment tensor source mechanism, defined by the strike ($\phi$), dip ($\delta$) and rake ($\lambda$), to simulate a planar faulting [Aki and Richards, 1980; Shearer, 1999], as shown in Figure 3-28.

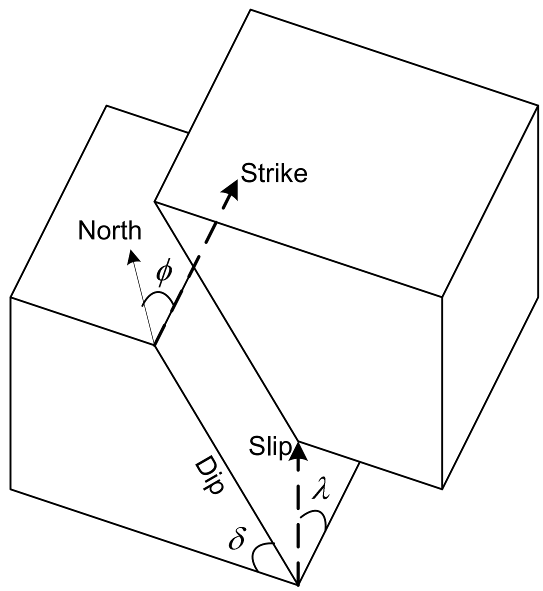


Figure 3-28: A planar fault defined by the strike and dip of the fault surface and the direction of the slip vector.

The forward experiment shown in Figure 3-4a is repeated with an exception that the point source is replaced by a moment tensor source, which represents a planar fault of $\phi = \delta = \lambda = 45^{\circ}$. Figure 3-29 shows a section of recorded traces for the forward propagation and Figure 3-30 shows the 3C seismogram recorded by the left-most receiver in the middle panel of Figure 3-29.

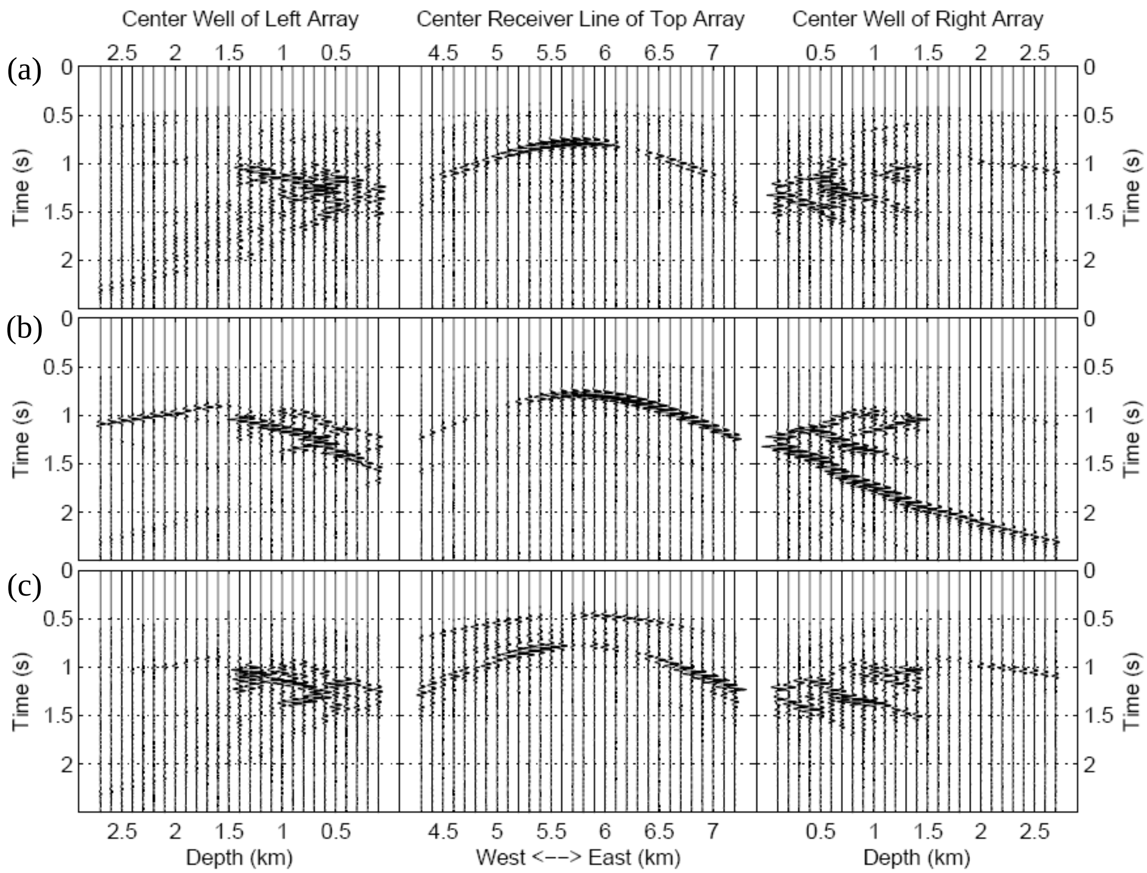


Figure 3-29: Recorded 3C seismograms due to a strike-slip fault during the forward propagation: (a) X, (b) Y, and (c) Z component. The left, middle, and right panels correspond to the same receiver line as in Figure 3-5.

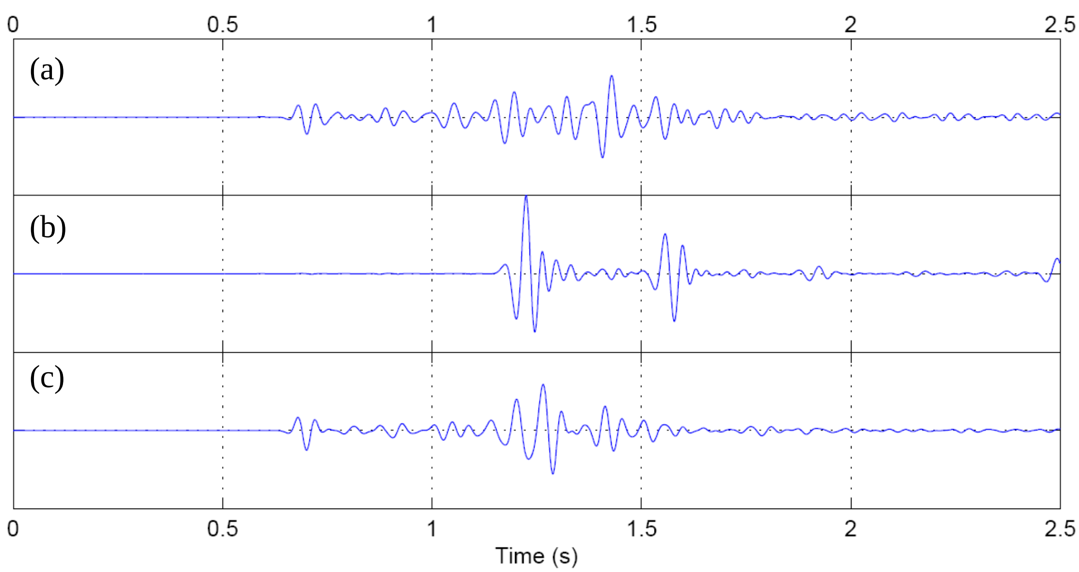


Figure 3-30: The 3C seismograms recorded by the left-most receiver in the middle panel of Figure 3-29: (a) X, (b) Y, and (c) Z component.

Comparing Figure 3-29 to Figure 3-5, we observe that a significant amount of shear energy released by the slipping fault is captured by the receiver array. The recorded signals are then back-propagated assuming a downhole-station-only setup as shown in Figure 3-4b. To better interpret the results, we plot the resulting P-wave field (Figure 3-31) and S-wave field (Figure 3-32) by taking the divergence and curl of the velocity fields. We can observe focal spots in both P-wave and S-wave results, although the S-wave results clearly have a better focus, which is probably due to the fact that the strike-slip fault source mechanism generates shear energy dominantly. The MPSNR scores of the S-wave results are 36.1dB, 38.7dB, and 35.2dB for the XY, XZ, and YZ planes, respectively. In comparison, the MPSNR scores of the P-wave results are 30.3dB, 33.1dB, and 33.0dB for the XY, XZ, and YZ planes, respectively.

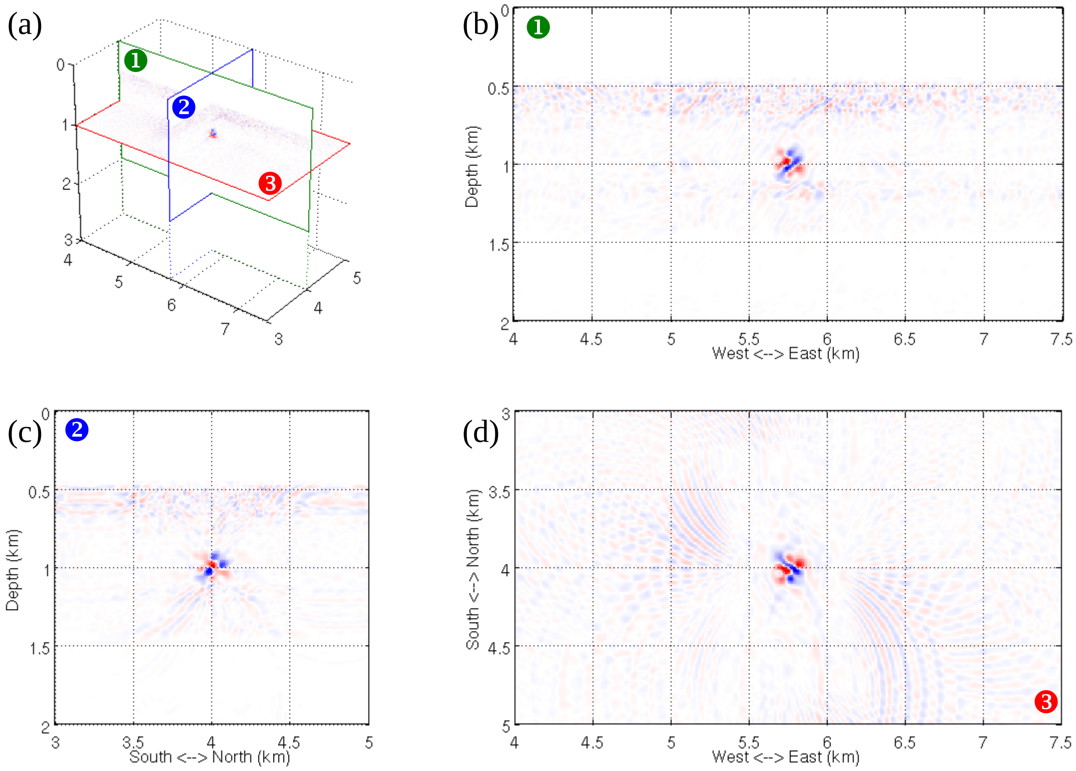


Figure 3-31: Retro-focused P-wave field in the case of a slipping fault with downhole receivers only (Figure 3-4c). (a): 3D view; (b) XZ plane; (c) YZ plane; (d) XY plane.

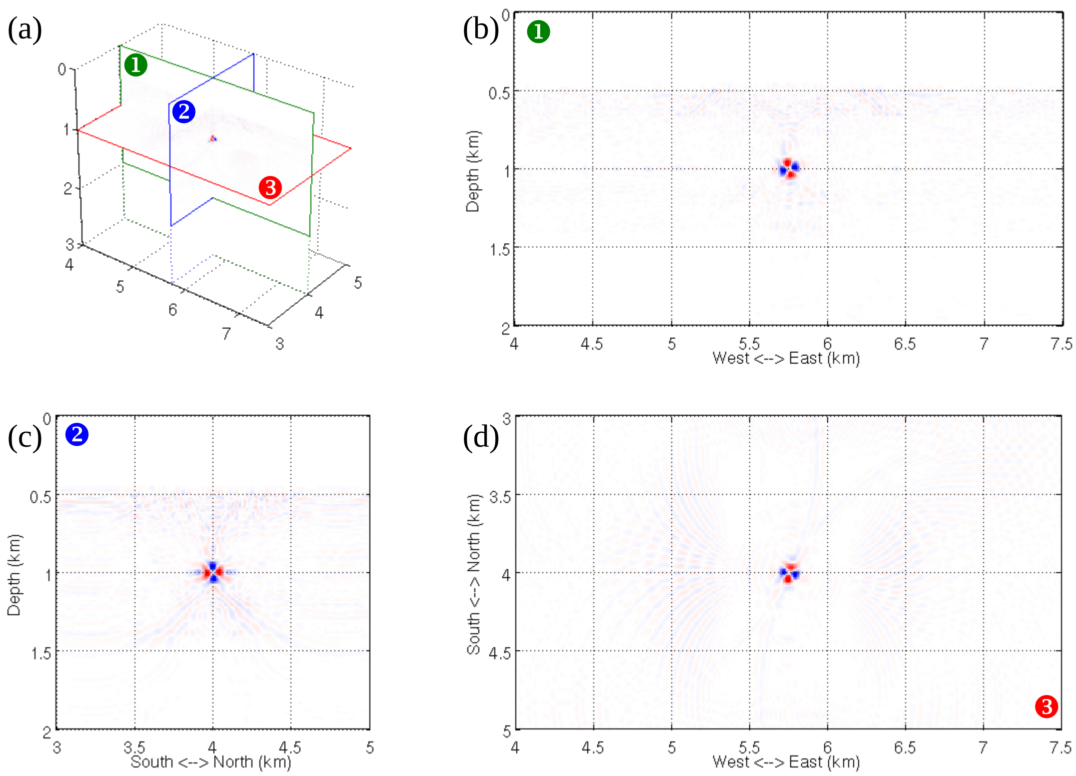


Figure 3-32: Retro-focused S-wave field in the case of a slipping fault with downhole receivers only (Figure 3-4c). (a): 3D view; (b) XZ plane; (c) YZ plane; (d) XY plane.

### 3.1.3 Field Data Test

In this section, I will show an example using actual field monitoring geometry as well as data recorded for one of the microseismic events. The actual station distribution is shown in Figure 3-2. A total of 5 wells are scattered in the field with 8 levels of stations in each well. Although the density of stations is far less than the worst case discussed in previous section, we are able to achieve fairly good source recovery.

A synthetic test with such a sparse network is performed before the real data experiment, in which a single source is introduced at X = 5.5 km, Y = 4 km, and Z = 0.75 km. The recorded 3C seismograms are shown in Figure 3-33. The traces within each

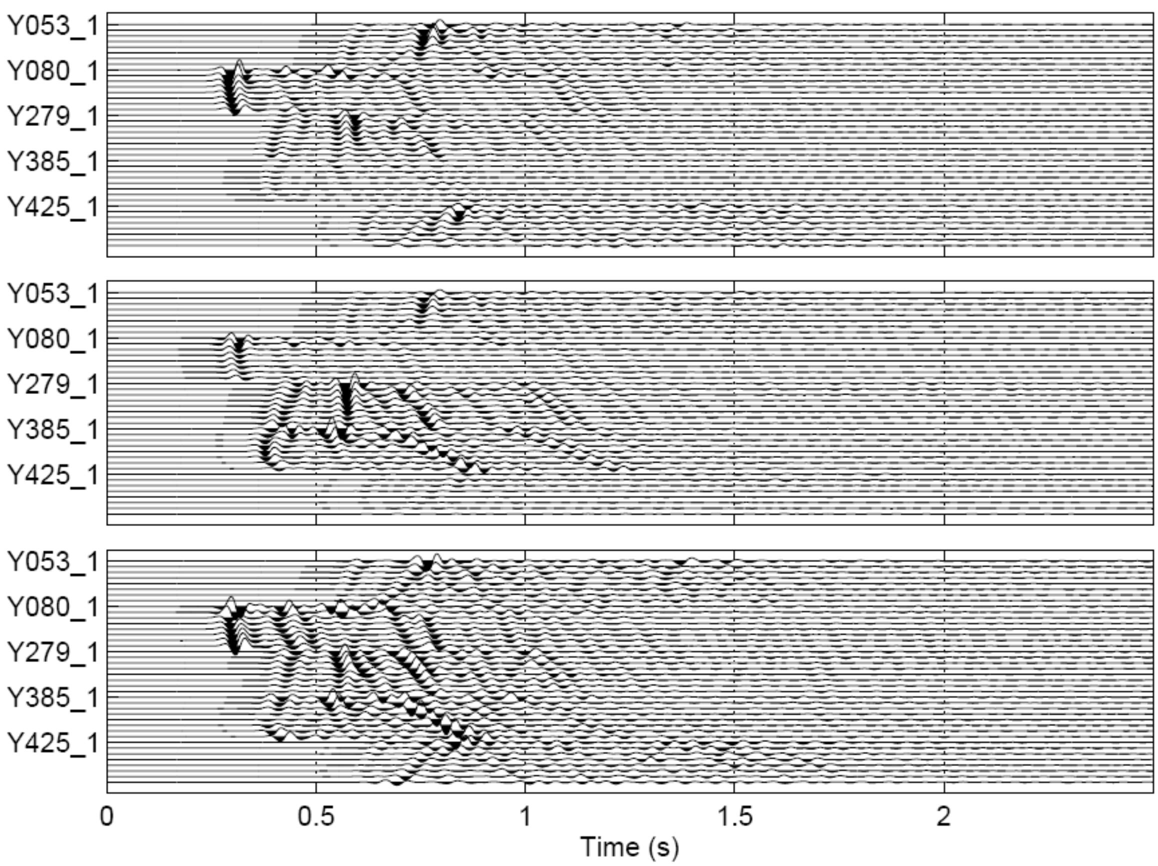


Figure 3-33: Synthetic 3C seismograms simulated using the actual downhole monitoring network. Traces are grouped according to the well locations (see Figure 3-1). Each well has 8 levels of stations. (a) X components; (b) Y components; (c) Z components.

panel are grouped according to the well position (see Figure 3-1 for reference). I then perform the same back-propagation operation as in previous experiments to this dataset. The snapshot of the wave field at the time of focusing is shown in Figure 3-34. It is encouraging to see a clear focal spot at the original source location (the empty diamond in Figure 3-34b), given we only use 40 stations in 5 wells. As shown by previous experiments (see Figure 3-15), for a single source problem, one can still achieve a clear focus even with very sparse well coverage, although there are a significant number of wave front artifacts in the XY plane, which is also observable in this example as shown in Figure 3-34b.

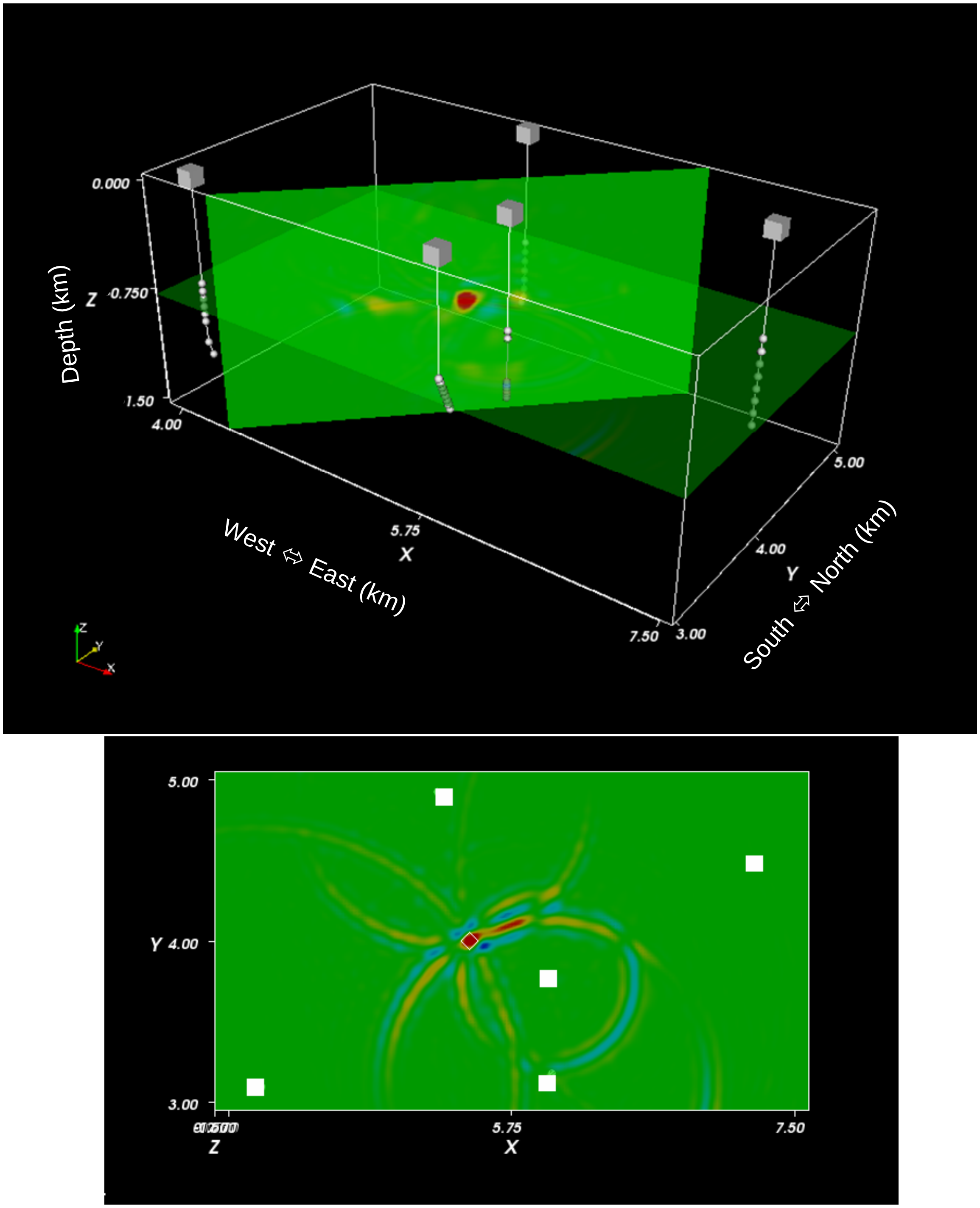


Figure 3-34: TRA focusing results for a synthetic dataset created using the actual field monitoring network. The source is located at (X=5.5 km, Y=4.0 km, Z=0.75 km), as indicated by the empty diamond. The TRA back-propagation is able to achieve a clear focus on the correct source location. Wave front smiles are observable due to the limited receiver coverage (see Figure 3-15 for a similar effect). (a) 3D view with two cross-sections passing through the focus; (b) 2D map view in XY plane at depth of 0.75 km.

A tetrahedral geophone configuration is used for each level of station in the field [Jones and Asanuma, 2004a; , 2004b]. This poses extra complexity in directly importing the raw data into the TRA process. To avoid the uncertainty of converting the tetrahedral geophone system into an orthogonal system, we use only the vertical component recordings from each level. The seismograms from a selected event (X=5.482 km, Y=4.189 km, Z=0.729 km) are shown in Figure 3-35. This event has been located independently by other techniques and is shown as the black diamond in Figure 3-36b.

We run the TRA process for this event and the results are shown in Figure 3-36. Although the wavefield is not as clean as the one shown in Figure 3-34, we are still able to identify the maximum energy spot in the snapshot easily. Calculation of the MPSNR score for the field data test gives a 29dB value, which falls between the “normal” case and “sparse” case as shown in Figure 3-16d. The focal spot is measured at X=5.400, Y=4.225, Z=0.690. As shown in the 2D map view in Figure 3-36b, the focal spot identified by TRA is consistent with results from other location algorithms, given the uncertainty of those location algorithms (around 200~300 m). The maximum value in Figure 3-36b (indicated as red bulb next to the back diamond) is about 2 times larger than the other possible peaks (indicated by the cyan circles), which shows again that the focal spot is significant to be located in contrast to other side peaks.

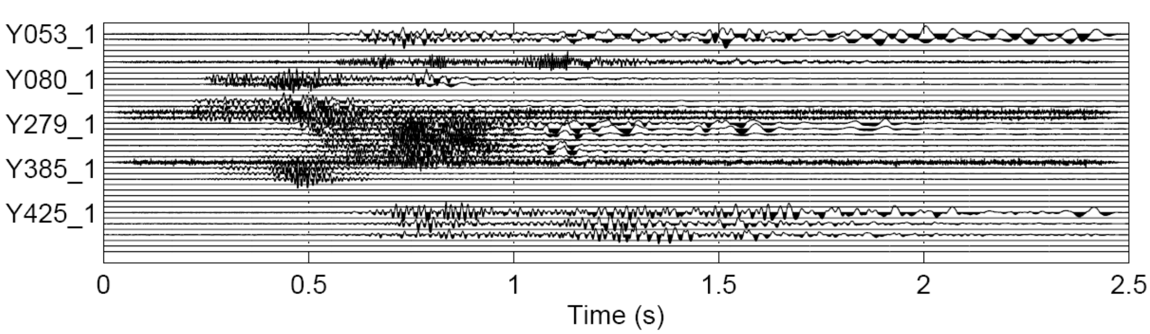


Figure 3-35: Vertical component recording for a microseismic event occurred in the field.

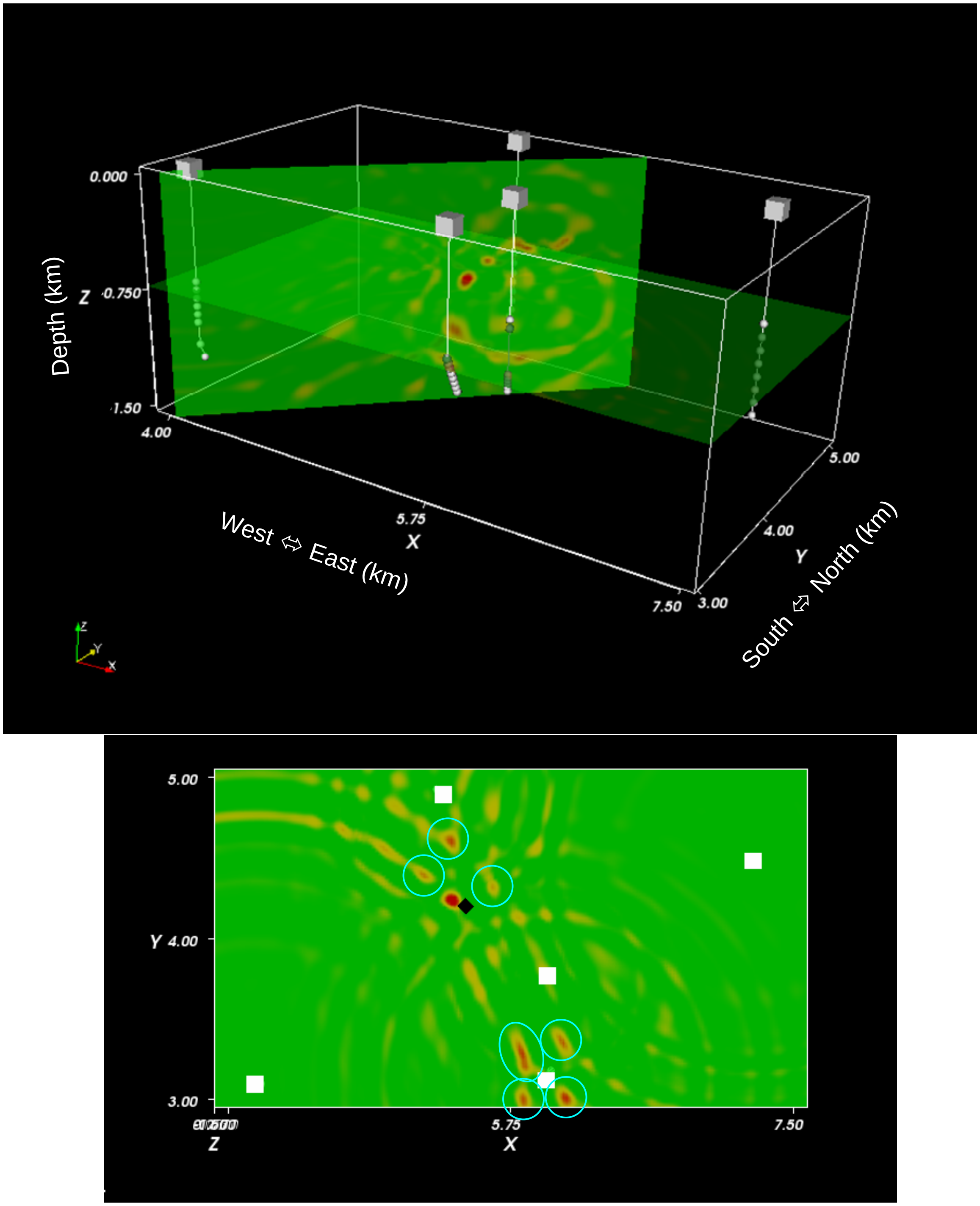


Figure 3-36: TRA focusing results for a real microseismic event. The source position located using independent study is at (X=5.482 km, Y=4.189 km, Z=0.729 km), as indicated by the black diamond. The TRA focus is located at (X=5.400, Y=4.225, Z=0.690). (a) 3D view with two crosssections passing through the focus; (b) 2D map view in XY plane at depth of 0.690 km. Cyan circles indicates other possible amplitude peaks at the time of focusing.

## 3.2 Focal Depth Estimation

Source depth is an important parameter for determining whether a seismic event is an earthquake or an explosion. For deep events (>30 km) focal depth can be determined from time differences between the primary phases (P, S) and surface reflected phases (pP, sP, sS, pS) which are frequently called depth phases. In the case of shallow events, the surface reflected phases are often buried in the codas of P and S waves. The scattered coda waves become particularly problematic for seismic events at regional distances. In this section we propose a new approach, based on TRA, for determining the source depth of shallow events.

In the previous section, we have demonstrated that TRA principles allow us to back-propagate the recorded seismogram given a priori earth model. By analyzing the energy distribution within the medium at time-zero, we can then locate the earthquake. This back-propagation operator requires an intense computational effort. In some situations where the lateral location of the earthquake is well constrained while the depth is poorly determined, one can greatly simplify the back-propagation operator with the help of the *empirical Green's function* [Li and Toksöz, 1993]. In this section, we will first introduce the methodology of this approach and demonstrate it with a simple numerical experiment. Then we test this method with recordings from several events whose focal depths were determined independently. Results show that the approach can provide reasonable estimation of focal depth of shallow events from seismograms recorded at regional distances. The method was found to be simple, robust, and possibly capable of automation in the future.

### 3.2.1 Methodology

Source depth determination methods have been an important area of research for many years. Langston and Helmberger [1975] created useful approximate expressions based upon generalized ray expansions for modeling the P, pP, and sP arrival times and amplitudes at teleseismic distances. Multi-channel and adaptive beam forming have been used to identify and decrease the uncertainty of P and pP events [Kemerait and Sutton, 1982]. Wavelet filtering for denoising and model based predictions of travel time step-out have been used to improve the signal strength and certainty of identifying the depth phases [Murphy *et al.*, 1999]. Spectral, cepstral, and cepstral F-statistic methods have also been used to infer the time delays between P, pP, and sP phases from periodic notches in the amplitude spectrum [Alexander, 1996; Bonner *et al.*, 2002; Kemerait and Sutton, 1982; Reiter and Shumway, 1999]. However, for shallow crustal events in areas with significant scattering recorded at regional distances, the depth phases are buried in the coda of the body waves and cannot be visually identified. In these cases, current methods are described by most authors as not being effective at identifying these obscured depth phases.

In this section we will present an approach to estimate the focal depth with a combination of the TRA technique and the *empirical Green's function* [Li and Toksöz, 1993]. The methodology is based on the zero-offset Green's function that I discussed in Chapter 2.2.1 – that is, the causal part of the recovered signal is equivalent as the signal recorded by a receiver co-located at the pseudo source position. From this perspective, the causal part of the recovered signal can be seen as the zero-offset Green's function between the original source and itself:

$$G(\mathbf{x}_s,\mathbf{x}_s,t)+G(\mathbf{x}_s,\mathbf{x}_s,-t)\approx\frac{2}{\rho c}\sum_j G(\mathbf{x}_j,\mathbf{x}_s,t)\otimes G(\mathbf{x}_j,\mathbf{x}_s,-t)\,. \tag{3-3}$$

In fact although TRA can recover most of the significant information near the origin time when the source is fired, the data also contains all the recorded reflections that would have been observed at the source location from all scatterers or reflectors in the medium. In other words, the recovered signal at the source location is the signal that would have been recorded if there had been a receiver co-located at the source location. And equation (3-3) shows that to recover those reflections due to the pseudo source, one can simply run auto-correlations of the seismograms recorded due to the original source and then stack them.

### 3.2.2 Demonstration with Synthetic Propagator

For accurate event source depth estimates it is important to determine the source time history and subsequent delay times associated with the pP paths. To illustrate focal depth determination by autocorrelation of the seismograms, we use a simple 1-D example as shown in Figure 3-37. The P and pP ray paths are approximately overlapping except for the near source side. We can assume the pP reflection also passes through the source

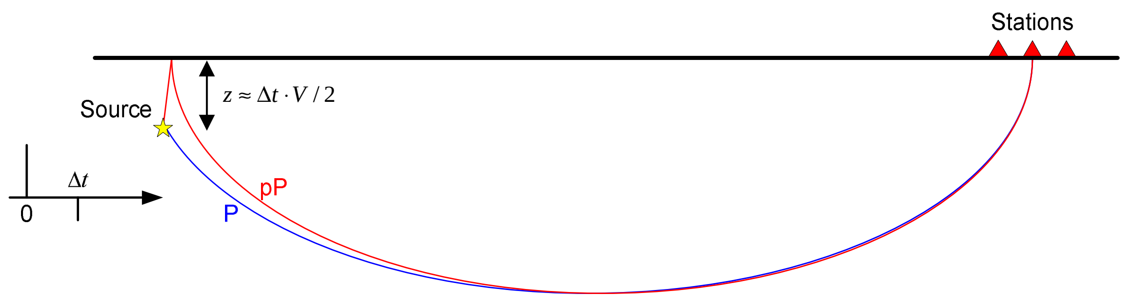


Figure 3-37: Schematic showing seismograms from a shallow seismic source that contains both P and pP codas captured at the regional stations.

region; hence, if we put a collocated receiver at the source position, it will record the initial spike fired by the seismic event and it will also record another spike that is caused by the free surface reflection after some time delay $\Delta t$. By assuming an averaged velocity value, we can estimate the depth of the source as $z \approx \Delta t \cdot V_P / 2$, which implies another assumption that the pP raypath is also passing through the original source. This assumption is more valid with large source-station distances.

Since the P and pP ray paths are approximately the same, we can formulate the problem in the time domain as a single propagator and a doublet source (P and pP) as shown in top left panel of Figure 3-38. We calculate the seismogram by convolving the source with a given Green's function (middle left panel of Figure 3-38) as the propagator

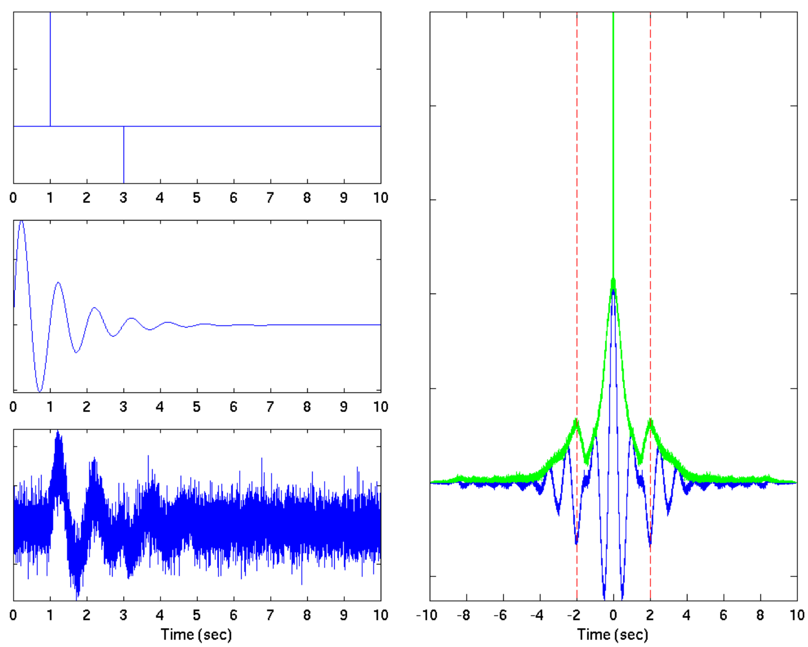


Figure 3-38: Synthesis of the autocorrelation of a P and pP trace. The top left trace shows the source function with P at one second and pP at three seconds. The middle left traces represents the propagator (i.e. Green's function). The bottom left trace is the "recorded" waveform given by the Green's function convolved with the source function plus random noise. The right trace shows the autocorrelation of the recorded trace (in blue) and its Hilbert transform derived envelope (in green). The red vertical lines show the correct time delay of 2 seconds.

and adding white noise, as shown in the bottom left panel of Figure 3-38. Then we calculate the autocorrelation function shown in the blue line in the right panel. Computing the envelope from the Hilbert transform of the autocorrelation eliminates the polarity differences between the phases. The green line shows the Hilbert transform-derived envelope with secondary peaks at $t = \pm 2$ seconds (shown by the red lines) which are caused by the surface reflected pP raypath. For earthquakes, pP may be of the same or opposite polarity relative to P, depending on the source mechanism and the distance or azimuth of the station.

### 3.2.3 Test on Real Events

We have chosen five earthquakes events to test the method on real events.

Event #1 occurred at Au Sable Forks, NY on Apr. 20th, 2002 with a ML magnitude of 5.3 and a catalogue depth of 11 km. Figure 3-39 shows the regional map of the event and the station distribution, and Figure 3-40 shows the recorded seismograms at

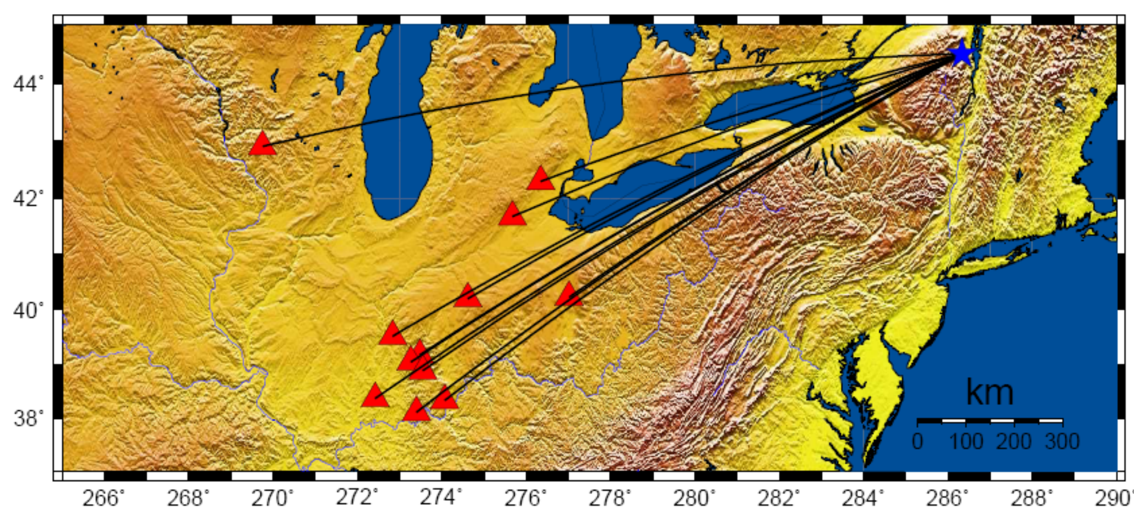


Figure 3-39: Map of North central and Eastern portions of the USA showing the station coverage (triangles) and epicenter location (blue star) of Event #1 at Au Sable Forks, NY - 2002, Apr. 20. ML = 5.3 and catalog depth is 11km.

selected stations. Figure 3-41 shows the autocorrelations of recorded seismograms in blue for each regional station and the sum of all the correlations in red. Figure 3-41 also shows the Hilbert envelope of the stacked autocorrelations in the solid black line. Clearly evident is the source pulse at zero lag and second peak corresponding to the pP event at a time delay of 3.7s. This gives an estimated focal depth of 10.2km using an average P velocity of 5.5km/s [Hughes and Luetgert, 1991]. To quantify the uncertainty in picking this second peak, the "full width at half maximum" (FWHM) is measured, as marked by the green line in Figure 3-41, which gives a depth range of 8.8km ~ 11.8km. Note that here we only count in the uncertainty due to the side lobe picking. Many other factors, including the uncertainty of the velocity and the error induced by assuming pP raypath goes through the original source, need to be considered in order to do a full uncertainty analysis. Also note that the velocity values we used in this study are taken from regional velocity models rather than a 1-D global velocity model. The purpose of using regional velocity models, which is assumed to be more accurate than the 1-D global model, is to reduce the uncertainty due to the velocity.

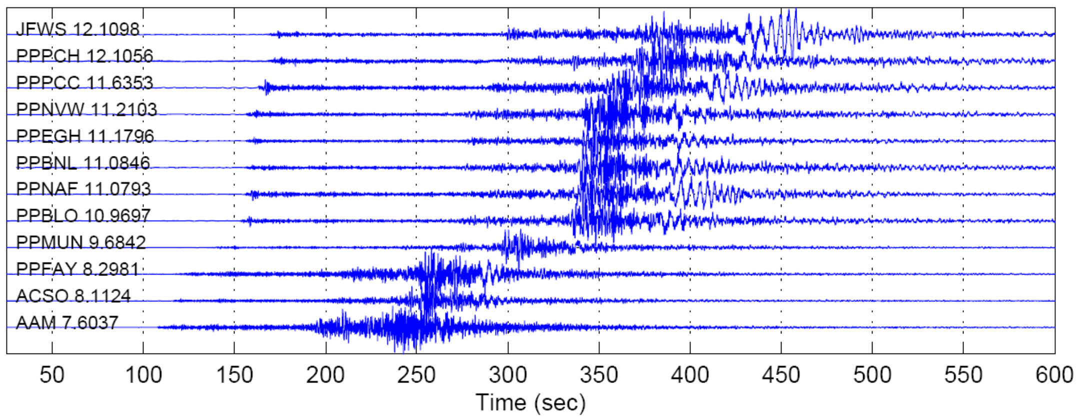


Figure 3-40: Seismograms recorded at selected stations for Event #1.

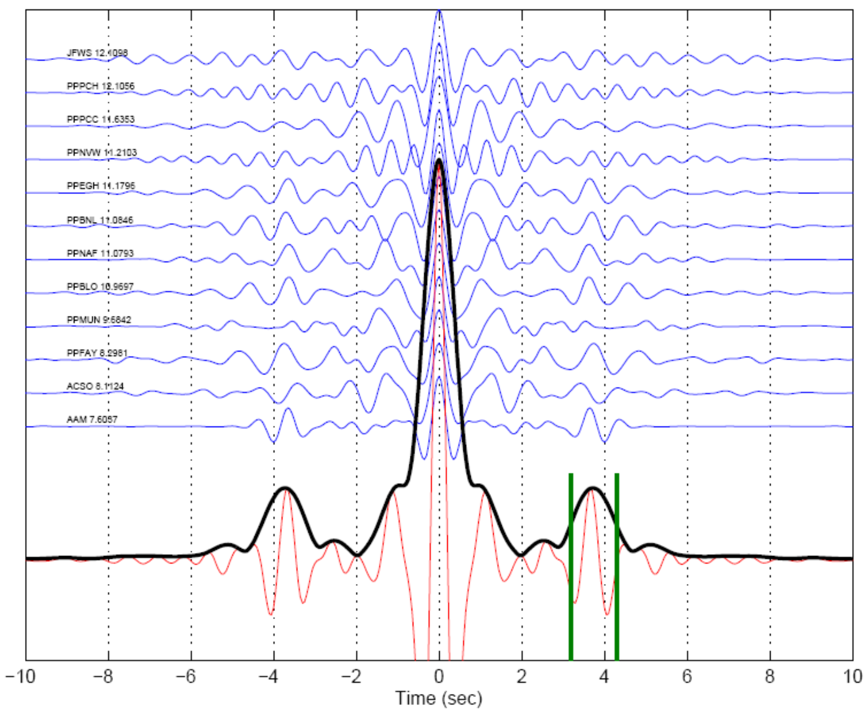


Figure 3-41: TRA analysis for Event #1. Autocorrelation of recorded seismograms are in blue and the sum of autocorrelations is in red. The Hilbert envelope of the stacked autocorrelations is shown in black. The peak of the second peak is at 3.7s and the green line indicates the FWHM (3.2s ~ 4.3s). Taking a P wave velocity of 5.5km/s, the estimated focal depth is 10.2km with a confidence range of 8.8km ~ 11.8km.

Event #2 is located in Turkey and occurred on Dec. 24th, 2000. It had a reported Mb magnitude of 4.6 and the catalogue depth was fixed at 10 km, which is the nominal value assigned to all very shallow events. Figure 3-42 shows the station coverage throughout Turkey and Figure 3-43 shows the corresponding recorded waveforms. The autocorrelation analysis is shown in Figure 3-44. The reflected depth phase shows a time delay of 2s, which corresponds to a depth of 4.5 km, using an average P wave velocity of 4.5 km/s. The FWHM range is 3.1 km ~ 5.3 km. Although we do not have an independent confirmation of this measurement, the event was very shallow and the “felt zone” was confined to a small area.

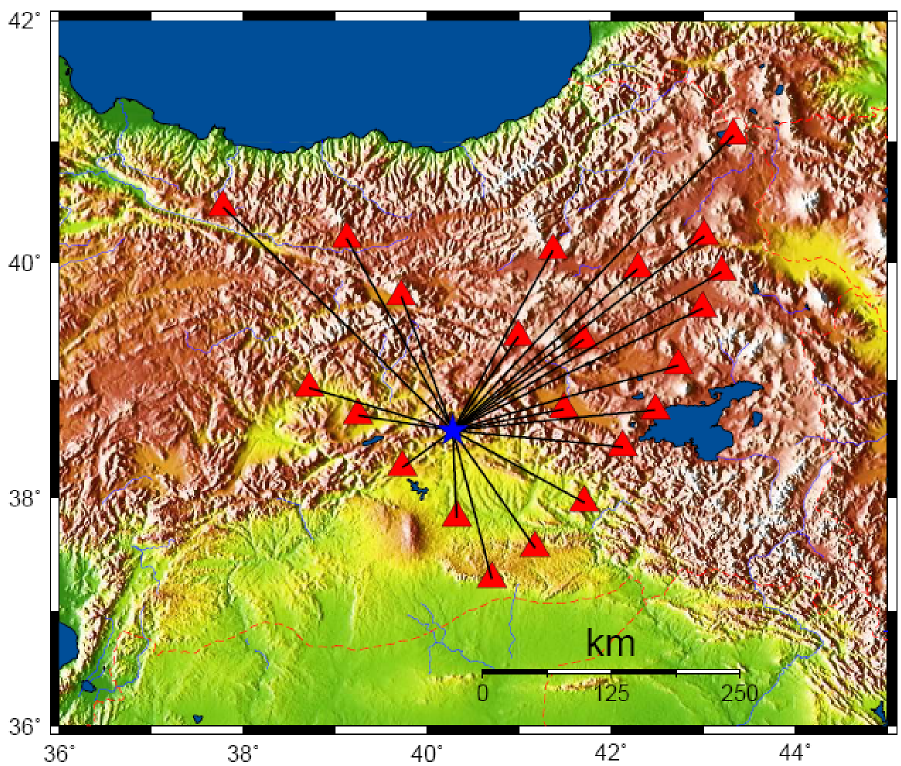


Figure 3-42: Map showing the station coverage (triangles) and epicenter location (blue star) of Event #2 in Turkey occurred on 24 Dec. 2000. Mb = 4.6 and catalogue depth is fixed at 10km.

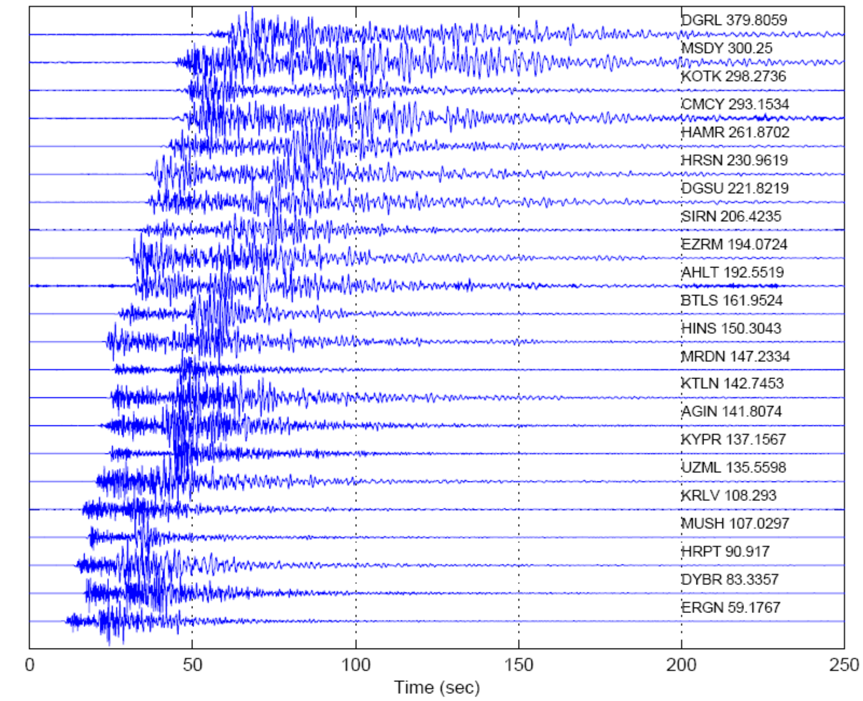


Figure 3-43: Seismograms recorded at selected stations for Event #2.

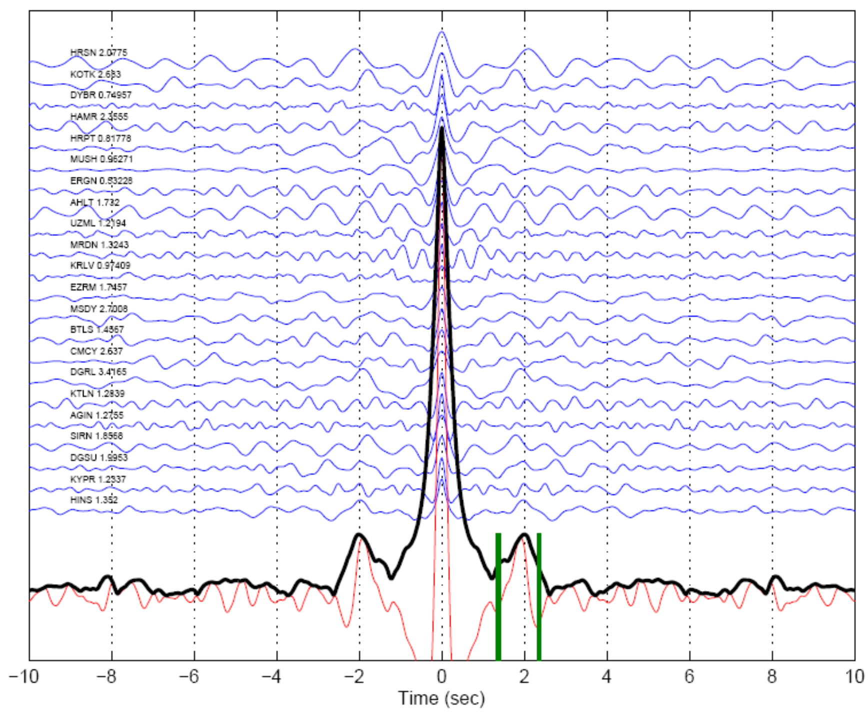


Figure 3-44: TRA analysis for Event #2. Autocorrelation of recorded seismograms is in blue and the sum of autocorrelationsis in red. The Hilbert envelope of the stacked autocorrelations is shown in black. The peak of the second peak is at 2.0s and the green line indicates the FWHM (1.4s ~ 2.4s). Taking a P wave velocity of 4.5km/s, the estimated focal depth is 4.5km with a confidence range of 3.1km ~ 5.3km.

Event #3 occurred at Yorba Linda, California on Sept. 3rd, 2002. It had a ML magnitude of 4.8 and catalogue source depth of 7.3 km. Figure 3-45 shows the map of southern California and the epicenter and station distribution. Figure 3-46 shows the recorded seismograms from selected stations. The autocorrelation analysis is shown in Figure 3-47, in which the second peak at a lag time of 4.3 s for the depth phase corresponds to a focal depth of 9.7 km, using an averaged P-wave velocity of 4.5 km/s. The FWHM range of this estimation is 8.4 km ~ 10.8 km.

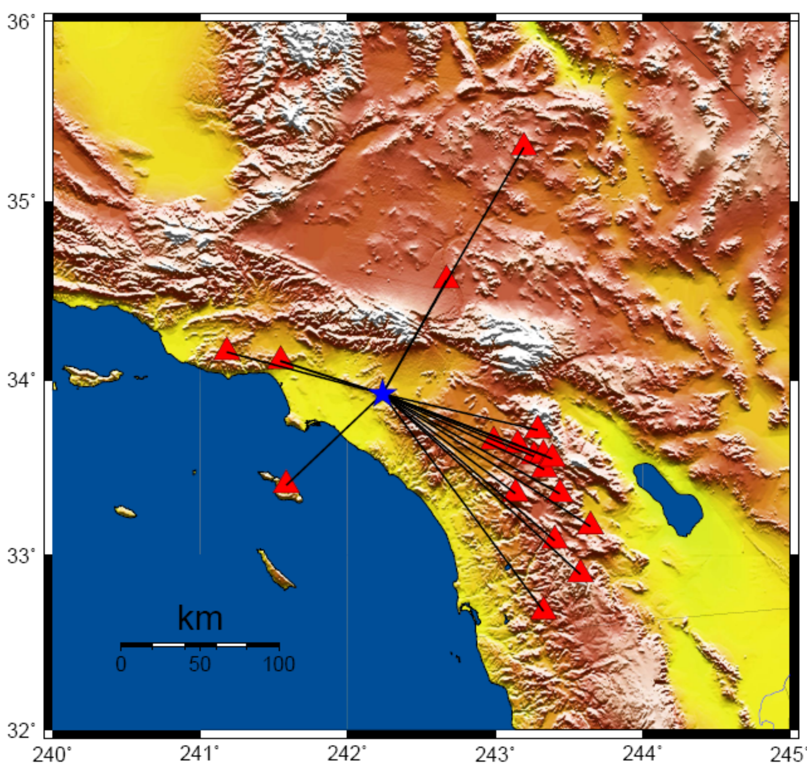


Figure 3-45: Map of southern California showing the epicenter and station locations for Event #3, Yorba Linda, CA on 3 Sept 2002. ML=4.8 and catalogue depth is 7.3 km.

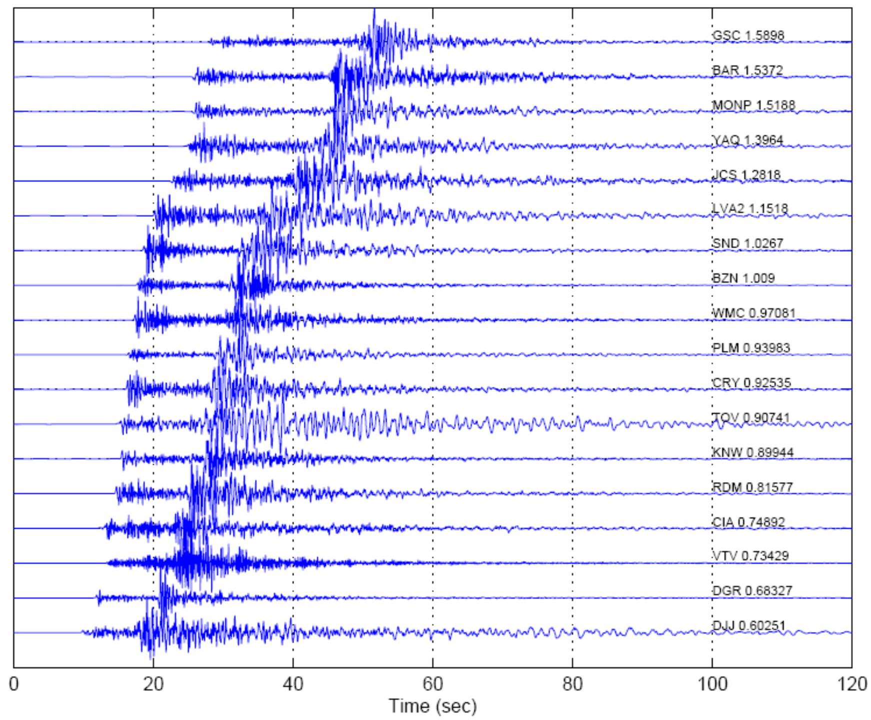


Figure 3-46: Seismograms recorded at selected stations for Event #3.

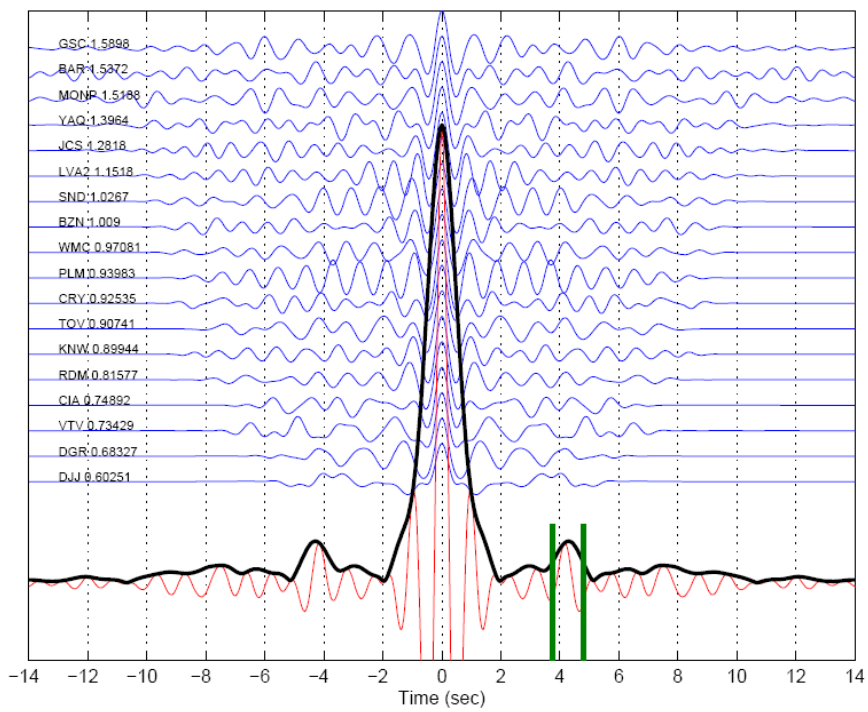


Figure 3-47: TRA analysis for Event #3. Autocorrelation of recorded seismograms is in blue and the sum of autocorrelations is in red. The Hilbert envelope of the stacked autocorrelations is shown in black. The peak of the second peak is at 4.3s and the green line indicates the FWHM (3.8s ~ 4.8s). Taking a P wave velocity of 4.5km/s, the estimated focal depth is 9.7km with a confidence range of 8.4km ~ 10.8km.

Event #4 occurred at Bingol, Turkey on May 1st 2003, with a Mw magnitude of 6.4. Figure 3-48 shows the seismogram recorded at selected stations in the teleseismic distance range, and Figure 3-49 shows the autocorrelation analysis for those stations. The depth phase appears with a time delay of about 6.1 s. Using a crustal P wave velocity of 4.5 km/s gives a focal depth of 13.7 km, with a FWHM range of 9.5 km ~ 18.9 km. Li and Toksöz [2004] studied this event in detail, using teleseismic and regional seismograms and local strong motion records. They found the predominant moment release occurred at 12 km. The Harvard moment tensor solution listed the depth as 15 km. These are all close to the value obtained from the TRA autocorrelation analysis.

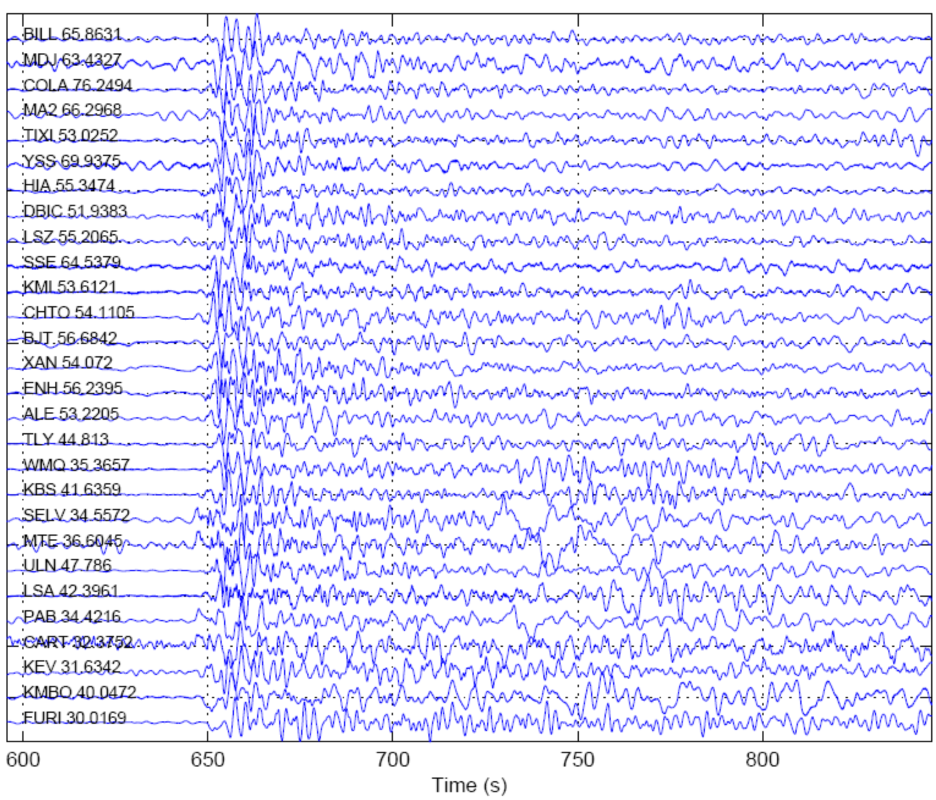


Figure 3-48: Seismogram for Event #4, recorded at selected stations at teleseismic distance. Event occurred at Bingol, Turkey on 1 May 2003, with a Mw magnitude of 6.4.

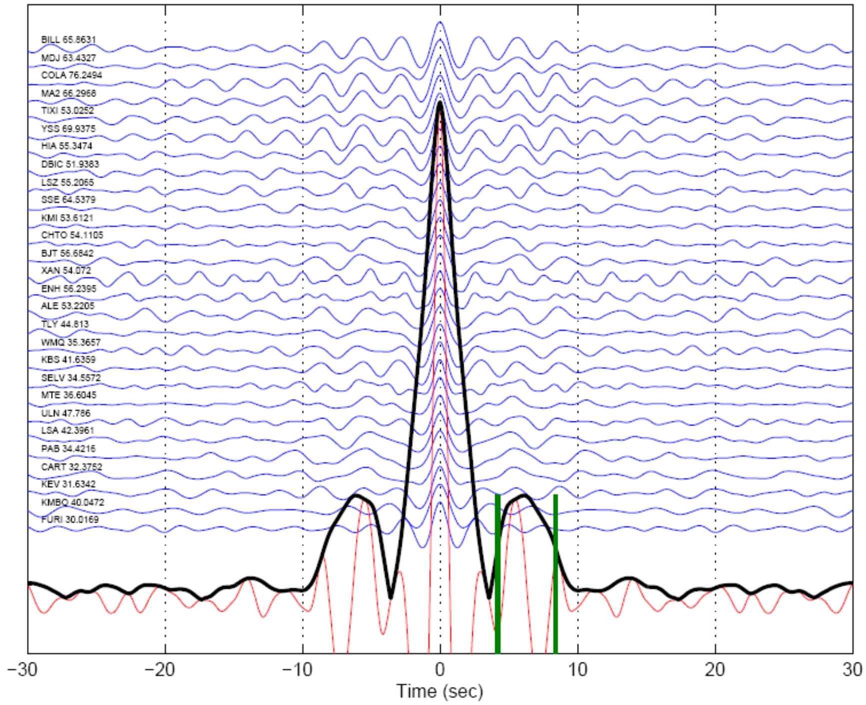


Figure 3-49: TRA analysis for Event #4. Autocorrelation of recorded seismograms is in blue and the sum of autocorrelations is in red. The Hilbert envelope of the stacked autocorrelations is shown in black. The peak of the second peak is at 6.1s and the green line indicates the FWHM (4.2s ~ 8.4s). Taking a P wave velocity of 4.5km/s, the estimated focal depth is 13.7km with a confidence range of 9.5km ~ 18.9km.

Event #5 is located in near Berkeley, California. Figure 3-50 shows the location for this California event recorded on the Berkley network. The event is listed as a 3.53 ML magnitude event with a source depth of 8.4 km. Figure 3-51a shows the vertical component of the recorded seismograms and Figure 3-52 shows the autocorrelation analysis for the P wave coda. The peak at 1.8 s marks the pP phase, which indicates a source depth of 4.4 km given a P-wave velocity of 5.0 km/s (FWHM range of 3.8km ~ 5.5km).

We also conduct a limited study of the S wave coda using this event. Figure 3-51b shows one horizontal component of the recorded seismograms, and Figure 3-53 shows the autocorrelation of the S-wave coda, in which the peak at 3.4 s reveals the sS phase.

Using a S-wave velocity of 2.6 km/s, the estimated focal depth is 4.3 km, which is quite consistent with the pP derived value. The FWHM range is 4.0km ~ 4.8km.

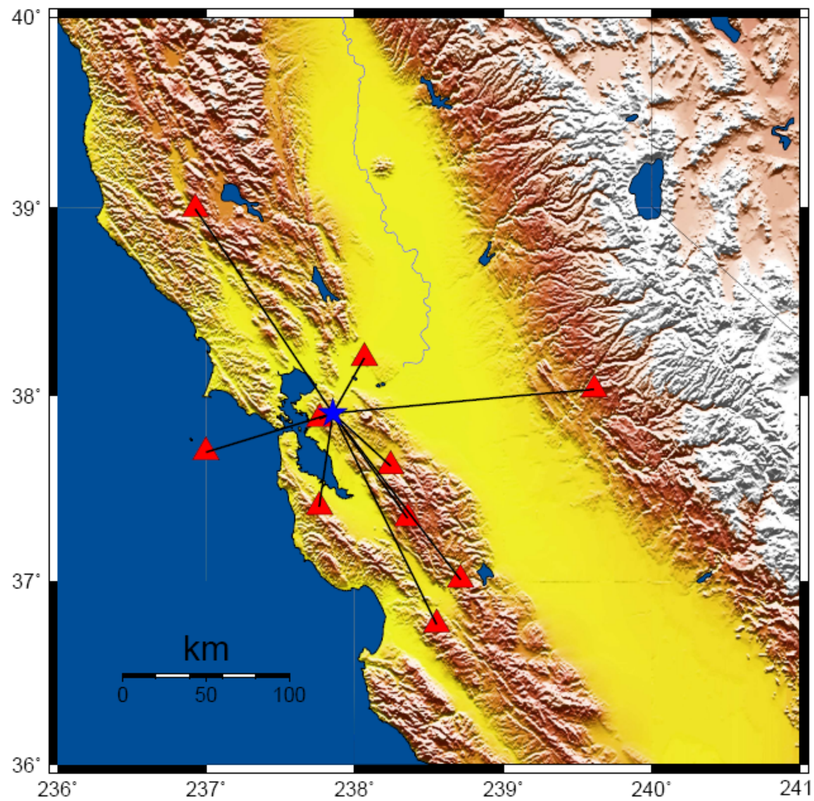


Figure 3-50: Map of showing the epicenter location (blue triangle), station locations (red triangles) and ray paths (black lines) for Event #5, located near Berkley, CA.

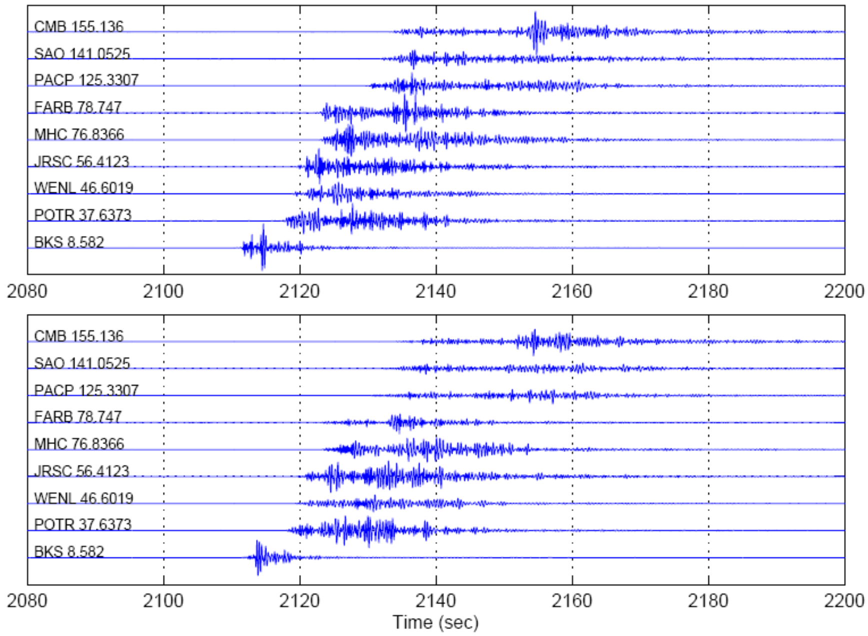


Figure 3-51: Seismograms recorded at selected stations for Event #5: (a) vertical components; (b) horizontal components.

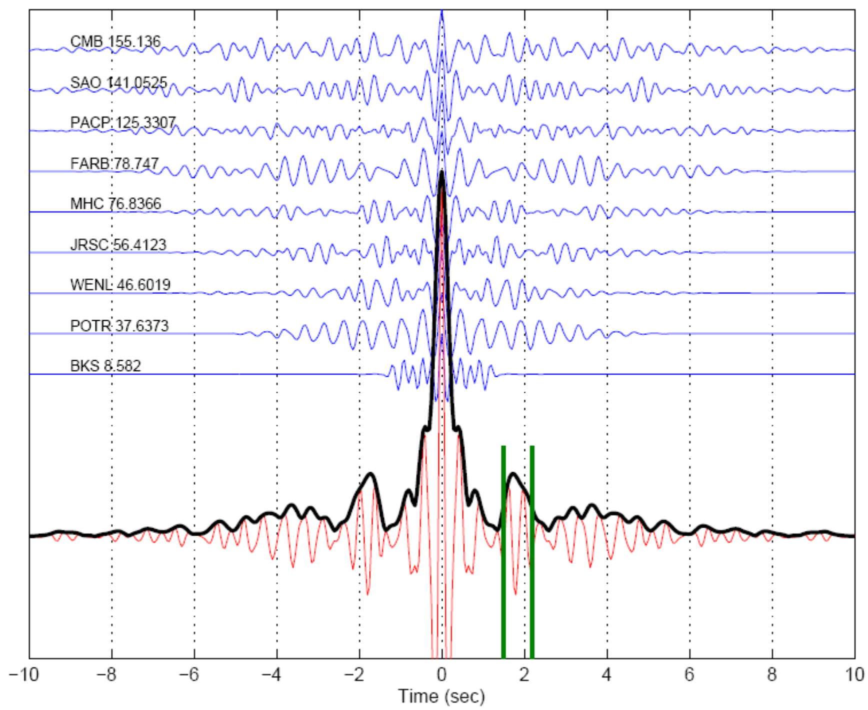


Figure 3-52: TRA analysis for P-wave coda of Event #5. Autocorrelation of recorded seismograms is in blue and the sum of autocorrelations is in red. The Hilbert envelope of the stacked autocorrelations is shown in black. The peak of the second peak is at 1.8s and the green line indicates the FWHM (1.5s ~ 2.2s). Taking a P wave velocity of 5.0km/s, the estimated focal depth is 4.4km with a confidence range of 3.8km ~ 5.5km.

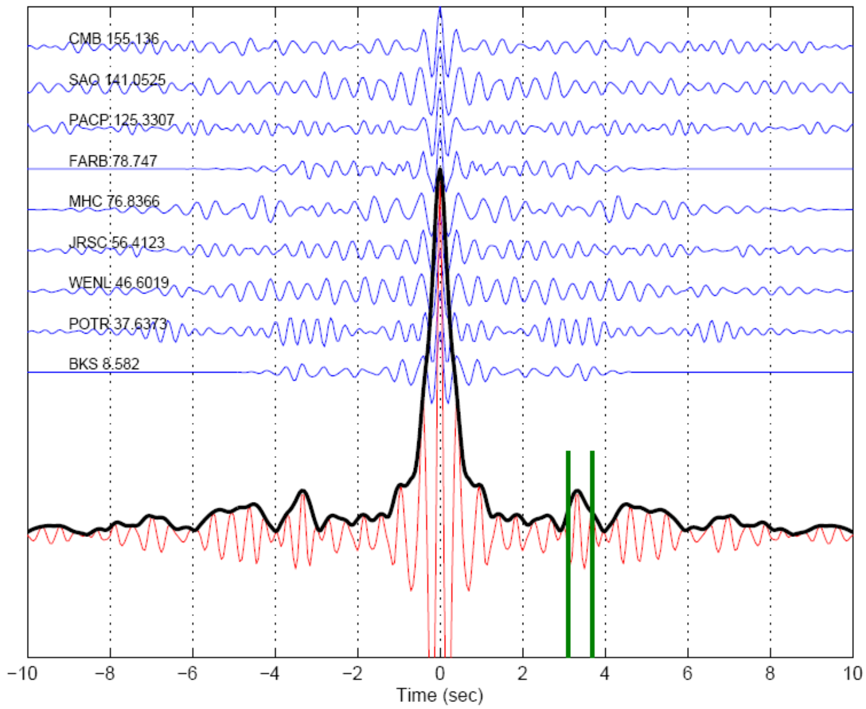


Figure 3-53: TRA analysis for S-wave coda of Event #5. Autocorrelation of recorded seismograms is in blue and the sum of autocorrelations is in red. The Hilbert envelope of the stacked autocorrelations is shown in black. The peak of the second peak is at 3.4s and the green line indicates the FWHM (3.1s ~ 3.7s). Taking a S wave velocity of 2.6km/s, the estimated focal depth is 4.3km with a confidence range of 4.0km ~ 4.8km.

Table 3-1 shows a summary of the depths for all the events studied. The source depths estimated by our analysis are very consistent with those reported. On all but one of these events, the pP phase is not evident on the seismogram because it is obscured by the coda energy. Even on the autocorrelations of individual seismograms, it is very difficult to identify the pP phase. It seems to require the full TRA method of stacking all the autocorrelations to pull out the fully back-propagated trace with the surface reflected energy. Further verification of this methodology using the P wave trains of numerous earthquake and explosion events is needed.

Table 3-1: Summary of focal depth of 5 studied events estimated using TRA analysis.

| **Event #** | **Location** | **Depth Reported** | **Depth Calculated from TRA** |
|---|---|---|---|
| 1 | Au Sable Forks, NY | 11 km | 11 km (8.8 km ~ 11.8 km)* |
| 2 | Turkey | 10 km, nominal | 4.5 km (3.1 km ~ 5.3 km)* |
| 3 | Yorba Linda CA | 7.3 km | 9.4 km (8.4 km ~ 10.8 km)* |
| 4 | Bingol, Turkey | 12 & 15 km | 13.5 km (9.5 km ~ 18.9 km)* |
| 5P | Berkeley, CA (pP coda) | 8.4 km | 4.4 km (3.8 km ~ 5.5 km)* |
| 5S | Berkeley, CA (sS coda) | 8.4 km | 4.3 km (4.0 km ~ 4.8 km)* |

In summary, we proposed an alternative approach, based on the concept of TRA and the *empirical Green's function* for determining the focal depth of shallow events. By applying TRA, one can back-propagate recorded seismic signals into the medium from a boundary surrounding the source and recover the source signal. By using the empirical Green's function, the back-propagation procedure was greatly simplified into an autocorrelation operation. The autocorrelation of the source signal can be recovered by summing all the autocorrelations of the recorded seismograms at the stations. This recovered signal will show a significant peak at a time delay that corresponds to the free surface reflection. By determining this time delay we can estimate the focal depth, assuming an averaged velocity above the source. We tested this methodology on five real seismic events. The focal depth values estimated using TRA analysis are close to the depth value provided by other independent studies. A complete uncertainty analysis would help us to better understand the advantages and limitations of this method.

* The depth range only reflects the error due to the time picking of the side lobe. A more complete uncertainty analysis is necessary to provide a more meaningful depth range.

# Chapter 4

# Applicability to Salt Flank Imaging

## 4.1 Introduction

In this chapter I will move on to the positive (causal) time domain of the TRA process and discuss another application, salt dome flank imaging. An accurate image of reservoir sediment structures at the flank of a salt dome is very important for computing reserves estimates and production development planning. Imaging subsalt sediments in the deep water Gulf of Mexico (GOM) requires seismic methods which handle distortions caused by complex salt tectonics. There are many variations of prestack depth migration methods to handle seismic data, including Kirchhoff [Gray and May, 1994; Bevc, 1997], beam based [Hill, 1990, 2001; Sun *et al.*, 2000; Gray, 2005] and reverse time [Baysal, *et al.*, 1983; Hokstad *et al.*, 1998; Biondi and Shan, 2002]. Proper handling of turning ray energy would help image the salt overhang [Hale *et al.*, 1992; Xu and Jin, 2006] and build a more accurate salt model [Siddiqui *et al.*, 2003; Wang *et al.*, 2006]. Typical imaging projects require multiple passes of migration, velocity analysis and model building in order to handle complex salt overburden. One problem facing deep GOM imaging objectives is that with surface seismic data there is only limited velocity resolution remaining at the depths of many subsalt plays. Wang *et al.* [2005] describe how the limited range of illumination angles in deep subsalt targets reduces the corresponding migration velocity analysis to nearly a poststack level. In addition, the complex overburden, e.g., a salt canopy, decreases illumination quality and makes velocity model building difficult [Guitton *et al.*, 2006]. Walkaway Vertical Seismic Profile (WVSP) data has the ability to increase the frequency bandwidth, i.e., resolution, and decrease uncertainty by removing half of the seismic raypath, which otherwise would have to travel back to the surface receivers. However, prestack depth migration of WVSP data suffers the same need for iterative velocity model building as surface seismic data.

In single-well imaging methods, data are acquired from a position physically closer to the reservoir. By locating both the sources and receivers in the same borehole, the seismic energy has a shorter distance to travel to the target and thus will have reflections with simpler raypaths; therefore simplifying the complexity of the wavefield and potentially enhancing the signal to noise ratio. Acoustic logging tools have been used to image features less than 20 m from the well bore [Hornby, 1989; Fortin *et al.*, 1991; Coates *et al.*, 2000]. More powerful downhole sources have been used to attempt to image farther away from the borehole [Majer *et al.*, 1997; Daley *et al.*, 2000]. Tests of single-well methods have shown promise, but may be limited by the power and directivity of downhole sources.

Redatuming of a WVSP dataset is a relatively new concept which attempts to mimic the single-well imaging method by moving mathematically the surface VSP sources to be as if they were located in the borehole with the receivers. Conventional redatuming methods [Berryhill, 1984] could be used for this process but would require a detailed velocity model of the overburden (e.g., the salt canopy) in order to backward propagate the prestack data to the new datum using a Kirchhoff integral formulation or finite-difference modeling algorithm.

Recent advances in seismic interferometry theory have shown that redatuming may be performed using simple cross correlations without the use of any velocity model. This new approach is a generalization of several related technologies: acoustic daylight imaging [Claerbout, 1976; Rickett and Claerbout, 1996], time-reversed acoustics [Fink, 1999, 2006], seismic interferometry [Schuster *et al.*, 2004; Schuster *et al.*, 2003; Derode, *et al.*, 2003; Snieder, 2004; Wapenaar, 2004; Wapenaar, *et al.*, 2005], and Virtual Sources [Bakulin and Calvert, 2004; Calvert *et al.*, 2004]. All of these techniques employ the time symmetry of the wave equation together with source-receiver reciprocity to estimate the impulse response between two passive receivers. This allows the redatuming process to use the extracted impulse response (or Green's function) instead of a modeled response based upon an iteratively derived velocity model.

In this chapter, we propose a strategy to image a salt flank and its associated abutting sediments through an overburden salt canopy with the help of redatuming. The foundation of this redatuming strategy is the Green's function reconstruction, which I have described in detail in the "Extension of TRA" section in Chapter 2. Given two stations inside a medium, $\mathbf{x}_A$ and $\mathbf{x}_B$, if we record all the response at these two stations due to an array of sources completely surrounding the medium, then by cross-correlating recorded signals and stacking, one can reconstruct the Green's function between the two stations. In mathematic terms, let $G(\mathbf{x}_A,\mathbf{x},t)$ and $G(\mathbf{x}_B,\mathbf{x},t)$ be the Green's functions recorded at $\mathbf{x}_A$ and $\mathbf{x}_B$, respectively, due to a source at the boundary of the medium, then the Green's function recorded at $\mathbf{x}_A$ due to a source at $\mathbf{x}_B$, $G(\mathbf{x}_A, \mathbf{x}_B, t)$, can be approximated as the summed cross-correlations:

$$G(\mathbf{x}_A, \mathbf{x}_B, -t) + G(\mathbf{x}_A, \mathbf{x}_B, t) \approx \int_{x \in \Omega} G(\mathbf{x}_A, \mathbf{x}, t) \otimes G(\mathbf{x}_B, \mathbf{x}, -t) \, \mathrm{d}\, x \tag{4-1}$$

This simple operation allows us to "move" the source from a medium boundary to locations within the medium. Combining with the advances on techniques such deviated/horizontal drilling and downhole receiver deployment, it allows us to look much closer into the medium without complex model analysis. Bakulin and Calvert [2004] and Bakulin *et al.* [2007] show examples of redatuming surface sources to receivers in a near-horizontal well just beneath the overburden. This may be an excellent way to remove the overburden artifacts on time lapse seismic imaging studies to detect the changes in reservoir properties. Others have applied variations of seismic interferometric redatuming to move surface sources into vertical or near vertical wells [Willis *et al.*, 2005; Willis *et al.*, 2006; Lu *et al.*, 2006; Hornby *et al.*, 2006; Hornby and Yu, 2007; Bakulin, *et al.*, 2007; Mateeva *et al.*, 2007a]. Bakulin *et al.* [2007] point out that due to the ray geometry, the redatumed pseudo shot records capture reflections from structures located somewhat parallel to the borehole: vertical salt flanks for near vertical wells, and horizontal beds for near horizontal wells. For structures perpendicular to the wellbore, the reflected energy is limited to a small area intersecting the well. The details of the mathematical description and discussion of seismic interferometric redatuming may be found in many places [Schuster, *et al.*, 2004; Snieder, 2004; Wapenaar, 2004; Wapenaar and Fokkema, 2005; Korneev and Bakulin, 2006; Willis, *et al.*, 2006; Lu, *et al.*, 2006].

In section 4.2, I'll demonstrate the performance and capabilities of applying redatuming to salt flank imaging on synthetic acoustic seismic data from a GOM style model. In this strategy, we first redatum the surface shots from a WVSP survey to be as if the source and receiver pairs had been located in the borehole at the positions of the receivers. This process creates effective downhole shot gathers by completely moving the surface shots through the salt canopy without any knowledge of the overburden velocity structure. The resulting shot gathers are considerably less complex since the WVSP ray paths from the surface source will be shortened and moved to be as if they started in the borehole, then reflected off the salt flank region and finally captured in the borehole. Since this process can be automated and performed quickly, it could be performed in the field, during acquisition, in near real time. After redatuming, we may apply multiple passes of prestack migration from the reference datum of the borehole. In our example, the first pass migration, using only simple vertical velocity gradient model, reveals the outline of the salt edge. A second pass of reverse-time prestack depth migration using the full, two-way wave equation, is performed with an updated velocity model that now consists of the velocity gradient and the salt dome. The second pass migration brings out the dipping sediments abutting the salt flank because these reflectors were illuminated by energy that bounced off the salt flank forming prismatic reflections. As with the redatuming step, the first pass of prestack migration could easily be performed in the field, as the data is collected, with a simple velocity model and first-arrival Kirchhoff migration algorithm. In this fashion, the aperture and data quality can be checked and could be used in making drilling decisions. In this target-oriented strategy, the computationally fast redatuming process eliminates the need for the traditional complex process of velocity estimation, model building, and iterative depth migration to remove the effects of the salt canopy and surrounding overburden. This may allow this strategy to be used in the field, in near real time.

In section 4.3, I further extend this strategy into the elastic world by studying its performance on synthetic elastic seismic data from a same GOM model. In the acoustic scheme the Green functions between receiver locations can be estimated by summing the cross-correlations of the pressure observed at the two receivers and excited by sources at the surface. An approximate representation for the Green's function between two passive receivers in an elastic medium has been derived by Wapenaar & Fokkema [2006]. This representation serves as the basis of our elastic scheme. In its simplest form, elastodynamic interferometry can be cast in terms of a sum of correlations of both P-wave source and S-wave source potentials. Hence, one requires the individual responses to P- and S-wave sources. In order to approximate the theoretically required source potentials, here we replace single sources at each shot position by a source-pattern defined by an 8-point-stencil for 3D or 4-point-stencil for 2D. In practice, it is in principle possible to decompose the data with a processing step (see [Wapenaar and Berkhout, 1989], for example). This allows us to investigate how the redatumed result is built up by the individual P- and S-wave source contributions and different velocity receiver components in the borehole. We test our elastic redatuming scheme on data simulated with an elastic finite difference algorithm. We extract elastic, multicomponent, Green's functions between receiver locations in a vertical borehole, from data recorded using P- and S-wave sources at the surface. The wavefields are redatuming into four parts: two related to the P-wave potential, and another two related to the S-wave potential.

These parts are migrated separately and form four independent images of the reservoir providing a more complete elastic description of the rocks.

## 4.2 Acoustic Modeling

### 4.2.1 Model Description

I will first illustrate the processing strategy using a synthetic, acoustic example. We create a 2-D data set representing a multi-level walkaway VSP for the model shown in

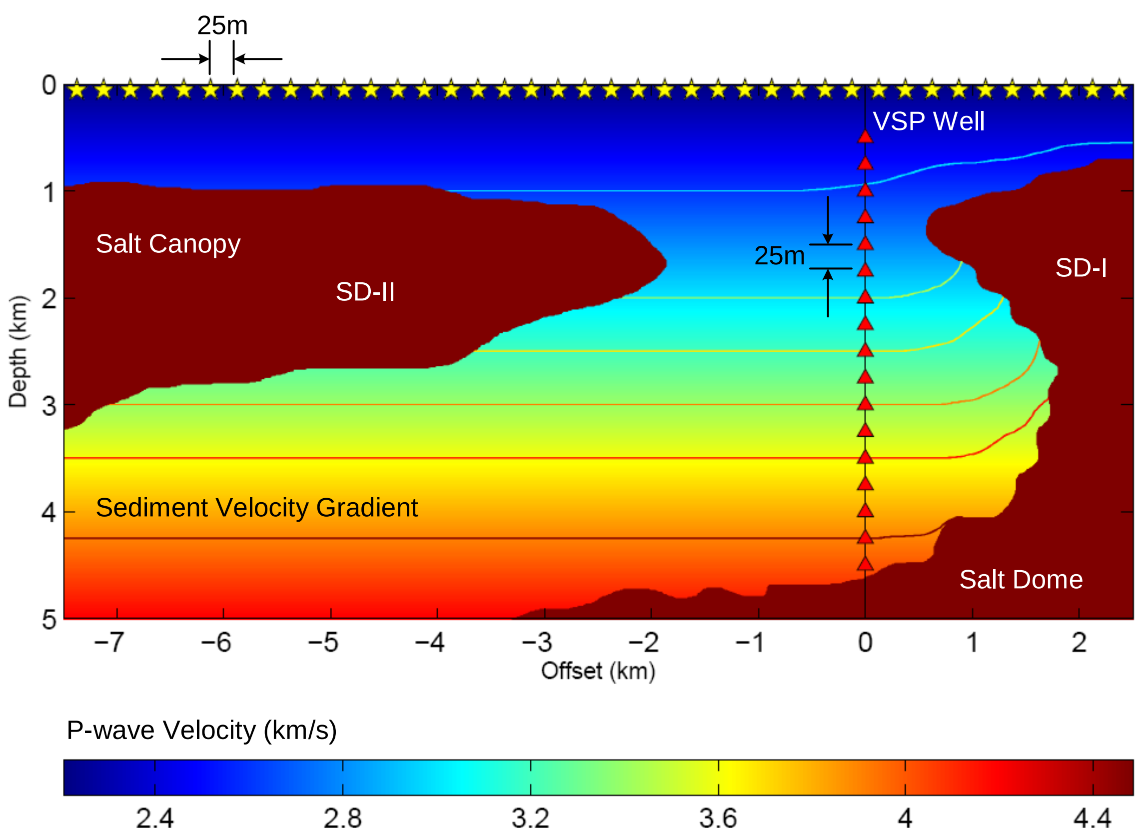


Figure 4-1: Walkaway VSP acquisition geometry for a synthetic GOM model composed of a simplified vertical velocity gradient and an embedded overhanging salt dome (SD-I) together with a second salt canopy nearby (SD-II). The yellow stars indicate the locations of the shots and the red triangles are the locations of the receivers. Note that not all 399 shots are shown (extending from -7.5 to 2.5 km laterally), and not all 161 receivers are shown (extending from 0.5 to 4.5 km in depth). The color bar shown is applicable for all figures in the text containing a velocity model.

Figure 4-1. The model is composed of a simplified GOM vertical velocity gradient, an embedded overhanging salt dome (SD-I) together with a salt canopy nearby (SD-II). The velocity gradient and values are taken from the EAGE/SEG salt dome model which represents typical GOM velocities [Aminzadeh *et al.*, 1997]. Both salt domes have a P-wave velocity of 4480 m/s. The background velocity is described by $v(z) = v_0 + Kz$, where $v$ is the velocity in m/s, $z$ is the depth in meters, $v_0$ is the velocity of the top layer ($v_0$ = 2200 m/s) and K is the velocity gradient ($K$ = 0.4 s$^{-1}$). Six reflectors are introduced on top of the $v(z)$ gradient as 15%-higher velocity spikes and the reflectors dip up towards the salt dome flank. Taking the well head as the origin, the walk away line consisting of 399 shots extends at the surface from -7.5 km to +2.5 km and the shot interval is 25 m. The receivers are placed in the borehole from a depth of 0.5 km to 4.5 km at a 25 m interval (total 161 receivers).

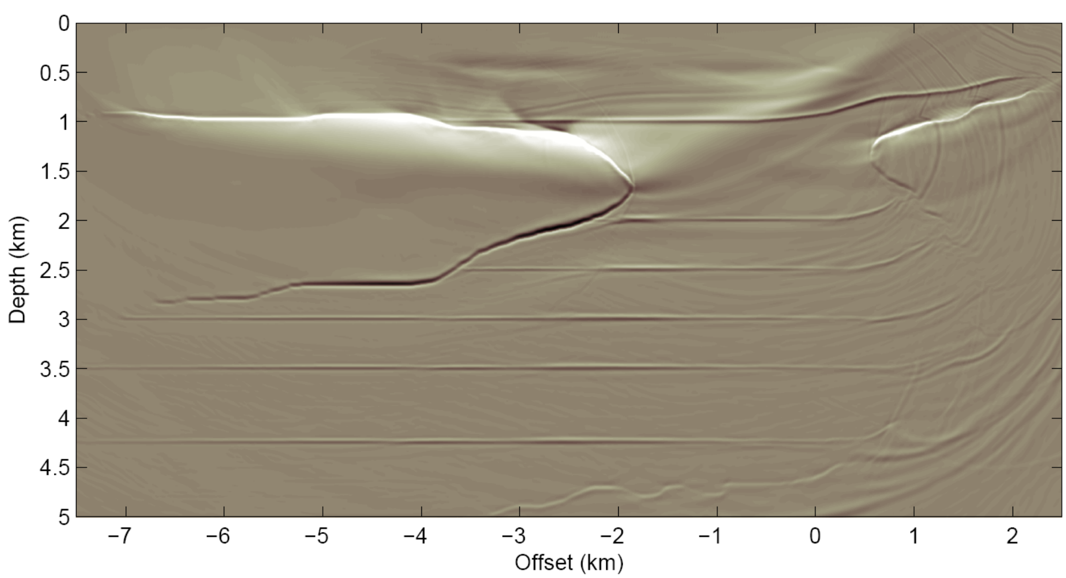


Figure 4-2: Image obtained from a conventional Kirchhoff prestack depth migration of a synthetic surface seismic data set using the exact forward velocity model shown in Figure 4-1.

Figure 4-2 shows an image obtained from a conventional Kirchhoff prestack depth migration of a synthetic surface seismic data set using the exact forward velocity model shown in Figure 4-1. In this image, we can see that even with the exact forward velocity model, the conventional surface seismic data migration has trouble to unveil the salt flank of the SD-I. For field data it would also require several iterative prestack depth migrations to achieve a velocity model that close to the true forward model.

This model creates four imaging challenges: The first is the complicating effect of the salt canopy upon the seismic energy reaching the well and subsequently the salt flank. Figure 4-3 shows a snapshot of the wavefield for a model (a) without the salt canopy, and (c) with the salt canopy. The corresponding common shot VSP records are shown in Figure 4-3 b and d. It is clear that the salt canopy has dramatically changed the wavefront that is marching forward to illuminate the salt flank. The redatuming process should remove this effect.

The second is the diverse range of structural dips at the salt flank. The vertical salt flank is parallel to the borehole and should be relatively easy to image. The horizontal portions of the layering are perpendicular to the well bore and will be very difficult to image away from the well. This is because the energy from downhole shots does not reflect back to the borehole from the horizontal layers, except when they intersect the well.

The third challenge is the vertical velocity variation which imparts strong "lateral" velocity variation (2.6 to 3.9 km/s) from the perspective of the downhole shot gathers. Here a prestack depth migration will properly handle the asymmetric ray paths.

The fourth challenge is the up dipping curvature of the layering at the salt dome edge. The energy reflected from this portion of the layer subsequently bounces off the salt edge, and therefore is multiply reflected, as shown in Figure 4-4a, and will not image with a one-way migration algorithm. A reverse-time depth migration algorithm which

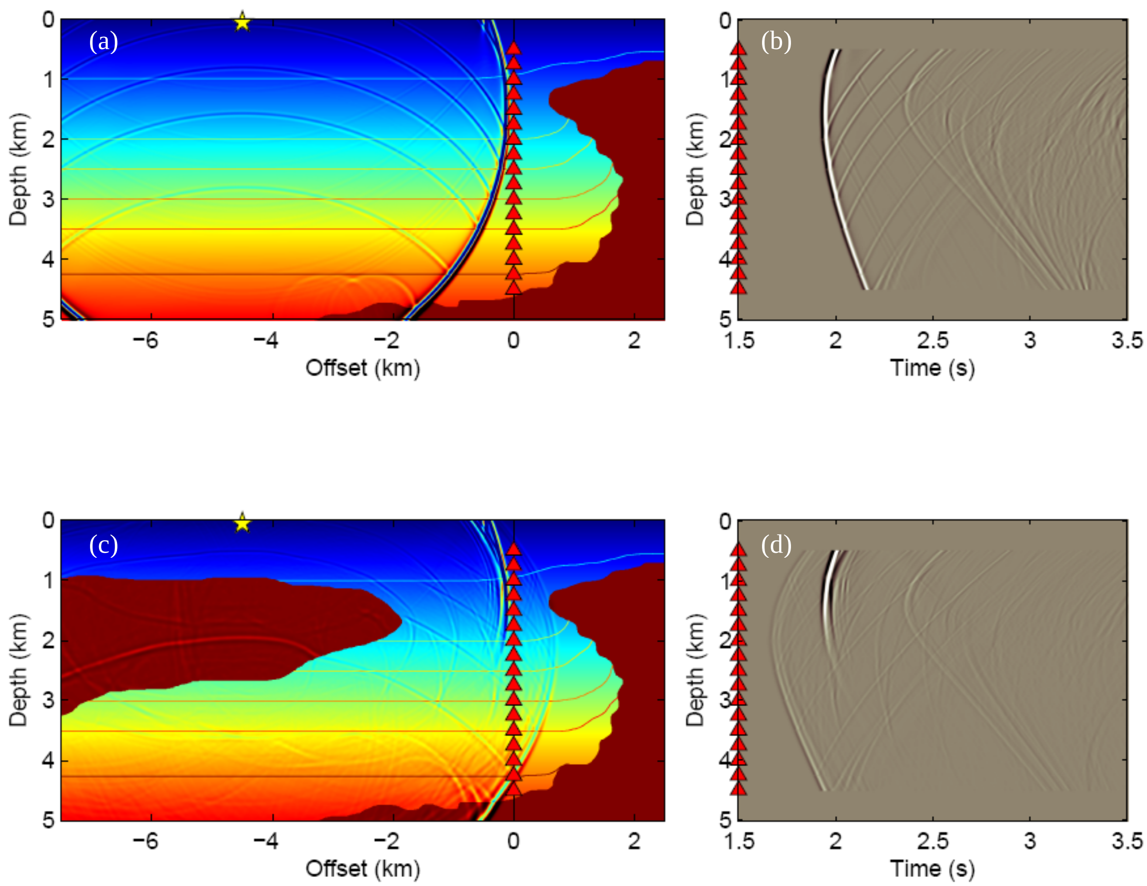


Figure 4-3: (a) Snapshot of wavefield at time = 2 s superimposed on corresponding model without the salt canopy. (b) Common shot VSP record for the model without the salt canopy. (c) Snapshot of wavefield at time = 2 s superimposed on corresponding model with the salt canopy. (d) Common shot VSP record for the model with the salt canopy. Notice the large distortion in arrival times and amplitudes caused by the salt canopy.

uses the two-way wave equation will overcome this challenge by back propagating the bounce off the salt correctly, as shown in Figure 4-4b, and described below.

To image the salt dome edge (SD-I) and the corresponding abutting sediments, and address the four challenges listed above, our proposed strategy consists of two parts: (1) redatum the surface source into the borehole, and (2) perform two passes of migration on the redatumed shot records. This two-step processing strategy is illustrated in Figure 4-5 using a flow chart. In the next two subsections, I will explain each of these two parts.

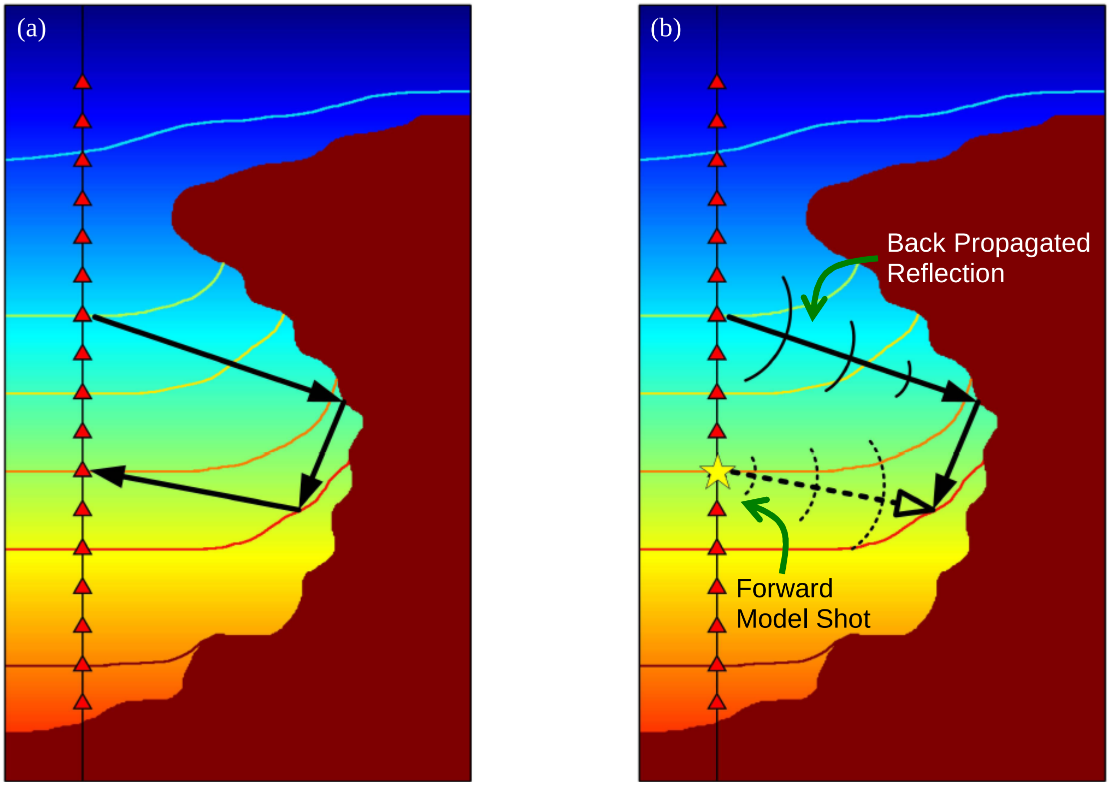


Figure 4-4: (a) Cartoon showing the ray paths of multiple reflections of the prismatic reflections. (b) Cartoon showing the migration process to image the prismatic reflections. The shot is forward modeled (dashed line). The recorded wavefield is back-propagated (solid line) using the full 2-way wave equation which allows bounces off the salt interface. An image is formed when the forward shot is time coincident with the back-propagated wavefield.

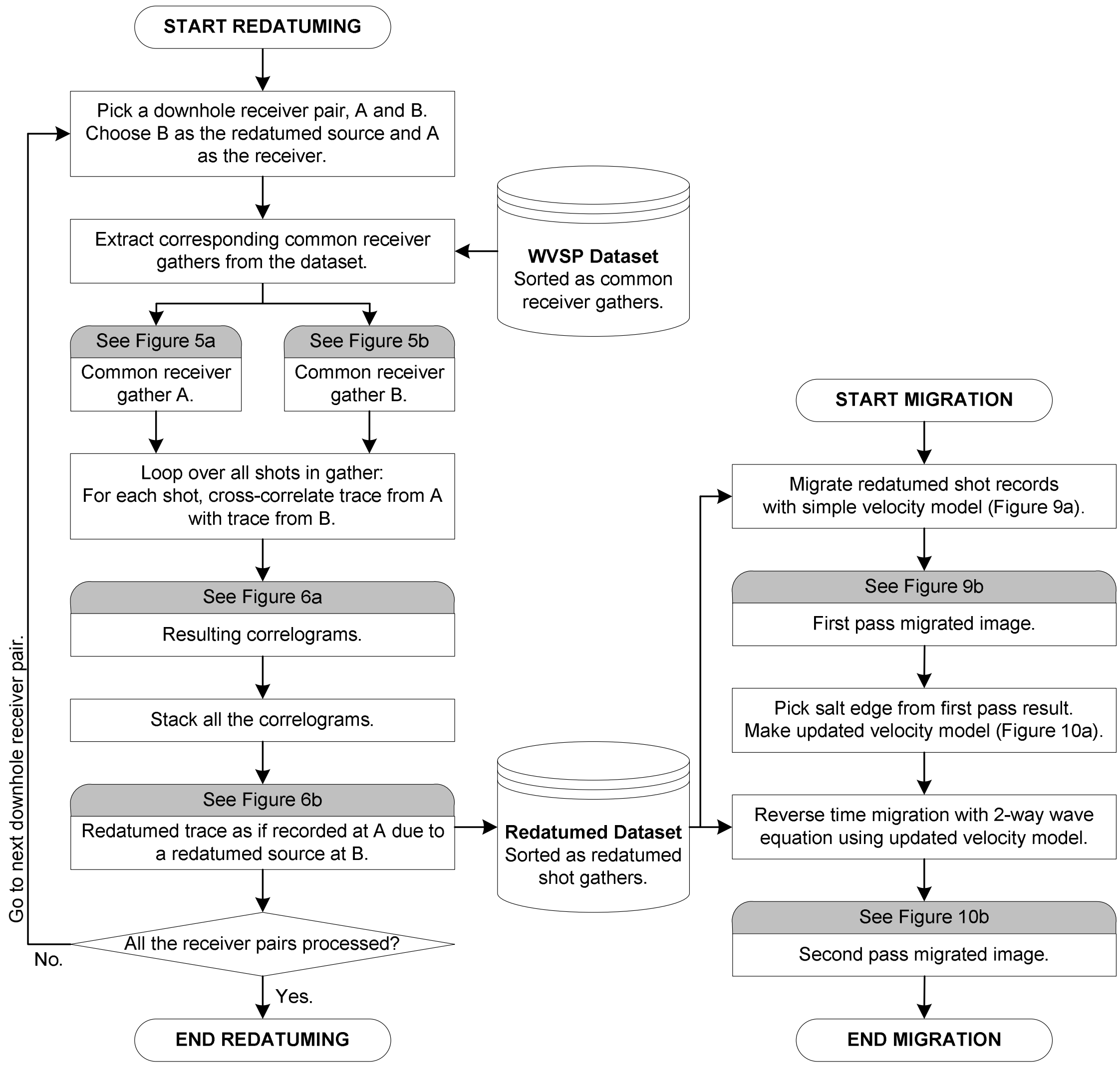


Figure 4-5: Flow chart illustrating the two parts of our proposed strategy: redatuming and migration.

### 4.2.2 Acoustic Redatuming

The first part applies redatuming to the WVSP traces. This will create new effective shot gathers which are as if both the sources and receivers were located in the borehole. To do this, we sort the WVSP data into common downhole receiver gathers. Next we select one of the actual downhole receiver locations to be an effective source location. Then we select another actual downhole receiver location to be an effective receiver location. Two representative common downhole receiver gathers at depths of 2

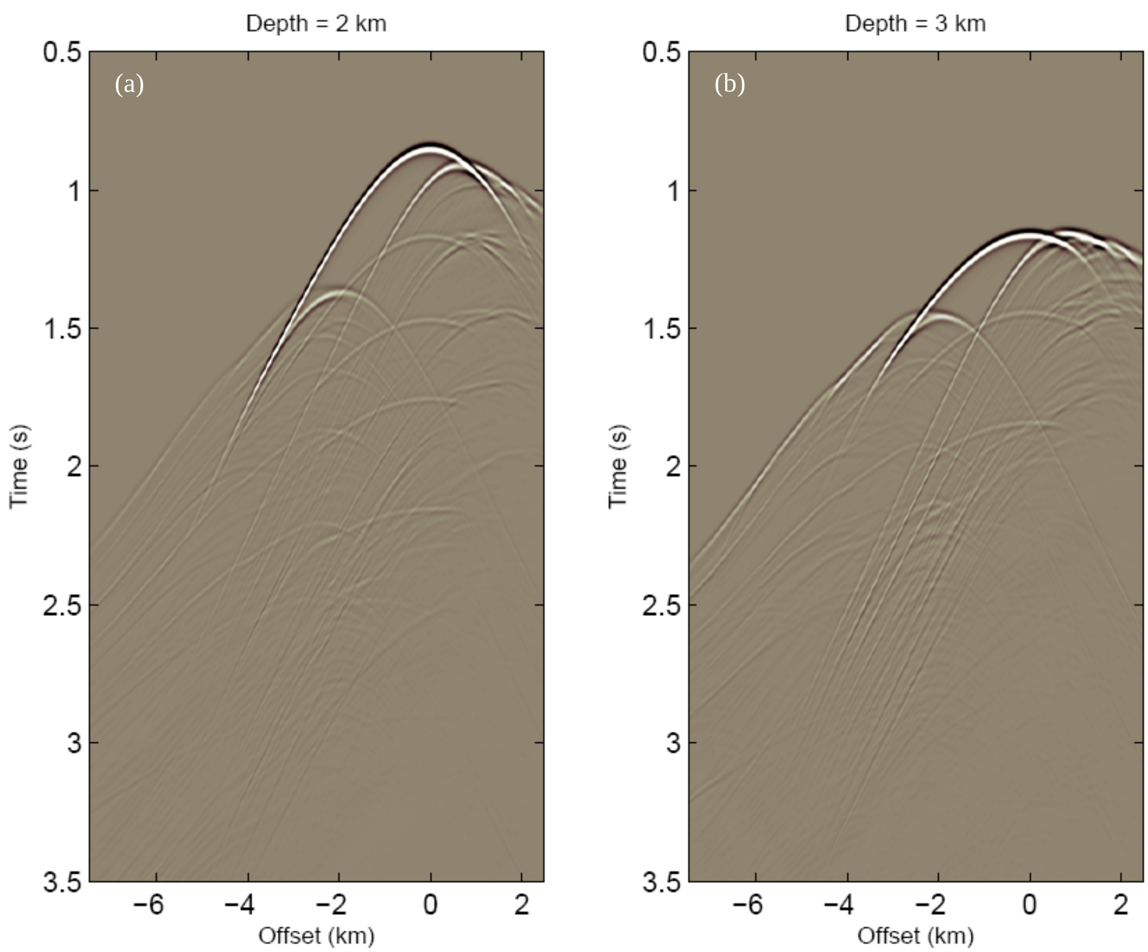


Figure 4-6: Common downhole receiver gathers at depths of (a) 2 km and (b) 3 km. Horizontal axes denote the offset of the corresponding shot for each trace.

km and 3 km, are shown in Figure 4-6. At the lowest level, operations on these two common-receiver gathers illustrate the basic building blocks of the redatuming process.

Suppose we want to estimate a recording of an effective shot located at a depth of 2 km by an effective receiver at a depth of 3 km. We use these two common receiver gathers from the original WVSP corresponding to the desired effective shot location (Figure 4-6a) and the effective receiver location (Figure 4-6b). There are a pair of traces, one trace from each of these two common-receiver gathers, corresponding to each surface shot. Each of these pairs of traces is cross-correlated. The horizontal axes in both common-receiver gathers shown in Figure 4-6 denote the shot offset for each trace. We start with the left-most shot offset at -7.5 km. We extract the corresponding traces from

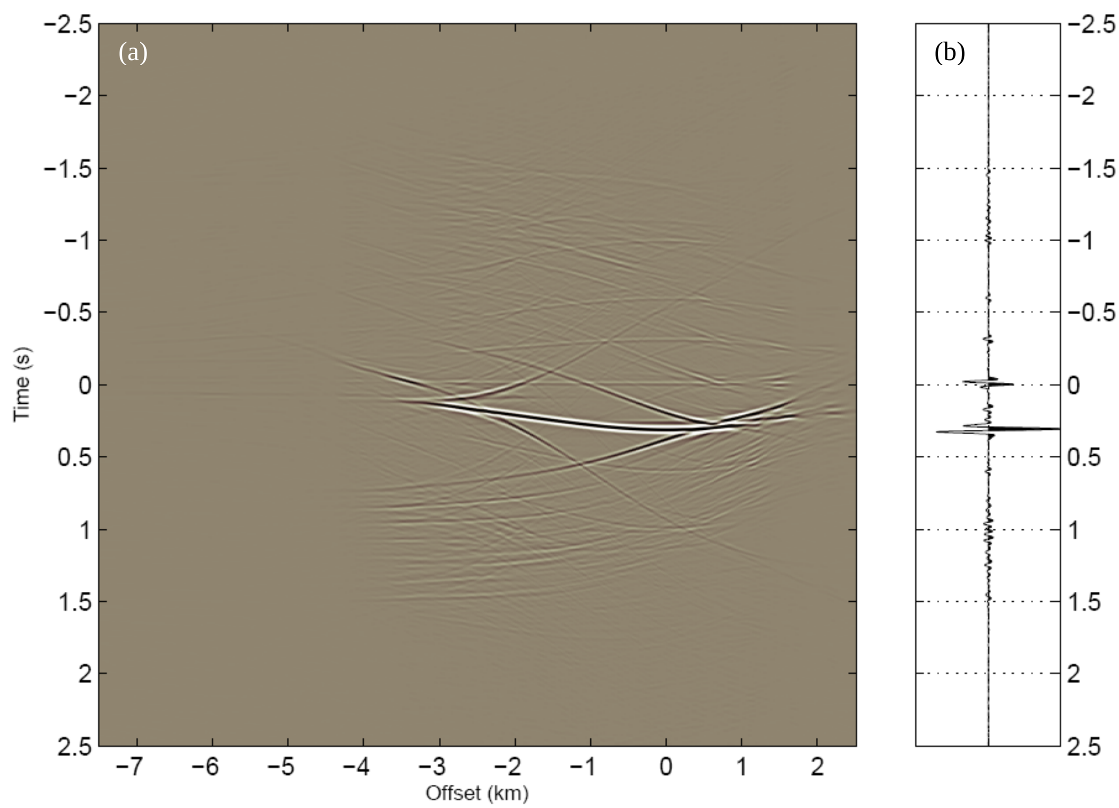


Figure 4-7: (a) Correlograms created by cross-correlating corresponding traces from Figure 4-6a and b; (b) estimate of the recorded trace due to an effective shot located at 2 km depth and a receiver at 3 km depth obtained by stacking all the traces in Figure 4-7a.

the common receiver gathers at depths of 2 km (left panel) and 3 km (right panel). Cross-correlating these two traces gives one correlated trace, or correlogram, which is shown as the left-most trace in Figure 4-7a. We repeat this operation for all shot offsets in this set of common receiver gathers which fills in the rest of the traces in Figure 4-7a. All the correlograms are stacked together to produce a single trace shown in Figure 4-7b. This single stacked trace becomes our estimate of the recorded trace due to an effective shot located at 2 km depth and a receiver at 3 km depth. The positive lags (causal portion) of the single stacked trace becomes our estimate of the recorded trace due to an effective shot located at 2 km depth and a receiver at 3 km depth [Wapenaar and Fokkema, 2006]. This trace is shown at a depth of 3 km in Figure 4-8a, which represents the complete redatumed shot record.

To estimate the traces for the next downhole receiver offset, we keep the common receiver gather corresponding to the effective shot location (at 2 km) and choose the common-receiver gather for the new desired effective receiver location. We then repeat the set of corresponding correlations as described above. By doing this for all receiver depth levels, we create an effective common downhole shot gather, such as in Figure 4-8a. This mimics a shot gather collected by the downhole receiver array due to a downhole source firing at the location that we choose to be the effective source location (at 2 km). For comparison, we show in Figure 4-8b the actual common shot gather modeled with a true source at a depth of 2 km, which we define as the benchmark case.

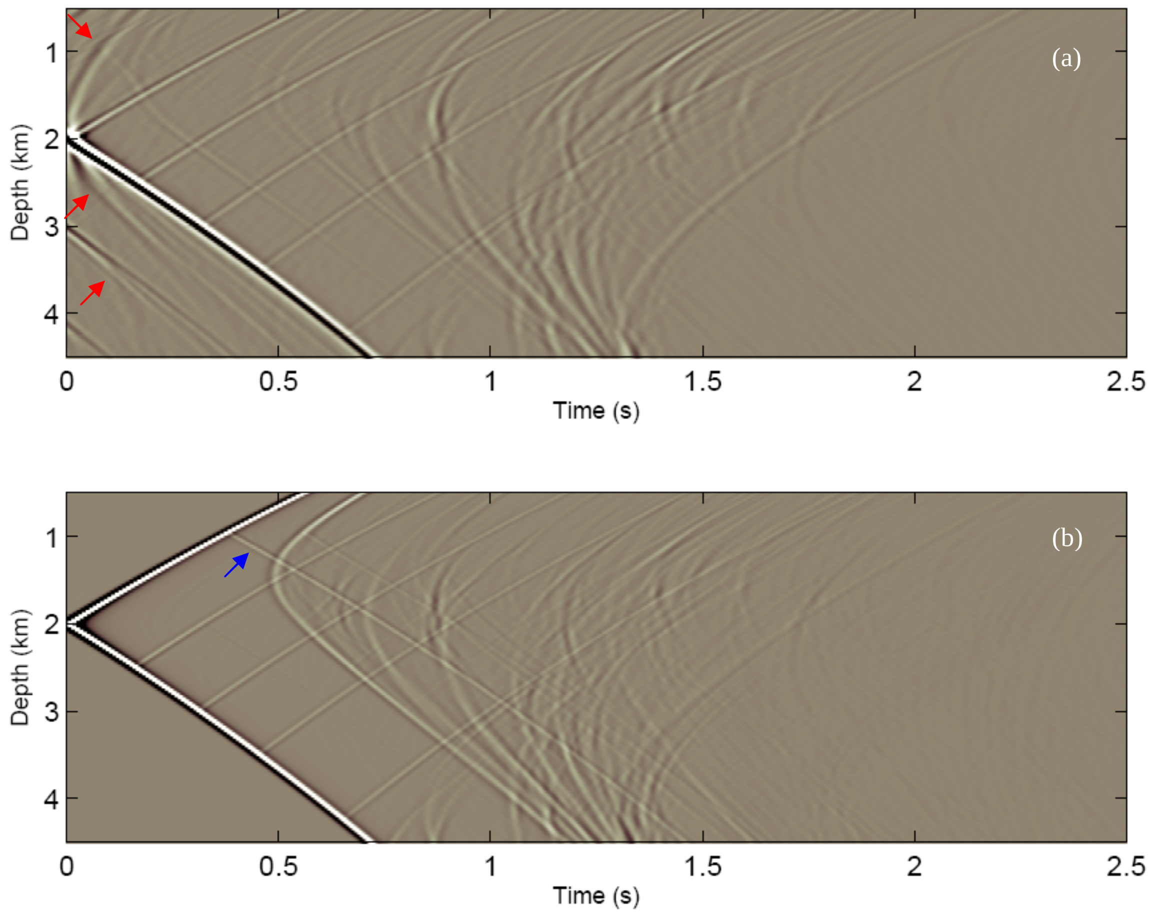


Figure 4-8: Common downhole shot gathers obtained (a) by redatuming WVSP data to be as if there were an effective source at a depth of 2 km, and (b) by placing an actual source at a depth of 2 km (benchmark case).

Comparing Figure 4-8a and b, we observe that these common shot gathers are similar, except that our redatumed downhole shot gathers include some spurious events (indicated by red arrows in Figure 4-8a) not present in the actual downhole record. Wapenaar and Fokkema [2006] describes these events as “ghost” events which are created by violations of the interferometric assumptions about complete source coverage, high frequency approximations and wavefield separation. Part of these spurious events comes from the acquisition aperture, which is limited to only surface shots. Although contaminated by these spurious events, the main reflections off the target salt flank (events which arrive after 0.75 sec) are present. We also observe that in Figure 4-8b, the linear downgoing event (indicated by a blue arrow) coming off of the first arrival at a depth of 1 km at time of 0.4 s is nearly absent in the redatumed traces (Figure 4-8a). This event is the downgoing specular reflection off of the underside of the flat laying sediment layer crossing the borehole location at a depth of 1 km. The omission of this energy is due to the fact that not very much of this energy is excited by a surface source. An actual downhole source creates upgoing energy which is reflected back downward when it encounters layers intersecting the borehole. Just as in the theory for migration, to be more correct we should put sources (or receivers) completely surrounding the area we wish to image. If this were possible, we would be able to reconstruct these down going reflections. (Van Manen *et al.* [2005] used this concept of sources all around the model for efficient simulation of wave propagation). However, since this is not practical for field scale surveys we must evaluate the effect of this limited aperture on the final results.

We observe that only the surface shot locations on the correlogram panel (Figure 4-7a) with events showing a zero time slope, or in other words a stationary phase point, contribute to the stacked trace (Figure 4-7b). To illustrate this concept we use a conceptual VSP model shown in Figure 4-9 containing a single reflector and two receivers. In Figure 4-9a, we select Receiver k to be the redatumed shot (or virtual source) location. The corresponding specular reflection point for Receiver m on the reflector is shown as point y. Each stationary phase point on the correlogram panel reveals the corresponding surface shot location (Shot i) from which the seismic ray passed through the redatumed shot location (Receiver k), then bounced off the specular reflection point (y) of the interface, and was captured at the borehole receiver (Receiver m). Rays starting at surface shots which do not pass through these three points (k, y and m) create

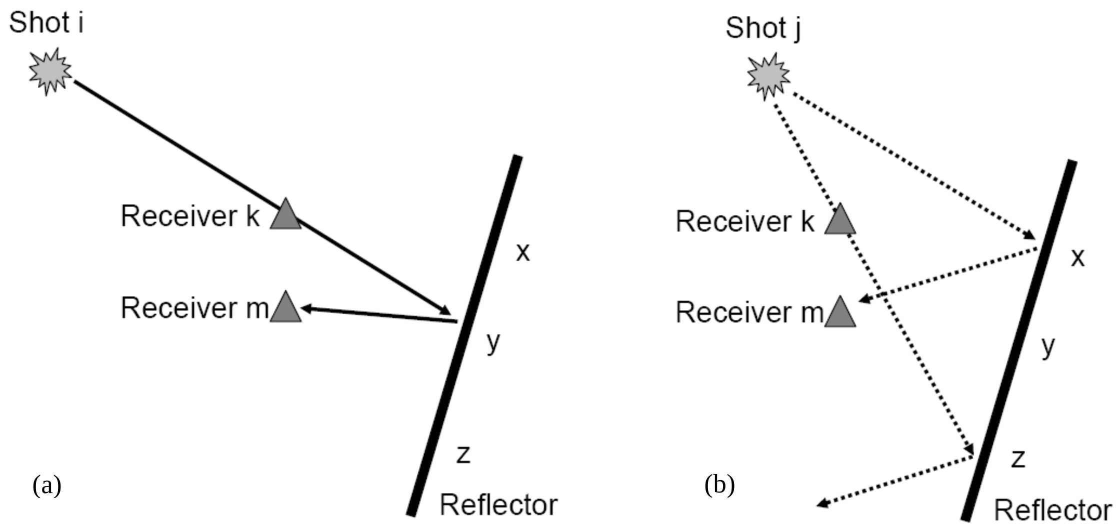


Figure 4-9: Diagram showing a ray path generating a stationary phase point in the correlograms. Receiver k is the location of the redatumed shot and Receiver m is the location of the redatumed receiver. (a) Contributing to the stationary phase point is the ray from Shot i, which travels through the redatumed shot (Receiver k) location, bounces off the specular reflection point y, and is captured by Receiver m. (b) Shot j does not contribute to the stationary phase point because the redatumed source, at Receiver k, is illuminating point z on the reflector, while Receiver m is recording energy from point x on the reflector.

the dipping portions of the correlograms and do not contribute to the final stacked trace. For example in Figure 4-9b, the ray passing through Receiver k from Shot j illuminates point z on the reflector, while the reflected energy recorded at Receiver m is from point x on the reflector. The events will correlate, but will not be at the minimum travel time for the specular reflection point for a source at Receiver k being recorded at Receiver m, so they will not be enhanced in the final stacked trace. We can see from this diagram that surface sources need to be used so that all reflected energy from the target to be imaged comes from rays that pass through the borehole array of receivers twice: once coming into the array as the illuminating energy, and once coming back as reflected energy from the target formations.

To obtain a complete redatumed downhole survey, we repeat this for all possible effective downhole source locations. Note that in order to redatum a surface shot to be in the borehole, we do not have to apply velocity analysis or complicated processing (such as statics or NMO corrections). In fact, there are no model dependent processing parameters required to move the surface shots into the borehole. We do not even need to know that there is a salt canopy complicating the raypaths of the energy. For the acoustic case, this feature allows the redatuming methodology to be performed in a fully automated fashion that requires virtually no human effort, except, for example, quality control edits.

The final step of the redatuming process is to prepare the data for migration. The redatumed shot gathers contain artifacts, described above, which would contaminate the migration. Many of these artifacts arrive before the direct arrivals. It is easy to eliminate these by simply applying a mute which removes everything up to and including the direct arrivals on the redatumed downhole shot gathers. We have not explored other methods of removing artifacts which occur later in time on the records yet.

This redatuming methodology gives kinematically correct results [Wapenaar and Fokkema, 2005], which is acceptable for structural imaging applications. In this paper we investigate the acoustic case – for elastic energy additional steps are needed to handle the multi-components. For example, the three components will need to be rotated into the proper orientation facing the salt flank. For stratigraphic and time-lapse applications more work is needed to ensure correct relative amplitudes.

The success of the redatuming step is determined by how much energy is reflected off the reflectors near the salt flank and captured by the receivers in the borehole. Because we are trying to image underneath the salt overhang, this is generally only possible in a medium with a generally increasing $v(z)$ vertical velocity profile. In other geometries and velocity regimes, other solutions are possible. For example, Bakulin and Calvert [2004] successfully capture the reflection energy and imaged horizontal reflectors using a horizontal well.

### 4.2.3 Imaging with Iterative Migrations

The second part of our strategy is to perform two passes of depth migration. The first pass defines the salt edge geometry and the second pass refines the image to capture the sediments. We have experimented with both Kirchhoff and reverse-time depth migration algorithms. For the first pass it is possible to use either method. However, we found that the sediment images are only obtainable using a reverse-time algorithm which employs the two-way wave equation. This is because the sediments are only illuminated by prismatic reflections [Cavalca and Lailly, 2005], which are created by energy which has bounced off the salt and then reflected by the sediments, and vice versa. In prestack reverse-time migration both the shot and recorded wave fields are extrapolated, and zero lag correlations between the wave fields form the image. To save CPU time and disk space, we used an analytically derived travel-time table for the forward propagated shot wave-field simulation. We used the full wave equation to back propagate the redatumed field data. Using a travel-time table is reasonable since our velocity model for the forward shot is a simple, linear $v(z)$ gradient function. However, we will image only half of the prismatic reflections – those that bounce off the salt first – and will not capture those that bounce off the sediment first.

For the first pass of migration, we need a generalized migration velocity model. To image and define the salt edge from the redatumed shot position, only the target oriented, background velocity between the salt flank and the borehole is required, which does not include the salt, as shown in Figure 4-10a. The spatial uncertainly introduced by using only a generalized velocity field between the salt and borehole is considerably less significant than for the entire path from the surface to the salt, which would have needed the complicated salt canopy.

We applied the same reverse time prestack depth migration to both the redatumed common-shot gathers and the actual modeled downhole common shot gathers (benchmark case). Figure 4-10b shows the migrated image using the redatumed data and Figure 4-10c shows the migrated image of the benchmark case. The image from the redatumed data is able to recover most of the salt edge in a similar fashion to the migrated benchmark results. Meanwhile both images illuminate very little of the dipping sediments.

Once the salt edge is delineated by the first pass of migration, we need to update our velocity model to include the salt for the second pass of migration. In practice we would do this by picking the interface between the salt and the background from the migrated image. However, we have not attempted to actually pick the salt edge from our first pass migrations. Instead, by using the actual salt edge (Figure 4-11a), we show the best result that might be possible.

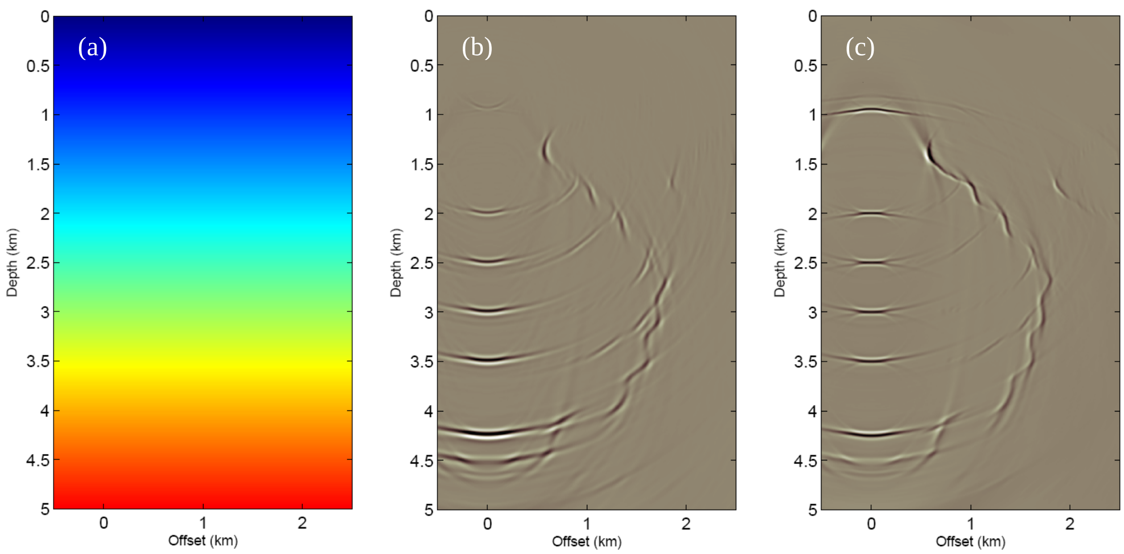


Figure 4-10: (a) Velocity model used in the first pass of migration with only the simple *v*(*z*) vertical velocity gradient; (b) migration results from reverse-time prestack depth migration of the redatumed data; (c) migration results from reverse-time prestack depth migration of the data created with downhole sources and receivers (benchmark case). (Velocity color bar is shown in Figure 4-1.)

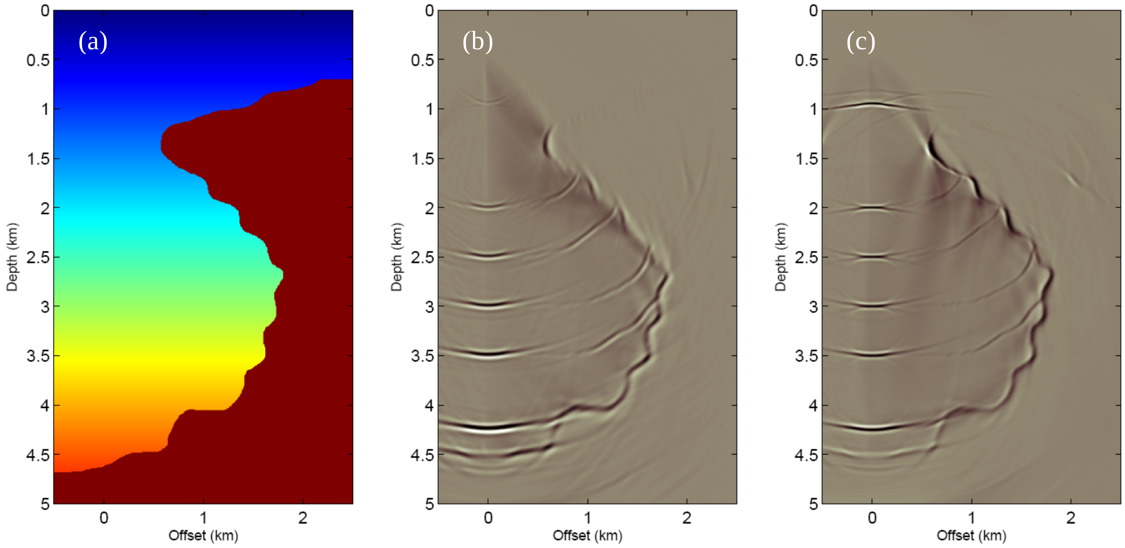


Figure 4-11: (a) Velocity model used in the second pass of migration which includes the salt dome that could be defined in the first pass; (b) migration results from reverse-time prestack depth migration of the redatumed data; (c) migration results from reverse-time prestack depth migration of the data created with downhole sources and receivers (benchmark case). (Velocity color bar is shown in Figure 4-1.)

For the second pass, we apply the reverse-time depth migration (which uses the two-way wave equation) to both the redatumed data and benchmark data. These migration results are shown in Figure 4-11b and c, respectively. Because we include the salt dome in the velocity model and are using a full wave equation algorithm, we are able to catch the energy that bounces off the salt flank and illuminates the sediments. These second pass images show very good delineation of both the dipping sediments and the salt edge. Some new artifacts, the large wavelength shadows in front of the salt edge, have crept into the image. These artifacts can be reduced with further refinement of the migration algorithm or post-processing of the data with high pass spatial filter [Yoon *et al.*, 2004; Fletcher *et al.*, 2005; Guitton, *et al.*, 2006].

Comparing the results of the first pass of migration for both the benchmark and the redatumed cases (Figure 4-10b and c), both image the edges of the bottom half of the salt dome with about the same quality. However, on the upper half of the salt dome, the undersides of the salt crenulations are much better defined in the benchmark image (Figure 4-10c). This is because the actual downhole source has a better chance to illuminate the underside of the salt and have the receivers capture the reflections. The redatumed shot records (Figure 4-8a) most likely suffers from a lack of aperture in the original WVSP. The sediment events have nearly the same amount of clarity on both the benchmark and redatumed images, with the benchmark case having slightly better quality.

The second pass of migration (Figure 4-11), which uses the salt dome velocity in the migration model, shows somewhat improved images of the salt interface. However the greatest improvement is seen in the sediments. Now the sediment interfaces are distinguishable for up to 0.75 km away from the salt edge until the dip of the sediments is nearly flat. At that distance the acquisition geometry does not seem to capture reflections from horizontal events, except immediately around the borehole. Thus the redatuming step followed by two passes of reverse-time migration has been able to capture the salt edge and dipping sediments. The reverse-time migration has been able to utilize the multipath arrivals, which have bounced off the salt edge, to make this improvement.

The two-step processing strategy eliminates the need for many iterative steps of prestack depth migration in order to build the velocity model for the overburden. These steps have been replaced by the redatuming process, which takes about ten percent of the total computational effort for the proposed strategy.

### 4.2.4 Comparison to WVSP Migrated Image

Instead of hand picking the outline from the first pass migration results in this example, we used the exact outline of the salt dome edge in the velocity model for the second pass of migration. Obviously, for field data we would have had to digitize the edge. However, the outline of the salt dome edge from the first pass of migration is well imaged and would not be very different from the exact model. So we believe our final results are representative of the best that could be expected but would not be too far from what is possible. We show that by moving the surface shots into the borehole and closer to the target area near the salt dome, higher order migration algorithms, using key multiple reflections, can be employed because the artifacts induced by the uncertainties of the velocity model have been greatly reduced.

The issue that remains is whether a conventional prestack depth migration of the original WVSP data set would produce a comparable image. To answer this question, we perform a reverse-time, prestack depth migration of the WVSP using the correct velocity model containing the salt canopy but with the salt dome removed, as shown in Figure 4-12a. In order to build this migration model for actual field data, multiple passes of prestack depth migration of surface seismic data and model building would need to be performed to first define the top of the salt canopy, and then the base of the salt canopy. Figure 4-12b shows the WVSP migrated result using the correct velocities for the left side of the model. As with the redatumed result, the salt edge is imaged well, but the sediments near the salt are missing.

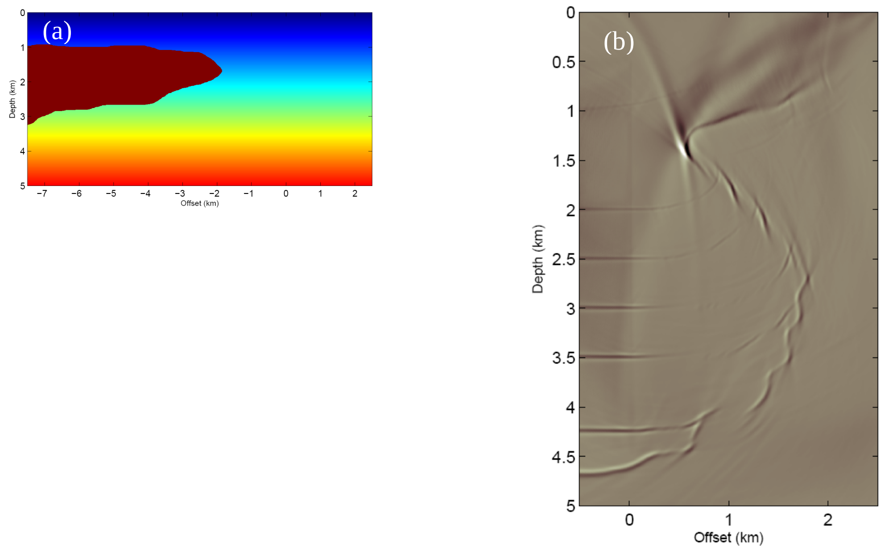


Figure 4-12: (a) Velocity model used in the first pass of WVSP migration which assumes that we already have a good knowledge of the salt canopy (SD-II); (b) migration results from reverse-time prestack depth migration of the WVSP data. (Velocity color bar is shown in Figure 4-1.)

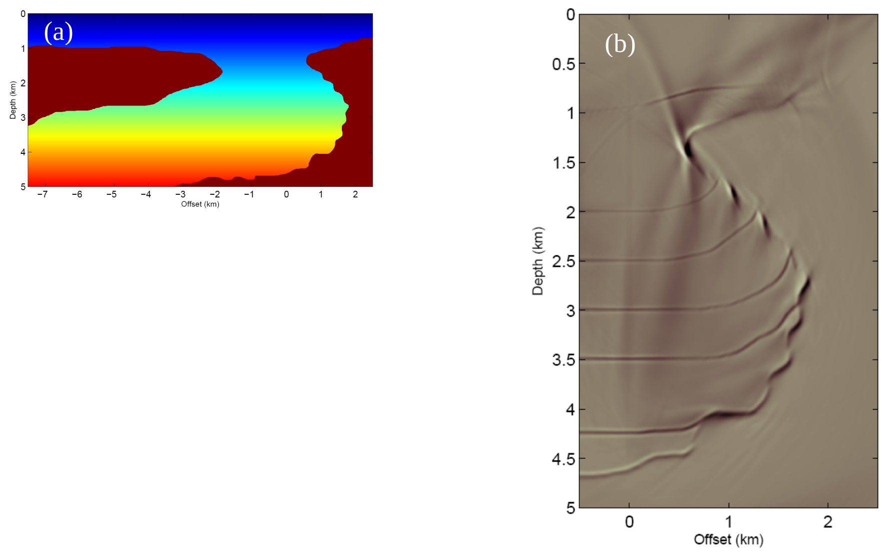


Figure 4-13: (a) Velocity model used in the second pass of WVSP migration which includes both the salt canopy (SD-II) and the salt dome (SD-I) that could be defined in the first pass; (b) migration results from reverse-time prestack depth migration of the WVSP data. (Velocity color bar is shown in Figure 4-1.)

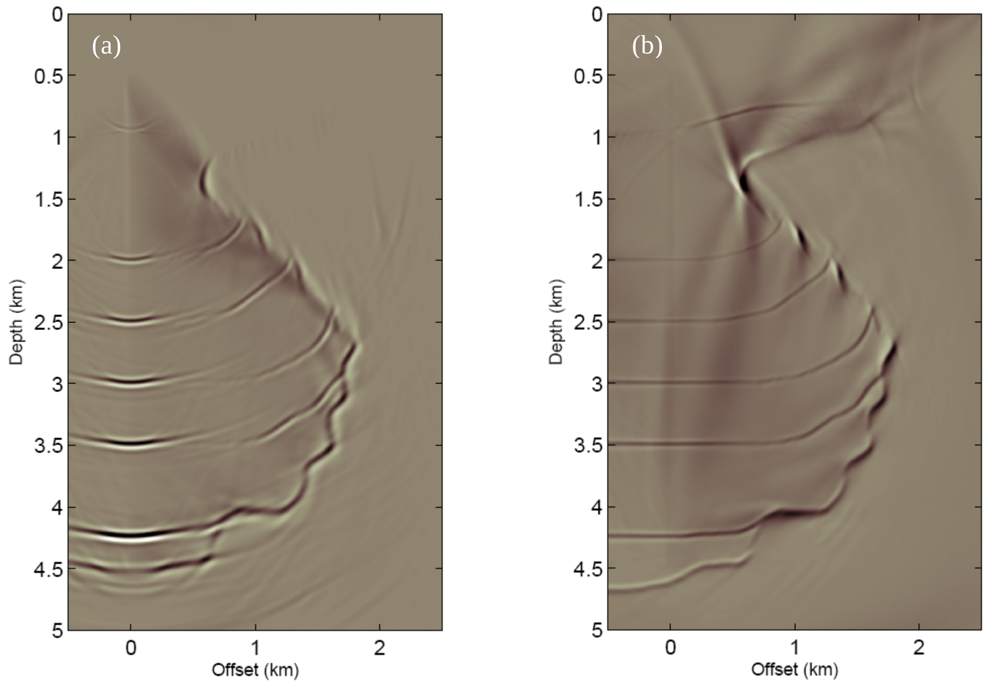


Figure 4-14: Comparison of second pass migration results of (a) the redatumed data, and (b) the WVSP data.

We next apply a second pass of depth migration to the WVSP using the correct velocity model containing the salt dome (Figure 4-13a). The final migrated result is shown in Figure 4-13b. The migrated WVSP image from Figure 4-13b and the migrated image of the redatumed VSP from Figure 4-11b are plotted side by side in Figure 4-14 for easier comparison. Overall we see that both methods have imaged most of the salt edge very well. However, the undersides of the crenulations on the top half of the salt dome are not very clear on either section. The WVSP image has reproduced the sediments reflections all the way across the section and up to the salt edges. The redatumed result captures the horizontal portion of the sediments only extremely close to the borehole, but obtains a reasonable image of the dipping portion near the salt.

In this section we have described a strategy to perform a short cut approach to image the sediments and salt edge around a salt flank through a complex overburden using a WVSP data set. Traditionally, depth migration utilizes numerous iterations of migration, velocity estimation, and model building. The short cut of redatuming the WVSP data, which is equivalent to the situation where an effective downhole survey would have been collected with shots and receivers in a single borehole, allows us to ignore all of the velocity issues associated with the overburden. We have not discussed the velocity estimation issue for the simple $v(z)$ background velocities used in our migrations. We believe that having relocated our frame of reference to be from the borehole perspective, the image uncertainty associated with velocity errors have been greatly reduced since the distance from the well bore to the salt flank is typically comparatively small. Also, we have not attempted to actually pick the salt edge from our first pass migrations to build the model for the second pass migration. Instead we show the best that might be possible by using the actual salt edge. Obviously, the success of this method on actual field data will depend on data quality, field acquisition parameters including aperture, source and receiver spacing, as well as the actual geometry of the salt bodies. Another aspect is the extension of this method to 3D. Images created from the redatumed shots are intrinsically contained within the plane of the surface shots and the receivers in the well. A 3D image volume, therefore, can be created from a sequence of 2D images from selected ranges of surface shots from a 3D VSP survey. I will discuss this in details in Chapter 5 with a 3D field experiment.

## 4.3 Elastic Modeling

So far, the development of interferometric redatuming schemes has focused on acoustic applications of redatuming the P or S wavefield separately. But, even in this case, the estimation of the dynamic part of the interferometric result is not yet fully understood. Schuster and Zhou [2006] review various interferometric redatuming schemes and conclude that they differ in the way schemes weigh cross correlations. (In fact, the schemes also differ in the way the data is windowed or muted before cross correlation.) In their derivation of elastodynamic Green's function representations, Wapenaar and Fokkema [2006] point out some causes for amplitude errors. For acoustic structural imaging, these amplitude errors are usually acceptable. In some imaging applications accurate handling of (relative) amplitudes in multicomponent data is very important. One use of multicomponent data in this context is the determination of the direction of reflections in (3D) VSP imaging with polarization analysis (see Chapter 5 for a 3D field example). This fact has sparked some interest in elastodynamic interferometric redatuming and how it affects the data.

In previous section, I introduced a processing strategy for imaging salt-dome flanks and dipping sediments in the acoustic medium approximation. In that model study, the only wavefield quantity involved in redatuming and migration is pressure. However, multicomponent data offers the possibility to extract elastic parameters which are becoming very important in characterizing complex reservoirs. We would expect that a full elastodynamic redatuming procedure would be capable of constructing a more complete reservoir image since it would use all components of the wavefield. However, the handling of elastic data in seismic exploration is has not yet become routine.

One approach to understanding the entire wavefield is to decompose it into the P and S wave contributions. Wavefield-based decomposition of the elastic wavefield is based on the notion that in a homogeneous isotropic solid the displacement can be represented as a superposition of scalar P-and S wave potentials. It is therefore possible to separate these contributions by applying curl and divergence (spatial differentiation) operators to the data. While Wapenaar and Berkhout [1989] and Holvik and Amundsen [2005] implement this in a processing step, the spatial derivatives may also be implemented in the field by deploying specially designed arrays of geophones [Robertsson and Muyzert, 1999; Robertsson and Curtis, 2002].

In this section, we apply the redatuming methodology outlined in previous section to elastic data. In the acoustic scheme the Green's function between receiver locations can be estimated by summing the crosscorrelations of the pressure observed at the two receivers which is excited by a series of sources at the surface. An approximate representation for the Green's function between two (passive) receivers in an elastic medium has been derived by Wapenaar and Fokkema [2006]. This representation serves as the basis of our elastic scheme. In its simplest form, elastodynamic interferometry can be cast in terms of a sum of correlations of both P-wave source and S-wave source potentials. Hence, one requires the individual responses to P- and S-wave sources. Draganov *et al.* [2007] recently followed a similar approach with approximate shear sources in a laboratory experiment. In order to approximate the source potentials required by the theory, we replace single sources at each shot position by a source-pattern defined by an 8- point-stencil for 3D, or a 4-point-stencil for 2D. (In principle, it may be possible to perform this decomposition of the data without the elaborate field effort, but only using a processing step as shown by Wapenaar and Berkhout [1989].) This allows us to investigate how the redatumed result is built up by the individual P- and S-wave source contributions and different velocity components of the receivers in the borehole.

### 4.3.1 Implementation Methodology

A general representation of the elastic Green's function between two locations in an elastic medium can be derived using the elastic reciprocity theorem of the time-correlation type [de Hoop, 1995]. However, we start with the approximate result from the analysis of Wapenaar and Fokkema [2006] for the extraction of the elastodynamic response between two points, $\mathbf{x}_A$ and $\mathbf{x}_B$, in a domain Ω (farfield approximation):

$$G_{p,q}^{v,f}(\mathbf{x}_A,\mathbf{x}_B,-t)+G_{p,q}^{v,f}(\mathbf{x}_A,\mathbf{x}_B,t)\approx \frac{2}{\rho V_P}\oint_{x\in\Omega}G_{p,0}^{v,\phi}(\mathbf{x}_A,\mathbf{x},t)\otimes G_{q,0}^{v,\phi}(\mathbf{x}_B,\mathbf{x}_i,-t)\,\mathrm{d}\,x + \frac{2}{\rho V_S}\oint_{x\in\Omega}G_{p,k}^{v,\psi}(\mathbf{x}_A,\mathbf{x},t)\otimes G_{q,k}^{v,\psi}(\mathbf{x}_B,\mathbf{x},-t)\,\mathrm{d}\,x \quad . \tag{4-2}$$

Here we follow a similar notation convention for the elastodynamic Green's function as used by Wapenaar and Fokkema [2006]. The quantity $G_{p,q}^{v,f}(\mathbf{x}_A,\mathbf{x}_B,t)$ on the left hand side of equation (4-2), denotes the causal time-domain Green's function, representing the particle velocity impulse response (denoted by the superscript *v*) recorded at $\mathbf{x}_A$ due to a force-type source (denoted by the superscript *f*) applied at $\mathbf{x}_B$. The subscripts *p* and *q* are the corresponding component indices ranging from 1 to 3. The right hand side is composed of two terms. The first term is a sum of cross-correlations (operator $\otimes$ denotes the convolution) of observed particle velocity at $\mathbf{x}_A$ and $\mathbf{x}_B$ due to P-wave sources at position $\mathbf{x}$ on a surface Ω. The second part is similar, but due to S-wave sources of different polarizations. We use $\phi$ to denote the P-wave potential, and $\psi$ to denote the S-wave potential. The subscript 0 indicates the single component of the P-wave source and the subscript *k* represents different components of the S-wave source (*k* ranges from 1 to 3). Note that these two parts do not contribute equally to the reconstructed Green's function. The weights of the two parts are related to $V_P$ and $V_S$, which are the P-wave and S-wave propagation velocity of the medium outside the domain boundary Ω (assuming homogenous and isotropic). In practice, this assumption may or may not be valid. However, for structural imaging applications if only kinematically correct results are expected, we can use an approximate $V_P/V_S$ ratio as the weights in equation (4-2).

Equation (4-2) states that the Green's function and its time-reversed version of a medium between $\mathbf{x}_A$ and $\mathbf{x}_B$ can be obtained by summing the cross-correlations of responses measured at $\mathbf{x}_A$ and $\mathbf{x}_B$ from sources at $\mathbf{x}$ on the surface Ω. In various applications of seismic interferometry, the nature of the actual sources and their locations differ. In "daylight imaging" (see Draganov *et al.* [2006], for example), the sources are assumed to be uncorrelated white noise on an arbitrarily shaped boundary in the subsurface, while the receivers are at the surface. In this case, one extracts reflection responses from transmitted waves. In solid-Earth seismology, energy can come from the interaction of ocean waves with the continental crust. Sources are therefore mostly confined to the (close vicinity of) the Earth's surface. With receivers also at the surface, one mainly extracts surface waves from the cross correlations (see Shapiro *et al.* [2005], for example). In some applications in active (exploration) seismology, the sources are at the free surface, while receivers are placed in a bore hole [Bakulin and Calvert, 2005; Lu, *et al.*, 2006; Willis, *et al.*, 2006]. The benefit of this particular application can be understood in terms of Huygens' principle as expressed in the Kirchhoff integral: by focusing the wave field from several sources onto a specific point in the subsurface, one creates an effective (secondary) source at that location (Berkhout [1997] refers to this as focusing in emission). The secondary source illuminates the target from the vantage point of the new datum (in this case the bore hole). By measuring the focusing operators directly, one does not have to assume a velocity model or apply statics.

In order to use equation (4-2) we need the response of P- and S-wave sources. In principle, the data from 3C sources and 3C receivers may be decomposed by a processing step [Wapenaar and Berkhout, 1989] to obtain these responses. However, for our purpose, we may construct artificially P- and S-wave source responses. We can then apply equation (4-2) directly to estimate the Green's function between two receivers in the borehole. We implement this by replacing a single source at each shot position $\mathbf{x}$ by a source pattern on an 8-point-stencil for 3D or 4-point-stencil for 2D.

The particle displacement in a solid can be decomposed as follows [Aki and Richards, 1980]:

$$\mathbf{u} = \nabla\Phi + \nabla\times\mathbf{\Psi} \qquad (4\text{-}3)$$

In a homogeneous, isotropic solid, $\Phi$ and $\mathbf{\Psi}$ represent the P-wave potential and S-wave potential respectively. Hence, by measuring the divergence and curl of the wavefield, one can measure independently the P or S wave contribution $\nabla^2\Phi$ and $\nabla\times\nabla\times\mathbf{\Psi}$ [Robertsson and Muyzert, 1999].We follow Wapenaar and Berkhout [1989] and define the P- and S-wave potentials as follows:

$$\partial_t\phi = -C\partial_k v_k \qquad (4\text{-}4)$$

and

$$\partial_t\psi_k = -\mu\varepsilon_{kmn}\partial_m v_n \qquad (4\text{-}5)$$

where $C = \lambda + 2\mu$ and $\lambda$ and $\mu$ are Lamé parameters. $\varepsilon_{kmn}$ is the alternating tensor with $\varepsilon_{123} = \varepsilon_{312} = \varepsilon_{231} = -\varepsilon_{213} = -\varepsilon_{321} = -\varepsilon_{132} = 1$. Note we consider now the particle velocity $v_k = \partial_t u_k$.

Next, let $G_{m,n}^{v,f}$ denotes the particle velocity observed in the *m*-direction, excited by an impulsive point force in the *n*-direction. Then, from equation (4-4) and (4-5), we have,

$$G_{m,0}^{v,\phi}(x_A, x, t) = -C(\mathbf{x})\partial_n G_{m,n}^{v,f}(x_A, x, t) \tag{4-6}$$

and

$$G_{m,k}^{v,\psi}(x_A, x, t) = -\mu(x)\varepsilon_{kln}\partial_l G_{m,n}^{v,f}(x_A, x, t) \tag{4-7}$$

Here the derivatives are taken with respect to the source coordinate **x**. Note also, that the material properties at the source location are needed. Approximating the first-order spatial derivatives using central differences, the particle velocity due to a P-wave source and the particle velocity due to an S-wave source can be approximated by setting off 3C force sources on an 8-point-stencil for 3D as shown in Figure 4-15(a) or a 4-point-stencil for 2D as shown in Figure 4-15 (b). Considering the 3-D case, each position **x** is surrounded by point sources, numbered with the bracketed superscript *s*, at $\mathbf{x}^{[s]}$, $s$ = 1..8 (see Figure 4-15 (a)]. In practice, one may decompose the wavefield if a dense distribution of 3C vibrators is available. However, here we create artificially P and S-wave sources. Using central differences, the curl operator acting (acting at the source position) in equation (4-7) can be approximated in 3D as follows:

$$\varepsilon_{kln}\partial_l G^{v,f}_{m,n}(x_A,x,t)=$$
$$\begin{cases}
\frac{1}{4L}\Bigg[\Bigg(\sum_{s=5,6,7,8} G^{u,f}_{m,3}(\mathbf{x}_A,\mathbf{x}^{[s]},t)-\sum_{s=1,2,3,4} G^{u,f}_{m,3}(\mathbf{x}_A,\mathbf{x}^{[s]},t)\Bigg) \\
\quad -\Bigg(\sum_{s=3,4,7,8} G^{u,f}_{m,2}(\mathbf{x}_A,\mathbf{x}^{[s]},t)-\sum_{s=1,2,5,6} G^{u,f}_{m,2}(\mathbf{x}_A,\mathbf{x}^{[s]},t)\Bigg)\Bigg], \quad k=1 \\
-\frac{1}{4L}\Bigg[\Bigg(\sum_{s=2,4,6,8} G^{u,f}_{m,3}(\mathbf{x}_A,\mathbf{x}^{[s]},t)-\sum_{s=1,3,5,7} G^{u,f}_{m,3}(\mathbf{x}_A,\mathbf{x}^{[s]},t)\Bigg) \\
\quad -\Bigg(\sum_{s=3,4,7,8} G^{u,f}_{m,1}(\mathbf{x}_A,\mathbf{x}^{[s]},t)-\sum_{s=1,2,5,6} G^{u,f}_{m,1}(\mathbf{x}_A,\mathbf{x}^{[s]},t)\Bigg)\Bigg], \quad k=2 \\
\frac{1}{4L}\Bigg[\Bigg(\sum_{s=2,4,6,8} G^{u,f}_{m,2}(\mathbf{x}_A,\mathbf{x}^{[s]},t)-\sum_{s=1,3,5,7} G^{u,f}_{m,2}(\mathbf{x}_A,\mathbf{x}^{[s]},t)\Bigg) \\
\quad -\Bigg(\sum_{s=5,6,7,8} G^{u,f}_{m,1}(\mathbf{x}_A,\mathbf{x}^{[s]},t)-\sum_{s=1,2,3,4} G^{u,f}_{m,1}(\mathbf{x}_A,\mathbf{x}^{[s]},t)\Bigg)\Bigg], \quad k=3
\end{cases} . \tag{4-8}$$

Although a P-wave source can be implemented differently, we choose to combine the already measured responses in a similar way as for the S-wave source:

$$\begin{aligned}
\partial_n G^{v,f}_{m,n}(x_A,x,t)= \\
&\frac{1}{4L}\Bigg[\Bigg(\sum_{s=2,4,6,8} G^{u,f}_{m,1}(\mathbf{x}_A,\mathbf{x}^{[s]},t)-\sum_{s=1,3,5,7} G^{u,f}_{m,1}(\mathbf{x}_A,\mathbf{x}^{[s]},t)\Bigg) \\
&+\Bigg(\sum_{s=5,6,7,8} G^{u,f}_{m,2}(\mathbf{x}_A,\mathbf{x}^{[s]},t)-\sum_{s=1,2,3,4} G^{u,f}_{m,2}(\mathbf{x}_A,\mathbf{x}^{[s]},t)\Bigg) \\
&+\Bigg(\sum_{s=3,4,7,8} G^{u,f}_{m,3}(\mathbf{x}_A,\mathbf{x}^{[s]},t)-\sum_{s=1,2,5,6} G^{u,f}_{m,3}(\mathbf{x}_A,\mathbf{x}^{[s]},t)\Bigg)\Bigg]
\end{aligned} . \tag{4-9}$$

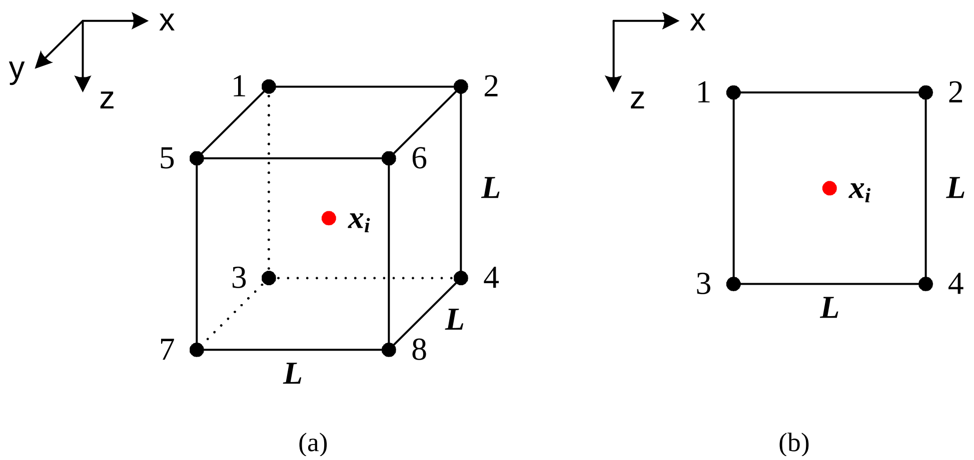


Figure 4-15: Illustration of (a) the 8-point-stencil shooting pattern for 3D acquisition and (b) the 4-point-stencil shooting pattern for 2D.

The response due to an effective P-wave source at $\mathbf{x}$ is then obtained by the sum of components and sources as prescribed by equation (4-9) and multiplied by the factor $C(\mathbf{x})$ [see equation (4-6)]. The response due to an effective S-wave source at $\mathbf{x}$ is then obtained by the sum of components and sources as prescribed by equation (4-8) and multiplied by the factor $\mu(\mathbf{x})$ [see equation (4-7)].

Once we have the responses $G_{p,0}^{v,\phi}(\mathbf{x}_A,\mathbf{x},t)$ , $G_{p,k}^{v,\psi}(\mathbf{x}_A,\mathbf{x},t)$ , $G_{q,0}^{v,\phi}(\mathbf{x}_B,\mathbf{x},t)$ , and $G_{q,0}^{v,\psi}(\mathbf{x}_A,\mathbf{x},t)$ , we can sum them as in equation (4-2). The result is a redatumed multicomponent data set with receivers and effective force sources in the borehole.

In 2D case, we will only use the stencil point 1, 2, 3, and 4 (Figure 4-15b) to compute the P-wave constituent equation (4-6) and S-wave constituent equation (4-7), in which "*p*" only takes value of 1 and 3, and "*k*" only takes value of 2.

### 4.3.2 Elastic Redatuming

We now apply elastic redatuming as prescribed by equation (4-2) to a synthetic 2D WVSP multicomponent dataset created using the simplified Gulf of Mexico (GOM) salt dome model shown in Figure 4-16. The model is composed of a simplified GOM vertical-velocity gradient, an embedded overhanging salt dome together with a salt canopy nearby. The velocities and gradient are taken from the EAGE/SEG salt dome model which represents typical GOM velocities. Both salt domes have a P-wave velocity of 4480 m/s and S-wave velocity of 2580 m/s. The background velocity is described by $V(z) = V_0 + K\, z$, where $V_0$ is the velocity of the top layer ($V_{P0}$ = 2200 m/s and $V_{S0}$ = 1270 m/s) and $K$ is the velocity gradient ($K$ = 0.4). Six reflectors are introduced on top of the $V(z)$ gradient as 15-% higher velocity spikes [Siddiqui, *et al.*, 2003]. The reflectors dip up towards the salt dome flank. The receivers (triangles) are placed in the borehole from a depth of 0.5 km to 4 km at 25 m intervals. The stars in Figure 4-16 represent the center (**x**) of each shooting pattern.

Each source pattern consists of a 4-point-stencil in a square shape around the center, as shown on the left of Figure 4-15. The interval between two adjacent centers of the source pattern is 25 m and the edge length of a 4-point-stencil square is $L$ = 10 m. Our aim is to extract from the conventional WVSP, a dataset as if it were acquired with both sources and receivers in the borehole. To this end we first create the synthetic data and then use these data as input for the redatuming. In the field, it would be difficult to create a pattern that generates purely S waves or P waves. However, an explosive source is a practical approximation of a P wave source and for this reason our examples of the partial Green function obtained from just the P-wave sources have significance for practical situations.

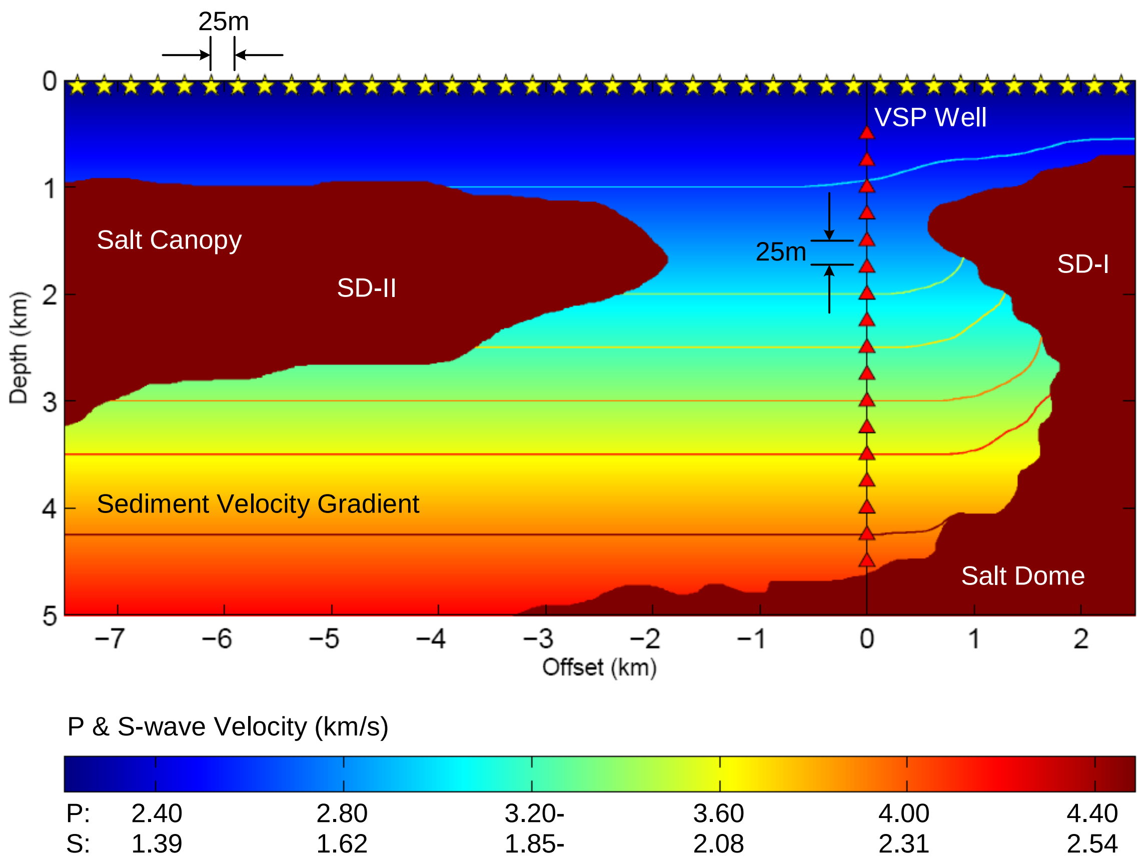


Figure 4-16: Walkaway VSP acquisition geometry for a synthetic GOM elastic model composed of a simplified vertical velocity gradient and an embedded overhanging salt dome (SD-I) together with a second salt canopy nearby (SD-II). The yellow stars indicate the locations of the shots and the red triangles are the locations of the receivers. Note that not all 399 shots are shown (extending from -7.5 to 2.5 km laterally), and not all 161 receivers are shown (extending from 0.5 to 4.5 km in depth). The color bar shown is applicable for all figures in the text containing a velocity model.

To understand the value of the full elastic data, we performed three experiments. In the first experiment we created the elastic WVSP survey data needed for applying full redatuming method in equation (4-2). In the second experiment, we created elastic data with downhole sources and receivers which provides the reference as what would be the theoretically best result possible from redatuming. And, in the third experiment, we created an acoustic WVSP dataset, to provide a reference for pure acoustic redatuming. As explained above, to estimate $G^{v,f}_{p,q}(\mathbf{x}_A,\mathbf{x}_B,t)$, we need the particle-velocity responses due to P- and S-wave sources $G^{v,\phi}_{p,0}(\mathbf{x}_A,\mathbf{x},t)$, $G^{v,\psi}_{p,k}(\mathbf{x}_A,\mathbf{x},t)$, $G^{v,\phi}_{q,0}(\mathbf{x}_B,\mathbf{x},t)$, and $G^{v,\psi}_{q,k}(\mathbf{x}_B,\mathbf{x},t)$, which we generated with equation (4-8) and (4-9) as explained above. Figure 4-17 shows the results of the simulation of the different components for a particular source position. The panels in Figure 4-17 depict individual components of the Green's tensor $G^{v,\phi}_{p,0}(\mathbf{x}_A,\mathbf{x},t)$ and $G^{v,\psi}_{p,k}(\mathbf{x}_A,\mathbf{x},t)$. The configurations are schematically depicted in the insets between the figures.

Figure 4-17a shows the particle velocity measured at a horizontal receiver in the bore hole, due to a P-wave source at the surface and Figure 4-17b shows the particle velocity measured at a vertical receiver in the bore hole, due to the same P-wave source. Figure 4-17c shows the particle velocity measured at a horizontal receiver in the bore hole, due to an S-wave source at the surface and Figure 4-17d shows the particle velocity measured at a vertical receiver in the bore hole, due to the same S-wave source. Note, that the individual components in these figures may contain both P- and S. In theory, the medium in a small area around the source is assumed to be homogeneous and the wavefield is in principle pure P or S only in this area. The salt dome and reflectors may thus cause conversions, resulting in mixing of P- and S-waves in data from only one source type. These data serve as the input for the redatuming. Figure 4-18a shows a modeled common shot gather where we have used a downhole, pure force source applied in the x-direction at a depth of 1.5 km. So, we next redatum the data sets created with surface shots and downhole receivers in order to match the downhole source results, one of which is shown in Figure 4-18a.

We now extract from these constituents the Green function $G^{v,f}_{p,q}(\mathbf{x}_A,\mathbf{x}_B,t)$. To do so, we first select one of the actual down-hole receiver locations to be an effective source location, for example, a receiver at depth of 1.5 km, $\mathbf{x}_B = (x, y, 1500)$, and select the corresponding common receiver gather (that is, all traces measured at this receiver, for different sources at the different surface locations: $G^{v,\phi}_{q,0}(\mathbf{x}_B,\mathbf{x},t)$, and $G^{v,\psi}_{q,k}(\mathbf{x}_B,\mathbf{x},t)$). Then we select another actual down hole receiver location to be an effective receiver location, for example, a receiver at depth of 3 km, $\mathbf{x}_A = (x, y, 3000)$, and select the corresponding common receiver gather [$G^{v,\phi}_{p,0}(\mathbf{x}_A,\mathbf{x},t)$ and $G^{v,\psi}_{p,k}(\mathbf{x}_A,\mathbf{x},t)$]. A succession of pair wise traces from the same surface shot is cross- correlated and summed with a weight based on the back- ground *Vp*/*Vs* ratio. The result is a set of correlogram, one for

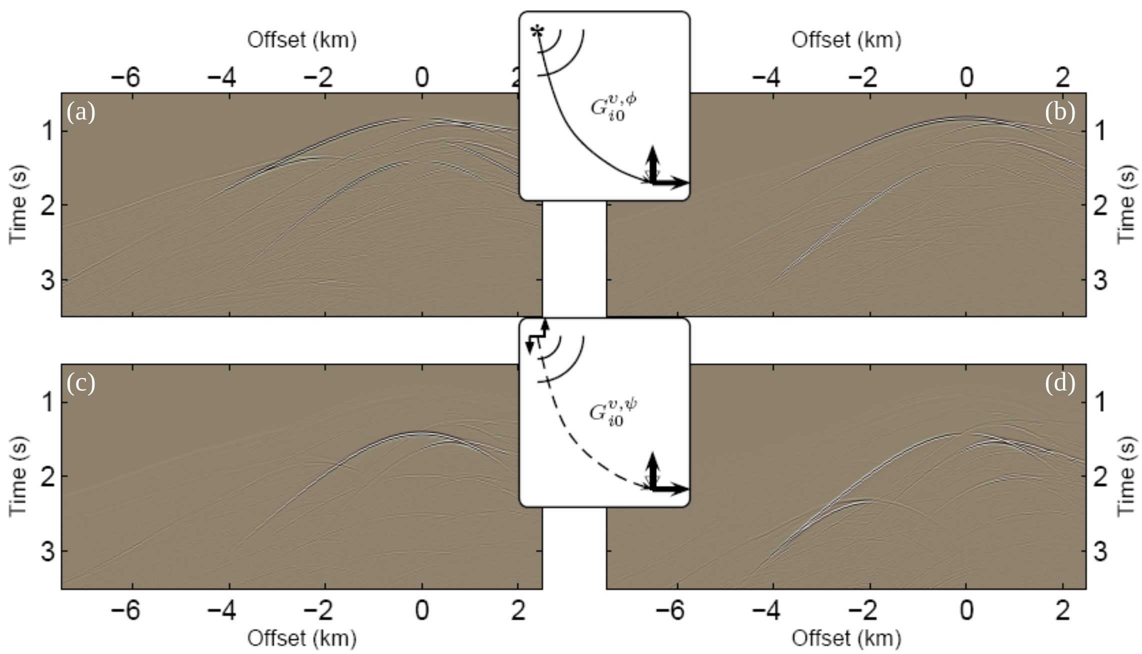


Figure 4-17: Common receiver gathers for a receiver at depth of 2 km: (a) the x-component and (b) the z-component of the particle velocity; (c) the P-wave constituent $H^{\phi,f}_{0,1}(x_i,x_A,t)$ and (d) the S-wave constituent $H^{\psi,f}_{2,1}(x_i,x_A,t)$. Horizontal axes denote the offset of the corresponding shot for each trace

each shot offset. Next, the correlogram is stacked (that is, a sum is performed over all sources) and one trace is obtained. This trace is the estimate of the desired Green function: $G_{p,q}^{v,f}(\mathbf{x}_A, \mathbf{x}_B, t)$.

To estimate another trace for another receiver due to the same effective source located at the depth of 1.5 km, we keep the common receiver gather corresponding to the effective source location (at 1.5 km) and select the common receiver gather for a new desired effective receiver location. We then repeat the set of corresponding correlations, summations and stacking operations as described above. By doing this for all receiver depth levels, we create the effective common down-hole shot gather, as shown in Figure 4-18b This mimics a shot gather of the x-component particle velocity collected by the downhole receiver array due to a down- hole force source directed in the x-direction at the location that we choose to be the effective source location (1.5 km), $G_{1,1}^{v,f}(\mathbf{x}_A, \mathbf{x}_B, t)$. The effective shot gather shown in Figure 4-18bcan also be seen as a weighted sum of two wave fields, one contributed by the P-wave source, and the other contributed by the S-wave source. If we denote by $\Phi_{p,q}^{v,f}$ the first term of equation (4-2) and by $\Psi_{p,q}^{v,f}$ the second term (even though we use the same symbols here, note that these terms do not exactly correspond to the scalar portentials defined in equation 4-3), then Figure 4-18c and Figure 4-18d represent $\Phi_{1,1}^{v,f}$ and $\Psi_{1,1}^{v,f}$, respectively.

Comparing the actual downhole shot, Figure 4-18a, and the redatumed result, Figure 4-18b, we observe that these common shot gathers are similar. However, our redatumed downhole shot gather includes some spurious events not present in the actual downhole record. Part of these spurious events are due to the acquisition aperture which is limited to only surface shots. Another possible reason for the seemingly spurious events may be that the P to S amplitude ratio may be different in the correlated results, such that some (S-wave) events may seem more pronounced in the interferometric Green's function. This problem of the proper relative weights of the P- and S- wave contributions is just one of the difficulties in elastic interferometry. Although contaminated by these spurious events, the main reflections off the target salt flank (that is, events which arrive after 0.4 sec) are present. We also observe that in Figure 4-18a, the three linear downgoing events coming off of the first arrival are absent in the redatumed gather Figure 4-18b. These events are the downgoing specular reflections off of the under side of the horizontal sediment boundaries crossing the borehole location. The omission of this energy is due to the fact that not very much of this energy is excited by a surface source. An actual downhole source creates upgoing energy which is reflected back downward. Just as in the theory for migration, to be more correct we should put sources completely surrounding the area we wish to image. If this were possible, we would be able to reconstruct these down going reflections. However, since this is not practical for field scale surveys we must evaluate the effect of this limited aperture on the final results. van Manen *et al.* [2006] did use this concept of sources all around the model for efficient interferometric simulation of wave propagation.

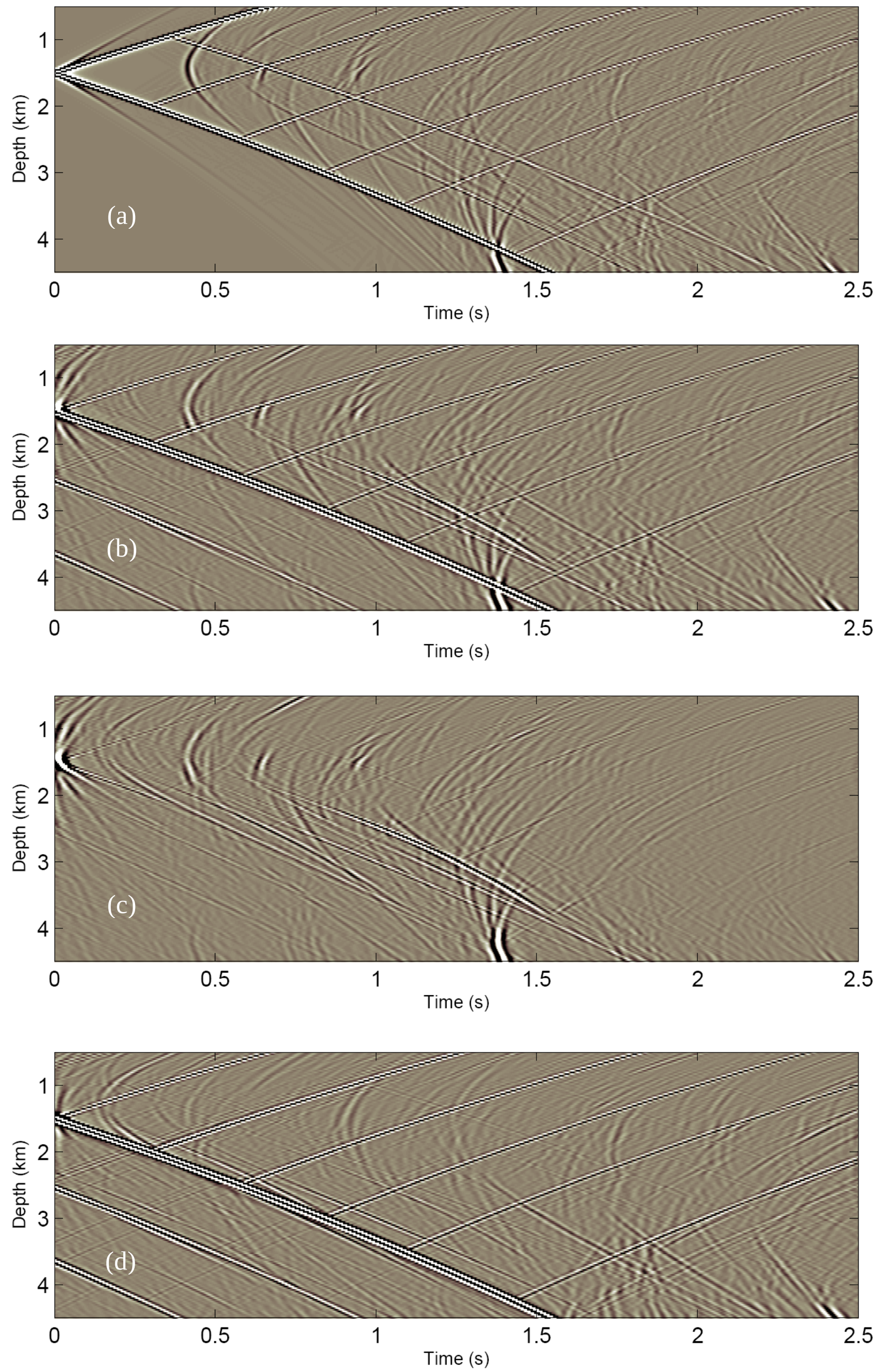


Figure 4-18: Common downhole shot gathers for a shot located at depth of 1.5 km: (a) obtained by a downhole horizontal force source and Vx receiver pairs (benchmark case); (b) obtained by full elastic redatummed response of horizontal force source and Vx receiver, which is equivalent to the weighted sum of (c) and (d); (c) the P-wave contribution to (b); (d) the S-wave contribution to (b).

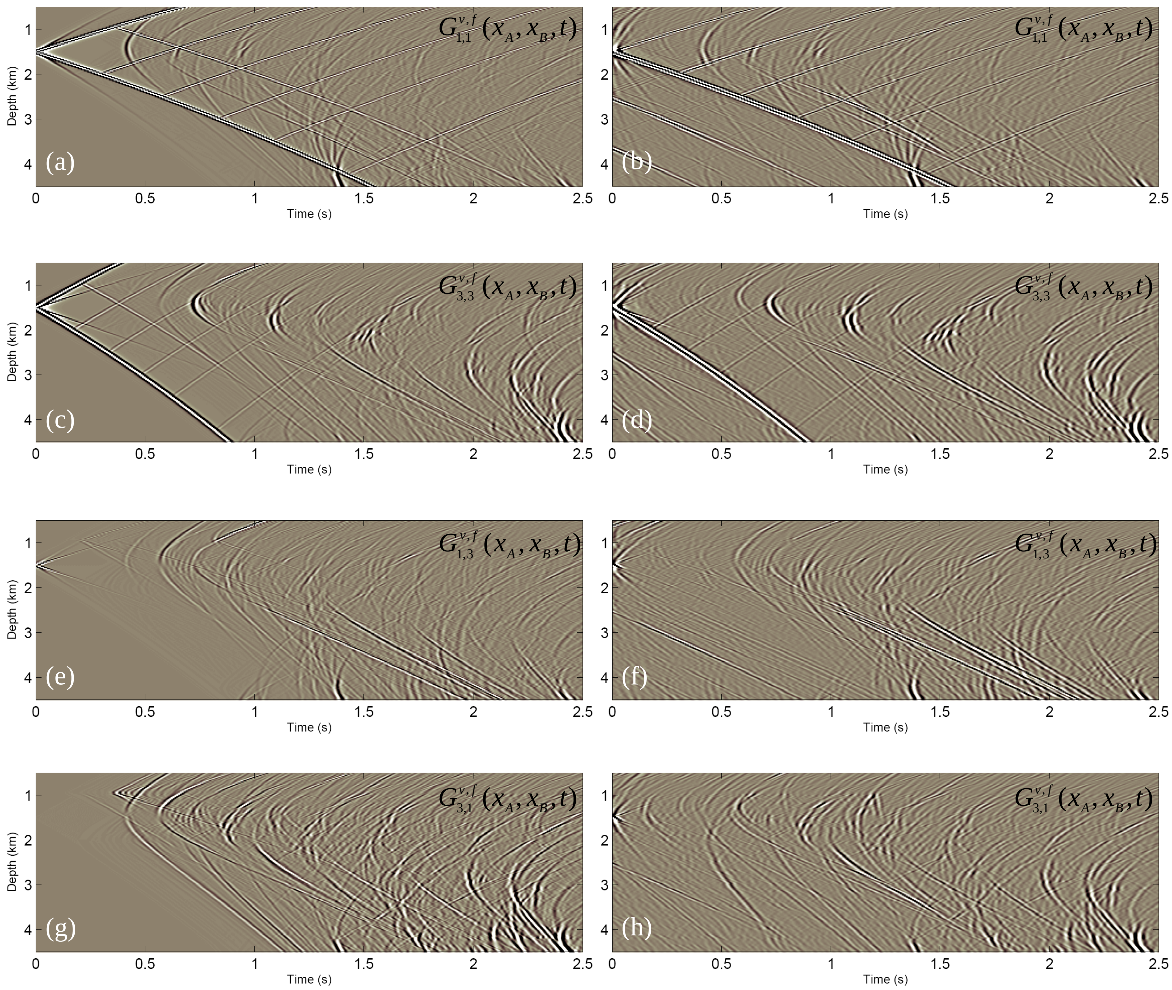

Figure 4-19: Four components of the full elastic responses: (Left) actual common downhole shot gathers at depth of 1.5km; (Right) effective shot gathers obtained from the redatumming the WVSP dataset.

In Figure 4-19, we compare the actual down hole shot gathers (panels in the left column) and the redatumed shot gathers (panels in the right column) for all four components of the elastic response, in which $G_{1,1}^{v,f}(\mathbf{x}_A, \mathbf{x}_B, t)$ is shown in Figure 4-19a and b, $G_{3,3}^{v,f}(\mathbf{x}_A, \mathbf{x}_B, t)$ is shown in Figure 4-19c and d, $G_{1,3}^{v,f}(\mathbf{x}_A, \mathbf{x}_B, t)$ in Figure 4-19e and f, and $G_{3,1}^{v,f}(\mathbf{x}_A, \mathbf{x}_B, t)$ in Figure 4-19g and h. Looking at these elastic responses, we observe the redatuming methodology described above approximates the actual downhole elastic responses quite well. In particular, we note that the artifacts mostly consist of dipping linear events. If we image the data, as will be shown later, these artifacts are suppressed due to destructive interference during the imaging operation, while the reflection hyperbolas from the salt dome flank sum constructively to produce the image.

To obtain a complete redatumed downhole survey, we repeat the elastodynamic redatuming for all possible effective down-hole source locations. In the end we obtain new effective shot gathers which approximate a dataset with both the sources and receivers located in the bore hole. Note that in order to redatum the shot to be in the borehole we do not have to apply velocity analysis or complicated processing (such as statics or NMO corrections). In fact, with the exception of a constant $Vp / Vs$ ratio term, there are no model dependent processing parameters required to move the surface shots into the bore hole. This feature allows the redatuming methodology be performed in a fully automated fashion that requires virtu- ally no human effort.

### 4.3.3 Imaging and Discussion

We use as a base reference case the prestack depth migrated image created from redatumed shot gathers from an acoustic model, shown in Figure 4-20a. Recall that in this case, the pressure field is measured and used for imaging. In this result we clearly see the salt edge and much of the sediment layers.

The ultimate migration algorithm would seem to be one that is fully elastic and uses all components of the wavefield simultaneously. However, this is actually problematic since it would allow for conversion between all wave types at all time steps, everywhere in the model. Without the correct velocity model and/or special damping, many serious artifacts (e.g. converted wave multiples) would be created at the formation boundaries. A more practical approach is to migrate each component separately with a single velocity type, i.e. P-wave or S-wave. We therefore prestack depth migrate each of the four components of the elastic responses separately, as if each were an acoustic wave field with the appropriate P- or S-wave velocity.

As noted in the previous section, equation (4-2) expresses that the shot gather shown in Figure 4-18b can be seen as a superposition of two parts: a field due to the P-wave source, $\Phi_{1,1}^{v,f}$ (Figure 4-18c) and a field due to the S-wave source, $\Psi_{1,1}^{v,f}$ (Figure 4-18d). Since the salt flank is almost vertical, the component of the P- wave contribution $\Phi_{1,1}^{v,f}$ has the greatest sensitivity to P reflections off of the salt edge. On the other hand, $\Psi_{1,1}^{v,f}$ should have better sensitivity to S reflections from the horizontal reflectors such as the beddings at the well bore. Our strategy is to separately migrate these contributions using the appropriate velocities.

In order to prepare the redatumed panels for migration, we mute the acausal (before zero time) events and the direct arrivals. After muting, we apply Kirchhoff pre-stack depth migration to redatumed downhole pseudo shot gathers like in Figure 4-18c and Figure 4-18d. The result of migrating and stacking all the redatumed horizontal component P wave records, $\Phi_{1,1}^{v,f}$ , is shown in Figure 4-20b. The velocity model used is only the background *Vp*(*z*) of the medium (without the salt or reflectors). Comparing our reference acoustic result, Figure 4-20a, and this elastic component, Figure 4-20b, we see that the migrated image from $\Phi_{1,1}^{v,f}$ shows good delineation of the salt flank and part of the dipping sediments. However, it does not image the horizontal bedding at the well bore.

Meanwhile, there is slightly more noise in Figure 4-20b, which may be due to some P-to-S converted energy in the redatumed shot-panel, migrated with the wrong velocity

Figure 4-20c is the migrated result from the vertically propagating S wave component, $\Psi_{1,1}^{v,f}$, using the S wave velocity, *Vs*(*z*), of the background velocity model (without the salt or reflectors). Here, we capture only the horizontal beds near the borehole and is missing the near vertical salt-dome flank.

In Figure 4-20d we show the result of migrating the horizontally propagating S-wave component, $\Psi_{3,3}^{v,f}$, with the S-wave, *Vs*(*z*), background velocity model. In this component, the source is acting vertically, creating horizontally propagating S waves, and the receiver is recording the vertical motion. Therefore, we expect that this S-wave contribution is more sensitive to the vertical reflectors. Indeed, the salt flank and part of the dipping sediments are imaged clearly in the result. In addition, because we use shear waves, the image of the salt flank has higher spatial resolution than to the image shown in Figure 4-20b using P waves.

Finally, we show in Figure 4-20e the results of migrating the vertically propagating P-waves, $\Phi_{3,3}^{v,f}$, which is mostly sensitive to horizontal reflectors. The combination of these images with proper weights is a topic of ongoing research. Still, it is clear that the proper combination of Figure 4-20b and Figure 4-20e should result in an image similar to the one in Figure 4-20a.

The process of performing elastic redatuming of the recorded wavefields has allowed us to create four different realizations of the subsurface. Two images provide P-wave reflectivity and two provide S-wave reflectivity. None of these contains the same information. Taken together they paint a more complete picture of the subsurface than is possible from any one of them. The images created from these four components will be sensitive to different aspects of ambient noise, formation fractures and fluid properties, and background velocity fields. More than ever, geoscientists and engineers need a more complete description of the reservoir. Elastic parameters provide another dimension of information not currently available from simple P-wave data. These images will potentially provide a rich source of information to augment our existing conventional VSP technology.

Our methodology includes a simple-minded acquisition effort to collect in the field the required spatial derivatives of the wavefields. Additional effort should be devoted to replace this step with a numerical decomposition step. However, this decomposition step requires a spatially homogeneous near-surface region which may limit its applicability. Alternatively, the additional field effort to collect the spatial directives of the P wavefield may be unnecessary in some cases since an explosive source, for example, is a likely to be a good representation of a P-wave source.

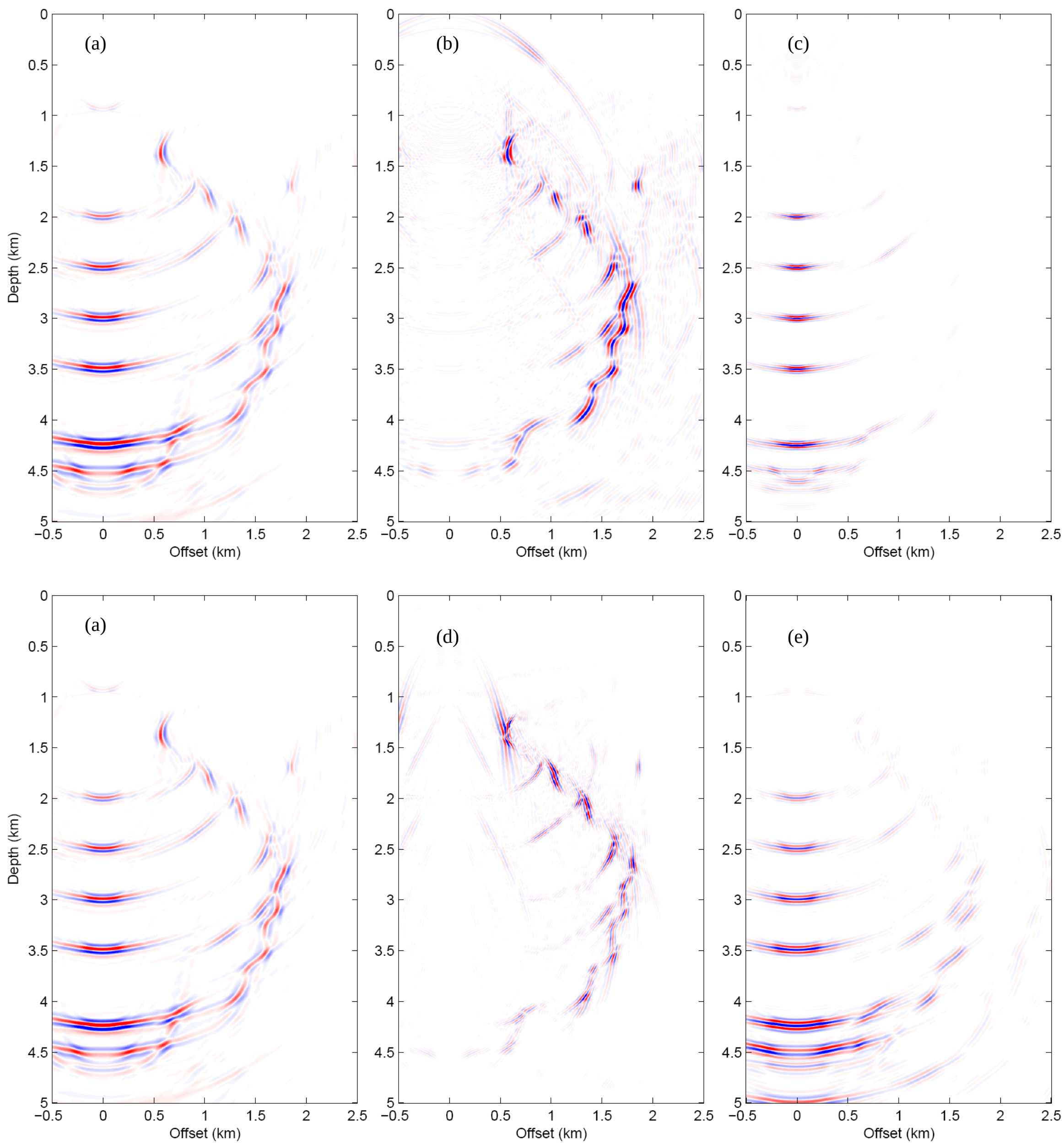


Figure 4-20: Migrated salt dome flank images obtained from (a) the redatummed acoustic responses in a pure acoustic model, (b) elastic redatummed shots of P-wave contribution from the response pair of fx force source and vx receiver migrated with P wave velocity, (c) elastic redatummed shots of S-wave contribution from the same response pair as (b) migrated with S wave velocity, (d) elastic redatummed shots of S-wave contribution from the response pair of fz force source and vz receiver migrated with S wave velocity, (e) elastic redatummed shots of P-wave contribution from the same response pair as (d) migrated with P wave velocity.

# Chapter 5

# Salt Flank Imaging – Field Experiment

Continuing from the synthetic analysis, in this chapter, I will apply the salt flank imaging strategy to a field experiment. We applied several strategies of TRA-based redatuming followed by prestack depth migration to a field 3D VSP dataset. The data consists of 15,632 surface shots acquired in concentric circles about the well head containing 29 (live) subsurface geophones. The salt flank geometry in the vicinity of the well is a complex 3D structure which is only partially defined on surface seismic images. Since most published virtual source methodologies to date have been 2D in nature, we create a 3D directional imaging strategy where the surface VSP shots are grouped into 10° wedges based on the shot to geophone azimuth. Then we rotate the horizontal geophone components within each wedge to create inline components pointing from the center of the wedge to the center of the receiver array. We leave the vertical components unchanged. We exclude shots on the west side of the survey and those with offsets less than 10,000 ft (3,048 m) as they are not likely to create reflections off the salt flank. We perform several tests varying the effective aperture by including various combinations of wedges in the redatuming. This process effectively steers the illumination direction of the virtual source. The best images seem to be obtained using virtual sources we create from a small range of azimuths (or small number of wedges). Each of these migrated volumes contains resolved images of the salt flank in a small angular swath with a small vertical extent. We cut and paste together a series of these well resolved image swaths to form a westward-looking 3D image of the salt flank. Thus the virtual shot gather created from one of the wedges contributes only to a small angular swath of the full output 3D image. Images created from the vertical component of motion appear to have better signal to noise ratios than those from the inline component. Additional increases in image resolution are obtained from an application of spike deconvolution of the redatumed traces. The limited number of geophone levels restricts the quality of the final image to a narrow, 300 meter high portion of the salt flank. The distance from the receiver array to the salt flank extracted from the final image is about 640 meters. This is about 80 meters farther than the distance interpreted from surface seismic data. The TRA-based redatuming methodology is particularly appropriate for such a complex problem because it does not require any knowledge of the velocity structure between the surface shots and the downhole receivers and the salt flank reflections are easily seen on the resulting virtual shot gathers. In contrast, prestack depth migrating the raw VSP records does not produce any identifiable salt flank image.

## 5.1 Field Description

This field data study is part of a research project at MIT Earth Resources Laboratory funded by Shell International Exploration and Production Inc. The purpose is to explore and apply new implementations of the virtual source methodology [Bakulin and Calvert, 2004, 2006; Bakulin, *et al.*, 2007; Mateeva *et al.*, 2007b] to complex problems such as salt flank imaging.

The field 3D VSP data used in this study was acquired by Shell Oil Company in the deep water Gulf of Mexico during the summer 2006. The objective of analyzing this field data is to test the effectiveness of imaging a salt dome flank at this field from a 3D VSP survey, as well as to develop and enhance existing 2D interferometric redatuming methodologies to more properly use 3D and 3 component (3C) data to image a 3D structure from single well. How to handle both 3D and 3C datasets are topics on the forefront of current virtual source research.

The acquisition geometry is shown in Figure 5-1 in a 3D perspective, where the white area denotes the interpreted salt structure in the area of interest. The well (shown in the green line) was drilled vertically to a depth of 12,000 ft (3,658 m). It then was deviated (at about 35°) and continued on subparallel to the salt flank. The VSP data was recorded by an array of thirty 3-component (3C) receivers (shown in yellow triangles) spaced 100 ft (30.5 m) apart, sitting close to the bottom of the well at measured depth ranging from 16,150 to 19,050 ft (4,923 to 5,806 m). The total aperture of the receiver array along the well is 2,900 ft (884 m). The 3D VSP survey consisted of total 15,632 shots (shown as red dots). The shots were fired in a spiral pattern around the well head to a maximum offset about 20,000 ft (6,000 m). A map view of the geometry is shown in Figure 5-2 where light gray area marks the salt, maroon dots denotes the shot locations and green triangles indicate the positions of receivers. The acquisition spiral geometry is defined with reference to the well head. However, the images we will create will be referenced from the downhole geophone positions. To facilitate the imaging process, we define a local coordinate system in which the positive X-axis points East, the positive Y-axis points North and the positive Z-axis points upward. The origin of the local coordinate system is chosen to be the center of the receiver array. Notice that the local coordinate system displayed in Figure 5-2 accentuates the fact that the well head, which is the center of the spiral of surface shot locations, is not the center of our coordinate system.

Figure 5-3a shows a surface seismic section that traverses the field through two salt structures, as indicated by the line AA’ in Figure 5-2. Note that the bottom of the leftmost salt is fairly well imaged, but its right flank is poorly imaged. Figure 5-3b shows the detailed interval velocity model for depth imaging, including the interpreted salt structure, of the same traverse. It is seen from the model that the receiver array is positioned nearly parallel to the interpreted salt flank.

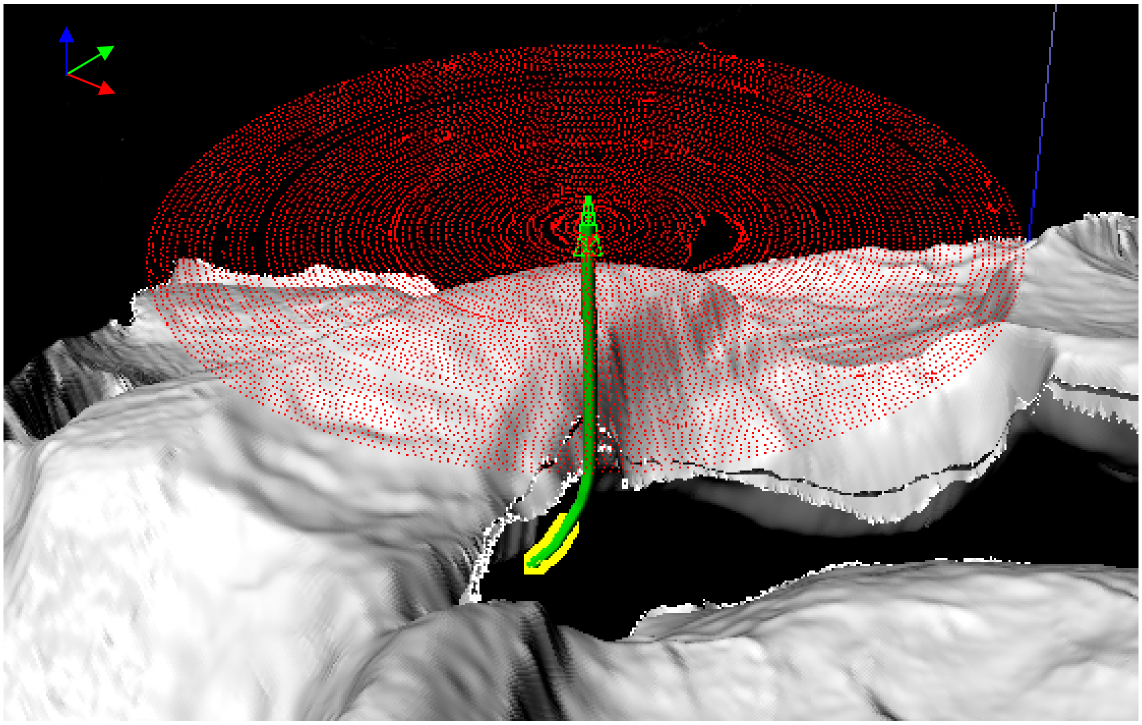

Figure 5-1: Salt structure geometry in a 3D view. White areas are the interpreted salt bodies, the green line denotes the well path, the yellow triangles show the receiver locations, and red dots are the locations of surface shots.

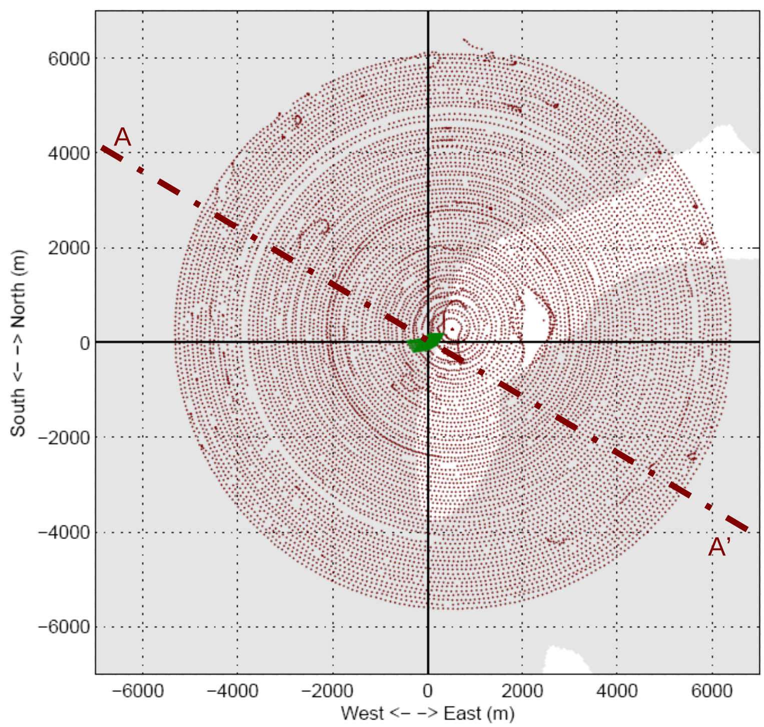


Figure 5-2: Map view of the acquisition geometry in a local coordinate system. Dashed-dotted line shows the traverse of the cross sections shown in Figure 5-3.

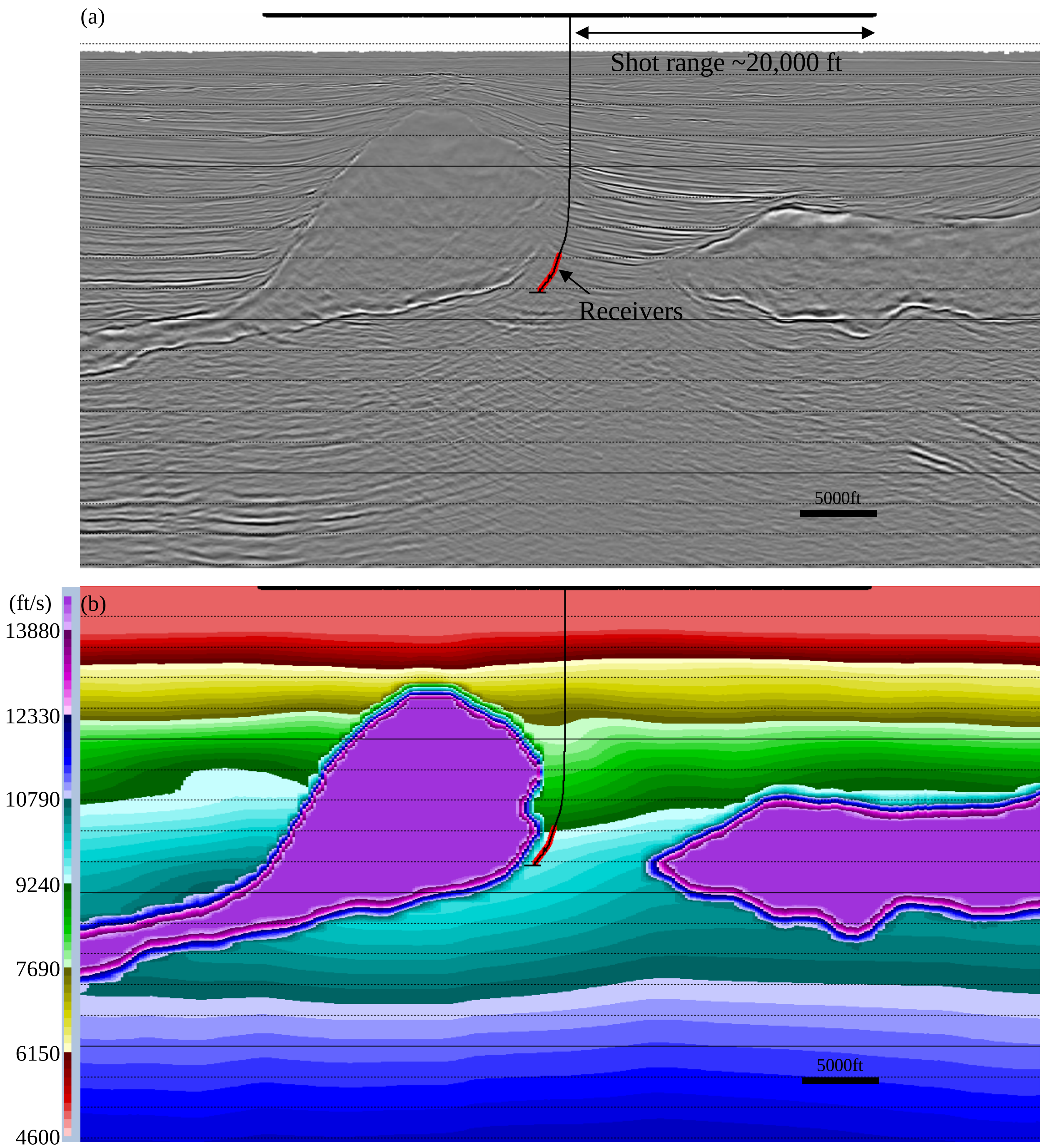


Figure 5-3: (a) Traverse (AA' in Figure 5-2) of surface seismic data in the area of interest; (b) Velocity profile of the same traverse showing the interpreted salt dome. In both images, blue line on the surface marks the extension of the VSP shot range and the red triangles denote the location of receivers.

## 5.2 Imaging Methodology

The specific acquisition geometry for this field and the complex structure of the salt pose several challenges to imaging the salt dome flank which we describe next.

- **Small Receiver Aperture:** The receiver array used is state-of-the-art in offshore settings, but has many fewer receivers than those used in the synthetic examples in our previous studies. As a result, the migrated virtual source images will also have a much smaller aperture. Figure 5-4 draws a schematic picture of how to image the salt flank using turning rays from VSP shots. While the virtual source method is a wave-based concept, it is easier to visualize the process in terms of rays. For a ray to contribute to the final image, it needs to start from a surface shot, pass one of the receivers, hit and be reflected by the salt flank, and then be captured by other receivers. This limits the illuminated imaging area by the receiver array size and geometry as well as by the shot locations.
- **Multicomponent Data:** The 3C data need special handling before being used for redatuming and imaging. Ideally, we would like to rotate the 3C data acquired such that one component is pointing towards the salt flank in order to capture the direct specular reflections from the salt interface. To do that properly, we need to determine the receiver orientations since they may be pointing in arbitrary azimuths in the borehole.
- **3D Geometry:** The 3D geometry of the salt poses another complexity. The receivers form a crooked line in 3 dimensions. Reflected energy from all azimuths is captured by the receiver array. Just as in surface seismic data acquired with a

single line of receivers, it is very difficult to determine the 3D spatial location from which the reflected energy originated. To date, most published virtual source redatuming methodologies are based on 2D geometry [Hornby and Yu, 2007; Lu *et al.*, 2007; Willis, *et al.*, 2006]. Reflections are expected to come from velocity contrasts located in a (typically vertical) 2D plane containing the shot and the receiver. Since both the acquisition geometry and the salt flank voliate this 2D plane assumption, we need to be clever and try to capture the reflected salt flank reflections by searching for them in portions of the downhole geophone records from surface shots. The virtual source redatuming operation can be considered a beam steering operation that could be used to preferentially illuminate in different subsurface directions.

To achieve the objective of imaging the 3D salt flank, we proposed the following directional (steered) imaging strategy, as shown in Figure 5-5:

(1) Pick a (first) direction pointing from the midpoint of the downhole receiver array (defined as the origin in our local coordinate system) toward the expected salt edge as the (first) preferred imaging direction.

(2) Define a wedge of shots on the surface such that the line connecting the center of this wedge and the local coordinate system origin (i.e., the midpoint of the receiver array) is aligned with the preferred imaging direction.

(3) Rotate the horizontal components of all receivers to be inline with the preferred imaging direction – aligned with the midpoint of receiver array and the center of shot wedge.

(4) Redatum the rotated, inline components into downhole virtual shot gathers, which are likely to illuminate the salt edge along the preferred imaging direction chosen in first step.

(5) Perform 3D prestack depth migration on the virtual source (redatumed) shot gathers from this specific wedge into a 3D imaging volume which is limited to an area around the salt flank. In the output migrated volume, due to the ray path considerations described above, only the angular swath along the preferred imaging direction will contain the specular reflections from the salt.

(6) Repeat (1) through (5) for all possible preferred imaging directions. In this case since the a priori knowledge of the salt model (Figure 5-5) shows that the salt edge is concaved towards the south-east direction, we choose the preferred directions ranging from –85° to +25° with respective to the east, each with an angular separation of 10° and a wedge width of 10°. (We will give details of this in a later section below).

(7) Combine all the migrated volumes into a final imaging volume by taking a volume swath about the preferred direction from each migrated volume – assuming that the best image quality within each migrated volume is along the preferred imaging direction.

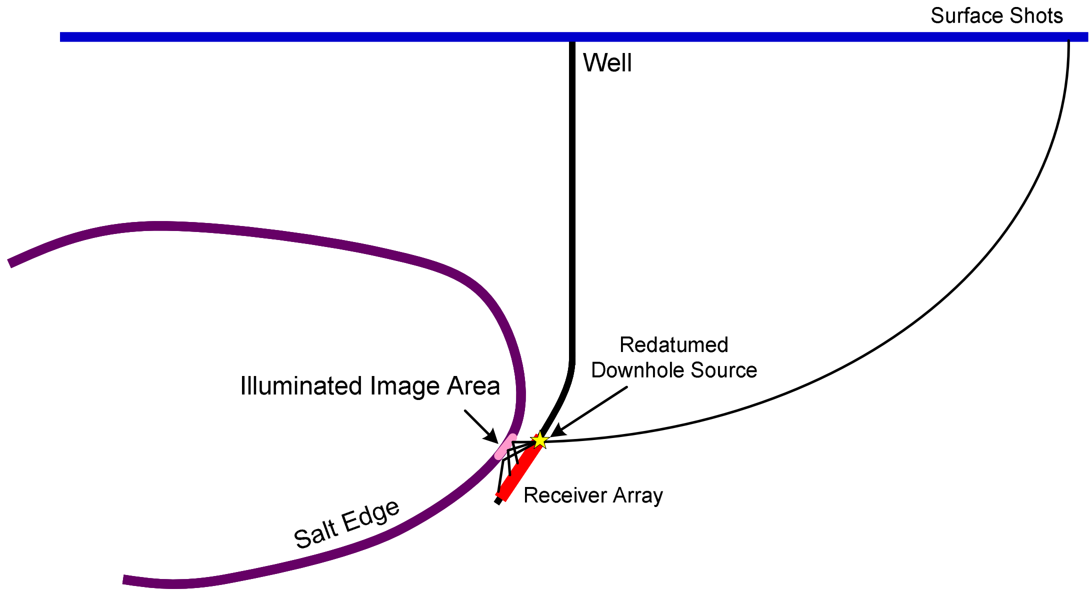


Figure 5-4: Schematic illustration (side view) of the imaging geometry showing the effective imaging aperture and stationary reflections.

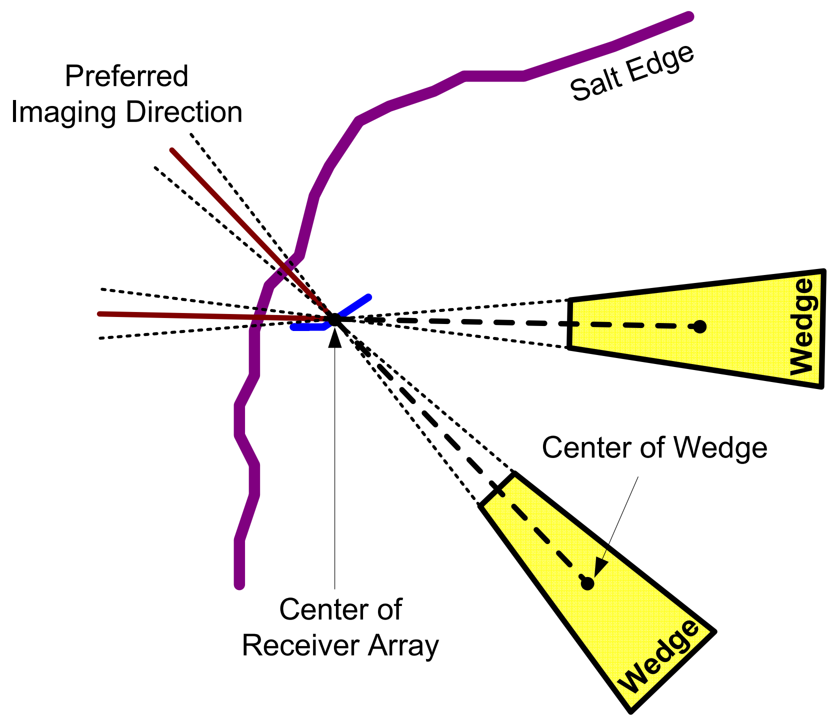


Figure 5-5: Schematic illustration (map view) showing the directional imaging strategy.

Before the imaging can begin, we perform two preprocessing steps. The first step enhances the signal to noise ratio of the data by applying an appropriate band pass filter and marking traces with exceptional high noise levels with a dead trace flag. The second step estimates and verifies the geophone orientation using first arrival hodogram analysis.

## 5.3 Preprocessing

### 5.3.1 Noise Abatement

Unlike noise-free synthetic data, field data contain many sources of noise. Figure 5-6a shows a typical common receiver gather with a relatively good signal-to-noise ratio in which the main events stand out clearly from the background noise. Its spectrum, shown in Figure 5-6d (blue line), also shows a nice signal band approximately from 3Hz to 35Hz. In contrast, Figure 5-7a shows a typical common receiver gather that contains a significantly higher noise background. By looking at its corresponding spectrum shown in Figure 5-7d (blue line), we find that there is a peak in the spectrum around 50Hz, whose origin is unknown, but may be related to electrical power generation interference. We also find a broad band of energy at a higher frequencies (60 to 100 Hz). In order to equalize the spectra for all shots and reduce what we expect is noise, we filter all shots to a common bandwidth of 3-35 Hz.

For gathers with relatively good signal-to-noise ratio (Figure 5-6a), the filter operation depresses the background noise level as shown in Figure 5-6b. For gathers with larger noise, we are able to significantly improve the signal-to-noise ratio by applying the band-pass filter as shown Figure 5-7b.

Although filtering can help to improve the data quality, there are traces where the background noise is so large that the signal is totally obscured. Those traces need to be eliminated before use in the redatuming process. We know that before the direct arrival, the geophones are basically recording the ambient noise. Therefore, assuming the noise level during that period of time is unchanged statistically for the whole trace, we can automatically scan for traces with high level of background noise by analyzing the first 2 seconds (before the earliest direct arrival) of each trace. We calculate the root mean square amplitude for that 2-second portion of trace for all three components and plot them in histogram as shown in Figure 5-8.

From the histogram, we see that most traces have a noise level less than 50 normalized units. Those traces having noise levels higher than 50 we mark as dead traces in our database and are not used in subsequent processing steps.

### 5.3.2 Geophone Orientation

In order to properly rotate the horizontal components we need to determine the geophone orientation. The well is deviated in this survey which provides an advantage in orienting the geophones. Each VSP tool level is equipped with a gimbaled geophone package. Each gimbaled assembly is manufactured so that gravity aligns the vertical (z) component phone automatically. In a well that is deviated, the horizontal (H1 and H2) phones are manufactured to align themselves so that one horizontal component is oriented within the plane of well deviation. The other horizontal component is supposed to be aligned orthogonal to that [Hardage, 2000]. While these are the nominal specifications for the tool, it is still necessary to verify that this mechanism is working properly.

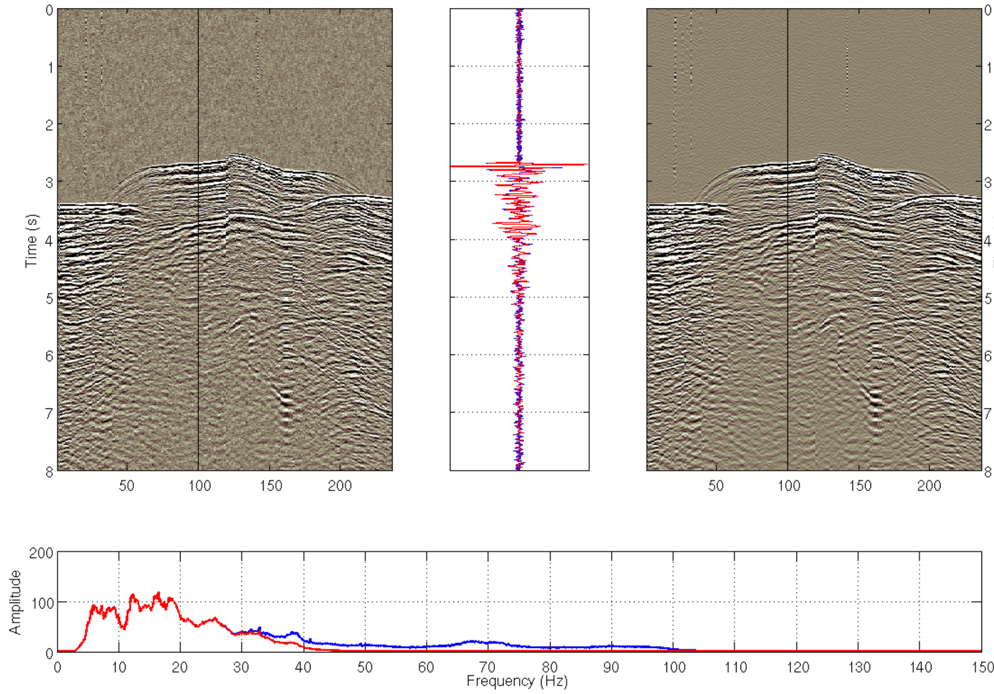


Figure 5-6: (a) A common receiver gather with relatively good signal to noise ratio; (b) the same gather after apply a band-pass filter; (c) a single raw trace in blue and its filtered version in red plotted on top of each other; (d) the stacked spectrum of the raw gather in blue compared to the stacked spectrum of the filtered gather in red.

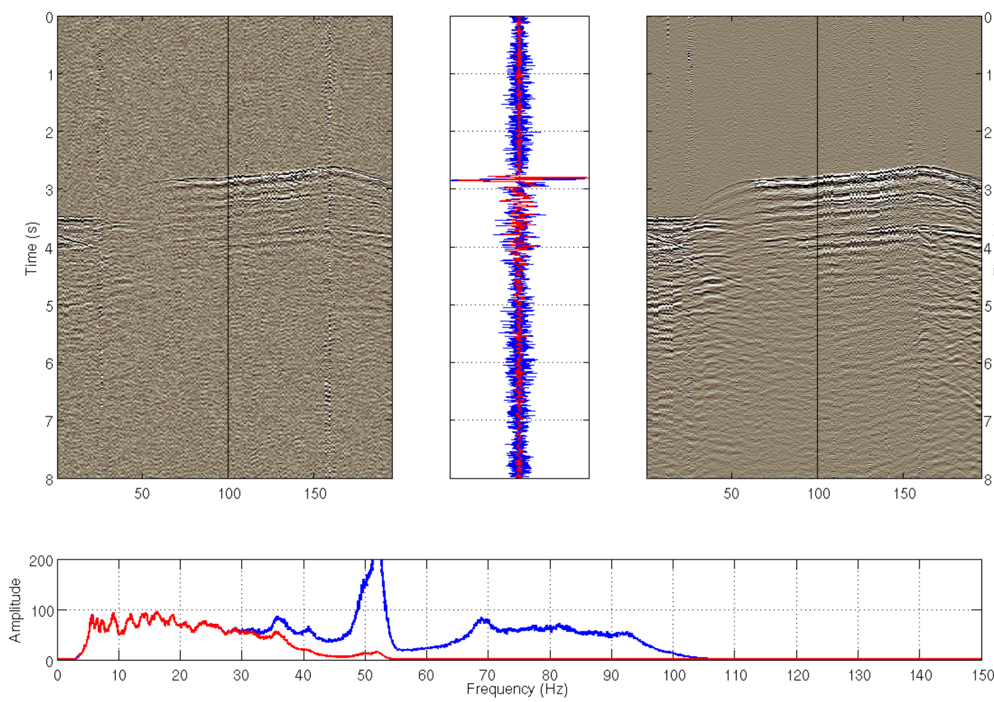


Figure 5-7: (a) Another common receiver gather with relatively bad signal to noise ratio; (b) the same gather after apply a band-pass filter; (c) a single raw trace in blue and its filtered version in red plotted on top of each other; (d) the stacked spectrum of the raw gather in blue compared to the stacked spectrum of the filtered gather in red.

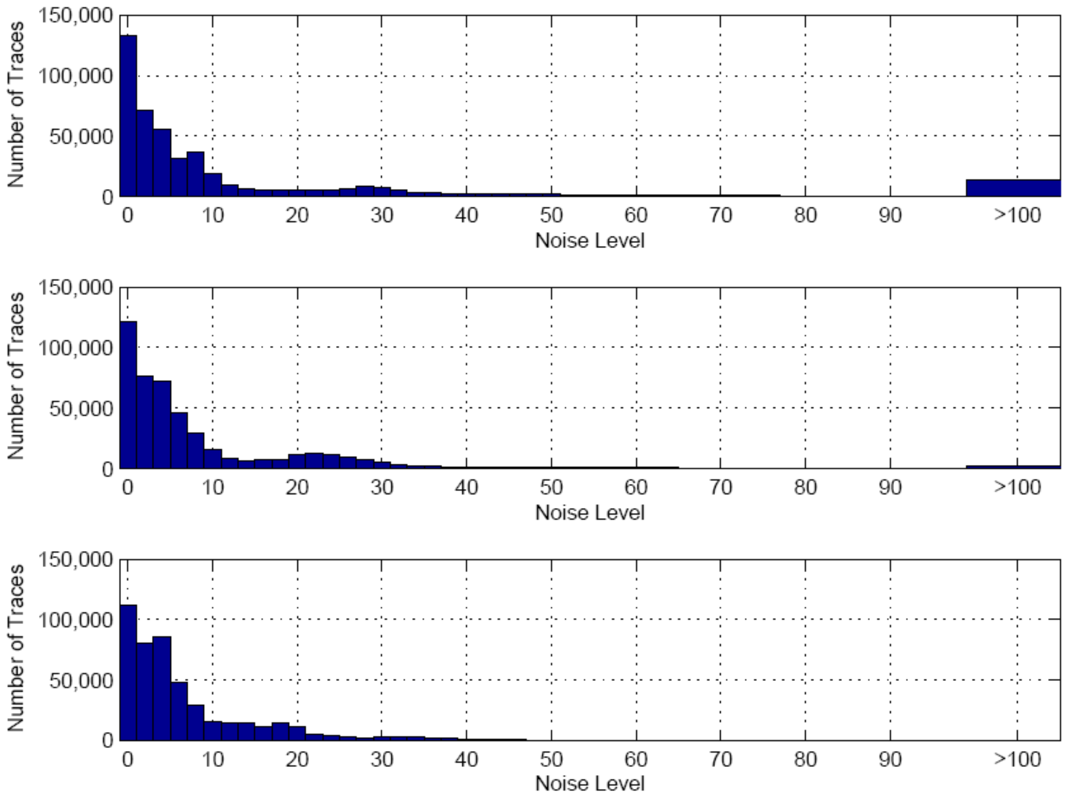


Figure 5-8: Ambient noise level histogram for (a) H1 component, (b) H2 component, and (c) Z component. Notice that the horizontal components (H1 and H2) have many traces with noise levels over 90.

We use a hodogram analysis to verify the predicted or nominal orientation of the VSP sondes by plotting the particle motion of the first arrivals on the H1 and H2 geophones for shots at multiple azimuths [DiSiena *et al.*, 1981].

The method is illustrated in Figure 5-9, in which the black lines indicate the world coordinates (relative to North/South and East/West) from the viewpoint of a particular receiver (the "origin"), and the blue and red lines indicate the unknown but physical geophone coordinates (H1 and H2). A hodogram analysis assumes that the media between the shot and receiver are isotropic and laterally homogeneous in the crossline direction such that the ray travels from the shot to the receiver in a vertical plane that passes through both the shot and the receiver, as shown in Figure 5-10. When a shot is fired at surface (yellow star), the ray is expected to travel along the inline direction marked with gray line. From the receiver side, if one plots the particle motion (black dots) of the first arrival, which will be the direct P-wave arrival, it should align with the inline direction. Therefore, in practice, we first scatter-plot the particle motion of the first 1-2 cycles of the signal in H1 versus H2 coordinates. Then we can fit a least squares line across these points. The angle of the best-fit line should be equal to [shot azimuth + angle between H1 and East ($\theta$)]. Knowing the shot position in world coordinates tells us the shot azimuth, i.e. the inline direction. The angle between H1 and East ($\theta$) is then given by [best-fit line angle – shot azimuth].

The assumption that the media between the shot and receiver are isotropic and laterally homogeneous in the crossline direction can break down especially for rays which pass through a salt dome, as it may drastically change the inclination and/or orientation of the ray path. This in return systematically biases the estimated orientation. In this field experiment, from Figure 5-3 we can see that on the west side of the well rays will encounter salt while on the east side they will encounter only the sediments. Thus the shots on the east side of the survey will allow a more accurate determination of the geophone orientations.

An example of the hodogram analysis is shown in Figure 5-11, in which we plot a series of hodograms corresponding to various shot azimuths for one of the receivers. Each hodogram has been rotated to align the measured first motion fit to be inline (or parallel) with that shot position and the receiver array. The field recorded horizontal axes are shown by the H1 (blue) and H2 (red) lines. So if the geophone package in the field were somehow “magically” oriented north/south and east/west, the H1 axis (blue line) would point north/south and the H2 axis (red line) would point east/west. It is clear from Figure 5-11 that this is not the case. Over most of the hodograms, the H1 axis (blue line) is tilted north-north-west and the H2 axis (red line) is tilted east-north-east.

Closer inspection reveals that the hodograms for shots on the east side show consistent orientation of the H1 and H2 axis. However, those shots on the west side show less consistency. For each receiver, we use the average orientation of the H1 axis for all shots analyzed on the east side as its estimated orientation. The results are shown in Figure 5-12 together with the nominal orientation that is determined by the well trajectory. From Figure 5-12, we find that most of the receiver orientations are consistent with the nominal orientations. This verifies that the geophone alignment mechanism is working fairly well for this field dataset.

There are a couple of receivers whose orientations do not match the nominal orientations. For receivers #1, #6 and #7, we had serious data quality (signal to noise) problem; hence our estimated orientations for those receivers are not believed to be accurate. Receivers #11 and #12 also show small deviations, which could be an error introduced by the kink of the well trajectory since the well changed the deviation angle at those positions. Overall, the hodogram analysis verifies the nominal geophone orientations are accurate and so we will use them when we rotate the horizontal components to create our desired inline direction.

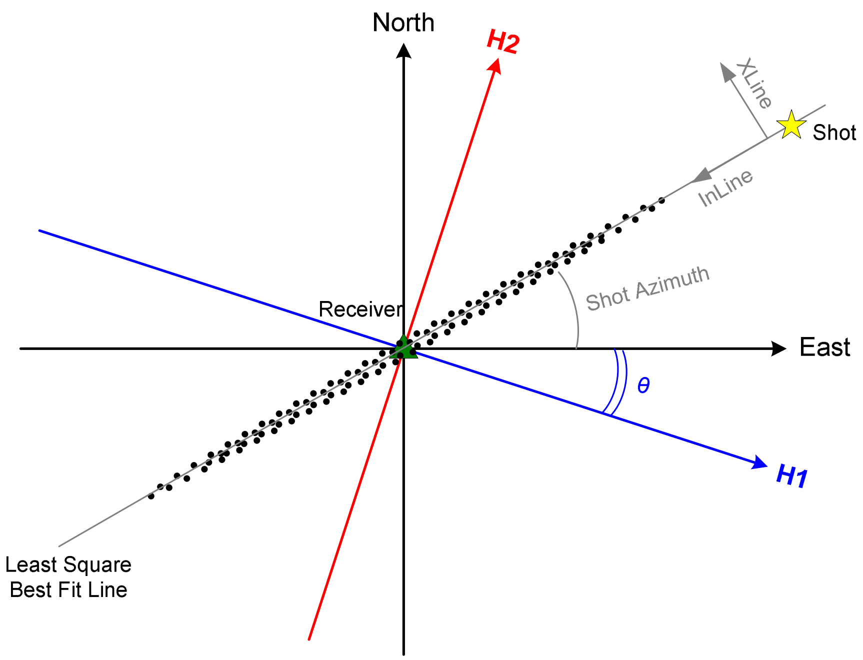


Figure 5-9: Cartoon showing a hodogram analysis to estimate geophone orientation in a 3D VSP survey. Black dots indicate X&Y particle velocity from the first arrival on a record. We measure the direction of particle motion relative to the horizontal axes (H1 and H2) using relative field coordinates as the angle = $\theta$ + shot azimuth. Since we know the azimuth of the shot azimuth from the field geometry, we can determine $\theta$, which allows us to orient the horizontal geophones relative to north and south.

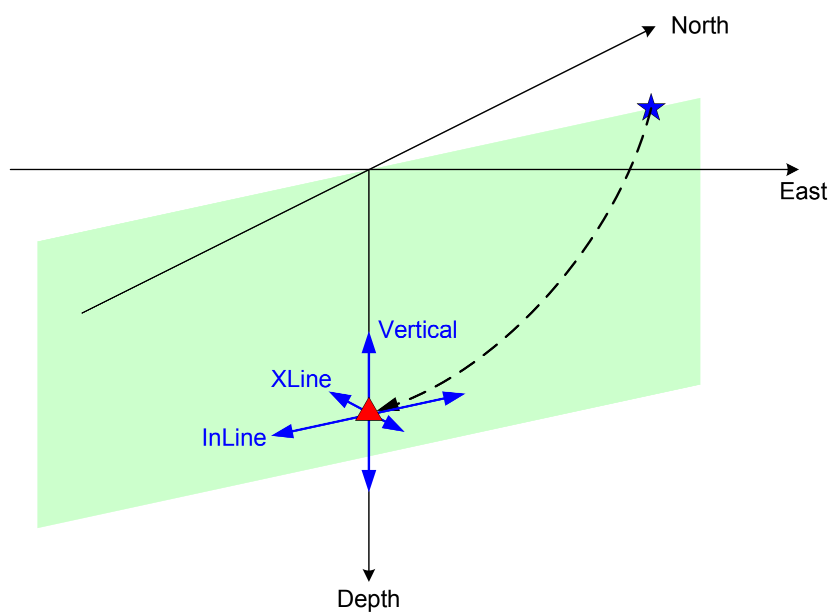


Figure 5-10: Illustration of a ray traveling from a surface shot to a downhole receiver within a vertical plane. This makes the assumption the media are isotropic and laterally homogeneous in the cross line direction.

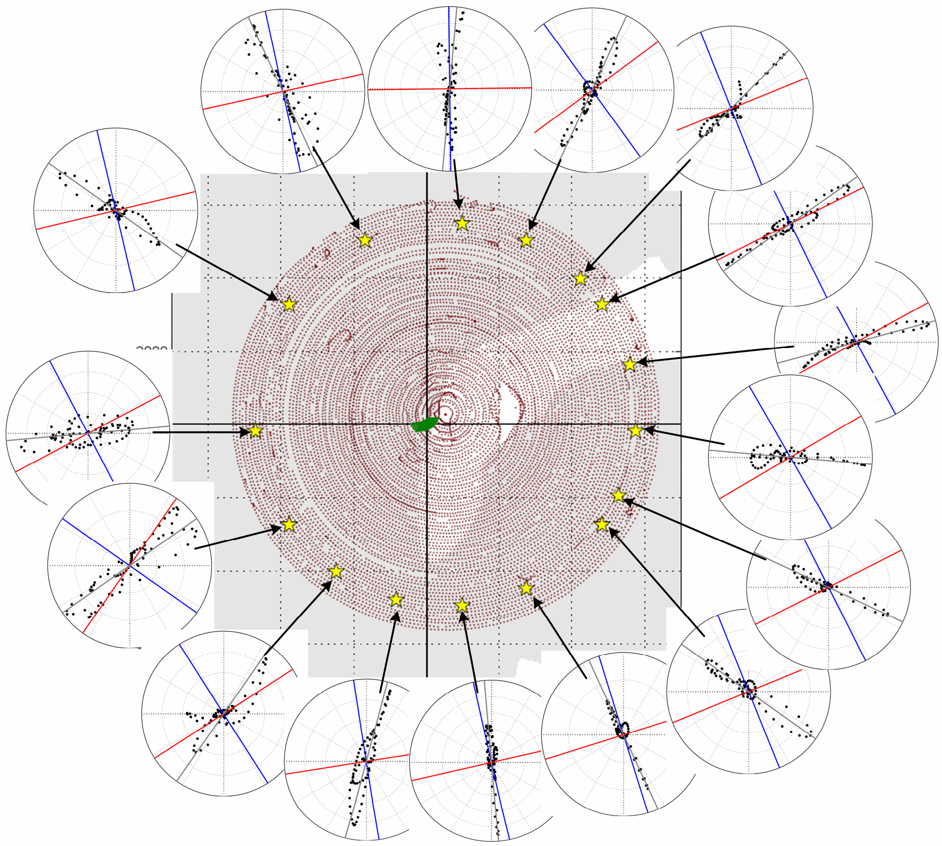

Figure 5-11: Example of a hodogram analysis for one receiver and a ring of shots on the surface. Stars indicate the shot locations for the corresponding hodograms. In each hodogram, the blue line denotes the H1 axis and the red line denotes the H2 axis.

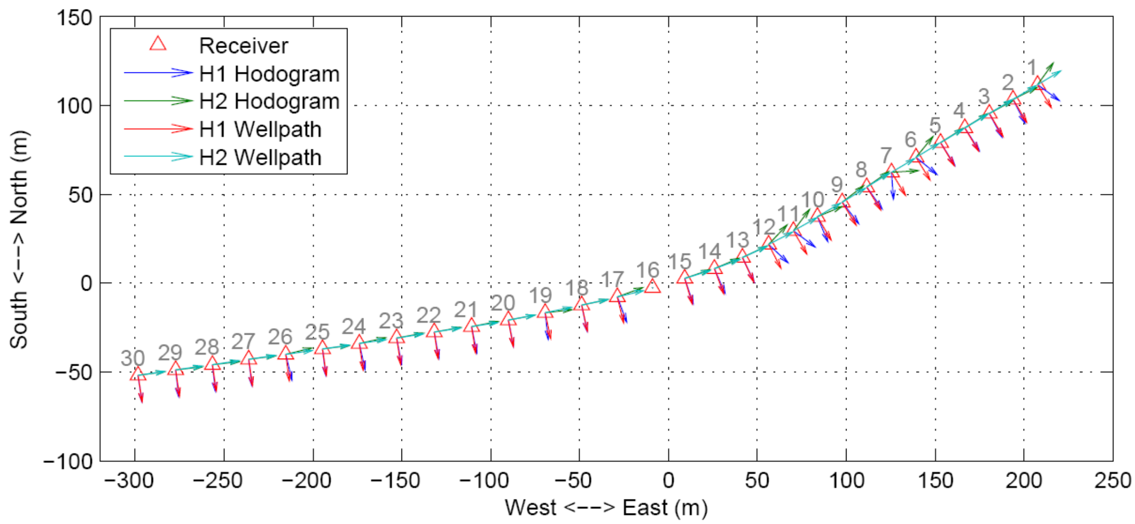


Figure 5-12: Map view of the receiver orientations – comparison between the well path determined orientation (the nominal orientation) and the hodogram estimated orientation.

## 5.4 Imaging Results

Now we apply our proposed directional imaging strategy. We first define a series of wedges that cover a range from –90° to +30° with respective to east and have distance from the center of the array larger than 10,000 ft (3048 m) as shown in Figure 5-13. The direction from the center of each wedge to the center of receiver array is defined as the preferred imaging direction of that wedge. The preferred imaging directions are 10° separated from each other and the wedge width is 10°, which results to a total of 12

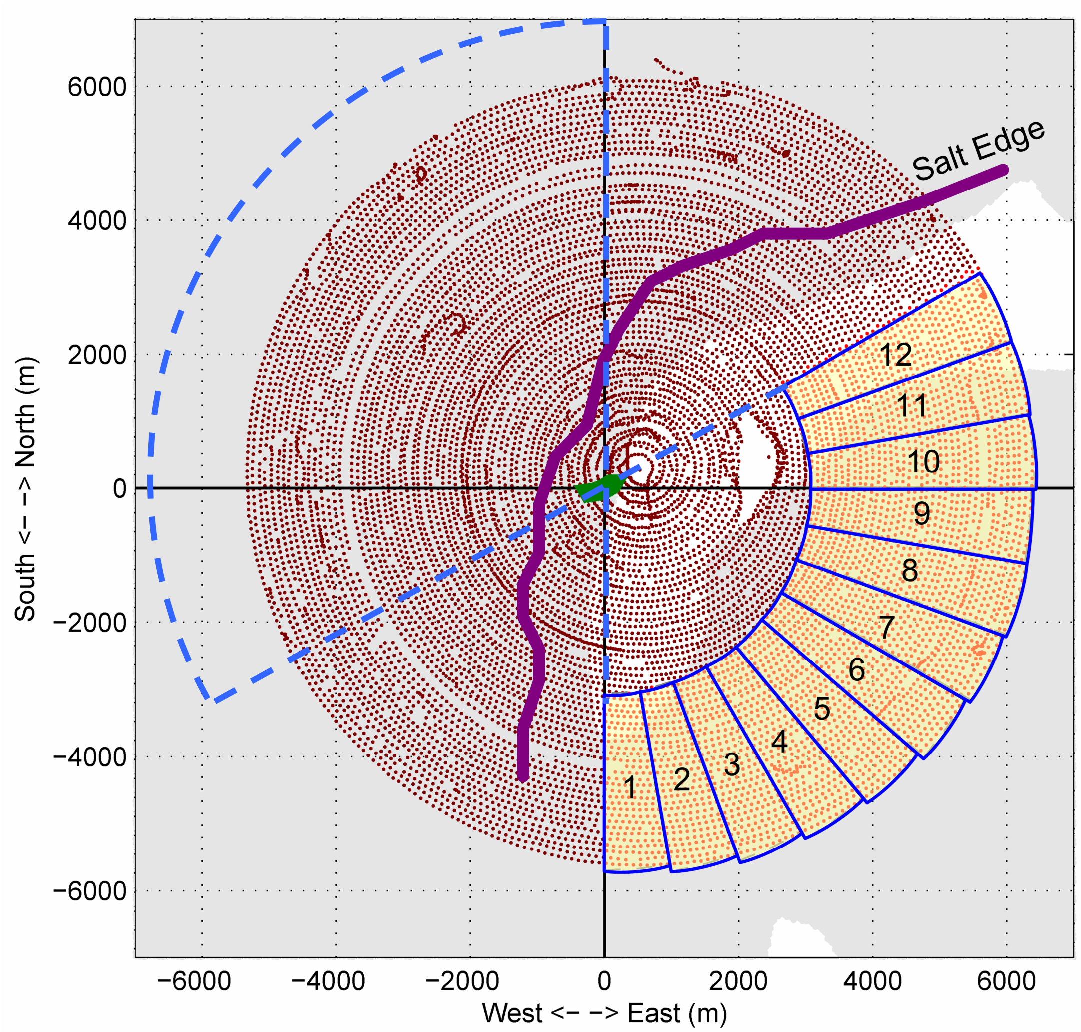


Figure 5-13: Map view of the 12 wedges chosen to be used in the directional imaging.

preferred imaging directions.

We choose this azimuth and distance coverage based on the following two reasons:

(1) The previously interpreted salt structure by Shell (Figure 5-1, Figure 5-2 and Figure 5-5) shown in map-view, is a concave salt flank facing to the southeast. A 3D ray tracing study, also performed by Shell (courtesy of J. Ferrandis), shows that the shot locations on the surface at about 6 km away from the well at an azimuth of about –35°, as shown in Figure 5-14, will provide optimal energy for creating down hole virtual sources which will reflect off the salt flank. . Since it is a complex 3D structure, choosing an azimuth range from –90° to +30° gives us additional illumination directions that will most likely be able to capture the salt flank energy and produce a more complete image of the salt flank.

(2) From the ray tracing study, it is not probable that we will have rays which have actually fully turned and are propagating back toward the surface. Figure 5-14 shows that the rays will be traveling nearly horizontal. These nearly horizontally propagating rays will illuminate the steeply dipping salt flank and then reflect back into the receiver array. Waves which are multiply reflected or scattered from the sediment or other salt bodies can also contribute to the illumination of the salt flank. These events will arrive much later in time on the VSP records. However, a full virtual source redatuming process will fold them back into the virtual shot gather at the proper temporal and spatial position. Energy from surface shots that have short source to receiver offsets will most likely not be able to bend and illuminate the salt flank. Hence, these shots will not add salt flank

reflection signal to the redatumed virtual source gathers. Therefore we omit shots that have offsets smaller than 10,000 ft (3048 m) in the redatuming process.

We choose the wedge width to be 10° so that there are enough shots (250 ~ 350 shots) within each wedge to perform the redatuming operation without losing the azimuth resolution. We will discuss the effect of choosing different wedge width on the imaging result in later sections.

The work flow we use is shown in Figure 5-15. The main differences between this flow and the one we have used previously for model data is as follows:

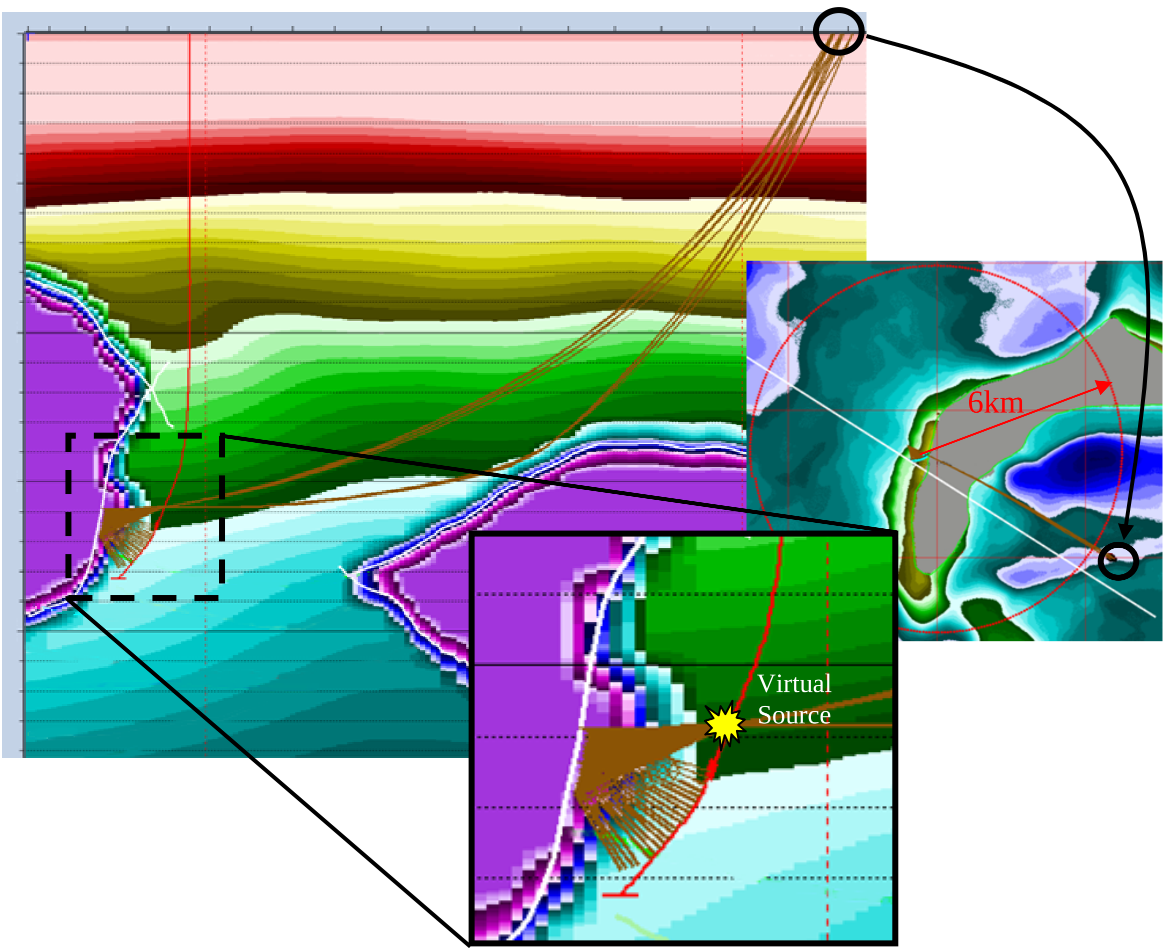


Figure 5-14: 3D ray tracing study to find surface shot locations such that a virtual source can be created at the top of the receiver array which successfully records reflections off the flank by the receiver array. The most successful surface shot locations are located about 6 km southeast of the well. (Courtesy of J. Ferrandis, Shell.)

(1) In our dataset, one receiver was dead (receiver #16) and is omitted in the processing. Some of the traces have been tagged as ”dead” due to high levels of identified noise. It is not unusual, therefore, that for one particular shot recorded on a trace by receiver A there is not a corresponding good trace from receiver B. As we loop through all the shots for a given pair of receivers, in order to perform cross-correlation between the traces, we need to make sure only shots that have valid traces for both receivers are processed.

(2) We want to rotate the horizontal components before they are cross-correlated. The rotation operation needs to be performed trace by trace. Within one wedge, all the traces need to be rotated and aligned in the preferred imaging direction of that wedge. We only rotate the horizontal components. In future work it is possible to include the vertical component in the rotation, given that the incident ray paths are not fully oriented in the horizontal plane.

As in all of our synthetic model analyses, we have not applied any mutes (gates) to the preprocessed VSP records before the virtual source redatuming is applied. Other studies [Bakulin, *et al.*, 2007] show the effect of applying mutes to reduce artifacts but it requires human interaction to pick the muting gate.

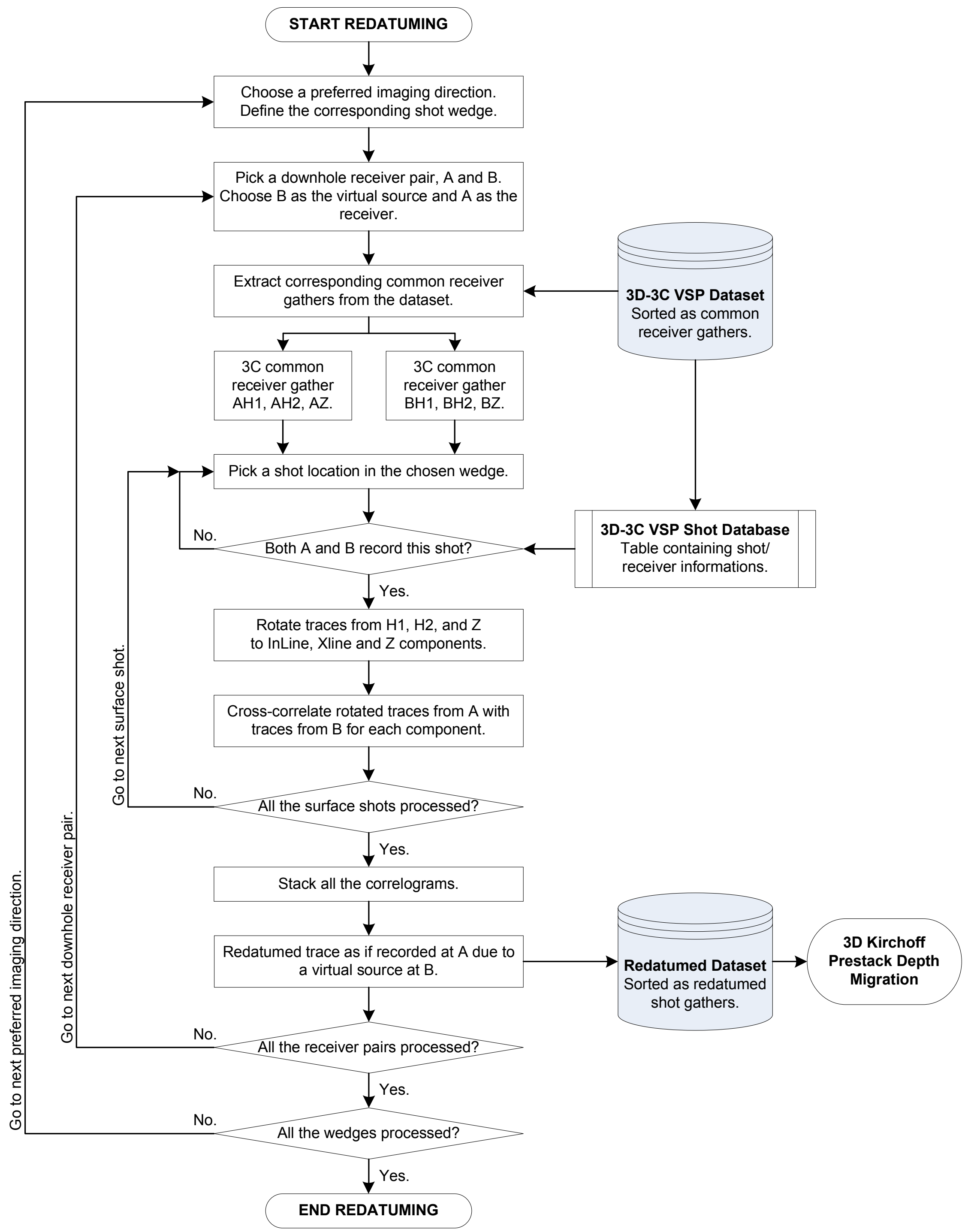


Figure 5-15: Flow chart illustrating the virtual source redatuming process for the field data.

Redatuming each VSP component (inline, crossline, and vertical) individually, we create pseudo-3C prestack virtual common shot gathers for each wedge. Note that the redatuming process described above does not create a complete elastodynamic Green's function between virtual sources and receivers. Figure 5-16 shows an example of the redatumed shot gathers for a virtual source located at the top of the receiver array. Several observations can be made in this figure.

(1) The two horizontal components of the original data are rotated to be aligned with the preferred imaging direction – one is the inline component and the other is the cross-line component. As expected, most of the energy therefore shifts onto the inline component (Figure 5-16a) which should contain the P and SV energy. Any unlikely SH energy should appear on the cross line component (Figure 5-16b). The cross line component should also contain any out of plane reflections coming from the side directions. The vertical component is unaltered from the original dataset since nothing was done to it.

(2) The vertical components of the redatumed shot gathers appear to have the best signal to noise ratio compared to the inline and cross-line components. This matches what we observed in the raw data.

(3) We observe a possible reflection event appeared on both inline component and vertical component across several wedges (Figure 5-16a- wedges #5 through #10, 16c- wedges #4 through #12). This event occurs at around 0.5 second.

(4) On the inline component, which is nominally pointing directly at the salt flank, this reflection event starts to appear from wedge #2 (azimuth = –75°) and its amplitude increases. Wedge #6 (azimuth = –35°) and wedge #7 (azimuth = –25°) seem to have the

largest amplitude for that event. On subsequent wedges, the amplitude of the event starts to decrease. This observation is consistent with the Shell 3D ray tracing study shown in Figure 5-14. In their study, the shots around azimuth of –25° contribute the most reflected salt flank energy in the creation of the virtual sources.

Figure 5-17 shows a complete set of virtual shot gathers for wedge #6 which has an azimuth -35°. The upper panel (a) shows the common shot gathers from the top half of the receiver array. The lower panel (b) shows the gathers from the bottom half of the receiver array. Again, we see the same reflection event that is in Figure 5-16. We also observe that as the "virtual source" moves to lower receivers, the event starts to fade in amplitude and then disappear. The reason is related to the limited imaging aperture as shown in Figure 5-4 and Figure 5-14. If the "virtual source" is sitting at the top of the receiver, the reflection off the flank can still be possibly recorded by the lower receivers. However, if the "virtual source" is sitting at the middle or lower part of the array, the chance that the reflections still be captured by other receivers becomes small. This is due to the model studies that indicate that the source-receiver offsets are not far enough to produce turning rays which pass through the lower receivers and are directed upward toward the salt flank.

Some other portions of the salt flank will be omitted from the final image due to the 3D variation in orientation the salt flank itself. Waves which pass through the receiver array may reflect off the salt flank in a direction away from the receivers and not be captured. Some of this energy could have possibly been captured by a second receiver string in another well if it were available and instrumented. The captured energy would then be available to help image additional portions of the salt flank.

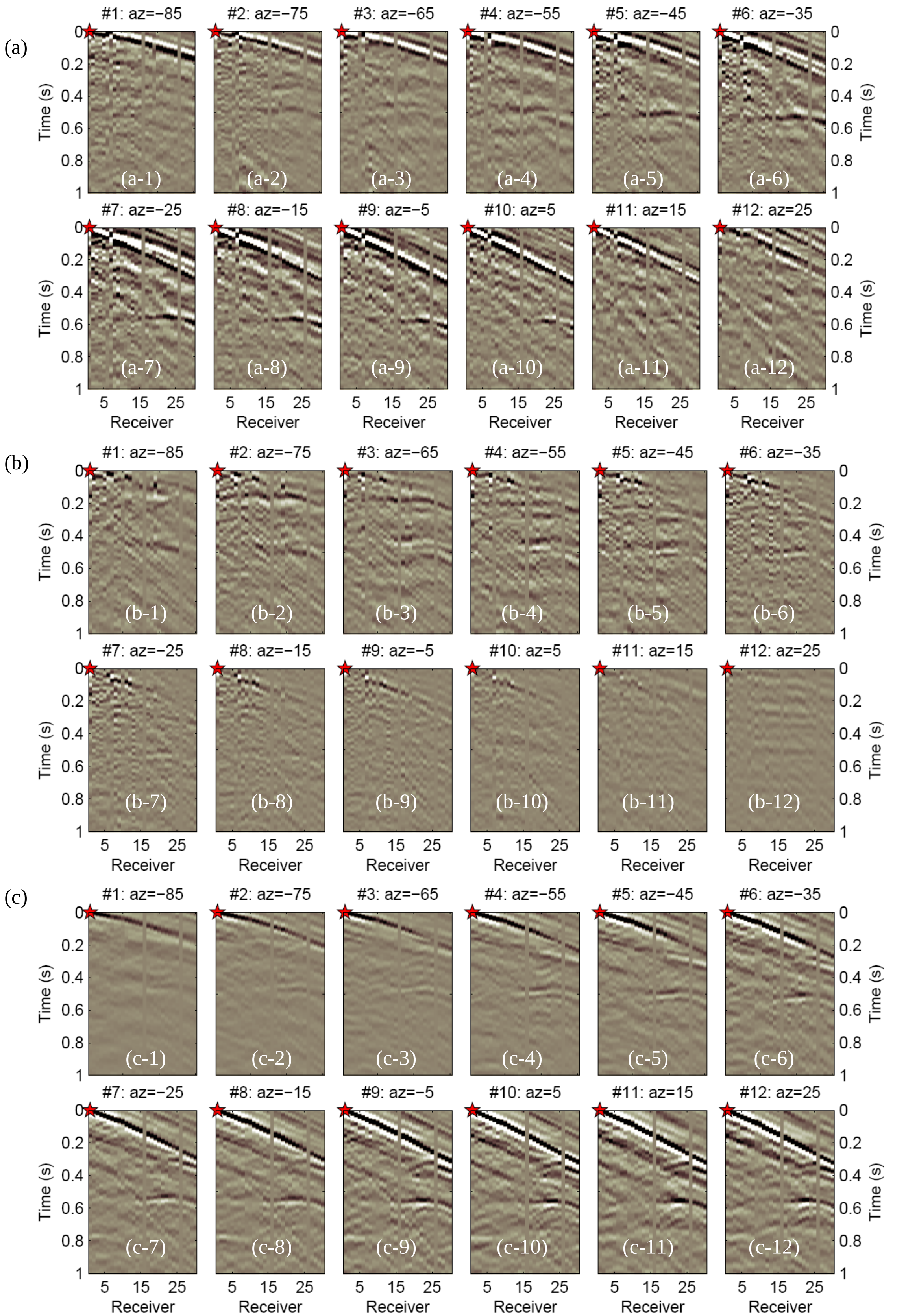


Figure 5-16: Redatumed pseudo -3C shot records from all wedges for a virtual source located at the first receiver: (a) inline; (b) cross-line; (c) vertical.

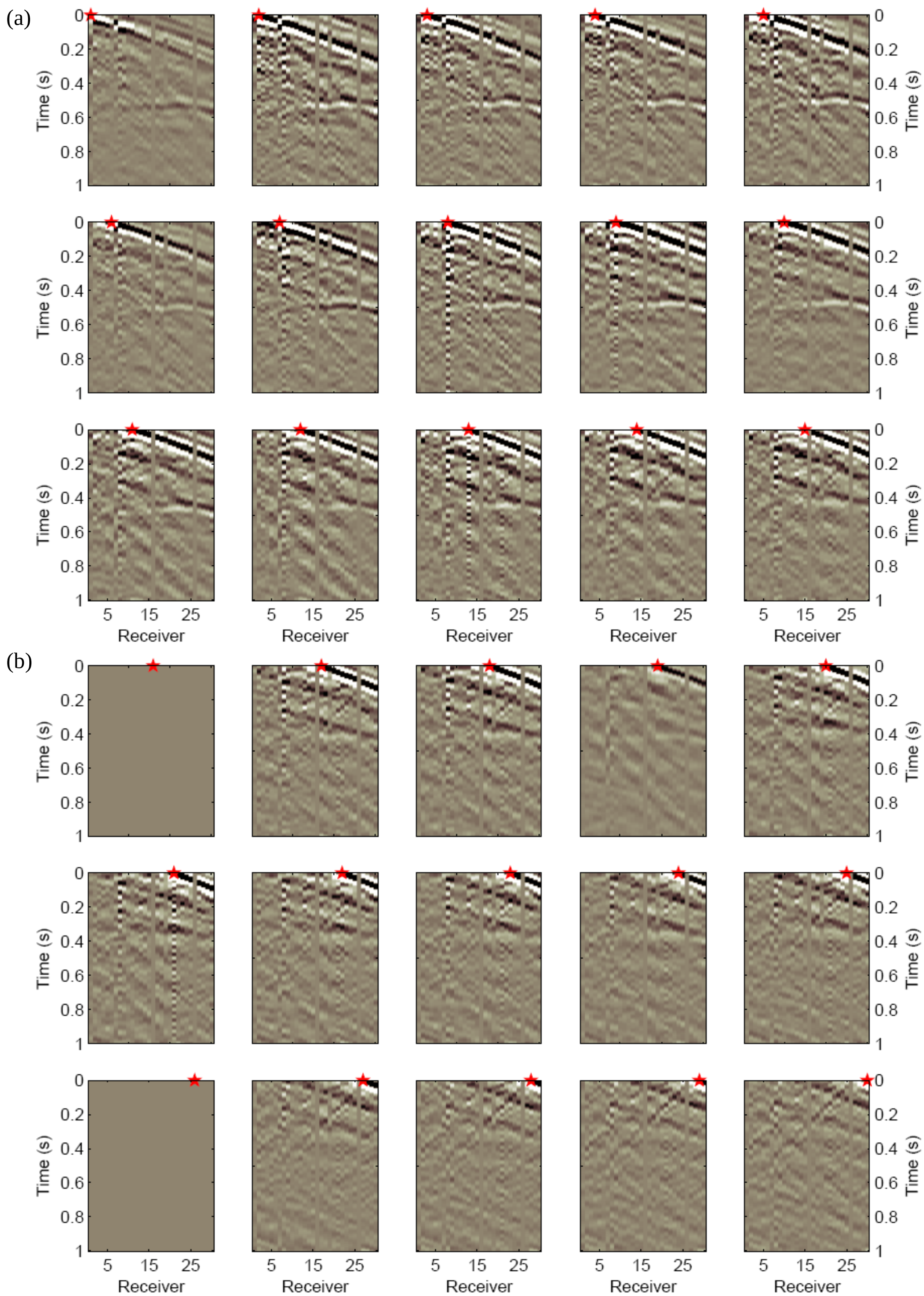


Figure 5-17: Complete common set of virtual shot gathers for wedge #6: (a) receivers 1 through 15, (b) receivers 16 through 30. Note receiver 16 was a dead, and receiver 26 has poor data quality and was omitted from redatuming process, hence both are shown as empty gathers. The red star shows the location of the virtual source.

We then perform Kirchhoff prestack depth migration of these redatumed virtual shot gathers. The migration volume is defined as a cube around the receiver array. A 3D view of the migration volume is shown in Figure 5-18, in which the interpreted base of salt from surface seismic is also plotted. A map view indicating the orientation and camera viewing angle is shown in the bottom right corner. The velocity is assumed to be constant at 9000 ft/s (2743 m/s) within the migration volume according to the surface seismic velocity analysis and borehole sonic log results (Although the algorithm is implemented as a depth migration, using a constant velocity forces the migration to be equivalent to a time migration for this case.) The constant velocity value used for migration reflects the fact that the rock velocities will not vary much within the small migration volume. In contrast to the conventional VSP migration which requires the full velocity field, the virtual source methodology only requires local velocity which could be determined with less uncertainty. As we did in the synthetic examples in previous studies, we mute early time artifacts and extraneous arrivals in the redatumed shot gathers. In this study we experiment with several mutes. Figure 5-19 shows a comparison of the same image plane migrated using two different mutes of the redatumed shot gather. In Figure 5-19a we mute only the direct arrival in the redatumed shot gathers while in Figure 5-19b, we mute everything except for a time window of 0.3 second around the visible reflection event that we identified on the shot gather. We can see that the salt flank reflection is well identified in both images. From now on, we will only show the results using the second mute. In addition, as stated above the virtual shot gathers for receivers 16 through 30 contain little or no energy from the identified reflection event. Therefore, we exclude those shot gathers from the migration.

For each wedge, corresponding to a specific preferred imaging direction (Figure 5-5), we migrate the corresponding redatumed virtual shot gathers into this volume. From the migrated output volume, we cut out a volume which is pie-shaped slice in map view which extends vertically through the entire image grid. This “preferred image volume” is centered at the preferred imaging direction with a width of 10° (as shown on the left side of Figure 5-5). We extract the corresponding preferred image volume from each migrated volume. We then combine them into a final image volume, which should cover the azimuth range as shown by the blue dashed line enclosed area on the left side of Figure 5-13. Figure 5-20 shows a series of vertical planes cut from the final image volume at four imaging directions (as indicated by the green line marked in the bottom right corner map view) which are most likely to produce reflected salt flank energy.

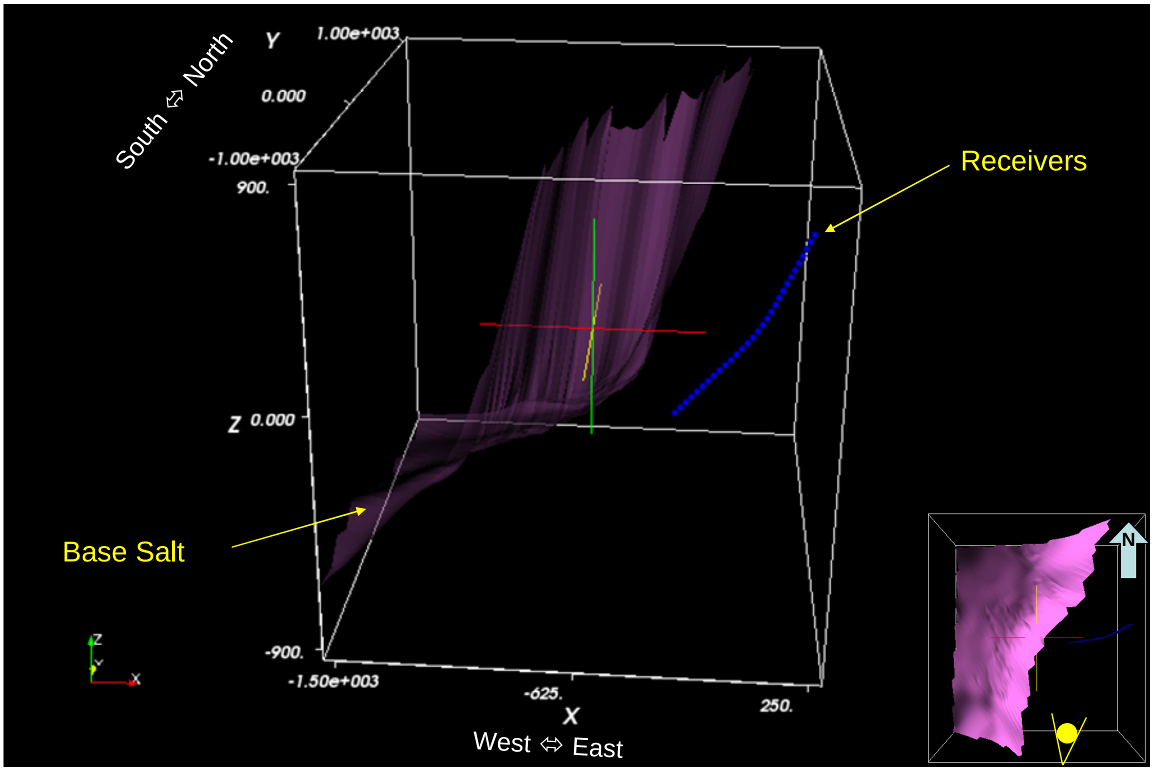


Figure 5-18: Geometry of the output migration volume in 3D view. The interpreted salt bottom is also plotted in purple. The origin is the center of the receiver array. A map view is shown in the bottom right corner to indicate the orientation of the volume in which the camera direction is marked by the yellow eyeball.

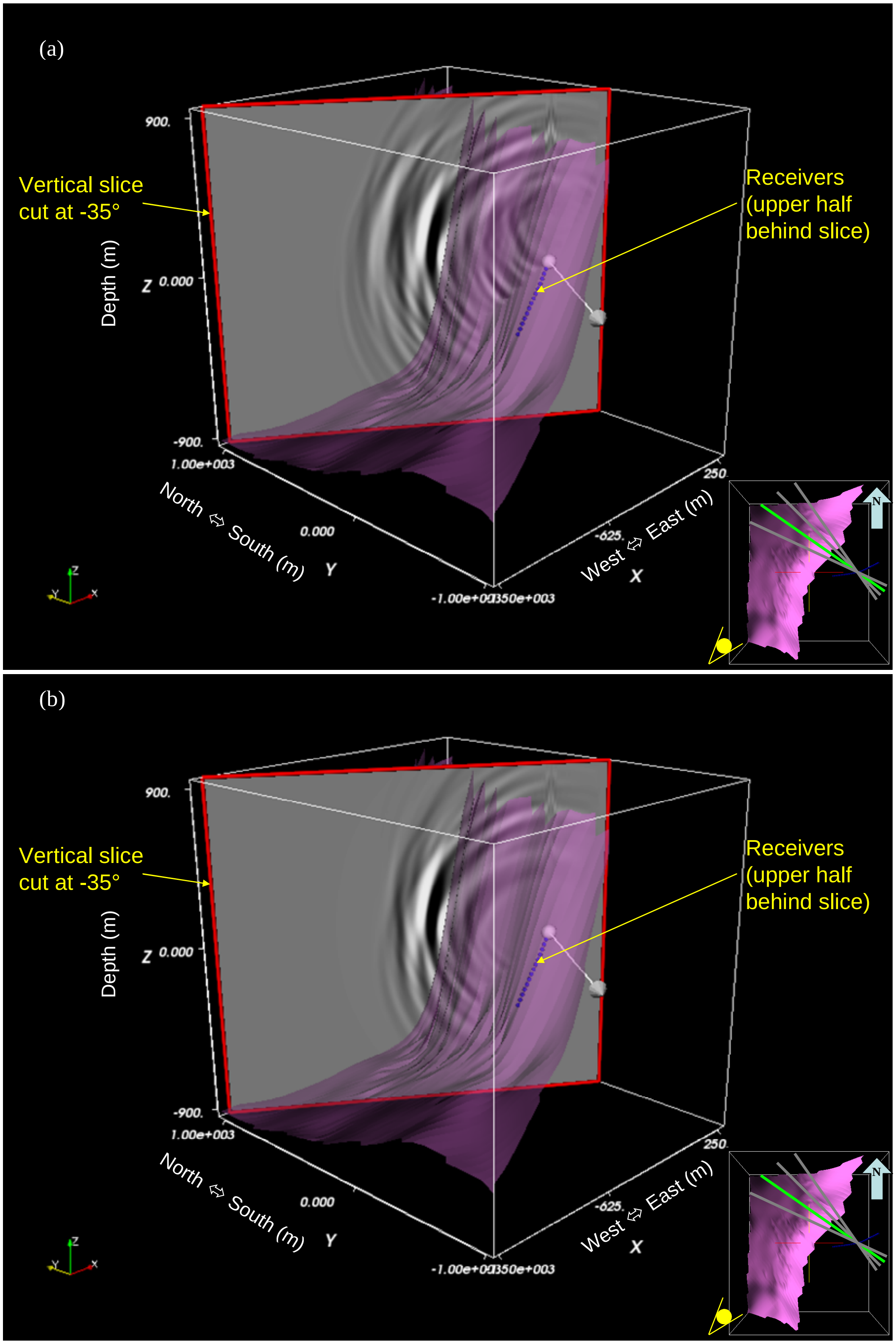


Figure 5-19: Vertical cut along a preferred imaging direction of the imaging volume migrated using the inline component of the redatumed shot gathers after (a) muting the direct arrival only, and (b) muting everything except a window around the event.

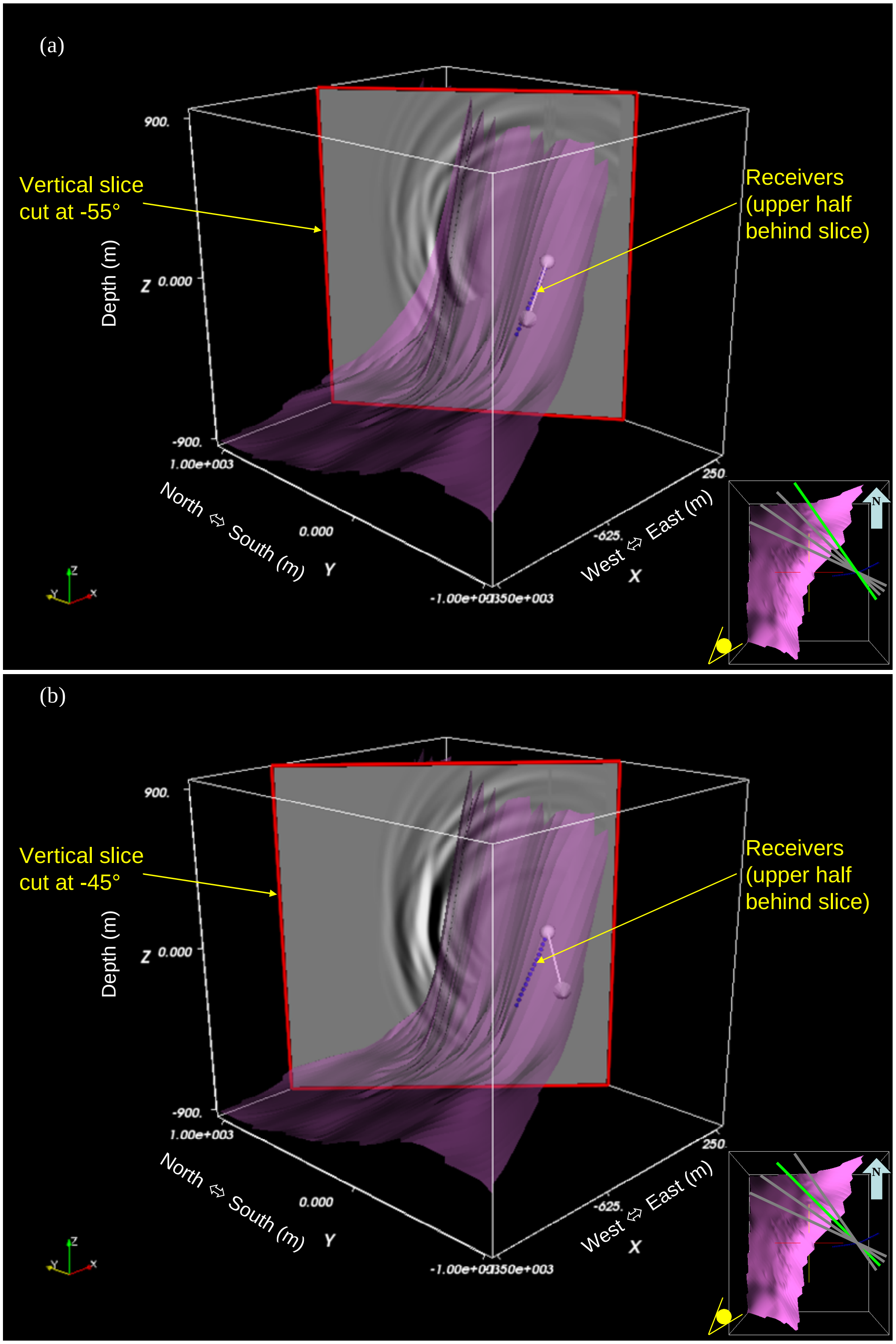
(a)
Vertical slice cut at -55°
Receivers (upper half behind slice)
Depth (m)
Z
900.
0.000
-900.
1.00e+003
North ⇔ South (m)
0.000
Y
-1.00e+003
350e+003
-625.
250.
West ⇔ East (m)
X
N
(b)
Vertical slice cut at -45°
Receivers (upper half behind slice)
Depth (m)
Z
900.
0.000
-900.
1.00e+003
North ⇔ South (m)
0.000
Y
-1.00e+003
350e+003
-625.
250.
West ⇔ East (m)
X
N

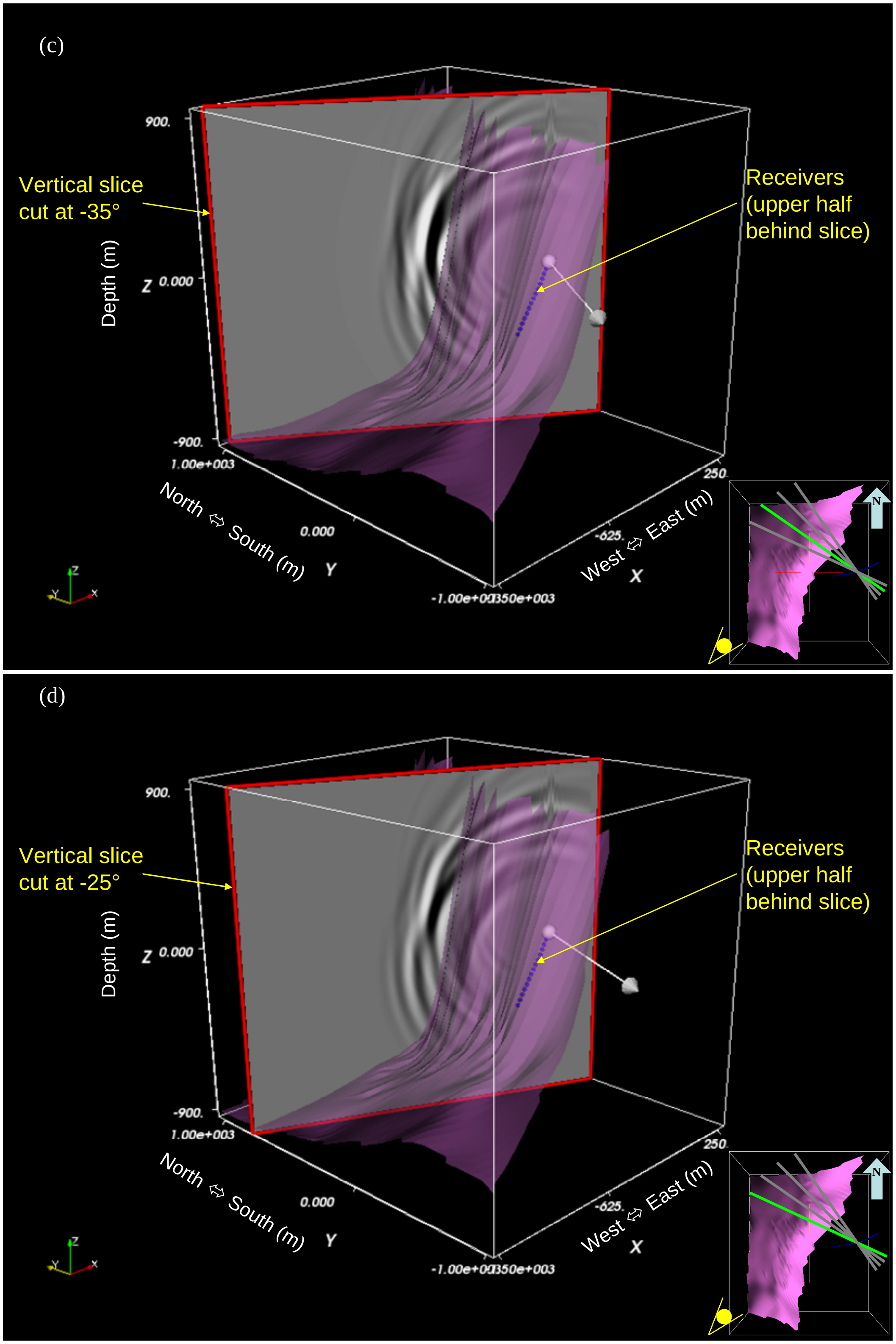


Figure 5-20: Migrated images cut along four preferred imaging directions using the inline component of the redatumed virtual shot gathers from the corresponding single wedges.

We plot these vertical image planes in a 2D view aspect for better interpretation, as shown in Figure 5-21. From the migrated image, it appears that the salt reflection is dominant at azimuths between –35° and –45° from east. It also appears that the reflection is about 640 m away from the center of the array, as measured on Figure 5-21c. This is 80 m farther than the surface seismic interpreted salt interface.

To validate this result, we put a simple point scatter where the maximum amplitude is observed in Figure 5-21c and then ray trace to estimate the arrival time of the reflection due to the scatter. These times are marked by red dashed lines in Figure 5-22. We see that the estimated arrival time and move-out due to the point scatter falls right on top of reflection event we observed on the redatumed virtual shot gathers.

We also experiment to enhance the sharpness of the result by applying a spiking deconvolution operator on the redatumed shot gather before applying the migration operator. Figure 5-23 shows the same series of vertical planes cut from the final image volume obtained by including the spiking deconvolution operator into the workflow. Comparing these images to the images in Figure 5-20, we observe that the spiking deconvolution operator effectively improves the resolution of the salt flank reflection, which could help to interpret the position of the salt edge.

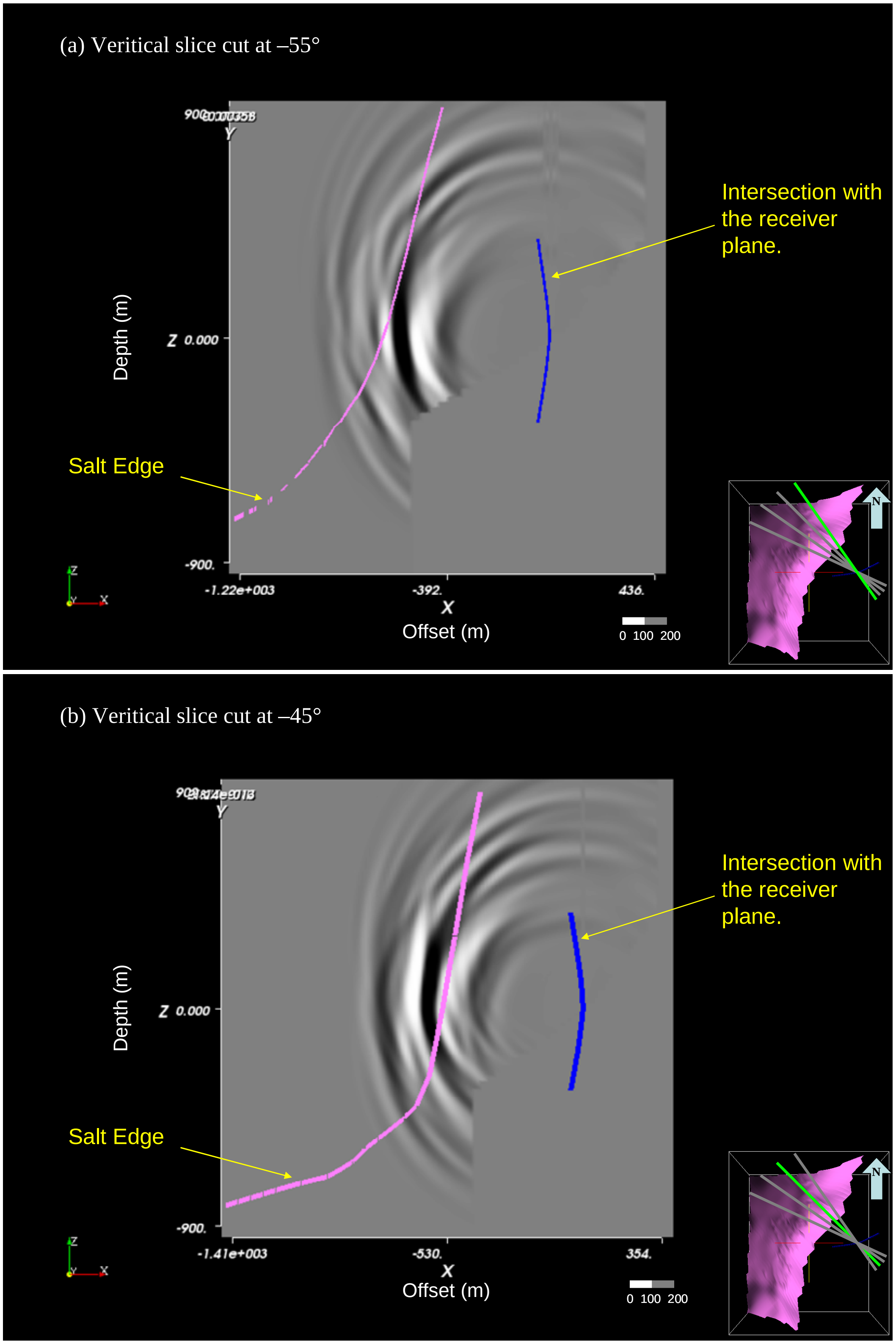
(a) Veritical slice cut at –55°
Intersection with the receiver plane.
Salt Edge
Depth (m)
Z 0.000
-900.
-1.22e+003
-392.
436.
X
Offset (m)
0 100 200
N
(b) Veritical slice cut at –45°
Intersection with the receiver plane.
Salt Edge
Depth (m)
Z 0.000
-900.
-1.41e+003
-530.
354.
X
Offset (m)
0 100 200
N

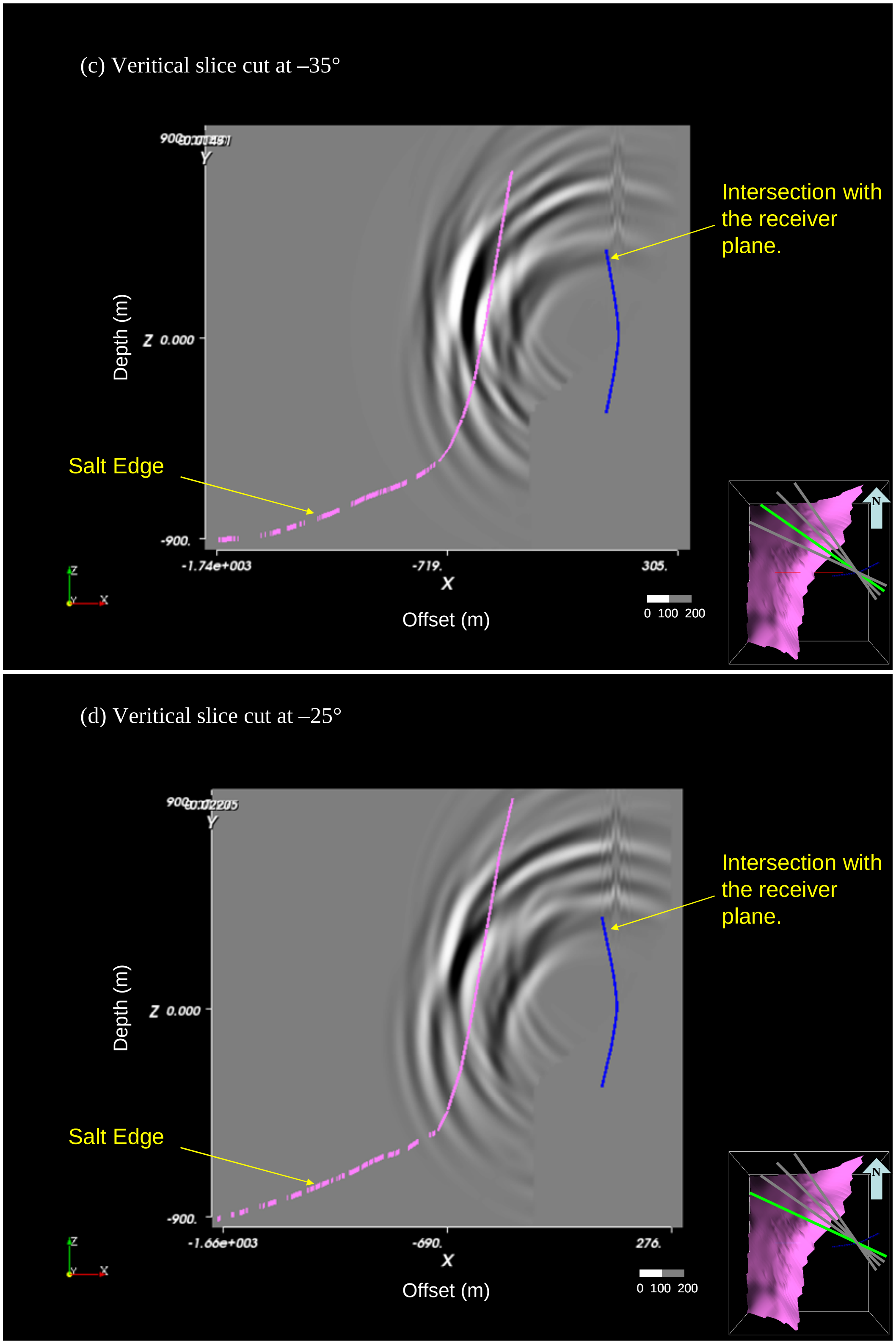


Figure 5-21: Corresponding images from Figure 20 shown in a 2D view. Also plotted are the salt edge (purple line) and the intersection of image plane with the receiver plane (blue line).

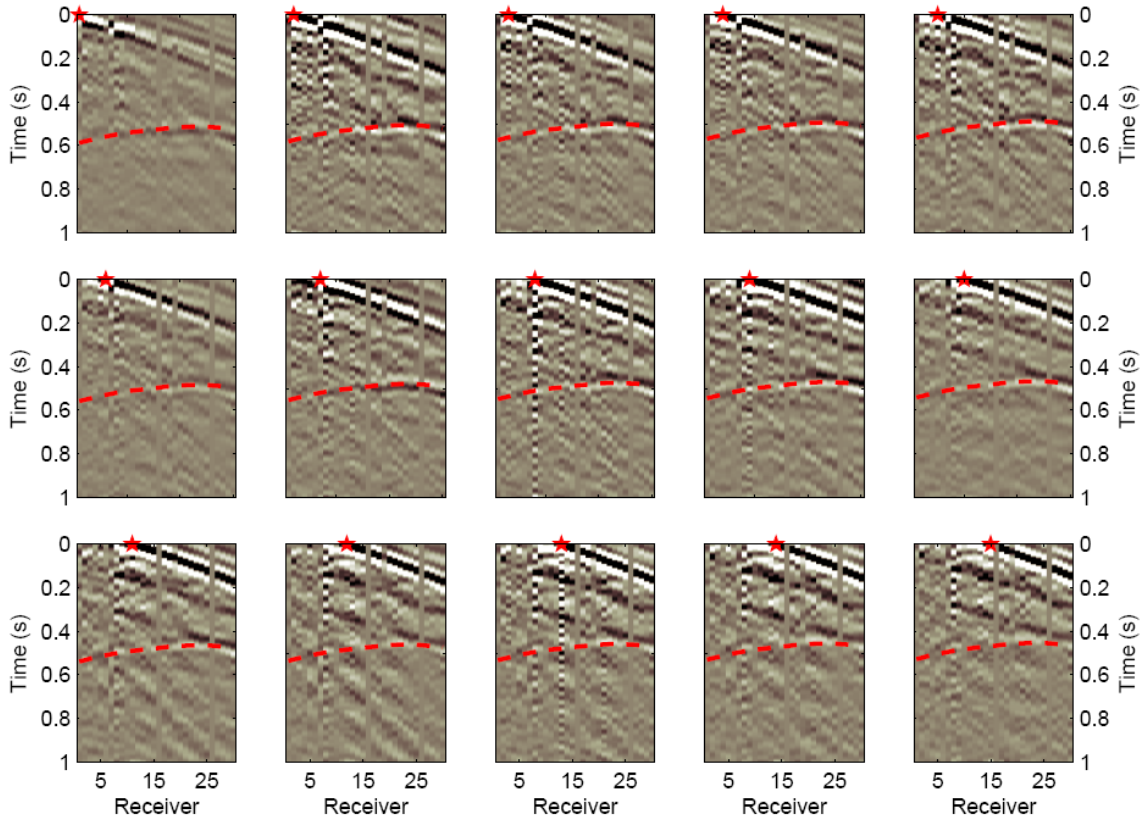


Figure 5-22: Arrival time of reflection due to a single point scatter plotted (in red) over the set of upper 16 redatumed virtual shot gathers.

We next use the vertical component for imaging and the corresponding results are shown Figure 5-24 for the four vertical cut planes at the same imaging direction as in Figure 5-20. The salt reflection appears again at the same position as indicated by the results migrated using the inline components. Figure 5-25 shows results of including the spiking deconvolution operator. We can again see an improvement of the sharpness of the reflection event.

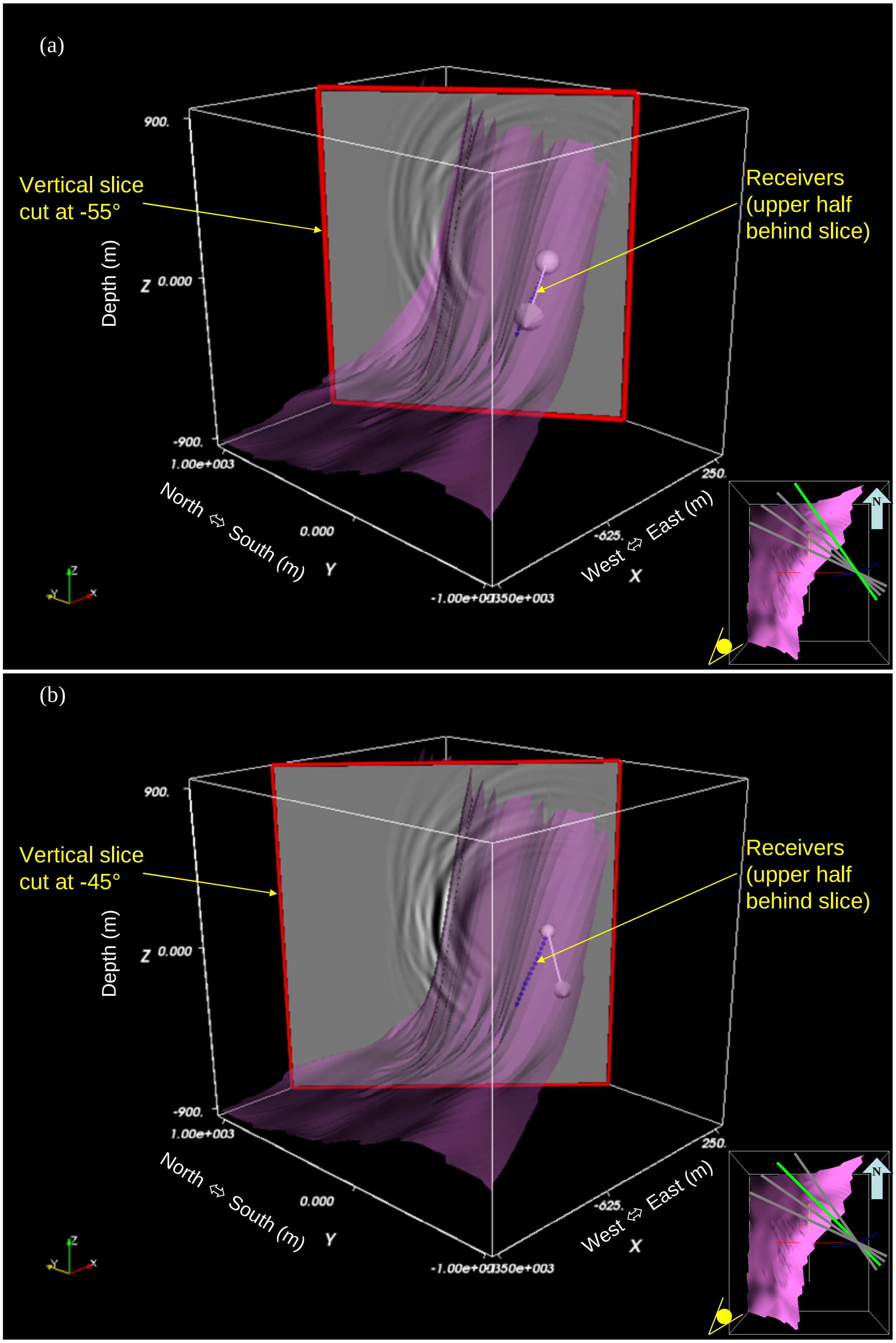
(a)
Vertical slice
cut at -55°
Receivers
(upper half
behind slice)
900.
Z 0.000
Depth (m)
-900.
1.00e+003
North ⇔ South (m) Y
0.000
-1.00e+003
-1350e+003
-625.
250.
West ⇔ East (m) X
N
(b)
Vertical slice
cut at -45°
Receivers
(upper half
behind slice)
900.
Z 0.000
Depth (m)
-900.
1.00e+003
North ⇔ South (m) Y
0.000
-1.00e+003
-1350e+003
-625.
250.
West ⇔ East (m) X
N

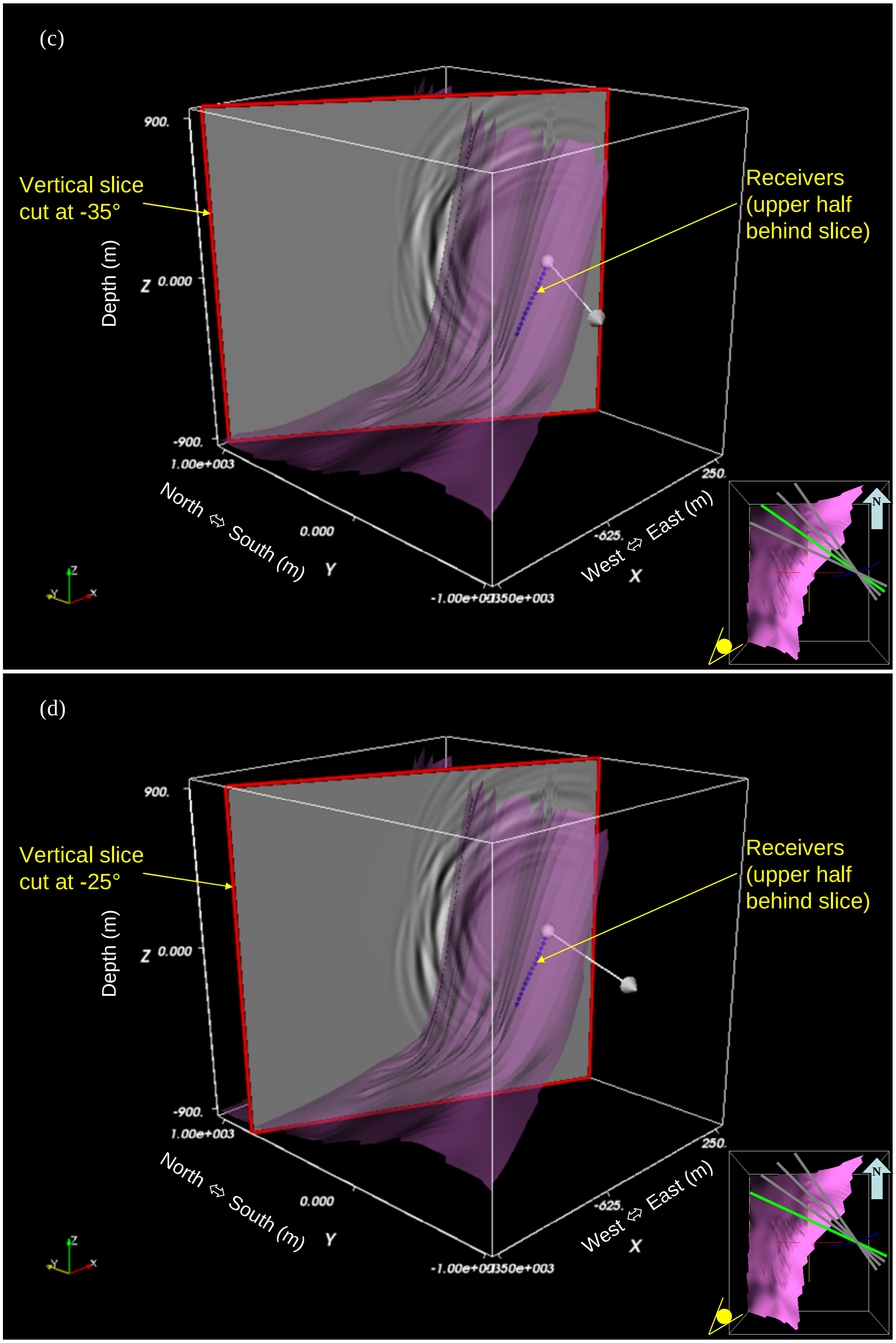


Figure 5-23: Migrated images cut along four preferred imaging directions using the inline component of the redatumed virtual shot gathers from the corresponding single wedges with spiking deconvolution applied.

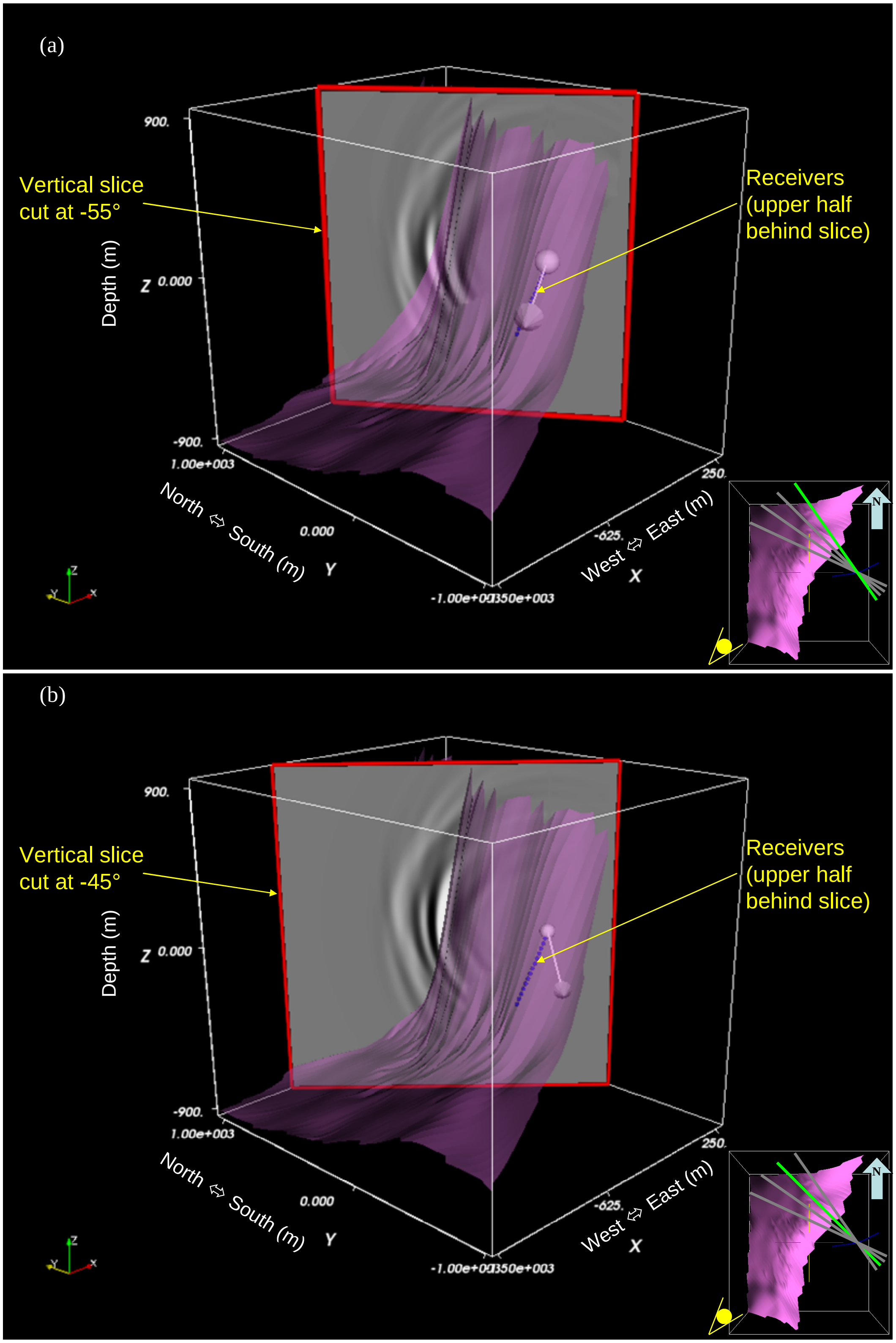
(a)
Vertical slice
cut at -55°
Receivers
(upper half
behind slice)
Depth (m)
Z
900.
0.000
-900.
1.00e+003
North ⇔ South (m)
Y
0.000
-1.00e+003
350e+003
West ⇔ East (m)
X
-625.
250.
N
(b)
Vertical slice
cut at -45°
Receivers
(upper half
behind slice)
Depth (m)
Z
900.
0.000
-900.
1.00e+003
North ⇔ South (m)
Y
0.000
-1.00e+003
350e+003
West ⇔ East (m)
X
-625.
250.
N

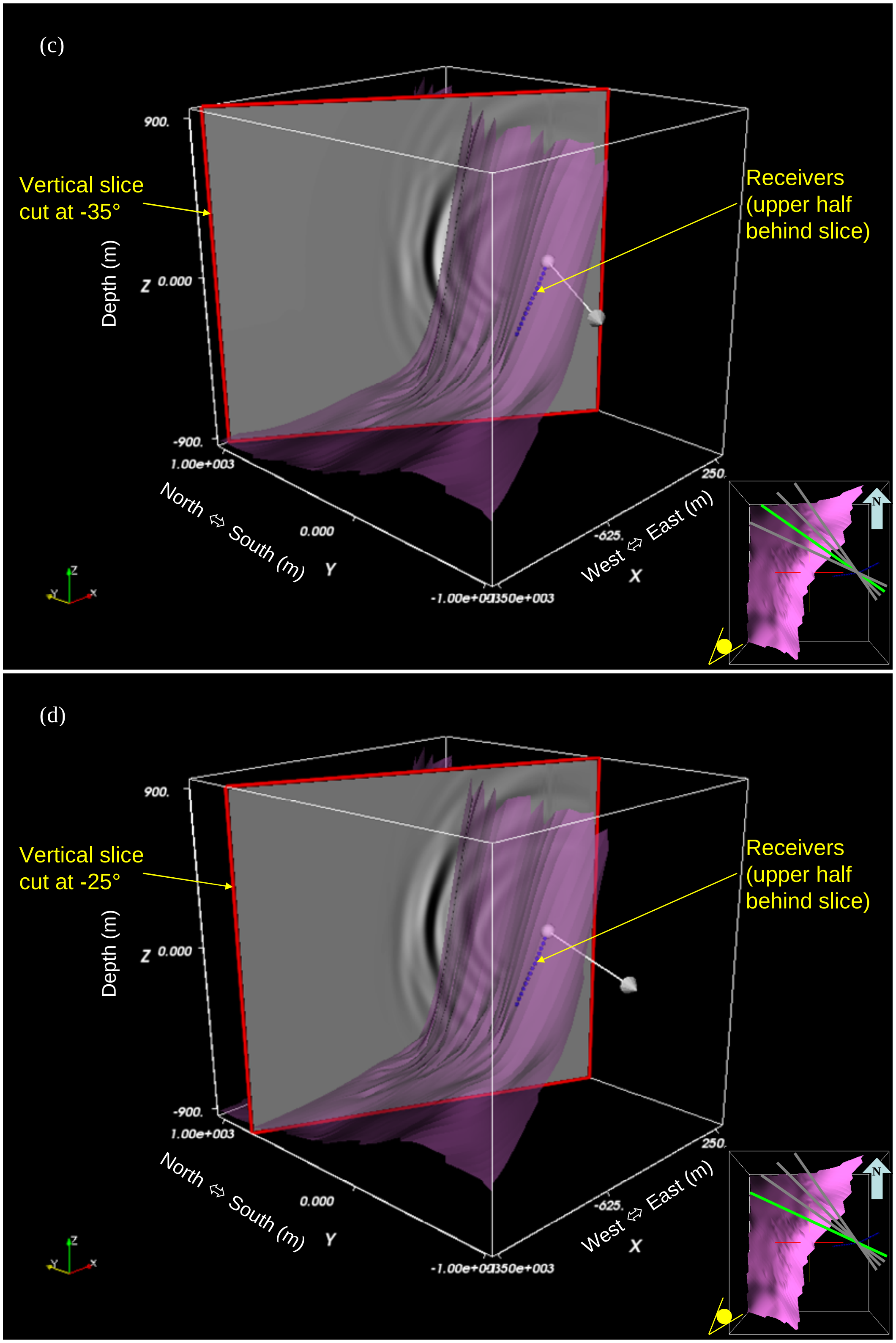


Figure 5-24: Migrated images cut along four preferred imaging directions using the vertical component of the redatumed virtual shot gathers from the corresponding single wedges.

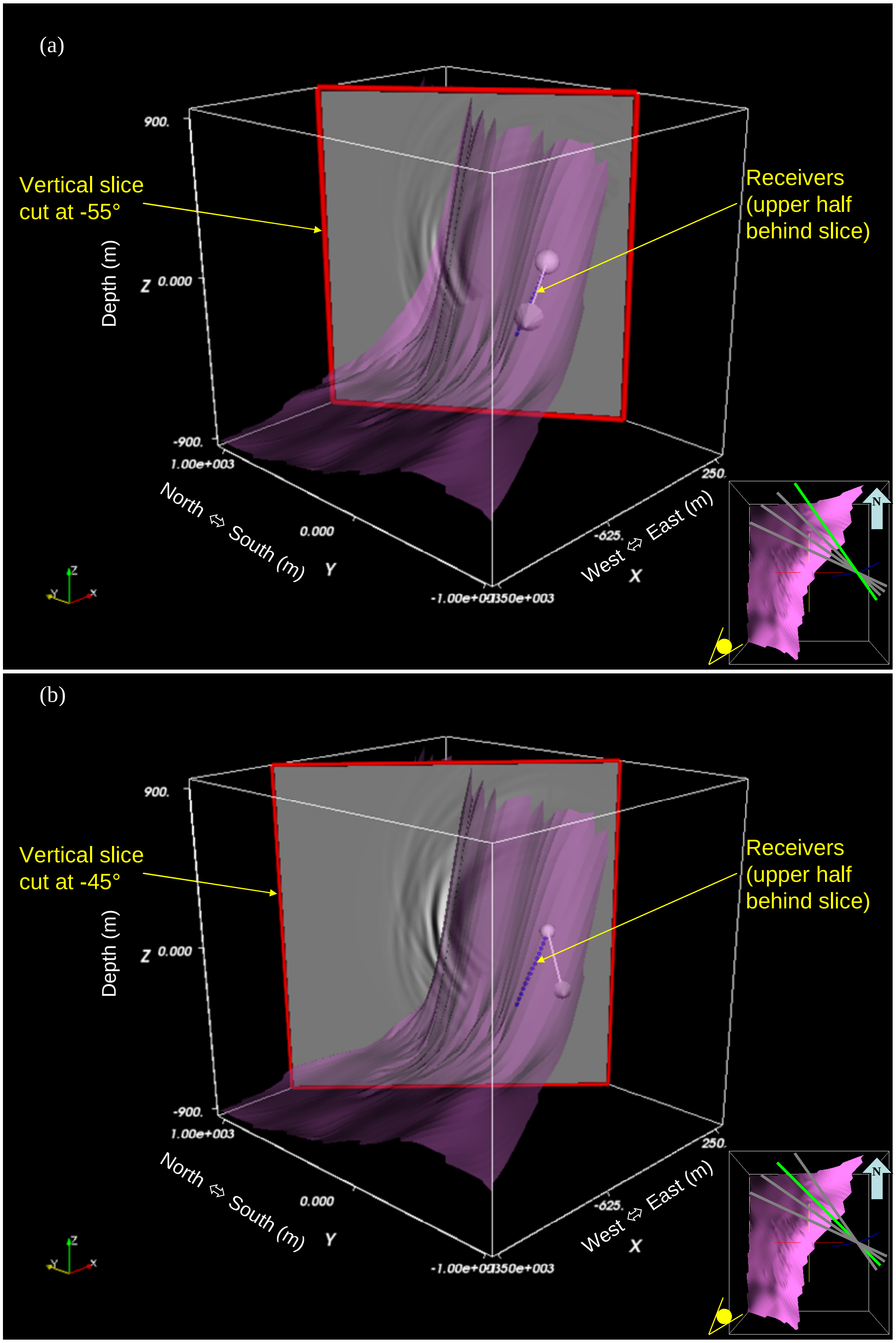
(a)
Vertical slice
cut at -55°
Receivers
(upper half
behind slice)
900.
Z 0.000
Depth (m)
-900.
1.00e+003
North ⇔ South (m)
0.000
Y
250.
-625.
West ⇔ East (m)
X
-1.00e+003
-1.50e+003
N
(b)
Vertical slice
cut at -45°
Receivers
(upper half
behind slice)
900.
Z 0.000
Depth (m)
-900.
1.00e+003
North ⇔ South (m)
0.000
Y
250.
-625.
West ⇔ East (m)
X
-1.00e+003
-1.50e+003
N

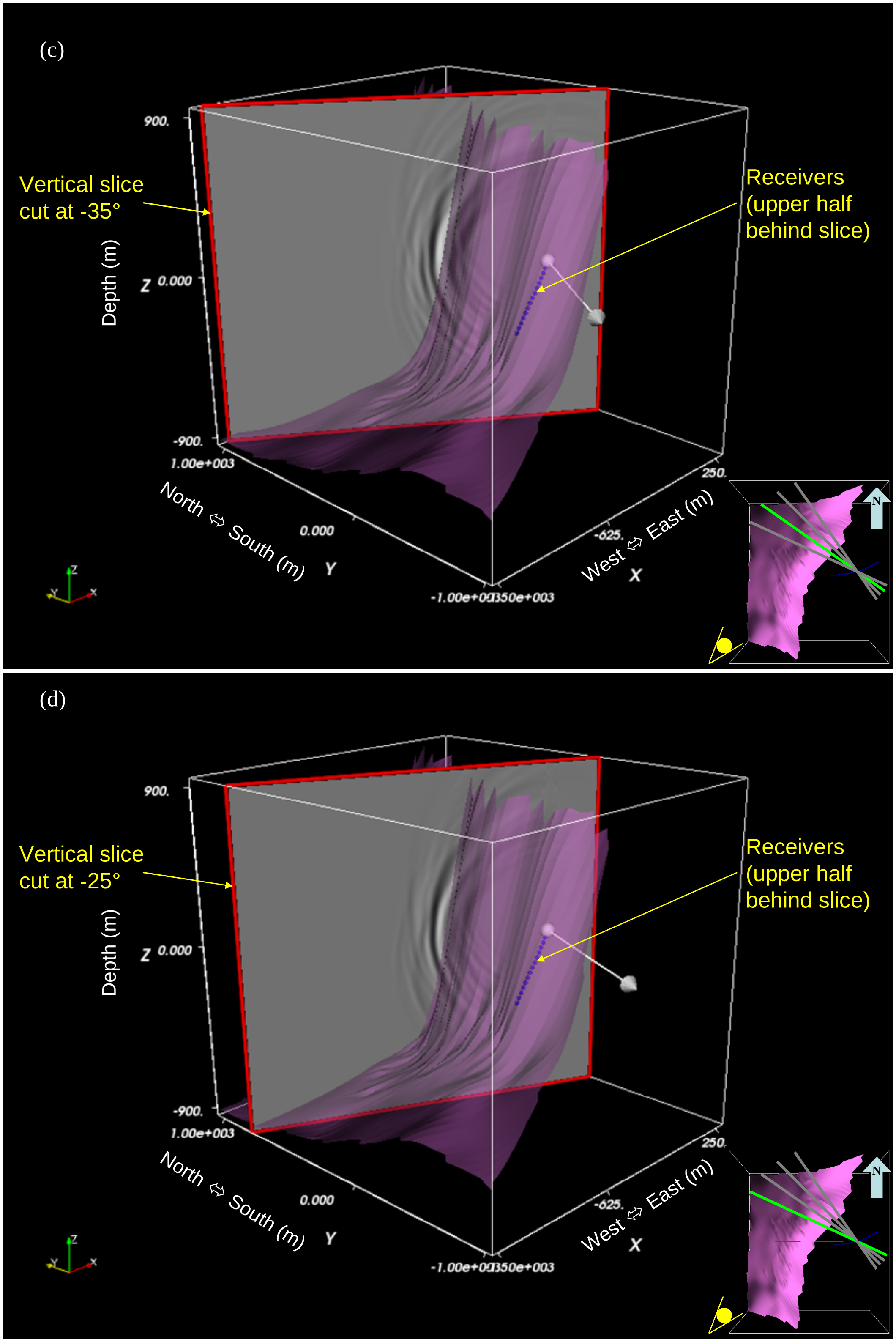


Figure 5-25: Migrated images cut along four preferred imaging directions using the vertical component of the redatumed virtual shot gathers from the corresponding single wedges with spiking deconvolution applied.

## 5.5 Discussions

### 5.5.1 Effect of Stacking Neighboring Wedges

We have arbitrarily constructed our wedges of shots to be 10° wide and to contain about 200-300 surface shots. A question arises as to what should be the appropriate size of these wedges. Since no rotation is applied to the vertical components, the virtual source redatuming followed by migration is linear. That is to say that we can add the individually redatumed and migrated wedges together to simulate a larger wedge. Thus we can combine the traces going into the final image in any order. On the other hand, in the tests we have shown, each inline horizontal trace from a single wedge is created using a single horizontal rotation angle determined from the midpoint of the wedge. Since the correct rotation angle for traces added to the wedge is increasingly incorrect as we increase it angular size, this process is not linear if we add neighboring wedges to simulate increasing the size of the wedge. However, we expect that if the angular separation of wedges is small then the process will be almost linear. If we stack together migrated images created from different wedges, the rotation of the horizontal components will be only slightly different. Obviously, as the width of the wedge gets large it becomes increasingly unacceptable. In this section we look at stacking the output from individual wedges. In the next section we look at increasing the wedge width directly.

In the previous section, we migrate redatumed virtual shot gathers for each wedge into a volume and then look at the vertical plane along the imaging direction corresponding to that specific one wedge. As discussed above, we can also stack migrated volumes from more than one imaging direction (wedge). For example, for the preferred imaging direction of –35°, we could cut the vertical plane from the single migrated volume corresponding to the –35° wedge (this corresponds to the results shown in previous section.). We can also add to that image volume two other migrated volumes corresponding to the two neighboring wedges, giving a sub-stack of images from –45°, –35° and –25°, and then cut the vertical plane at the same direction (–35º). The question is whether making the aperture wider by stacking more wedges will produce a sharper, better resolved image.

Figure 5-26 shows the imaging result at direction of –35° from different sub-stacked volumes migrated using the inline component of the redatumed shot gathers. The wedges that are stacked are marked in green on the map view of the volume at the bottom right corner. It appears that stacking more wedges into the imaging volume does not improve the final image but degrades the sharpness and clarity of the salt reflection. Figure 5-27 shows the imaging result at direction of –35° from different sub-stacked volumes migrated using the vertical component of the redatumed shot gathers. The sub-stack degradation on the vertical component seems to be less when compared to inline component. However, the salt reflection appears to loose resolution as more wedges are added together.

For completeness, we have repeated these tests using spiking deconvolution on virtual shot gathers for the inline components in Figure 5-28 and the vertical components in Figure 5-29. As before, the sharpest resolution is found from the single wedge images.

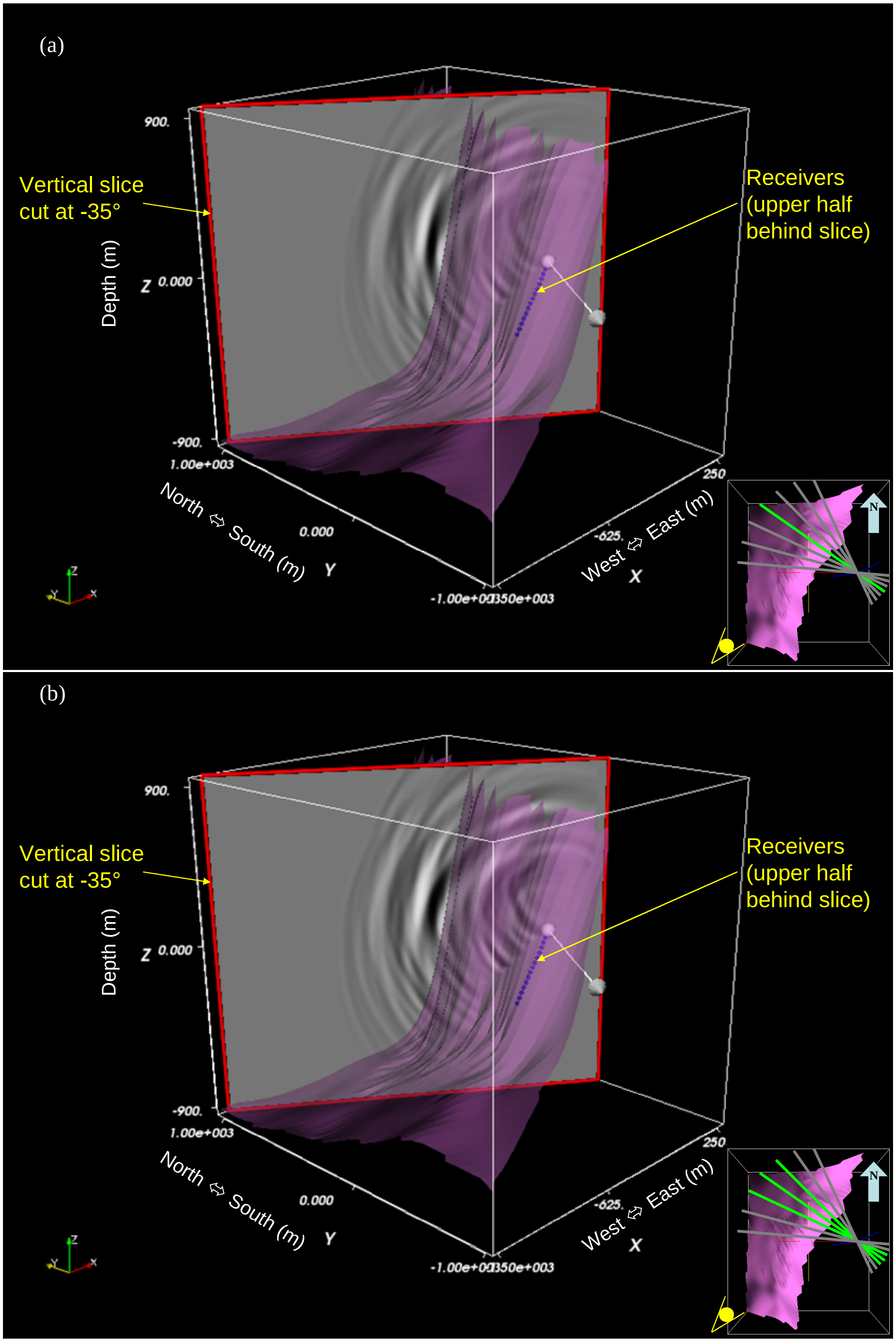
(a)
Vertical slice
cut at -35°
Receivers
(upper half
behind slice)
900.
Z 0.000
Depth (m)
-900.
1.00e+003
North ⇔ South (m)
0.000
Y
-1.00e+003
250
-625.
West ⇔ East (m)
X
N
(b)
Vertical slice
cut at -35°
Receivers
(upper half
behind slice)
900.
Z 0.000
Depth (m)
-900.
1.00e+003
North ⇔ South (m)
0.000
Y
-1.00e+003
250
-625.
West ⇔ East (m)
X
N

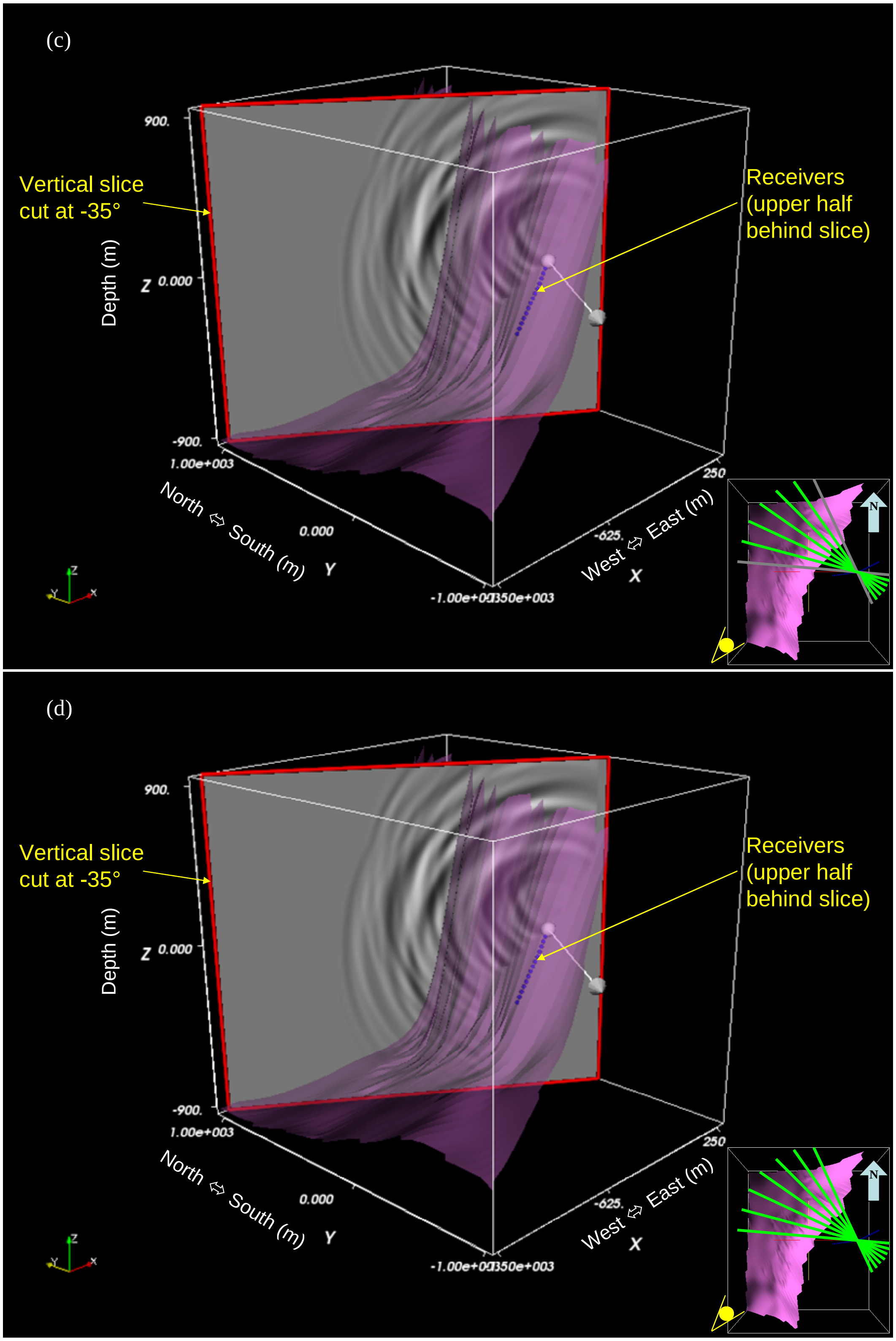


Figure 5-26: Vertical plane cut at imaging direction of –35° in sub-stacked volumes migrated using inline component: (a) –35° wedge only; (b) –45°, –35° and –25° wedges; (c) –55°, –45°, –35°, –25° and –15° wedges; (d) –65°, –55°, –45°, –35°, –25°, –15° and –5° wedges.

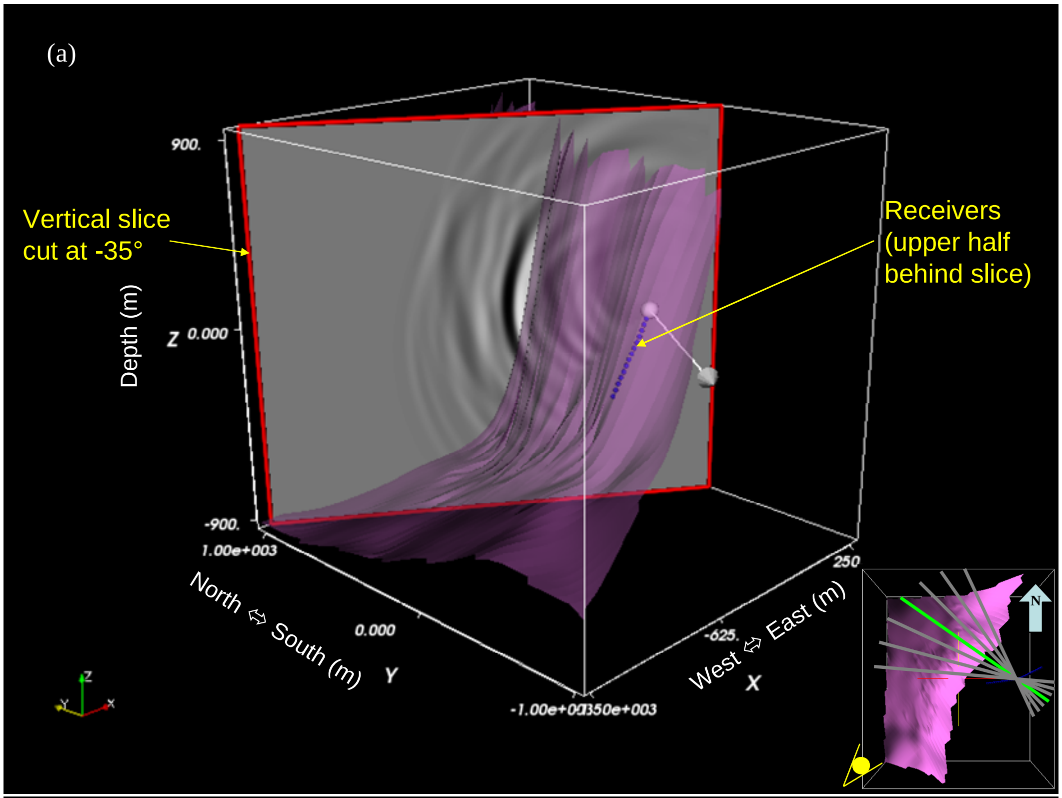
(a)
Vertical slice
cut at -35°
Receivers
(upper half
behind slice)
900.
Z 0.000
Depth (m)
-900.
1.00e+003
North ⇔ South (m)
0.000
Y
-1.00e+003
350e+003
250
-625.
West ⇔ East (m)
X
N

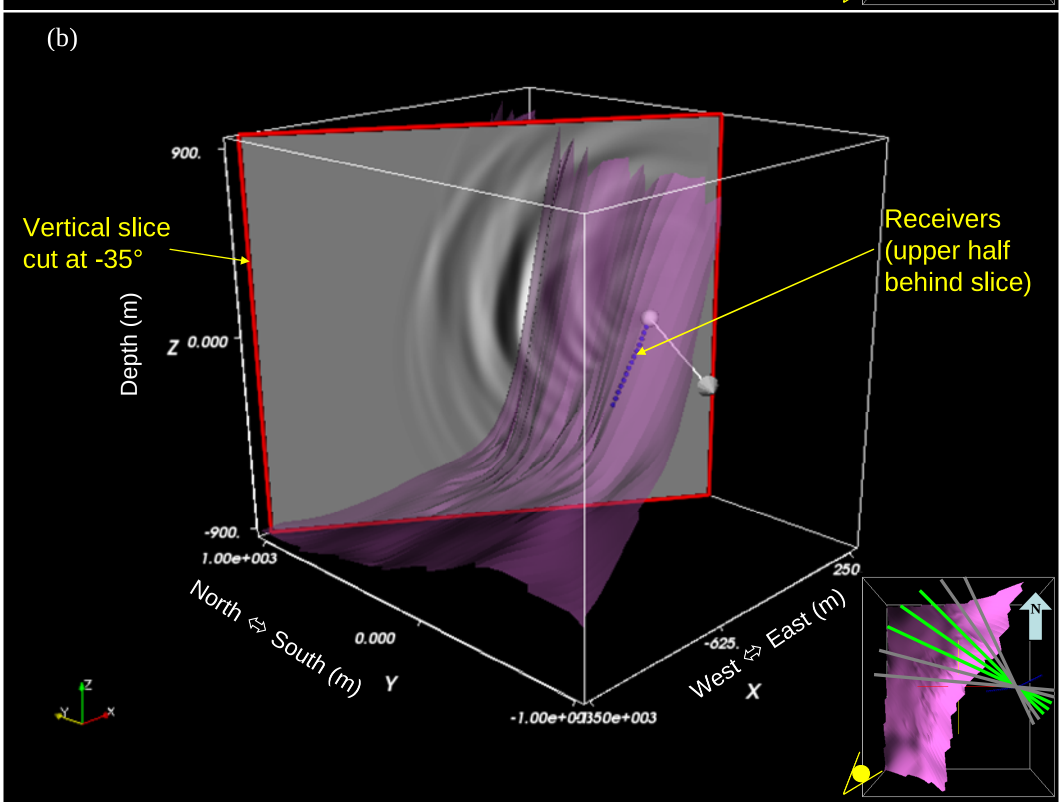
(b)
Vertical slice
cut at -35°
Receivers
(upper half
behind slice)
900.
Z 0.000
Depth (m)
-900.
1.00e+003
North ⇔ South (m)
0.000
Y
-1.00e+003
350e+003
250
-625.
West ⇔ East (m)
X
N

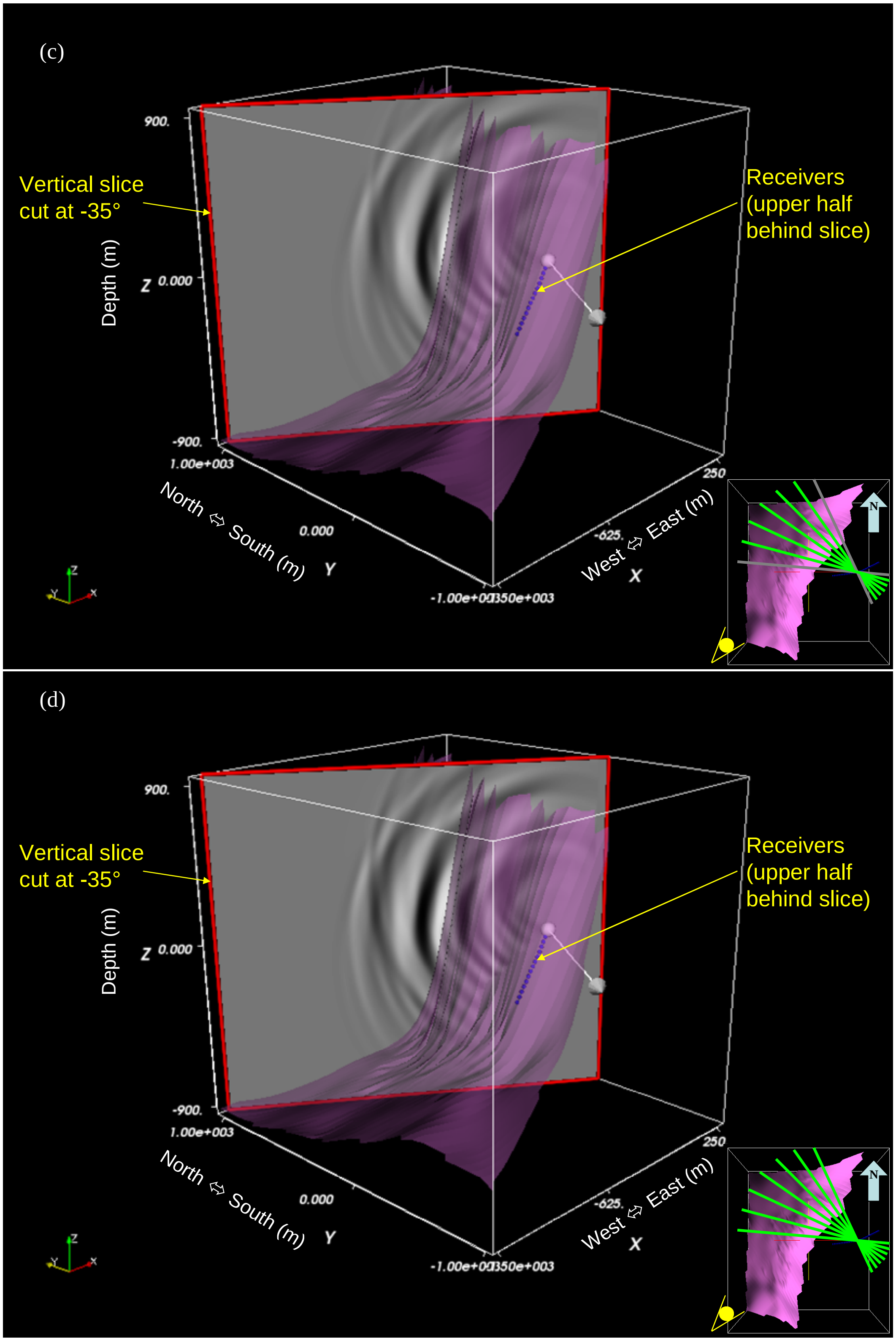


Figure 5-27: Vertical plane cut at imaging direction of –35° in sub-stacked volumes migrated using vertical component: (a) –35° wedge only; (b) –45°, –35° and –25° wedges; (c) –55°, –45°, –35°, –25° and –15° wedges; (d) –65°, –55°, –45°, –35°, –25°, –15° and –5° wedges.

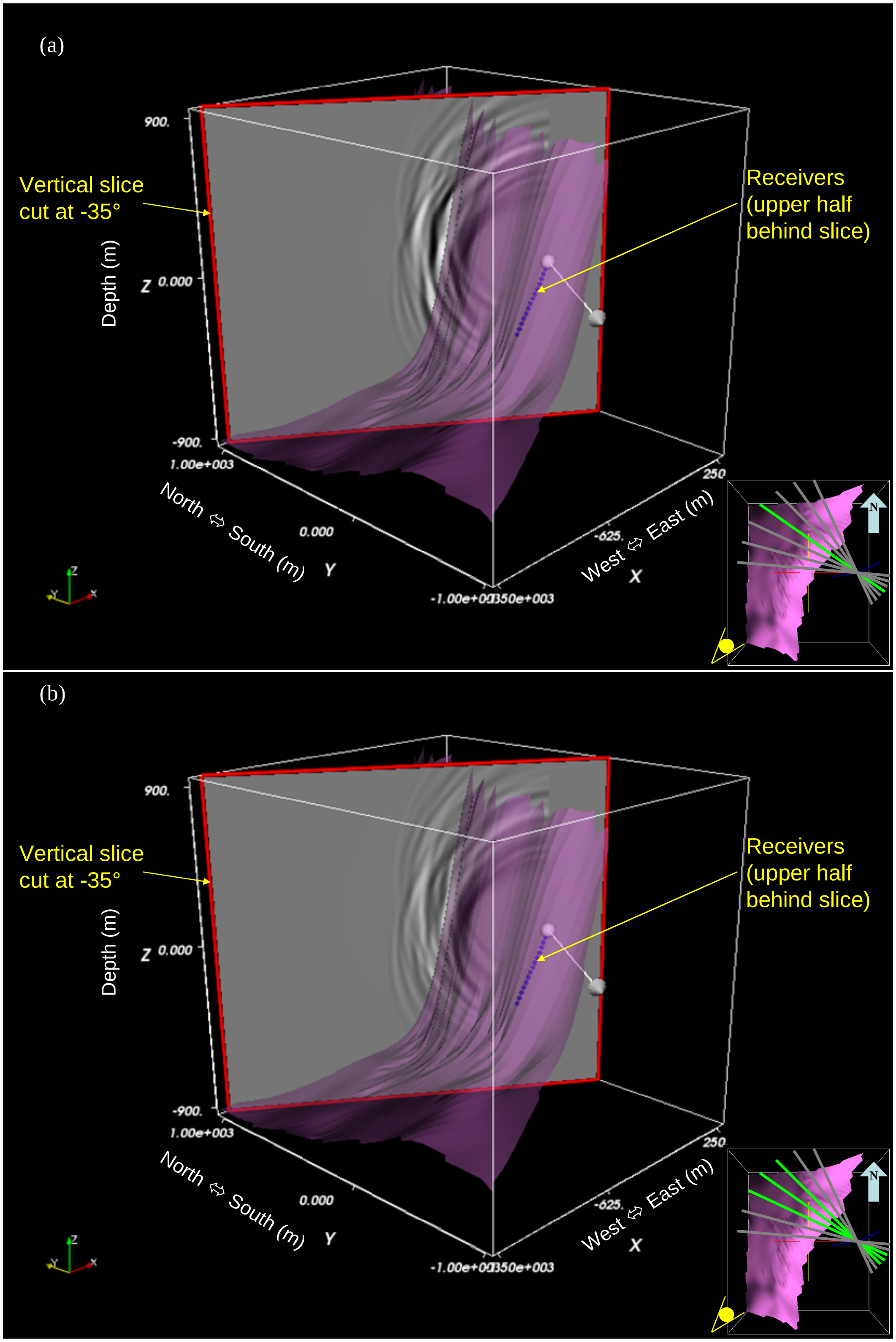
(a)
Vertical slice
cut at -35°
Receivers
(upper half
behind slice)
Depth (m)
Z
900.
0.000
-900.
1.00e+003
North ⇔ South (m)
Y
0.000
-1.00e+003
-1350e+003
West ⇔ East (m)
X
-625.
250
N
(b)
Vertical slice
cut at -35°
Receivers
(upper half
behind slice)
Depth (m)
Z
900.
0.000
-900.
1.00e+003
North ⇔ South (m)
Y
0.000
-1.00e+003
-1350e+003
West ⇔ East (m)
X
-625.
250
N

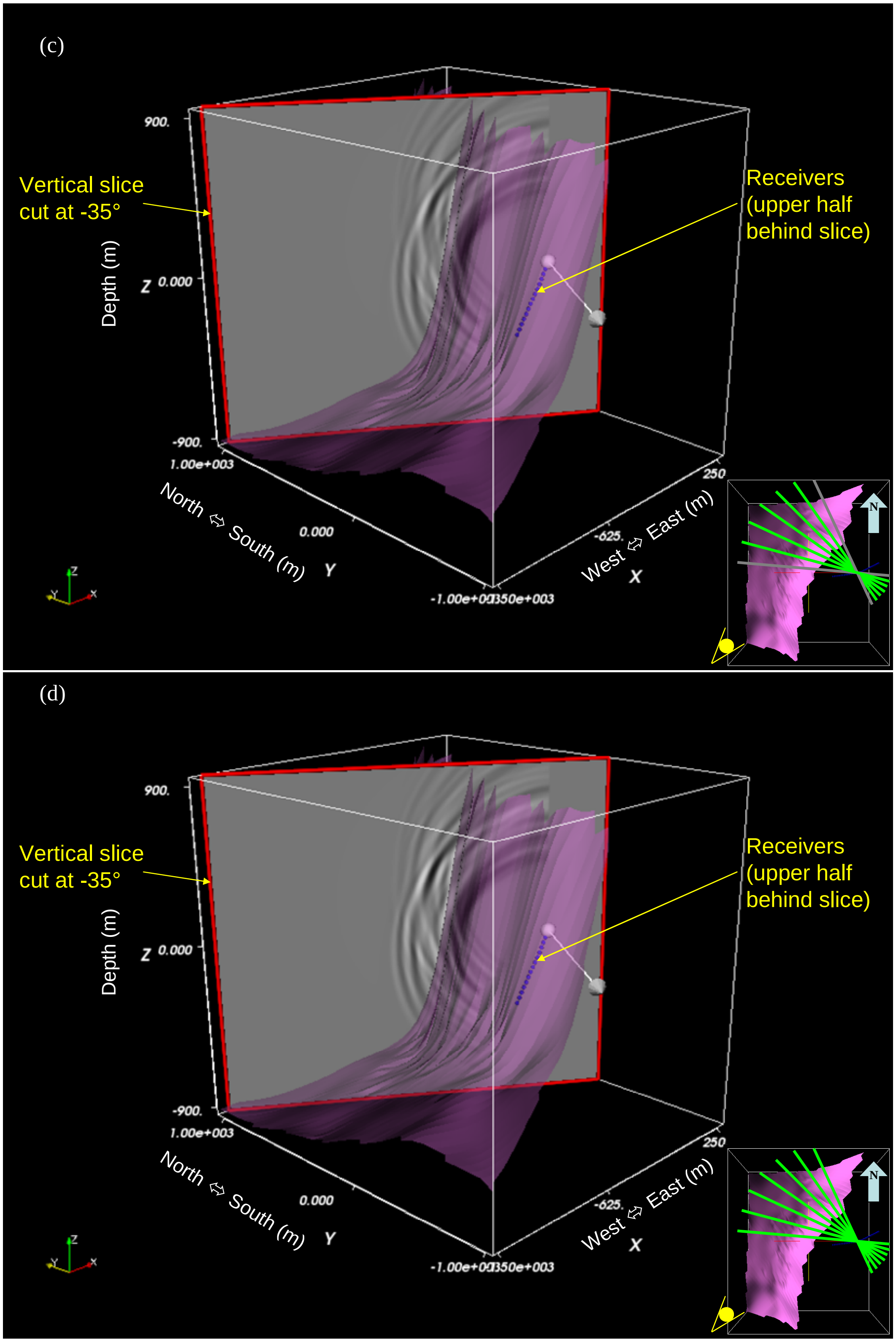


Figure 5-28: Vertical plane cut at imaging direction of –35° in sub-stacked volumes migrated using inline component after applying spiking deconvolution: (a) –35° wedge only; (b) –45°, –35° and –25° wedges; (c) –55°, –45°, –35°, –25° and –15° wedges; (d) –65°, –55°, –45°, –35°, –25°, –15° and –5° wedges.

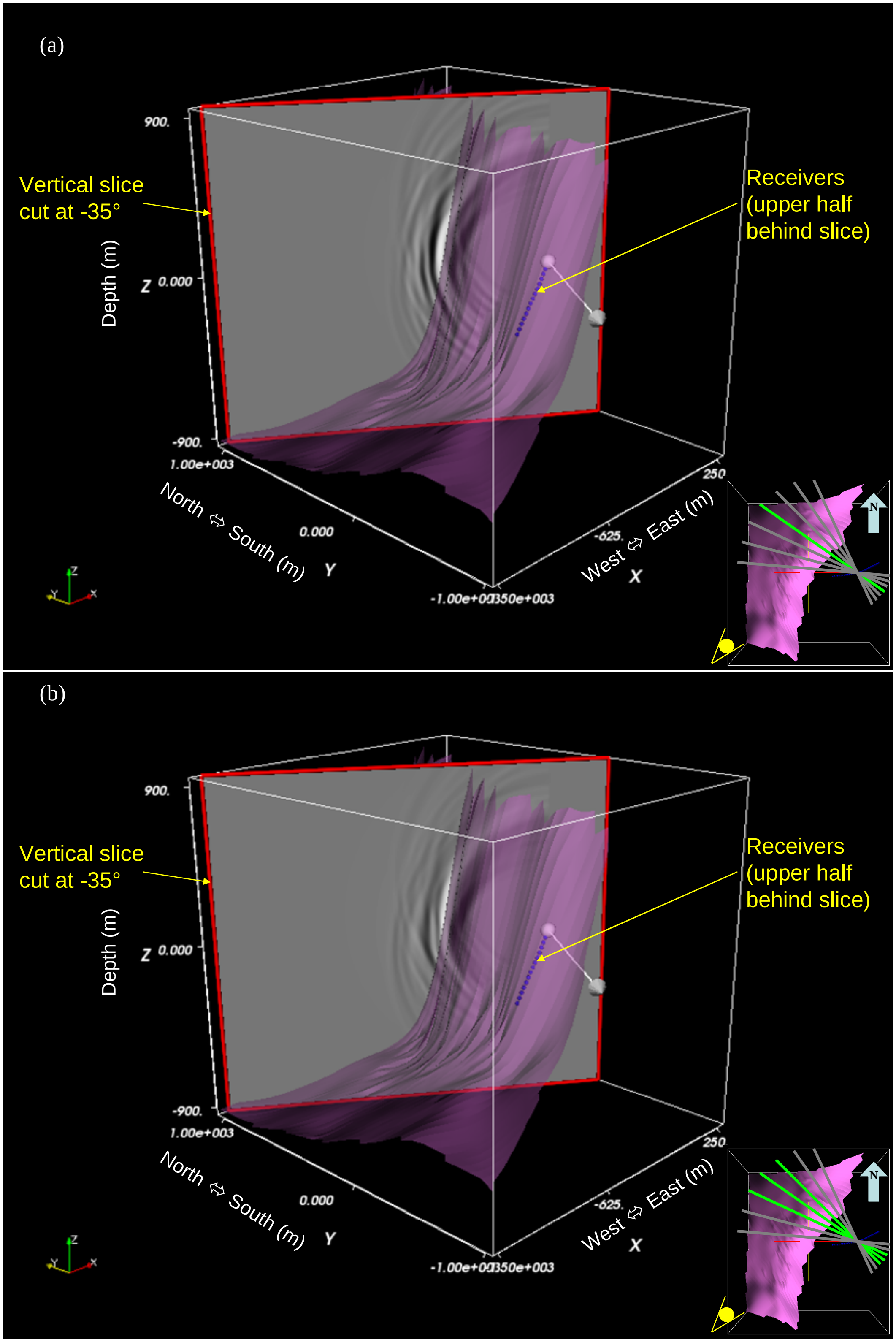
(a)
Vertical slice
cut at -35°
Receivers
(upper half
behind slice)
Depth (m)
Z 0.000
900.
-900.
1.00e+003
North ⇔ South (m) Y
0.000
-1.00e+003
350e+003
West ⇔ East (m) X
-625.
250
N
(b)
Vertical slice
cut at -35°
Receivers
(upper half
behind slice)
Depth (m)
Z 0.000
900.
-900.
1.00e+003
North ⇔ South (m) Y
0.000
-1.00e+003
350e+003
West ⇔ East (m) X
-625.
250
N

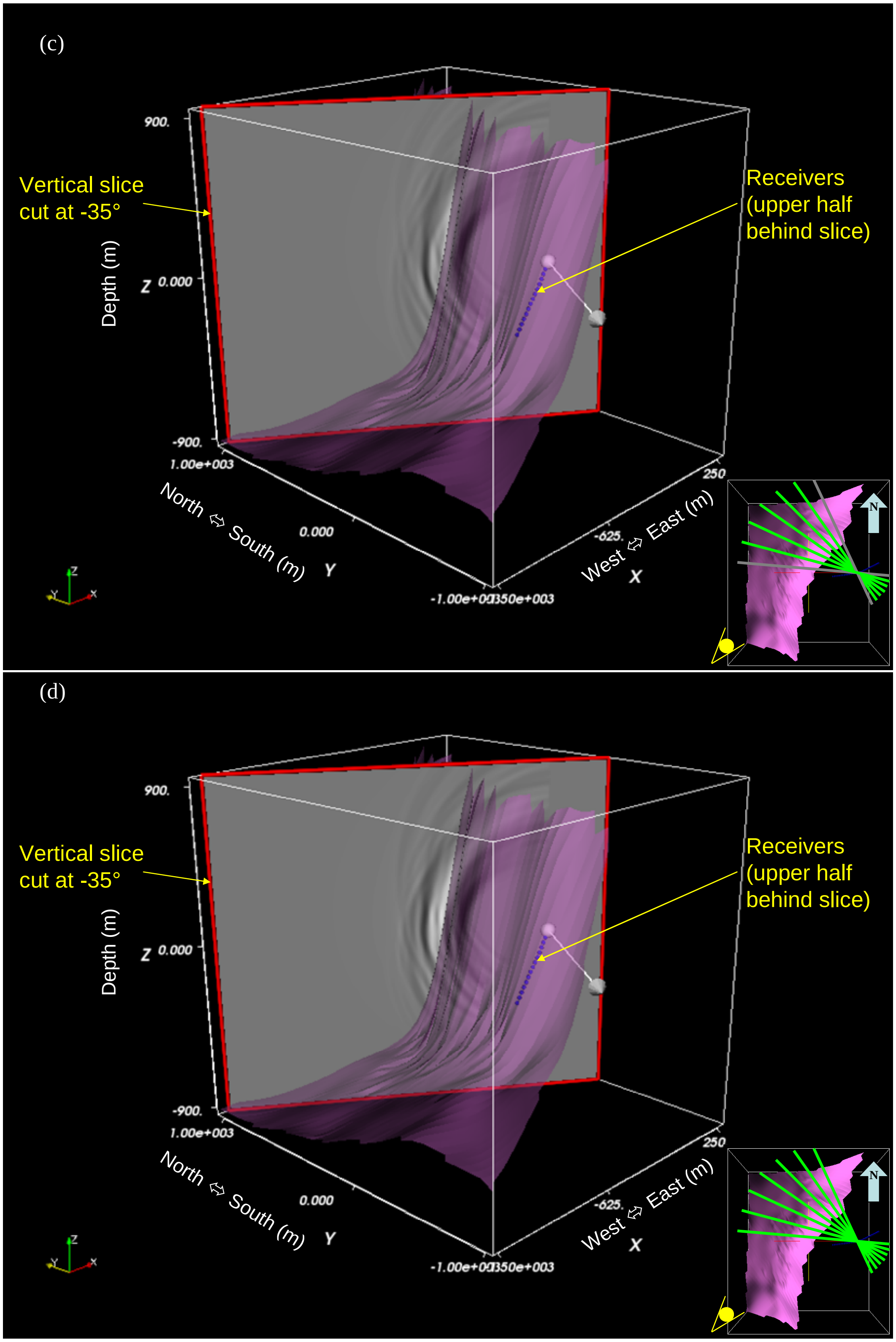


Figure 5-29: Vertical plane cut at imaging direction of –35° in sub-stacked volumes migrated using vertical component after applying spiking deconvolution: (a) –35° wedge only; (b) –45°, –35° and –25° wedges; (c) –55°, –45°, –35°, –25° and –15° wedges; (d) –65°, –55°, –45°, –35°, –25°, –15° and –5° wedges.

### 5.5.2 Effect of Increasing Wedge Width

To further determine the optimal size of the wedges to use, we look at increasing the size of a single wedge itself. We increase the wedge width gradually while keeping the preferred imaging direction unchanged. We start with a 10° wedge centered at –35°, rotate H1 and H2 components into inline (along –35°) and cross-line components, redatum shots that falls into that wedge, and migrate the redatumed virtual shot gathers. This result is the one shown in previous section. Then we increase the wedge width to 20°, 30°, 40°, 50°, and 60°, and repeat the above imaging processes. The comparisons of the results are shown in Figure 5-30 for inline component and Figure 5-31 for vertical component. By increasing the width of the wedge, the output results from the inline components appear to have more artifacts and more noise. As we found before when we stacked the wedges in the previous section, the wedge width seems to have less impact on the vertical component image, which is probably due to the reason that the vertical is has not been rotated in this experiment and hence there is no directivity involved in this component.

From these studies, it appears that for this dataset separately redatuming and migrating a series of 10° wedges provides the sharpest images of the salt flank reflection. By merging together small angular swaths of these individually processed wedges into a 3D volume we obtain the best quality images.

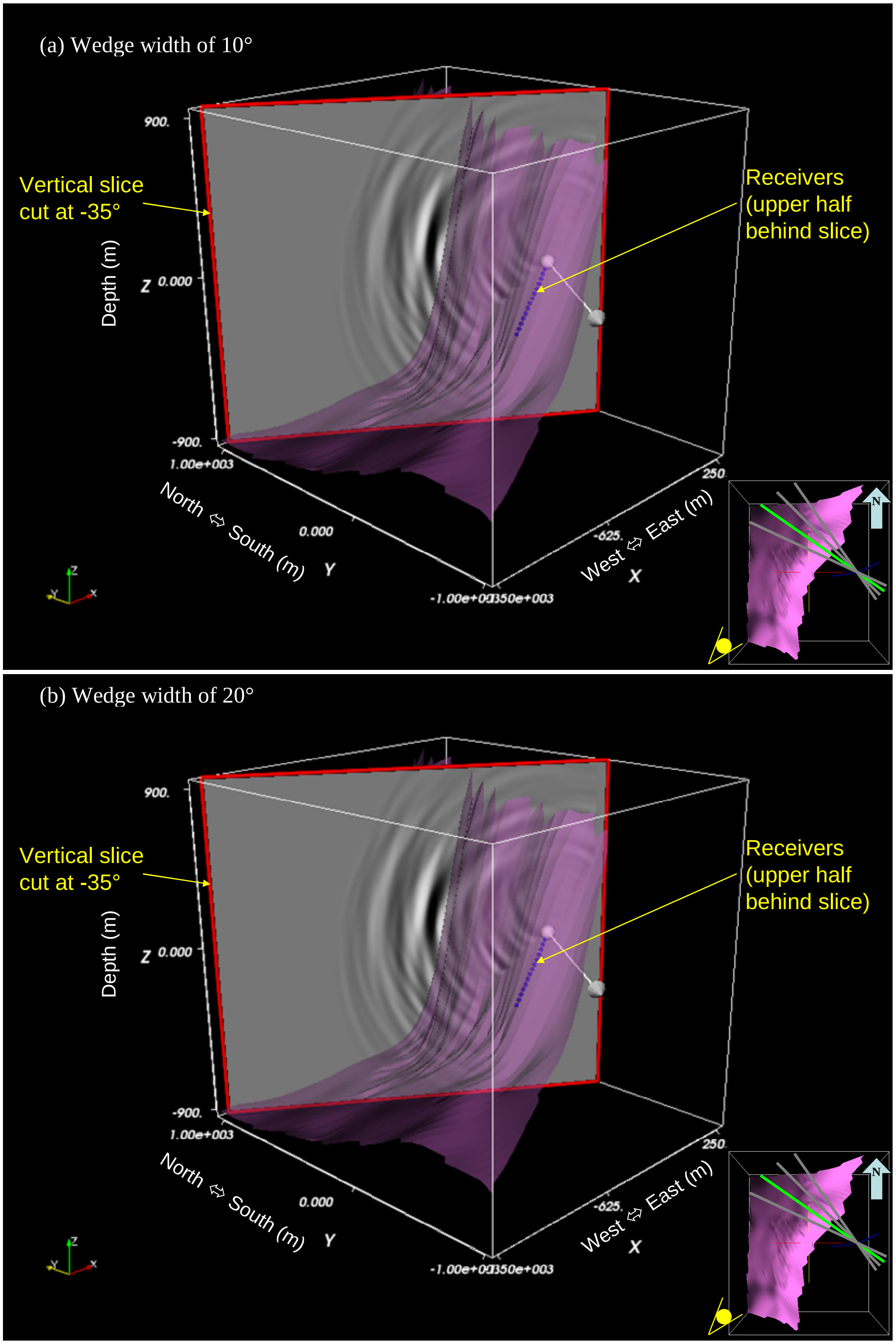
(a) Wedge width of 10°
Vertical slice cut at -35°
Receivers (upper half behind slice)
Depth (m)
Z 0.000
900.
-900.
1.00e+003
North ⇔ South (m)
0.000
Y
-1.00e+003
350e+003
-625.
250.
West ⇔ East (m)
X
N
(b) Wedge width of 20°
Vertical slice cut at -35°
Receivers (upper half behind slice)
Depth (m)
Z 0.000
900.
-900.
1.00e+003
North ⇔ South (m)
0.000
Y
-1.00e+003
350e+003
-625.
250.
West ⇔ East (m)
X
N

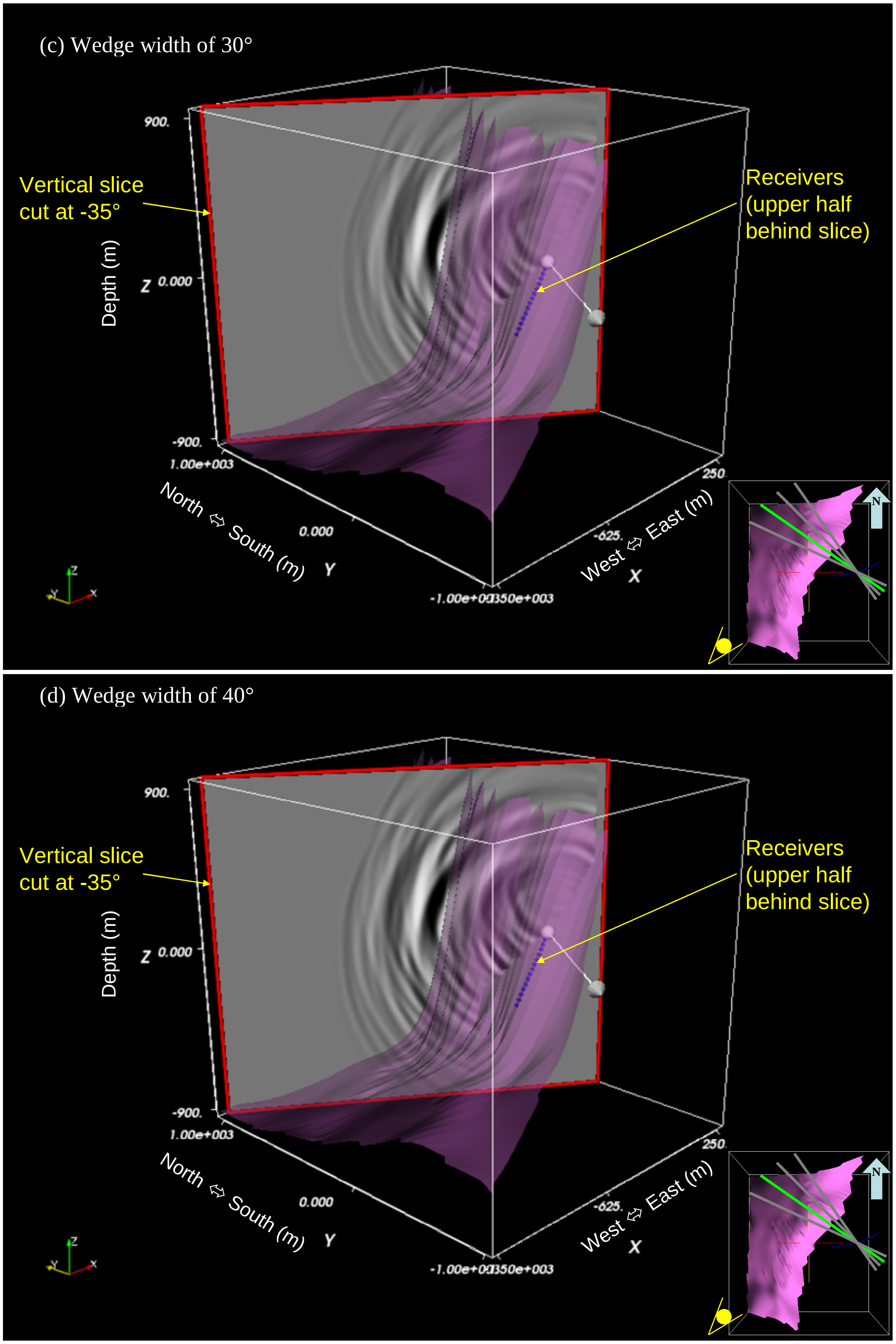
(c) Wedge width of 30°
Vertical slice
cut at -35°
Receivers
(upper half
behind slice)
Depth (m)
Z 0.000
900.
-900.
1.00e+003
North ⇔ South (m) Y
0.000
-1.00e+003
350e+003
West ⇔ East (m) X
-625.
250.
(d) Wedge width of 40°
Vertical slice
cut at -35°
Receivers
(upper half
behind slice)
Depth (m)
Z 0.000
900.
-900.
1.00e+003
North ⇔ South (m) Y
0.000
-1.00e+003
350e+003
West ⇔ East (m) X
-625.
250.

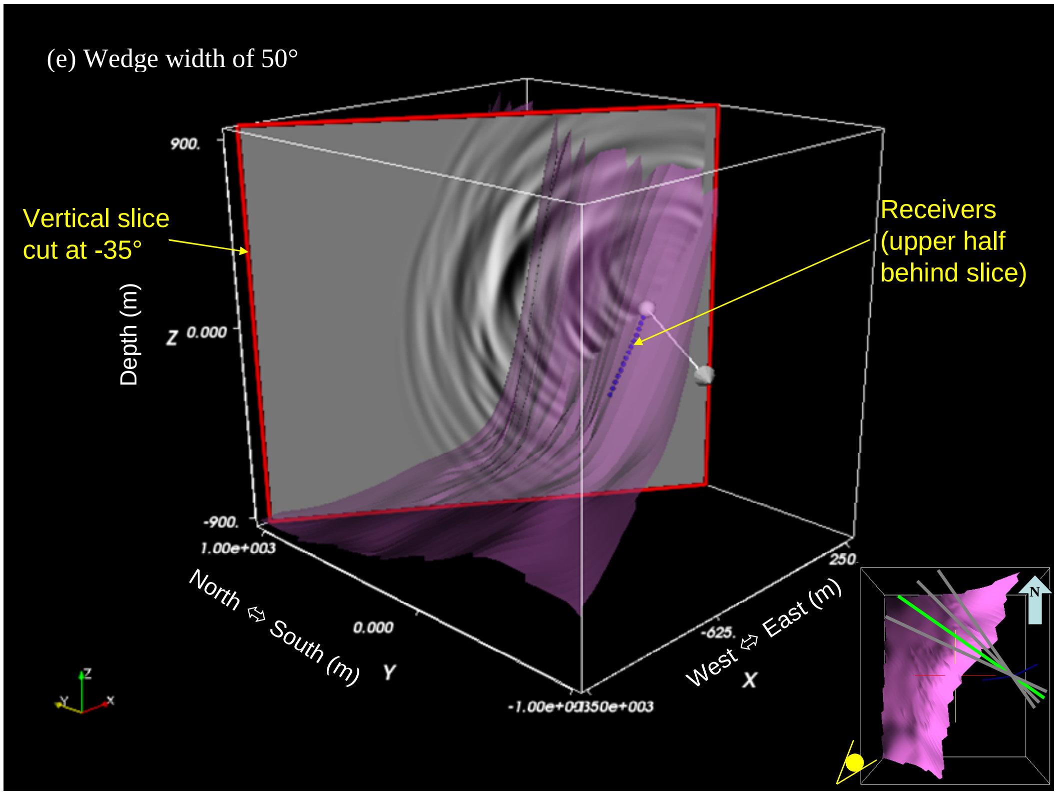


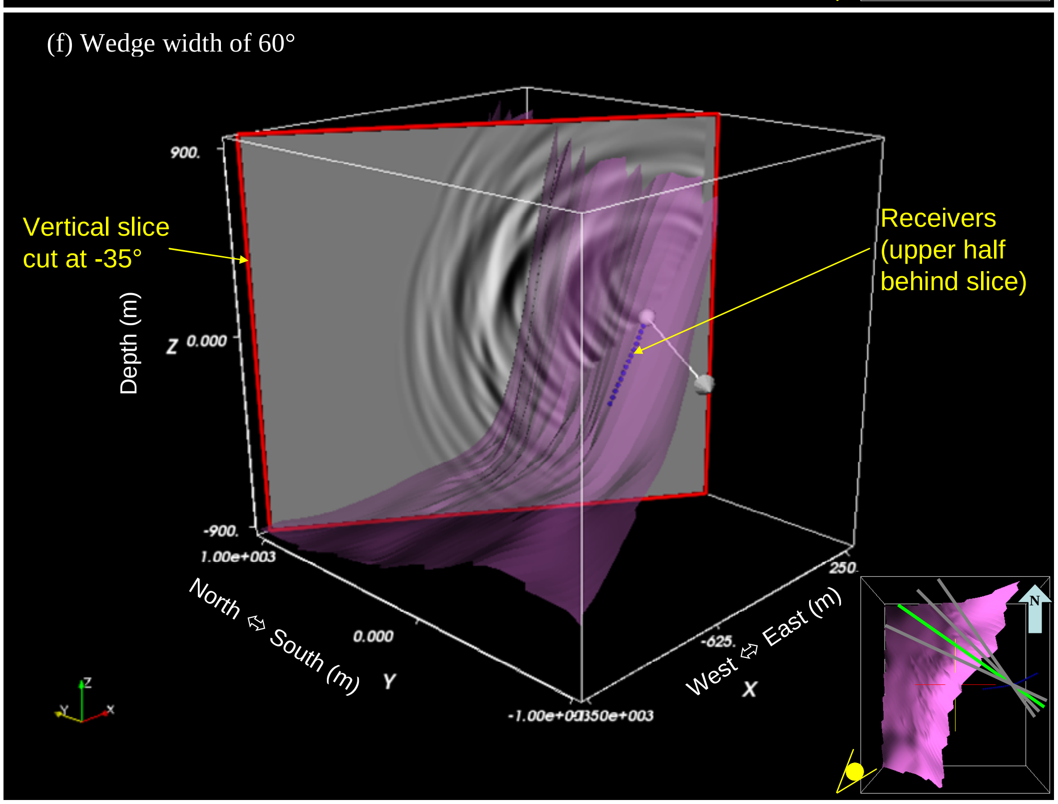


Figure 5-30: Images at –35° in migrated volumes using the shot gathers created from inline components of surface shots located within a wedge of angle: (a) –30° to –40°; (b) –25° to –45°; (c) –20° to –50°; (d) –15° to –55°; (e) –10° to –60°; (f) –5° to –65°.

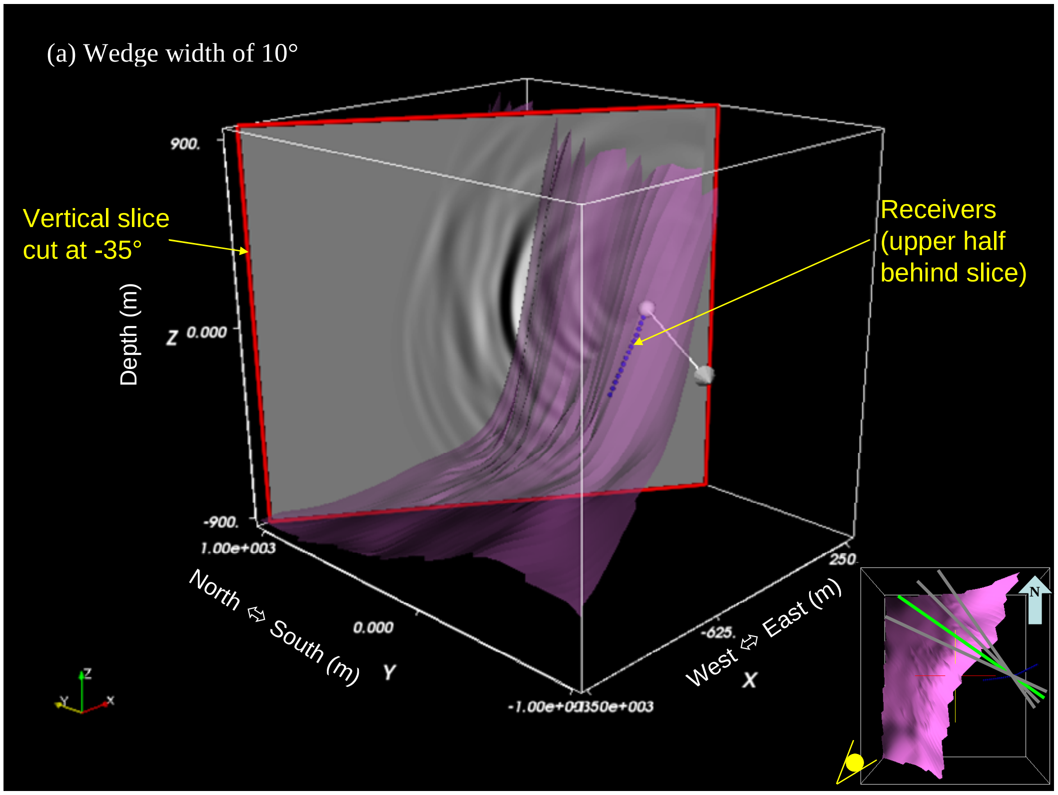
(a) Wedge width of 10°
Vertical slice
cut at -35°
Receivers
(upper half
behind slice)
Depth (m)
Z 0.000
900.
-900.
1.00e+003
North ⇔ South (m)
0.000
Y
-1.00e+003
-350e+003
-625.
250.
West ⇔ East (m)
X
N

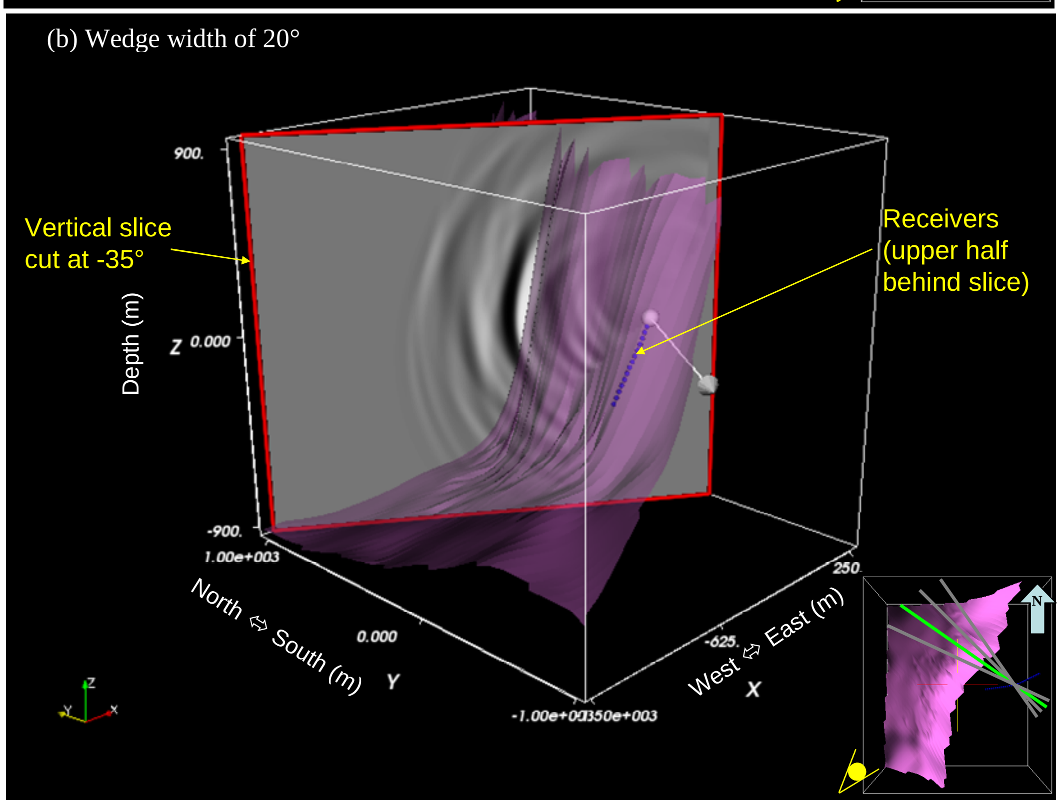
(b) Wedge width of 20°
Vertical slice
cut at -35°
Receivers
(upper half
behind slice)
Depth (m)
Z 0.000
900.
-900.
1.00e+003
North ⇔ South (m)
0.000
Y
-1.00e+003
-350e+003
-625.
250.
West ⇔ East (m)
X
N

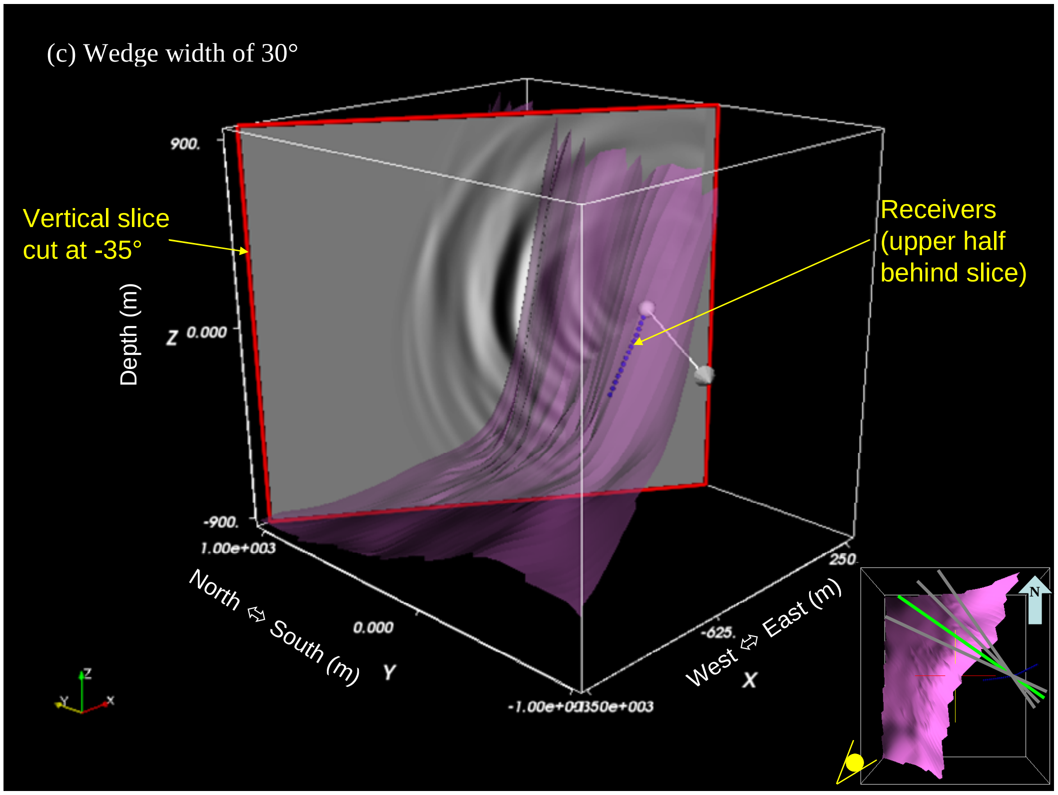
(c) Wedge width of 30°
Vertical slice
cut at -35°
Receivers
(upper half
behind slice)
Depth (m)
Z 0.000
900.
-900.
1.00e+003
North ⇔ South (m)
Y
0.000
-1.00e+003
350e+003
-625.
250.
West ⇔ East (m)
X
N

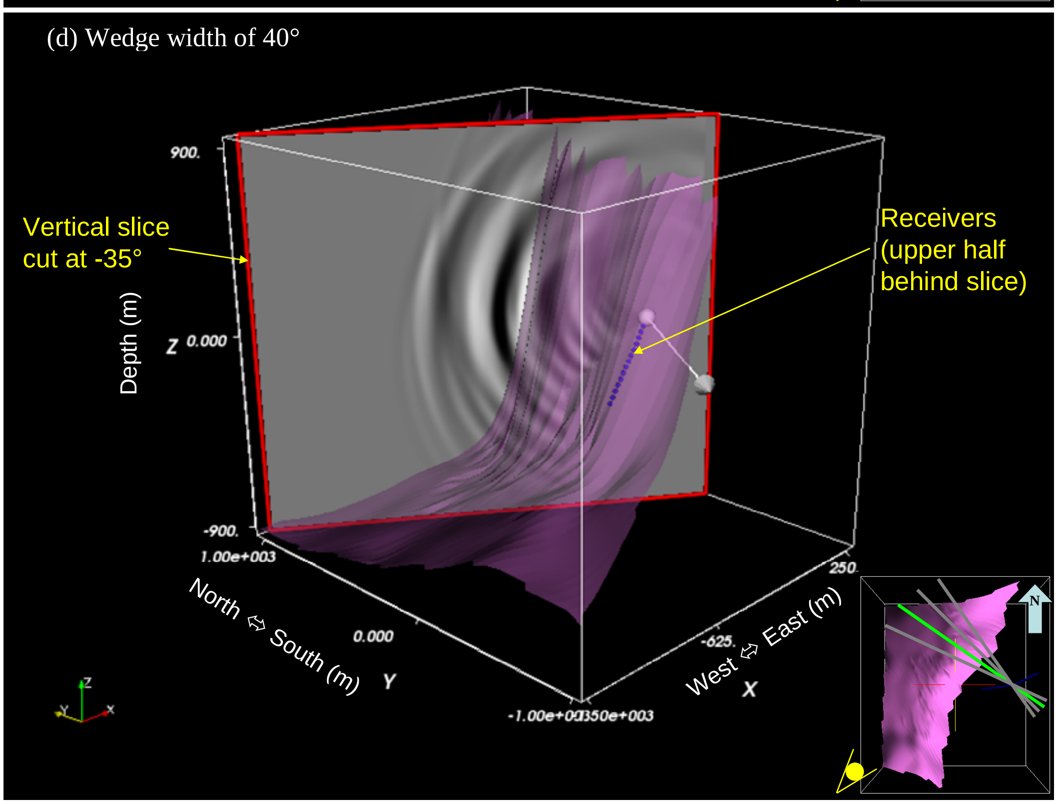
(d) Wedge width of 40°
Vertical slice
cut at -35°
Receivers
(upper half
behind slice)
Depth (m)
Z 0.000
900.
-900.
1.00e+003
North ⇔ South (m)
Y
0.000
-1.00e+003
350e+003
-625.
250.
West ⇔ East (m)
X
N

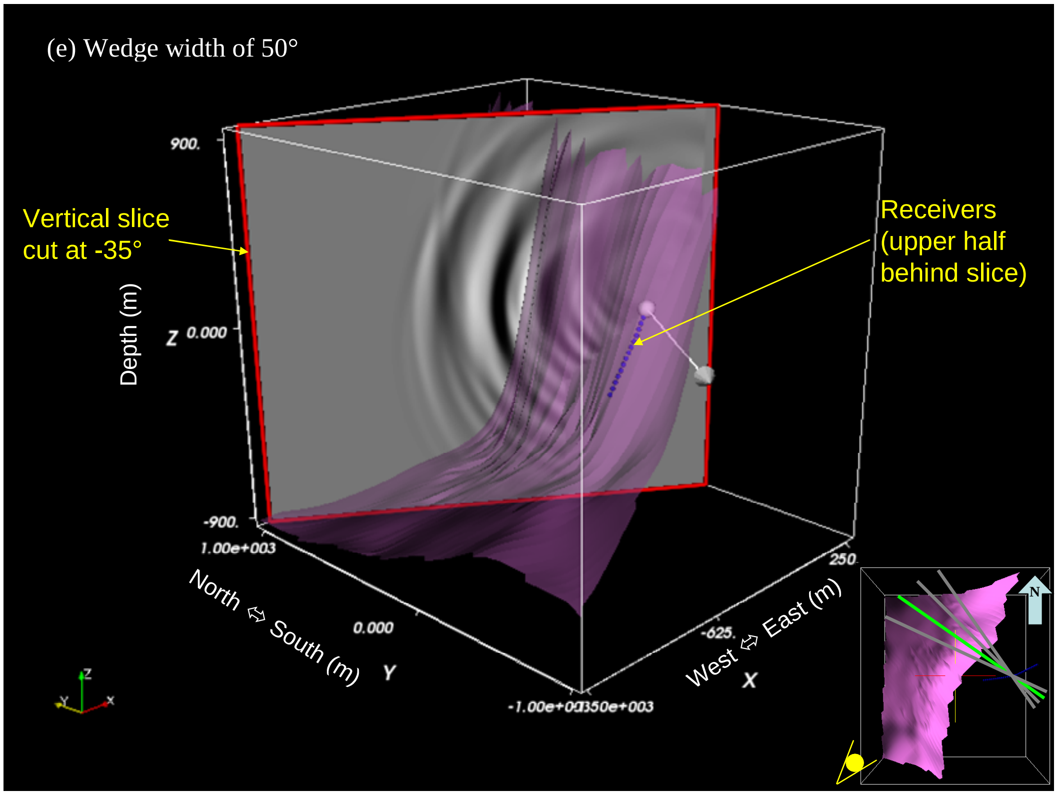


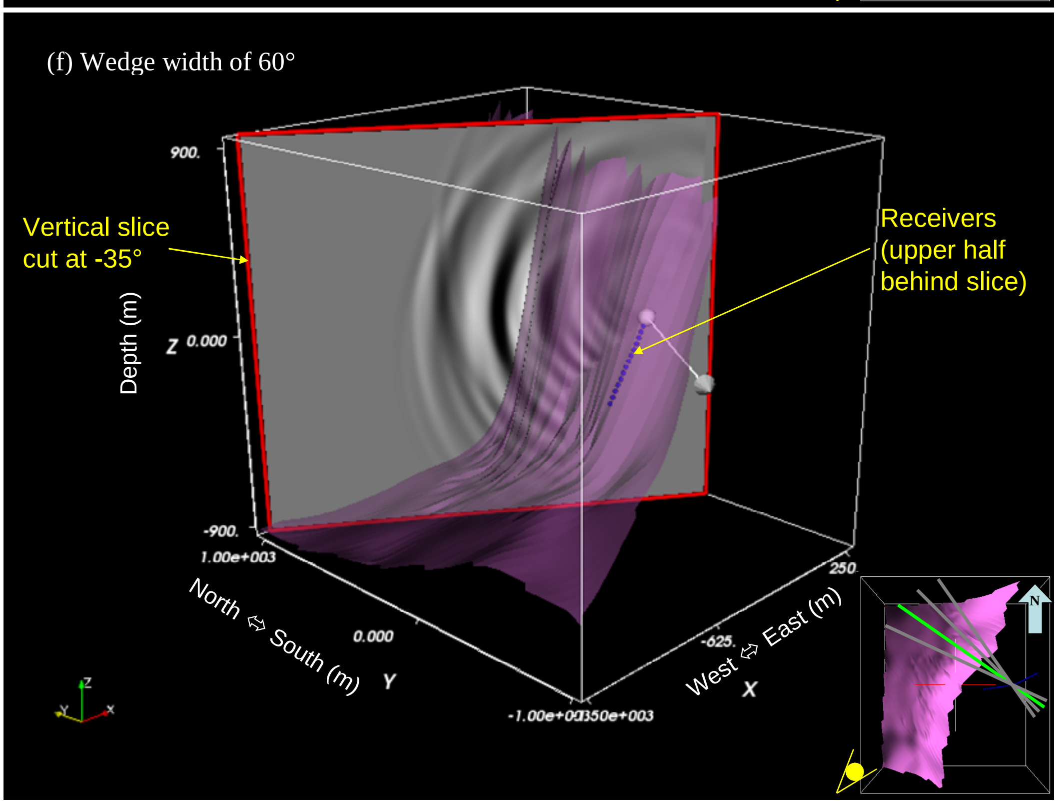


Figure 5-31: Images at –35° in migrated volumes using the shot gathers created from vertical components of surface shots located within a wedge of angle: (a) –30° to –40°; (b) –25° to –45°; (c) –20° to –50°; (d) –15° to –55°; (e) –10° to –60°; (f) –5° to –65°.

### 5.5.3 Comparison to Prestack VSP Migration Results

We next compare the virtual source images to the results obtained from more conventional 3D prestack depth migration of the preprocessed VSP data. We first select the sets of shots we wish to use for the migration. Figure 5-32 shows the wedges we used for the virtual source analysis numbered from 1 to 12. The wedges used for the VSP migrations are shown in darker orange. Figure 5-33 shows a bandpass filtered VSP record from the center of each of wedges 1 through 12. We see it is difficult to identify the salt flank reflections in this raw data section in contrast to the virtual source gathers in Figure 5-16 where the salt reflection is clearly separated.

We migrated two different sets of VSP data, one using shots within wedges #5 through #8 defined in Figure 5-32, and the other one using shots within wedge #0. Wedge #0 is new for this study and is defined as shots with offsets less than 5,000 ft (1524 m) and azimuths between –90° and +30°. Wedge #0 should provide a mostly vertical view of the sediments, whereas the other wedges may provide the salt flank imaging.

To perform a VSP migration, we first create a 1D sediment velocity model by averaging two velocity profiles extracted from the velocity model of the field provided by Shell as shown in Figure 5-34. We used a 1D velocity profile to simplify the migration process which would have required large quantities of disk space to store the travel time tables or snap shots of the wave field if we have used a 2- or 3D velocity field. It also demonstrates the value of the virtual source technology where we only require a single velocity to image the salt flank for this dataset. Then we apply conventional Kirchhoff prestack depth migration using this 1D model and image the 3D volume around the downhole geophones.

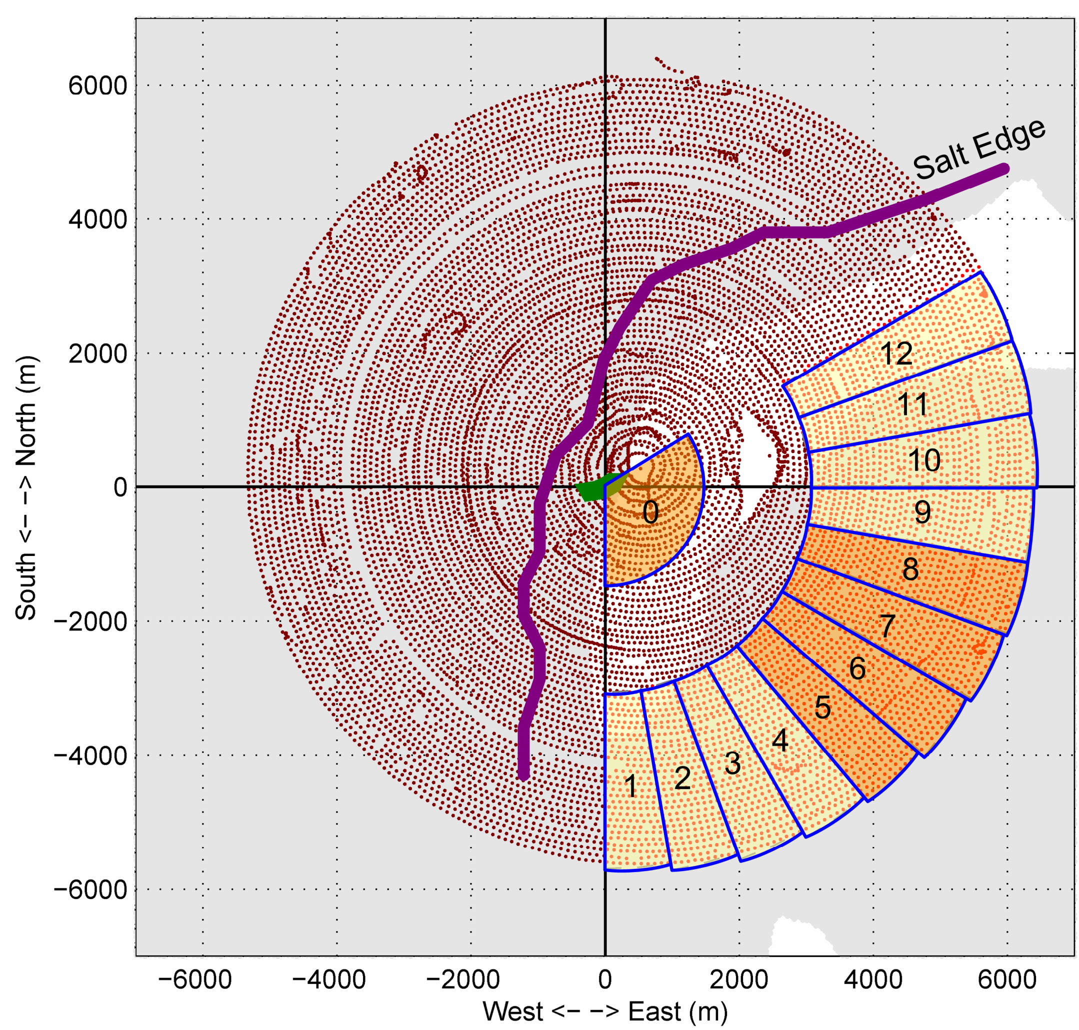


Figure 5-32: Map view of the wedges used in the VSP migration – far offset wedge #5, #6, #7, #8 and near offset wedge #0.

For wedges #5 through #8, we migrate each wedge separately, and show them in Figure 5-35. Then we stack all the 4 wedges together and show the result in Figure 5-36a. As a comparison, the migration result using only near offset shots in wedge #0 is shown in Figure 5-36b. In Figure 5-35 and Figure 5-36 we have added green volumes which are thresholded values from the 3D image. They show the highest amplitude reflections in the migrated volume, indicating the lateral extent of the imaged sediments. The migrated VSP images in Figure 5-35 and Figure 5-36, have failed to image the salt edge, but provide images of sediments next to the well.

If we believe our virtual source derived images of the salt flank, then the reflections of the salt flank must be contained in the raw VSP records. With more careful muting (or gating) and f-k filtering it may be possible to extract the salt reflections from the raw records and then migrate them with conventional prestack depth migration. However, the value that we see from the virtual source process is that none of this careful muting or filtering is needed in order to image the salt flank and you don’t need a velocity model for the overburden.

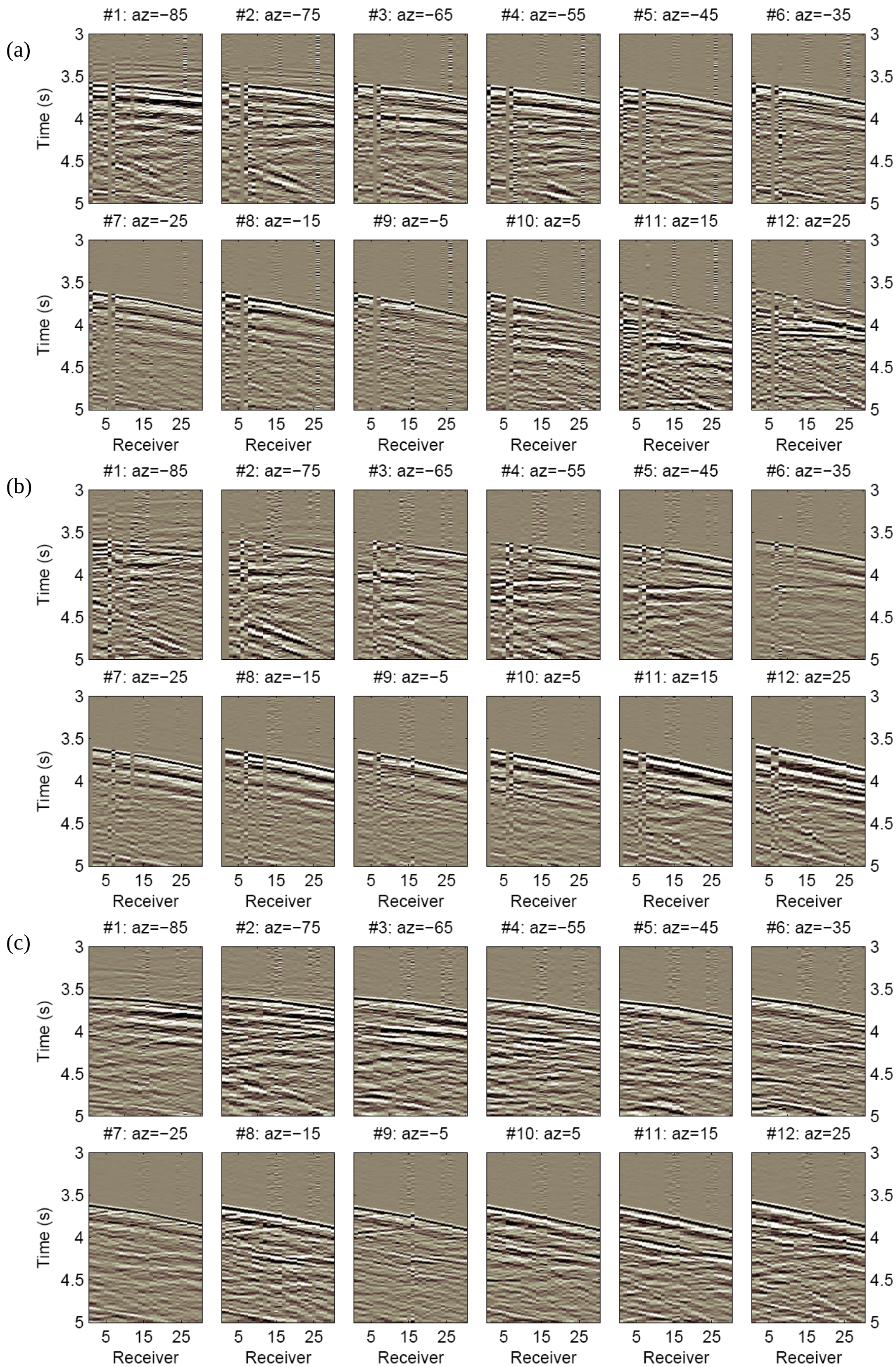


Figure 5-33: VSP common shot gathers from all wedges for a shot at the center of each wedge: (a) H1; (b) H2; (c) vertical.

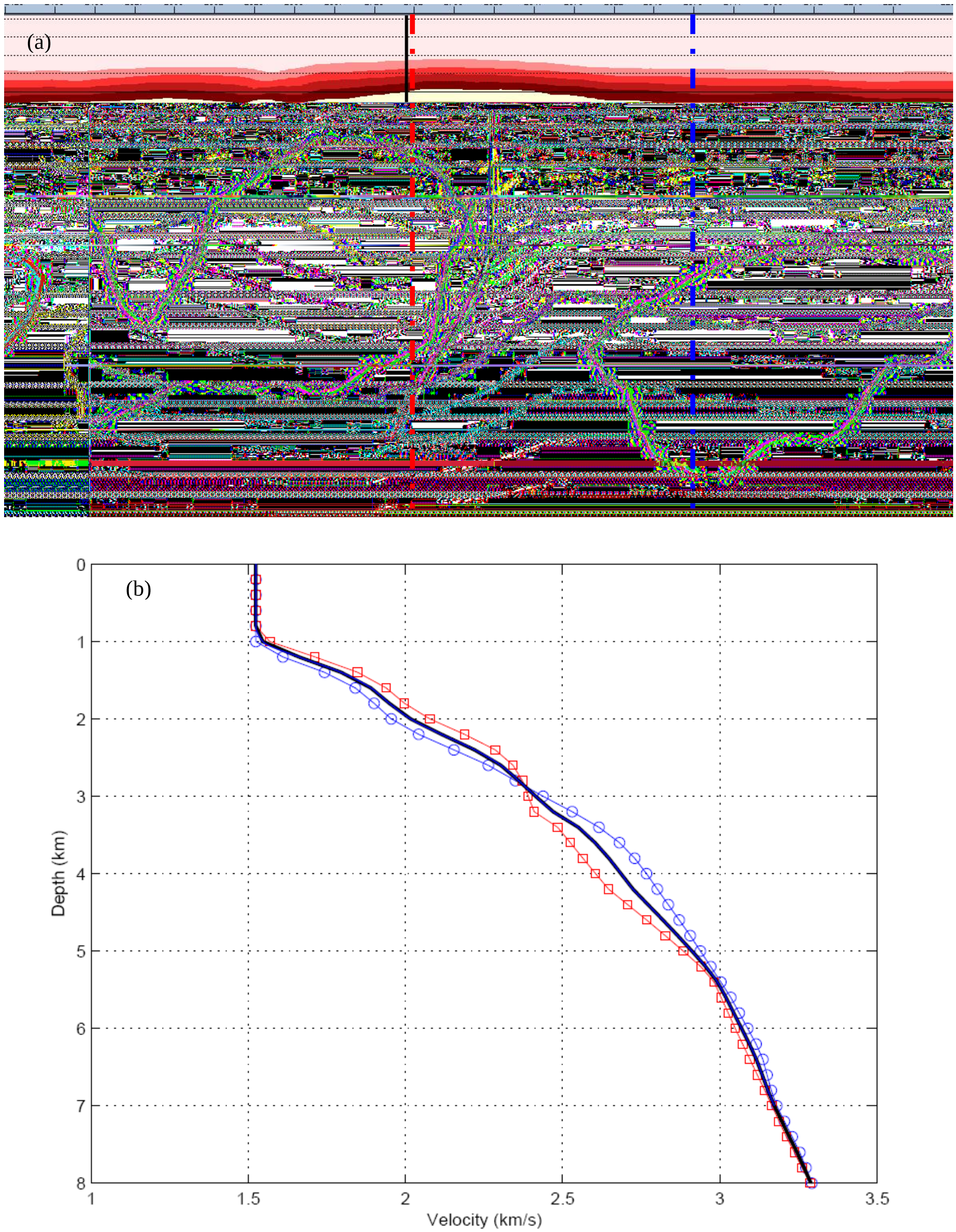


Figure 5-34: (a) Velocity model along a traverse across the field. Two vertical profiles are extracted at positions marked by the blue and red dashed line. (b) Velocity profiles at the two extracted position (in blue and red) and the average (in black) are used as the 1D velocity model to create the travel time table for VSP migration.

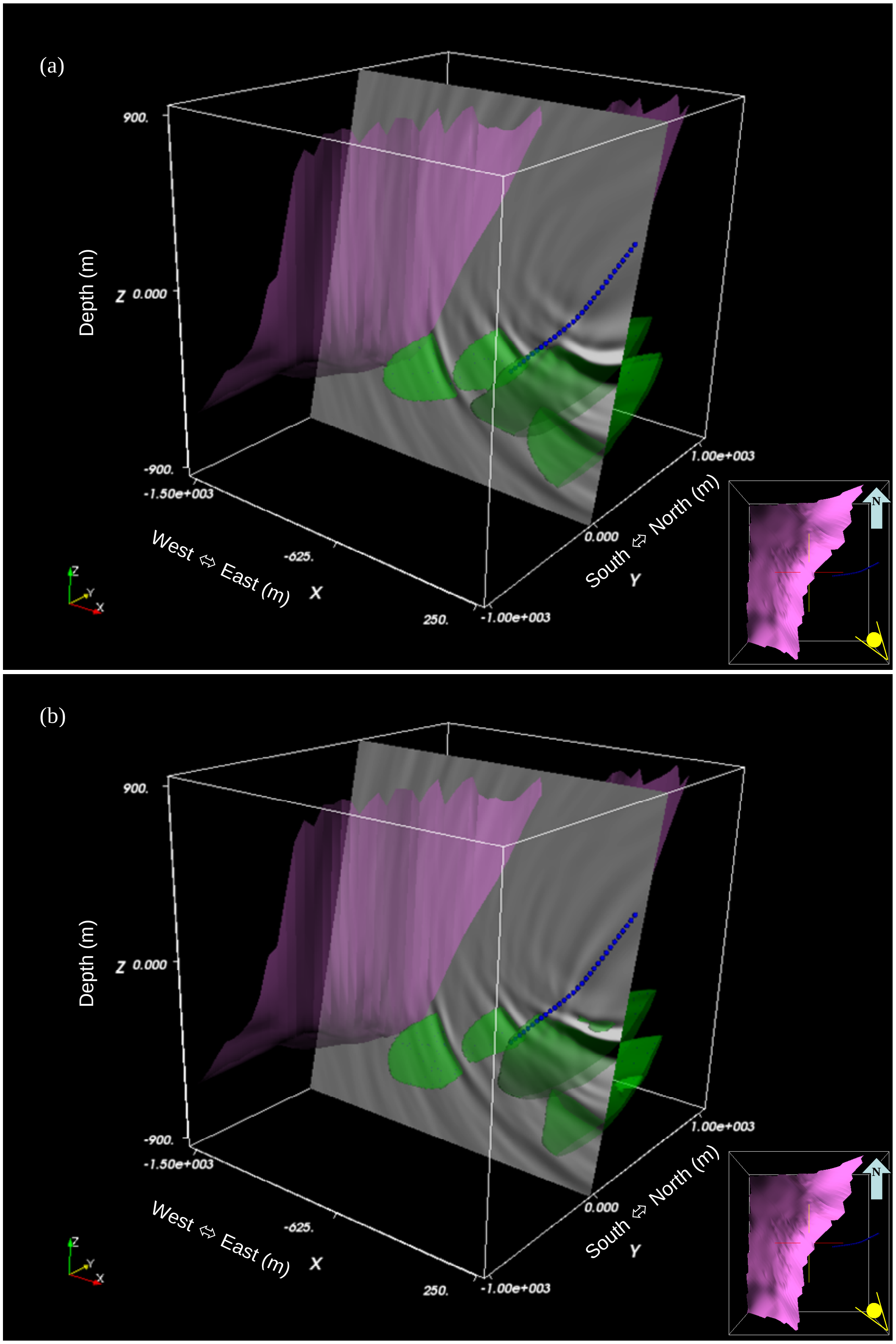
(a)
900.
Z 0.000
Depth (m)
-900.
-1.50e+003
West ⇔ East (m) X
-625.
250.
-1.00e+003
0.000
South ⇔ North (m)
Y
1.00e+003
N
(b)
900.
Z 0.000
Depth (m)
-900.
-1.50e+003
West ⇔ East (m) X
-625.
250.
-1.00e+003
0.000
South ⇔ North (m)
Y
1.00e+003
N

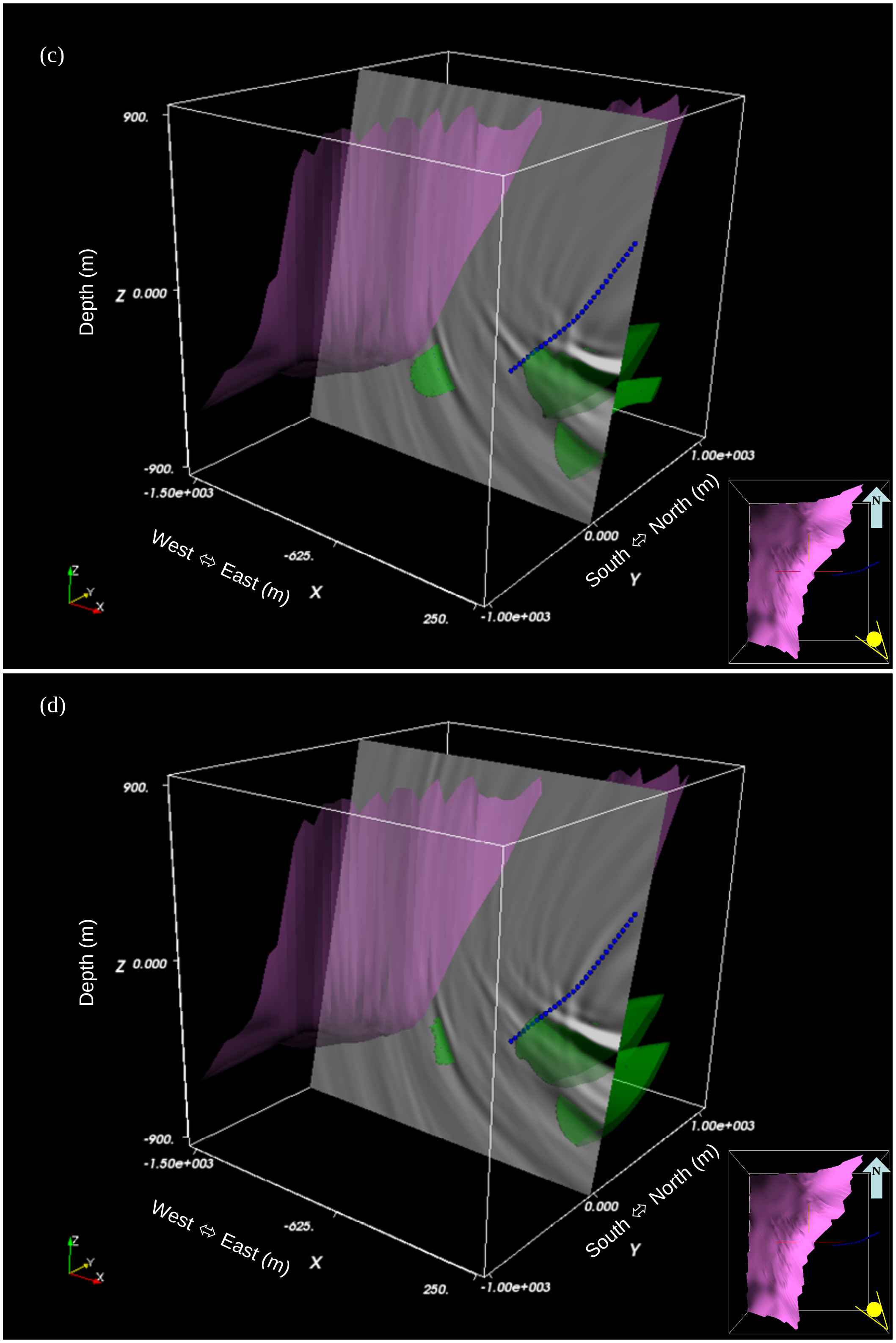


Figure 5-35: Traverse across the receivers in the migrated volume using the vertical component of the raw VSP data for shots located within wedge (a) –50° and –40°, (b) –40° and –30°, (c) –30° and –20°, (d) –20° and –10°. A total of about 300 shots are migrated in each wedge.

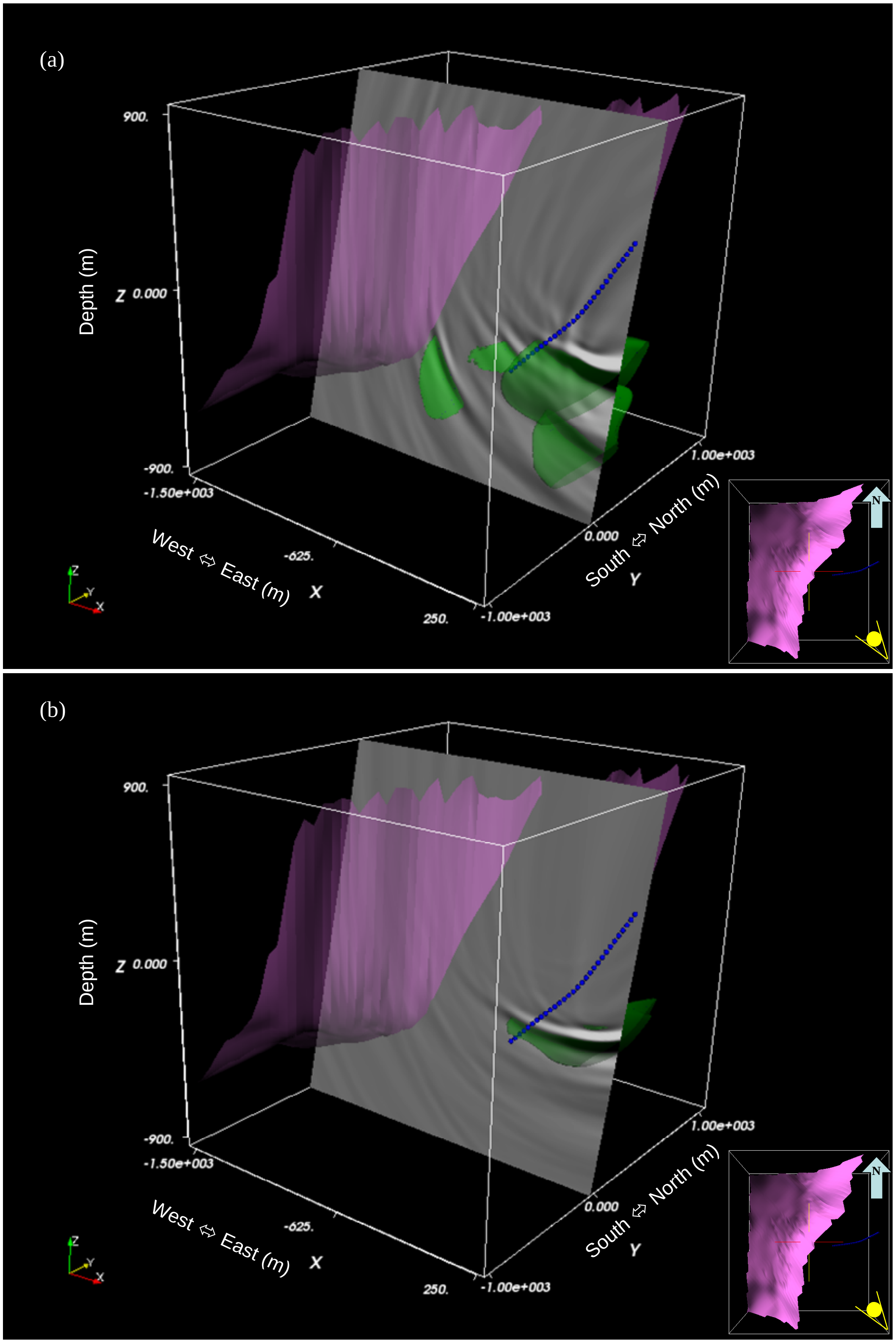


Figure 5-36: Comparison of traverse across the receivers in the migrated volume using the vertical component of the raw VSP data for shots located (a) at far offset larger than 10 kft and azimuths from –50° to –10°, (b) at near offset less than 5 kft and azimuths from –90° to +40°.

## 5.6 Summary and Recommendations

In the chapter we detail the results of our TRA-based redatuming and prestack depth migration of a field 3D VSP data for imaging the eastern side of the salt dome flank. With band pass filtering and trace killing we are able to increase the overall signal to noise ratio of the data. We verify that the horizontal components are oriented within a reasonable tolerance of the nominal specifications for the gimbaled geophone array. Simple ray tracing and hodogram analyses show that only the east/southeast shots should contribute reflected energy off of the salt dome flank to the redatumed shot records.

Twelve wedge shaped bins of shot gathers on the south-east side of the field are created which are defined to be 10 degrees wide with respect to the surface expression of the midpoint of the receiver array. In addition, the wedges only contain shots which are over 10,000 ft away from the surface expression of the midpoint of the receiver array.

We use a Kirchhoff prestack depth migration developed in-house to migrate the redatumed shot gathers. This algorithm was previously used to migration the synthetic data with great success. However, because the migration velocity chosen for this dataset is a constant 9,000 ft/sec, which is sufficiently accurate in this study, the migration is equivalent to a prestack time migration.

The effectiveness of each data preparation step and aperture selection is performed by first redatuming the selected shots and then prestack depth migrating the resulting redatumed virtual shot gathers. Tests show reduced migration artifacts are obtainable by applying a two-sided mute which isolates the salt flank reflection on the redatumed gathers. Several aperture tests are run which reveal that the best images are obtained by restricting the contribution of each wedge of shot gathers to the imaging space in the 3D output volume in a similar 10º wedge on the opposite side of the down hole receivers from the shot gathers. The final image is then created by merging the results from the migration of each wedge separately, for their corresponding 10º output wedges.

Tests show that separate migrated images from the inline horizontal and vertical components yield similar quality images of the salt flank. Given a vertical salt flank, if the ray paths from the shots were in fact truly horizontal at the depth of the receiver array, then we would have expected that the inline horizontal image would be far superior to the vertical component image. There would be no P-wave energy on the vertical component for rays arriving horizontally. Since this is not what we observe, then the shots in this survey are still too close to produce full upward turning ray energy. This also means that the deeper geophones will not be capable of being used as virtual sources since they will not be able to "emit" energy upwards to be eventually captured by the upper receivers.

We find that increased resolution of the migrated image can be obtained by performing spiking deconvolution on the redatumed virtual shot gathers before migration. In this study we use a simple algorithm to implement the deconvolution. More advanced methods may show further improvements. Even better results may be obtainable if the spiking deconvolution is applied before the redatuming step.

The final migration shows that the salt flank is located about 640 m away from the receiver array. This is about 80 m farther away from the borehole than was previously interpreted from the surface seismic data. This result is very consistent with previous study at the same field given uncertainties on positioning of steep events from surface seismic data. The best image seems to be on -35º output image slice. This corresponds to the predicted best illumination direction. However, the image is limited in the vertical extent to be about 300 m tall. This is so small because of the limited aperture of 29 downhole geophones. Significantly better resolution and a larger vertical image would likely be possible if there were 60 or more downhole geophones. This additional aperture will further reduce the migration sweeps and artifacts in the image. Simple ray tracing from the receiver array to the measured salt flank distance in the migrated image and back to the receiver array overlays on the redatumed shot records which confirms the validity of the image.

As a final test, we prestack depth migrate the VSP data from their original shot locations using a simple 1D velocity model. The migrated VSP images produce good horizontal sediment reflections but fail to reproduce the salt flank obtained from the redatumed virtual shot records. In some ways this is perplexing because both methods start with exactly the same input data – the VSP shot records. However, the difference is the requirement for the full velocity field from the surface down to the salt dome for the prestack migration of the VSP data. It may still be possible to mute and filter the VSP records to isolate the salt flank reflection energy. With this additional work an improved image of the salt flank might be obtainable from prestack depth migrating the carefully processed VSP records. On the other hand, the redatumed, virtual source records only require a simple model of the velocity field from the receiver array to the salt flank (a distance of only about 700 m) and no specialized preprocessing or f-k velocity filtering.

From this study we make three suggestions for future virtual source surveys for salt flank imaging. First, it seems probable that the number of surface VSP shot locations could be drastically reduced. In order to image the salt flank near the well bore, only shots collected in a spread of azimuths on the sediment side of the salt dome need to be collected (e.g. wedges 3-10 in Figure 32). Of course a traditional VSP near the well bore and/or a walk above VSP is always important to acquire for velocity determination. Second, additional geophone levels need to be collected to allow for a larger imaging aperture. This could either be from a longer tool array, or a short array which is moved and the survey re-shot. Third, a more complete image might be obtained with data recorded in additional monitoring wells. These additional VSP records could be collected in side tracks of the same well. In many cases there may not be a nearby well to increase the image quality. But there is always the chance of increasing the vertical aperture by moving the receiver array and re-shooting the survey. For this survey, the reduced number of surface shot positions would have probably paid for the effort of moving up the tool to get more geophone levels.

# Chapter 6

# Summary

The objective of this thesis is to investigate the applications of Time Reversed Acoustics (TRA) to two problems: locating seismic sources and imaging subsurface structures. The basic concept in TRA is the time symmetry embedded in the wave equation. In TRA experiments, one first records the sound wave during forward propagation at an enclosed boundary surrounding the medium, and then reinjects the recorded time-reversed signal at the boundary. The energy will back-propagate through the medium and focus on the original source location.

The back-propagation time frame can be divided into the acausal time domain (before focus) and the causal time domain (after focus) separated by the "time-zero", which is the time when the focus is formed. The acausal time domain denotes the period during which the time-reversed waves injected into the medium are back-propagating and forming the focus. In the causal time domain, the focused energy accumulated at "time-zero" will act as a pseudo source at the focal spot. It develops a wavefield that propagates in a positive time axis as if there were a physical source at that focal point. Studying the acausal process of TRA enables us to locate the source, such as an earthquake, inside a medium. The causal domain allows us to create a new datum through the TRA-based redatuming operators, which is the key to bypassing complex overburdens without knowledge of its properties, and then imaging the subsurface structures, such as salt flanks.

We demonstrate TRA's focusing characteristics and its applicability for earthquake location using a synthetic 3D elastic model that is abstracted from an actual reservoir field. A point source is first excited at the location inside the field. All the receivers record the 3C seismograms for a period of time that is long enough for the generation of both P and S waves. Then, the seismograms (without gating for different phases) are time-reversed and injected back at the receiver locations as sources. At the end of the input signal, snapshots of the wavefield are captured and interpreted. Results show a clean and clear focal spot at the original source location. Different monitoring schemes are tried to test the TRA focusing quality and resolution. Then we experiment using real data acquired in the same field. Both results show that TRA is able to resolve the source location with sparse monitoring stations, within the tolerance of artifacts. The station separation for a cost-effective network is related to the closest distance between two neighboring events. A meaningful future work in this application is to develop a complete uncertainty analysis tool for location using TRA techniques. The sensitivity of the retro-focusing with respect to the velocity perturbation needs to be investigated to fully demonstrate the capability of this technique. It is also interesting to study whether this technique can be extended to a tele-seismic scale in which the stations are typically clustered irregularly on the surface.

In some circumstances where the lateral location of the earthquake is well-constrained while the depth is poorly determined, one can estimate the focal depth with little effort by using TRA combined with the *empirical Green's function*. This is particularly valuable in focal depth estimation for shallow earthquakes where the primary phase and surface related phases are usually mixed in the coda wave. Using the *empirical Green's function* simplifies the back-propagation procedure into an autocorrelation operation. The autocorrelation of the source signal can be recovered by summing all the autocorrelations of the seismograms recorded at the monitor station array. This recovered signal will show a significant peak at a time delay that corresponds to the free surface reflection. By determining this time delay, we can estimate the focal depth assuming an average velocity above the source. We test this methodology on five real seismic events. The focal depth values estimated using TRA analysis are close to the depth values provided by other independent studies. Future work in this application includes a more elegant and complete uncertainty analysis of the estimated focal depth by incorporating the errors in the velocity model and in the method assumptions. It would also be interesting to perform the field test with much larger sample events such that a statistical fitness of the method can be obtained.

By extrapolating seismic data to a new datum in the subsurface, the effects of the complex near-surface region can be minimized. The physical measurement of the wave field at the new datum allows for the introduction of novel redatuming techniques, based on the principles of TRA and source receiver reciprocity. We present an acoustic redatuming strategy for imaging the salt dome flank when there is an obscuring salt canopy present in the immediate area. The first step of the strategy performs a redatuming of a walk-away VSP data set so that we obtain effective downhole shot gathers. Redatuming the shots allows us to move our perspective closer to the salt flank. Then we apply two passes of prestack depth migration. The use of a reverse-time algorithm, using the two-way wave equation for the second pass, allows us to image both the salt dome edge and the dipping sediments. The method is target oriented and is at least three times faster than a comparable imaging effort on the original walk-away VSP data. It also eliminates the need for iterative depth migrations to reveal the complex overburden. The final image we obtain of the salt edge and the dipping sediments, while not as complete as the walk-away VSP results, provides a short cut method to obtain a comparable image. As with all migration algorithms, the proposed method requires an adequate acquisition aperture to capture the salt dome and sediment reflections. The accuracy of the final image is also dependent on the accuracy of the target-oriented velocity model just as with other migration algorithms.

We then modify this acoustic redatuming method and imaging method for elastic data. Because the solution is posed in terms of wavefield potentials, spatial derivatives of the P- and S-wave fields are approximated directly by additional field acquisition effort. The redatuming step is cast as a sum of the contributions from P- and S-wave sources. We apply this methodology on a 2D elastic model composed of a simplified Gulf of Mexico vertical velocity gradient and an embedded overhanging salt dome. Our results show that the reconstructed elastic responses between downhole receivers are a good approximation of the actual elastic responses obtained by putting of sources in the bore hole. By applying acoustic migration on single components of the entire elastic response, we obtain four independent images of the salt flank and sediments. These four images provide full P- and S-wave characteristics of the reservoir, providing new reservoir analysis tools. Additional work on wavefield separation may allow a reduction in field effort to a more conventional P- and S-wave acquisition effort.

We apply this TRA-based redatuming strategy followed by prestack depth migration to a 3D field VSP dataset provided by Shell International Exploration and Production Inc. The data consists of 15,632 surface shots acquired in concentric circles around the well head containing 29 (live) subsurface geophones. The salt flank geometry in the vicinity of the well is a complex 3D structure which is only partially defined on surface seismic images. We create a 3D directional imaging strategy where the surface VSP shots are grouped into 10° wedges based on azimuth between the shot and the geophone. Then we rotate the horizontal geophone components within each wedge to effectively steer the illumination direction of the pseudo source created by the TRA-based redatuming. The limited number of geophone levels restricts the quality of the final image to a narrow, 300 meter high portion of the salt flank. The distance from the receiver array to the salt flank, extracted from the final image, is about 640 meters, which is about 80 meters farther than the distance interpreted from surface seismic data. The TRA-based redatuming methodology is particularly appropriate for such a complex problem because it does not require any knowledge of the velocity structure between the surface shots and the downhole receivers. In addition, the salt flank reflections are easily seen on the resulting virtual shot gathers. In contrast, prestack-depth-migrating raw VSP records does not produce any identifiable salt flank image.

# References


Aki, K., and P. G. Richards, 1980, Quantitative Seismology: Theory and Methods: WH Freeman.

Alexander, S. S., 1996, A new method for determining source depth from a single regional station: *Seismic Res. Ltrs*, **67**, 63.

Aminzadeh, F., J. Brac, and T. Kunz, 1997, 3-D Salt and Overthrust Models: SEG/EAGE 3D Modeling Series No. 1: Society of Exploration Geophysicists.

Bakulin, A., and R. Calvert, 2004, Virtual source: new method for imaging and 4D below complex overburden: *SEG Technical Program Expanded Abstracts*, **23**, 2477-2480.

Bakulin, A., and R. Calvert, 2005, Virtual Shear Source: a new method for shear-wave seismic surveys: *SEG Technical Program Expanded Abstracts*, **24**, 2633-2636.

Bakulin, A., and R. Calvert, 2006, The virtual source method: Theory and case study: *Geophysics*, **71**, SI139-SI150.

Bakulin, A., A. Mateeva, K. Mehta, P. Jorgensen, J. Ferrandis, I. S. Herhold, and J. Lopez, 2007, Virtual source applications to imaging and reservoir monitoring: *The Leading Edge*, **26**, 732-740.

Baysal, E., D. D. Kosloff, and J. W. C. Sherwood, 1983, Reverse time migration: *Geophysics*, **48**, 1514-1524.

Berkhout, A. J., 1997, Pushing the limits of seismic imaging, Part I: Prestack migration in terms of double dynamic focusing: *Geophysics*, **62**, 937-953.

Berryhill, J. R., 1979, Wave-equation datuming: *Geophysics*, **44**, 1329-1344.

Berryhill, J. R., 1984, Wave-equation datuming before stack: *Geophysics*, **49**, 2064-2066.

Bevc, D., 1997, Imaging complex structures with semirecursive Kirchhoff migration: *Geophysics*, **62**, 577-588.

Biondi, B., and G. Shan, 2002, Prestack imaging of overturned reflections by reverse time migration: *SEG Technical Program Expanded Abstracts*, **21**, 1284-1287.

Bonner, J. L., D. T. Reiter, and R. H. Shumway, 2002, Application of a Cepstral F Statistic for Improved Depth Estimation: *Bulletin of the Seismological Society of America*, **92**, 1675-1693.

Borcea, L., G. Papanicolaou, C. Tsogka, and J. Berryman, 2002, Imaging and time reversal in random media: *Inverse Problems*, **18**, 1247-1279.

Calvert, R., A. Bakulin, and T. Jones, 2004, Virtual sources, a new way to remove overburden problems: *66th Annual International Meeting, EAEG, Expanded Abstracts*, 234-237.

Cavalca, M., and P. Lailly, 2005, Prismatic reflections for the delineation of salt bodies: *SEG Technical Program Expanded Abstracts*, **24**, 2550-2553.

Claerbout, J., 1976, Fundamentals of Geophysical Data Processing: McGraw Hill.

Coates, R., M. Kane, C. Chang, C. Esmersoy, M. Fukuhara, and H. Yamamoto, 2000, Single Well Sonic Imaging: High-Definition Reservoir Cross-Sections from Horizontal Wells: *SPE/Petroleum Society of CIM*, 65457.

Daley, T. M., E. L. Majer, R. Gritto, and J. M. Harris, 2000, Progress and issues in single well seismic imaging: *SEG Technical Program Expanded Abstracts*, **19**, 1552-1555.

de Hoop, A. T., 1995, Handbook of radiation and scattering of waves: Academic Press: London.

Delsanto, P. P., P. A. Johnson, M. Scalerandi, and J. A. TenCate, 2002, LISA simulations of time-reversed acoustic and elastic wave experiments: *Journal of Physics D Applied Physics*, **35**, 3145-3152.

Derode, A., E. Larose, M. Campillo, and M. Fink, 2003, How to estimate the Green's function of a heterogeneous medium between two passive sensors? Application to acoustic waves: *Applied Physics Letters*, **83**, 3054-3056.

Derode, A., A. Tourin, and M. Fink, 2000, Limits of time-reversal focusing through multiple scattering: Long-range correlation: *The Journal of the Acoustical Society of America*, **107**, 2987.

DiSiena, J. P., J. E. Gaiser, and D. Corrigan, 1981, Three component VSP - orientation of horizontal components for shear wave analysis: *51st Annual SEG Meeting*.

Draeger, C., D. Cassereau, and M. Fink, 1997, Theory of the time-reversal process in solids: *The Journal of the Acoustical Society of America*, **102**, 1289.

Draganov, D., K. Wapenaar, and J. Thorbecke, 2006, Seismic interferometry: Reconstructing the earth's reflection response: *Geophysics*, **71**, SI61-SI70.

Draganov, D., K. Wapenaar, and J. Thorbecke, 2007, Green's function retrieval by crosscorrelating deterministic transient source responses: application to ultrasonic data: *The Journal of the Acoustical Society of America*, Accepted.

Feuillade, C., and C. S. Clay, 1992, Source imaging and sidelobe suppression using time-domain techniques in a shallow-water waveguide: *The Journal of the Acoustical Society of America*, **92**, 2165.

Fink, M., 1999, Time-reversed acoustics: *Scientific American*, **281**, 91-97.

Fink, M., 2006, Time-reversal acoustics in complex environments: *Geophysics*, **71**, SI151-SI164.

Fink, M., D. Cassereau, A. Derode, C. Prada, P. Roux, M. Tanter, J. L. Thomas, and F. Wu, 2000, Time-reversed acoustics: *Rep. Prog. Phys*, **63**, 1933?1995.

Fletcher, R. F., P. Fowler, P. Kitchenside, and U. Albertin, 2005, Suppressing artifacts in prestack reverse time migration: *SEG Technical Program Expanded Abstracts*, **24**, 2049-2051.

Fortin, J., N. Rehbinder, and P. Staron, 1991, Reflection Imaging Around a Well With the EVA Full-Waveform Tool: *Log Analyst*, **32**, 271-278.

Gray, S. H., 2005, Gaussian beam migration of common-shot records: *Geophysics*, **70**, S71-S77.

Gray, S. H., and W. P. May, 1994, Kirchhoff migration using eikonal equation traveltimes: *Geophysics*, **59**, 810-817.

Guitton, A., B. Kaelin, and B. Biondi, 2006, Least-square attenuation of reverse time migration artifacts: *SEG Technical Program Expanded Abstracts*, **25**, 2348-2352.

Hale, D., N. R. Hill, and J. Stefani, 1992, Imaging salt with turning seismic waves: *Geophysics*, **57**, 1453-1462.

Hardage, B. A., 2000, Vertical Seismic Profiling: Principles: Elsevier Science Ltd.

Hellman, K. J., M. E. Willis, and T. K. Young, 1986, Evaluation of a reverse-time prestack migration algorithm: *SEG Technical Program Expanded Abstracts*, **5**, 330-332.

Hill, N. R., 1990, Gaussian beam migration: *Geophysics*, **55**, 1416-1428.

Hill, N. R., 2001, Prestack Gaussian-beam depth migration: *Geophysics*, **66**, 1240-1250.

Hinkelman, L. M., D. L. Liu, L. A. Metlay, and R. C. Waag, 1994, Measurements of ultrasonic pulse arrival time and energy level variations produced by propagation through abdominal wall: *The Journal of the Acoustical Society of America*, **95**, 530.

Hodgkiss, W. S., H. C. Song, W. A. Kuperman, T. Akal, C. Ferla, and D. R. Jackson, 1999, A long-range and variable focus phase-conjugation experiment in shallow water: *The Journal of the Acoustical Society of America*, **105**, 1597.

Hokstad, K., R. Mittet, and M. Landro, 1998, Elastic reverse time migration of marine walkaway vertical seismic profiling data: *Geophysics*, **63**, 1685-1695.

Holvik, E., and L. Amundsen, 2005, Elimination of the overburden response from multicomponent source and receiver seismic data, with source designature and decomposition into PP-, PS-, SP-, and SS-wave responses: *Geophysics*, **70**, S43-S59.

Hornby, B. E., 1989, Imaging of near-borehole structure using full-waveform sonic data: *Geophysics*, **54**, 747-757.

Hornby, B. E., and J. Yu, 2007, Interferometric imaging of a salt flank using walkaway VSP data: *The Leading Edge*, **26**, 760-763.

Hornby, B. E., J. Yu, J. A. Sharp, A. Ray, Y. Quist, and C. Regone, 2006, VSP: Beyond time-to-depth: *The Leading Edge*, **25**, 446-452.

Hughes, S., and J. H. Luetgert, 1991, Crustal structure of the western New England Appalachians and the Adirondack Mountains: *Journal of Geophysical Research*, **96**, 16471-16494.

Jones, R., and H. Asanuma, 2004a, The tetrahedral geophone configuration: geometry and properties: *SEG Technical Program Expanded Abstracts*, **23**, 9-12.

Jones, R. H., and H. Asanuma, 2004b, Optimal Four Geophone Configuration, Vector Fidelity and Long-Term Monitoring: *66th EAGE Conference*.

Kemerait, R. C., and A. F. Sutton, 1982, A multidimensional approach to seismic event depth estimation: *Geoexploration*, **20**, 113-130.

Korneev, V., and A. Bakulin, 2006, On the fundamentals of the virtual source method: *Geophysics*, **71**, A13-A17.

Kuperman, W. A., W. S. Hodgkiss, H. C. Song, T. Akal, C. Ferla, and D. R. Jackson, 1998, Phase conjugation in the ocean: Experimental demonstration of an acoustic time-reversal mirror: *The Journal of the Acoustical Society of America*, **103**, 25.

Langston, C. A., and D. V. Helmberger, 1975, A procedure for modelling shallow dislocation sources: *Geophys. JR Astr. Soc*, **42**, 117-130.

Larmat, C., J.-P. Montagner, M. Fink, Y. Capdeville, A. Tourin, and E. Clévédé, 2006, Time-reversal Imaging of Seismic Sources- Application to the Sumatra earthquake *Geophysical Research Letters*, **33** L19312.

Levin, S. A., 1984, Principle of reverse-time migration: *Geophysics*, **49**, 581.

Li, X., S. Kuleli, and M. N. Toksoz, 2004, The rupture process of the 1 May 2003 Bingol, Turkey M w 6.4 Earthquake: *Seismological Research Letters*, **74**, 286.

Li, Y., and N. Toksöz, 1993, Study of the source process of the 1992 Ms= 7.3 earthquake with the empirical Green 抯 function method: *Geophys. Res. Letters*, **20**, 1087-1090.

Lu, R., M. Willis, X. Campman, J. Ajo-Franklin, and M. N. Toksöz, 2006, Imaging dipping sediments at a salt dome flank - VSP seismic interferometry and reverse-time migration: *SEG Technical Program Expanded Abstracts*, **25**, 2191-2195.

Lu, R., M. E. Willis, X. Campman, J. Ajo-Franklin, and M. N. Toksoz, 2007, Redatumming through a salt canopy --- Another salt-flank imaging strategy: *SEG Technical Program Expanded Abstracts*, **26**, 3054-3058.

Majer, E. L., J. E. Peterson, T. Daley, B. Kaelin, L. Myer, J. Queen, P. D'Onfro, and W. Rizer, 1997, Fracture detection using crosswell and single well surveys: *Geophysics*, **62**, 495-504.

Mateeva, A., J. Ferrandis, A. Bakulin, P. Jorgensen, C. Gentry, and J. Lopez, 2007a, Shell steers virtual sources for salt, subsalt imaging: *Offshore*, **67**, 94-96.

Mateeva, A., J. Ferrandis, A. Bakulin, P. Jorgensen, C. Gentry, and J. Lopez, 2007b, Steering virtual sources for salt and subsalt imaging: *SEG Technical Program Expanded Abstracts*, **26**, 3044-3048.

Mehta, K., A. Bakulin, J. Sheiman, R. Calvert, and R. Snieder, 2007, Improving the virtual source method by wavefield separation: *Geophysics*, **72**, V79-V86.

Murphy, J. R., R. W. Cook, and W. L. Rodi, 1999, Improved focal depth determination for use in CTBT monitoring: *Proceedings of the 21 stAnnual Seismic Research Symposium on Monitoring a Comprehensive Nuclear Test Ban Treaty*, 50-55.

Reiter, D., and R. H. Shumway, 1999, Improved Seismic Event Depth Estimation Using Cepstral Analysis: *Weston Geophysical Scientific Report WBCA6*.

Rickett, J., and J. Claerbout, 1996, Passive seismic imaging applied to synthetic data: *Stanford Exploration Project*, **92**, 83-90.

Robertsson, J. O. A., and A. Curtis, 2002, Wavefield separation using densely deployed three-component single-sensor groups in land surface-seismic recordings: *Geophysics*, **67**, 1624-1633.

Robertsson, J. O. A., and E. Muyzert, 1999, Wavefield separation using a volume distribution of three component recordings: *Geophysical Research Letters*, **26**, 2821-2824.

Schuster, G., J. Yu, J. Sheng, and J. Rickett, 2004, Interferometric/daylight seismic imaging: *Geophysical Journal International*, **157**, 838-852.

Schuster, G. T., F. Followill, L. J. Katz, J. Yu, and Z. Liu, 2003, Autocorrelogram migration: Theory: *Geophysics*, **68**, 1685-1694.

Schuster, G. T., and M. Zhou, 2006, A theoretical overview of model-based and correlation-based redatuming methods: *Geophysics*, **71**, SI103-SI110.

Shapiro, N. M., M. Campillo, L. Stehly, and M. H. Ritzwoller, 2005, High-Resolution Surface-Wave Tomography from Ambient Seismic Noise: *Science*, **307**, 1615-1618.

Shearer, P. M., 1999, Introduction to Seismology: Cambridge University Press.

Siddiqui, K., S. Clark, D. Epili, N. Chazalnoel, and L. Anderson, 2003, Velocity model building methodology and PSDM in deep water Gulf of Mexico: A case history: *SEG Technical Program Expanded Abstracts*, **22**, 442-445.

Snieder, R., 2004, Extracting the Green's function from the correlation of coda waves: A derivation based on stationary phase: *Physical Review E*, **69**, 46610.

Song, H. C., W. A. Kuperman, W. S. Hodgkiss, T. Akal, and C. Ferla, 1999, Iterative time reversal in the ocean: *The Journal of the Acoustical Society of America*, **105**, 3176.

Sun, Y., F. Qin, S. Checkles, and J. P. Leveille, 2000, 3-D prestack Kirchhoff beam migration for depth imaging: *Geophysics*, **65**, 1592-1603.

Sutin, A., P. Johnson, and J. TenCate, 2003, DEVELOPMENT OF NONLINEAR TIME REVERSED ACOUSTICS (NLTRA) FOR APPLICATIONS TO CRACK DETECTION IN SOLIDS: *Proceedings of the 5th World Congress on Ultrasonics*, 121?124.

Thomas, J. L., F. Wu, and M. Fink, 1996, Time Reversal Focusing Applied to Lithotripsy: *ULTRASONIC IMAGING*, **18**, 106-121.

van Manen, D., A. Curtis, and J. O. A. Robertsson, 2006, Interferometric modeling of wave propagation in inhomogeneous elastic media using time reversal and reciprocity: *Geophysics*, **71**, SI47-SI60.

van Manen, D., J. Robertsson, and A. Curtis, 2005, Modeling of Wave Propagation in Inhomogeneous Media: *Physical Review Letters*, **94**, 164301.

Wang, B., F. Audebert, D. Wheaton, and V. Dirks, 2006, Subsalt velocity analysis by combining wave equation based redatuming and Kirchhoff based migration velocity analysis: *SEG Technical Program Expanded Abstracts*, **25**, 2440-2444.

Wang, B., F. Qin, F. Audebert, and V. Dirks, 2005, A fast and low cost alternative to subsalt wave equation migration perturbation scans: *SEG Technical Program Expanded Abstracts*, **24**, 2257-2260.

Wapenaar, C. P. A., and A. J. Berkhout, 1989, Elastic wave field extrapolation: Elsevier.

Wapenaar, K., 2004, Retrieving the Elastodynamic Green's Function of an Arbitrary Inhomogeneous Medium by Cross Correlation: *Physical Review Letters*, **93**, 254301.

Wapenaar, K., and J. Fokkema, 2005, Seismic interferometry, time reversal and reciprocity: *67th Annual International Meeting, EAEG, Expanded Abstracts*, G-031.

Wapenaar, K., and J. Fokkema, 2006, Green's function representations for seismic interferometry: *Geophysics*, **71**, SI33-SI46.

Wapenaar, K., J. Fokkema, and R. Snieder, 2005, Retrieving the Green's function in an open system by cross correlation: A comparison of approaches (L): *The Journal of the Acoustical Society of America*, **118**, 2783-2786.

Whitmore, N. D., 1983, Iterative depth migration by backward time propagation: *SEG Technical Program Expanded Abstracts*, **2**, 382-385.

Willis, M. E., R. Lu, D. Burns, M. N. Toksöz, X. Campman, and M. V. d. Hoop, 2005, A novel application of time reversed acoustics: salt dome flank imaging using walk away VSP surveys: *MIT Earth Resources Laboratory Industry Consortium Annual Report*.

Willis, M. E., R. Lu, X. Campman, M. N. Toksöz, Y. Zhang, and M. V. d. Hoop, 2006, A novel application of time-reversed acoustics: Salt-dome flank imaging using walkaway VSP surveys: *Geophysics*, **71**, A7-A11.

Xu, S., and S. Jin, 2006, Wave equation migration of turning waves: *SEG Technical Program Expanded Abstracts*, **25**, 2328-2332.

Yoon, K., K. J. Marfurt, and W. Starr, 2004, Challenges in reverse-time migration: *SEG Technical Program Expanded Abstracts*, **23**, 1057-1060.